# Multiscale study of microstructural evolution and damage in rail steels

Kumar, Ankit

**DOI**
10.4233/uuid:00f46cda-0b41-48a1-a7c4-f050c13d90fb

**Publication date**
2019

**Document Version**
Final published version

**Citation (APA)**
Kumar, A. (2019). *Multiscale study of microstructural evolution and damage in rail steels*. [Dissertation (TU Delft), Delft University of Technology]. https://doi.org/10.4233/uuid:00f46cda-0b41-48a1-a7c4-f050c13d90fb

**Important note**
To cite this publication, please use the final published version (if applicable).
Please check the document version above.

# Multiscale study of microstructural evolution and damage in rail steels

Ankit Kumar

# Multiscale study of microstructural evolution and damage in rail steels

Dissertation

For the purpose of obtaining the degree of doctor
at Delft University of Technology,
by the authority of the Rector Magnificus prof.dr.ir. T.H.J.J. van der Hagen,
chair of the Board for Doctorates,
to be defended publicly on
Thursday 27 June 2019 at 10:00 hours

by

Ankit Kumar
Master of Technology in Metallurgical and Materials Engineering
Indian Institute of Technology, Roorkee, India
born in Bijnor, Uttar Pradesh, India

This dissertation has been approved by the promotors:

Prof. dr. ir. J. Sietsma and Prof. dr. ir. R. H. Petrov

Composition of the doctoral committee:

| | |
|---|---|
| Rector Magnificus | chairperson |
| Promoters: | |
| Prof. dr. ir. J. Sietsma | Delft University of Technology |
| Prof. dr. ir. R. H. Petrov | Ghent University |
| | |
| Independent members: | |
| Prof. dr. ir. R. P. B. J. Dollevoet | Delft University of Technology |
| Prof. dr. ir. L. A. I. Kestens | Delft University of Technology |
| Prof. dr. D. Juul Jensen | Technical University of Denmark |
| Prof. dr. F. G. Caballero | National Centre for Metallurgical Research (CENIM-CSIC), Spain |
| | |
| Other Member: | |
| Dr. Dipl.-Ing. M. Herbig | Max Planck Institute for Iron Research, Germany |

The research described in this thesis was carried out in the Department of Materials Science and Engineering, Delft University of Technology, the Netherlands and Max Plank Institute for Iron Research, Düsseldorf, Germany.

Dr. Dipl.-Ing. M. Herbig has contributed greatly to this dissertation as a daily supervisor.

This research was carried out under project number F91.10.12475b in the framework of the research program of the Materials innovation institute (M2i), the Netherlands (www.m2i.nl).







chauhan.ankit007@gmail.com
ISBN xxxxxxxxxxxxxxx
An electronic version of this dissertation is available at
http://repository.tudelft.nl/

**Table of Contents**

# 1 Introduction

## 1.1 Background and industrial relevance

The Dutch rail infrastructure manager ProRail is responsible for the Dutch rail network in three main aspects: building, maintenance, and safety. The company ensures the daily safe transport of 1,200,000 passengers and 100,000 tonnes of products with 6550 trains on 7000 km of track. Therefore, permanent infrastructural integrity is of crucial importance to guarantee disruption-free operations. ProRail has set a goal to achieve zero avoidable disturbances on its entire rail network by 2020. In recent years, ProRail statistics show a sharp increase of uncontrolled damage phenomena in curved rails, switches and more specifically in crossing noses. Switches and curved tracks are primarily made from conventional pearlitic steels with eutectoid composition. They are subjected to rolling contact fatigue and wear, which leads to the formation of detrimental microstructural features on the rail surface such as the White and Brown Etching Layers (WEL & BEL). These layers are considered to be the main cause of crack initiation and propagation in switches and curved tracks leading to final fracture. Similarly, crossing noses are also subjected to rolling contact fatigue and irregular wear during wheel-rail contact. Additionally, the severe impact fatigue loading that exists in crossing noses leads to degradation of their geometry and material. Currently, every week two crossings are replaced urgently which means an average of 100 urgent replacements per year. In general, 300 crossings per year are planned for regular replacement which causes disruption in normal transport flow and high maintenance, replacement and monitoring costs. This number may grow further if no corrective actions are taken. Each unforeseen replacement of a crossing takes several hours, or even up to several days; a time period during which the transport flow through the place of replacement is deviated or delayed, spreading as ink stain through the rail network.

The type of damage found in curved rails, switches and crossings includes irregular wear, plastic deformation, cracking, flaking, head checks, squats, and partial brittle fracture [1–6]. From the material's point of view, several microstructural features such as phases, grain orientation, grain/phase/twin boundaries and intermetallic inclusions, can affect the damage mechanisms in the steels used in curved rail tracks, switches and crossings [7–12]. Also, the

defects generated in the material during manufacturing such as porosity or voids, together with the microstructural changes in rails during the service (such as formation of the WEL/BEL, formation of nanocrystalline layer on rail surface, and strain induced martensitic formation), can lead to damage in rails [4,7,9,10,13–17]. Therefore, there is an essential need of scientific research with a strong focus on damage in different rail steels in relation with their microstructure and exploitation conditions.

## 1.2 Research objective

This thesis is written within the framework of Ph.D. Project F91.10.12475b of the Materials innovation institute under FOM "*Physics of Failure"* program. The main objective of this research is to elucidate the physical mechanism of failure in different rail steels in relation with their microstructure. Three primary steel grades are investigated in this research, *i.e.* conventional pearlitic steels, austenitic Hadfield steels and complex carbide free bainitic steels. Microstructure changes in pearlitic steels such as the formation of the WELs and the BELs under rolling contact fatigue are investigated from macroscale to atomic scale with the aim to understand their formation mechanism. Scientific ideas are further proposed to avoid such microstructural alterations in pearlitic steels. A detailed understanding of fracture behaviour of the WELs is established in relation with their microstructural features such as the presence of austenite phase, strain induced austenite to martensite transformation, grain size, dislocation density, and carbon segregation at grain boundaries and dislocations.

Further, we investigate the microstructural changes in Hadfield steels under impact fatigue loading in the crossing nose and identify the microstructural features at macro and nanoscales such as interfaces, inclusions, casting defects, nano-twins and dislocation structures, which are responsible for crack initiation and crack growth. We also examine the damage mechanism in complex carbide free bainitic in relation with their microstructure. The knowledge obtained from this work can be used for more accurate assessment of damage development in presently used steels.

Finally, we propose a design of high strength and damage-resistant bainitic steel for application in switches and crossings based on the acquired understanding of microstructural damage in rail steels. The proposed design strategy also incorporates the complex loading conditions in rail crossings, thermodynamic and microstructural points of view, and composition selection based on displacive bainitic transformation.

## 1.3 Outline

Chapter 2 provides a comprehensive overview of the current understanding of damage in several rail steel grades in relation with their microstructure under rolling and impact

fatigue loading conditions. The microstructures of conventional pearlite, austenitic Hadfield steels, and complex bainitic steels are extensively discussed.

In chapter 3, we examine the microstructural evolution of WELs and BELs under wheel-rail interaction. Further, the formation mechanism of these layers is discussed in this chapter based on characterisation of their microstructure from macroscale to atomic scale and on thermodynamic simulations. In order to understand these mechanisms, temperature profiles at the wheel-rail interface are simulated using a finite element model. Furthermore, we investigate the cementite dissolution and austenite formation mechanisms in the WELs and BELs based on the diffusional calculations.

Charter 4 focuses on the *in-situ* fracture toughness measurements of WELs. Furthermore, the WELs fracture response is studied in relation with their microstructural features, *i.e.* grain size, presence of austenite, strain induced austenite to martensite transformation and the carbon segregation on dislocations and grain boundaries. We also compared the estimated fracture toughness values of the WELs with different microstructures such as pearlite, cold drawn pearlitic wires containing carbon saturated nanocrystalline ferrite/deformation induced martensite, and nanocrystalline Fe thin films.

In chapter 5, we investigate the mechanism of damage initiation and propagation in Hadfield steel crossings in relation with microstructural features such as casting porosity, intermetallic inclusions, strain induced austenite to martensite transformation, and deformation twinning. This chapter also covers the fatigue crack growth in the microstructure in relation to different twin boundary orientations under laboratory scale low cycle fatigue testing.

Chapter 6 focuses on the *in-situ* strain partitioning and damage in continuously cooled carbide free bainitic steels using micro Digital Image Correlation (μ-DIC). We investigate the strains partitioning between different microstructural constituents such as martensite, upper bainite, lath bainite, and blocky or thin film austenite during uniaxial tensile tests. We also establish understanding of active damage nucleation and propagation mechanisms in relation with different microstructural constituents such as phases, interphases, and grain/phase boundaries. In addition, the microstructural changes such as stain induced transformation of blocky austenite into martensite are investigated during interrupted tensile testing coupled with the determination of the austenitic fraction in X-ray diffraction analysis. Thus, a strong understanding of damage in complex microstructure of continuously cooled carbide free bainitic steels is established.

In chapter 7, we propose a design of high strength and damage resistant carbide free bainitic steels for application in rail crossings. Our understanding of damage in relation with microstructure in different steel grades is the main basis for the current design strategy. Further, the thermodynamics aspects, the concepts of displacive transformation

mechanisms, and loading conditions in crossings are also taken into account for this design. The designed microstructure is tested for static and impact fatigue performance. We also investigate the *in-situ* strain partitioning response of the designed bainitic microstructure under uniaxial tensile loading conditions. Strengthening mechanisms due to fine grain size, nano-cementite precipitation, and carbon segregation at the dislocations are also discussed. We compare our experimental observations such as carbon partitioning in austenite and bainite phase fraction in the final microstructure with the predictions of displacive bainitic transformation theory.

Chapter 8 lists the future recommendations for this research field.

## References


[1] M. Steenbergen, R. Dollevoet, On the mechanism of squat formation on train rails – Part I: Origination, Int. J. Fatigue. 47 (2013) 361–372. doi:10.1016/J.IJFATIGUE.2012.04.023.

[2] A. Al-Juboori, D. Wexler, H. Li, H. Zhu, C. Lu, A. McCusker, J. McLeod, S. Pannil, Z. Wang, Squat formation and the occurrence of two distinct classes of white etching layer on the surface of rail steel, Int. J. Fatigue. 104 (2017) 52–60. doi:10.1016/J.IJFATIGUE.2017.07.005.

[3] A. Al-Juboori, H. Zhu, D. Wexler, H. Li, C. Lu, A. McCusker, J. McLeod, S. Pannila, J. Barnes, Evolution of rail surface degradation in the tunnel: The role of water on squat growth under service conditions, Eng. Fract. Mech. 209 (2019) 32–47. doi:10.1016/J.ENGFRACMECH.2019.01.018.

[4] W. Lojkowski, M. Djahanbakhsh, G. Bürkle, S. Gierlotka, W. Zielinski, H.-J. Fecht, Nanostructure formation on the surface of railway tracks, Mater. Sci. Eng. A. 303 (2001) 197–208. doi:10.1016/S0921-5093(00)01947-X.

[5] Y. V Ivanisenko, R.Z. Valiev, W. Lojkowski, A. Grob, H.-J. Fecht, Nanostructure Formation and Carbides Dissolution in Rail Steel Deformed by High Pressure Torsion, Ultrafine Grained Mater. II. (2013). doi:doi:10.1002/9781118804537.ch6.

[6] X. Feng, F. Zhang, C. Zheng, B. Lü, Micromechanics behavior of fatigue cracks in Hadfield steel railway crossing, Sci. China Technol. Sci. 56 (2013) 1151–1154. doi:10.1007/s11431-013-5181-x.

[7] J.E. Garnham, C.L. Davis, The role of deformed rail microstructure on rolling contact fatigue initiation, Wear. 265 (2008) 1363–1372. doi:10.1016/J.WEAR.2008.02.042.

[8] G. Baudry, A. Pineau, Influence of strain-induced martensitic transformation on the

low-cycle fatigue behavior of a stainless steel, Mater. Sci. Eng. 28 (1977) 229–242. doi:10.1016/0025-5416(77)90176-8.

[9] J. Kang, F.C. Zhang, X.Y. Long, B. Lv, Cyclic deformation and fatigue behaviors of Hadfield manganese steel, Mater. Sci. Eng. A. 591 (2014) 59–68. doi:10.1016/J.MSEA.2013.10.072.

[10] Q. Zhou, L. Qian, J. Meng, L. Zhao, F. Zhang, Low-cycle fatigue behavior and microstructural evolution in a low-carbon carbide-free bainitic steel, Mater. Des. 85 (2015) 487–496. doi:10.1016/j.matdes.2015.06.172.

[11] M. Steenbergen, R. Dollevoet, On the mechanism of squat formation on train rails – Part II: Growth, Int. J. Fatigue. 47 (2013) 373–381. doi:10.1016/J.IJFATIGUE.2012.04.019.

[12] J.H. Xiao, F.C. Zhang, L.H. Qian, Contact stress and residual stress in the nose rail of a high manganese steel crossing due to wheel contact loading, Fatigue Fract. Eng. Mater. Struct. 37 (2013) 219–226. doi:10.1111/ffe.12108.

[13] W. Österle, H. Rooch, A. Pyzalla, L. Wang, Investigation of white etching layers on rails by optical microscopy, electron microscopy, X-ray and synchrotron X-ray diffraction, Mater. Sci. Eng. A. 303 (2001) 150–157. doi:10.1016/S0921-5093(00)01842-6.

[14] S. Li, J. Wu, R.H. Petrov, Z. Li, R. Dollevoet, J. Sietsma, “Brown etching layer”: A possible new insight into the crack initiation of rolling contact fatigue in rail steels?, Eng. Fail. Anal. 66 (2016) 8–18. doi:10.1016/J.ENGFAILANAL.2016.03.019.

[15] J. Wu, R.H. Petrov, M. Naeimi, Z. Li, R. Dollevoet, J. Sietsma, Laboratory simulation of martensite formation of white etching layer in rail steel, Int. J. Fatigue. 91 (2016) 11–20. doi:10.1016/J.IJFATIGUE.2016.05.016.

[16] S.B. Newcomb, W.M. Stobbs, A transmission electron microscopy study of the white-etching layer on a rail head, Mater. Sci. Eng. 66 (1984) 195–204. doi:10.1016/0025-5416(84)90180-0.

[17] J. Takahashi, K. Kawakami, M. Ueda, Atom probe tomography analysis of the white etching layer in a rail track surface, Acta Mater. 58 (2010) 3602–3612. doi:10.1016/J.ACTAMAT.2010.02.030.

# 2

# Damage mechanisms of steel grades used in railway applications

## 2.1 Introduction

In this chapter, we discuss the fundamental failure mechanisms which are identified in literature in various steel grades used in railway applications. In order to come to generic knowledge on these mechanisms, a range of steel microstructures are discussed here, ranging from relatively simple pearlite to the complexity of bainite-based microstructures. Additionally, deformation and damage mechanisms in the fully austenitic microstructure of cast Hadfield steels are also discussed. To understand the damage in these steel microstructures, it is important to first understand the specific loading conditions which occur in rail components such as rail crossings, switches and curved tracks.

Railway switches and crossings are used to guide the train over a straight or a divergent track. They are subjected to impact fatigue, Rolling Contact Fatigue (RCF) and wear during the wheel-rail interaction. The gap between the wing rails and the crossing nose (as shown in Fig. 2.1(a)) is responsible for the cyclic impact loading on the crossing nose [1]. These complex loading conditions lead to in-service defects such as irregular wear, accumulated plastic deformation and flaking on the surface of the crossing nose, as shown in Fig. 2.1(b). Similar flaking and defects, such as squats, are also reported in the case of curved tracks and switches due to RCF loading [2,3].

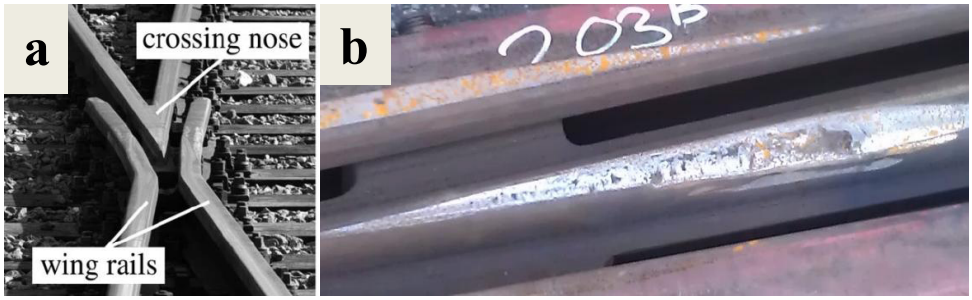


Fig. 2.1 (a) Image of a railway crossing; (b) Degraded crossing nose showing severe wear and flaking on its surface.

These surface and subsurface defects in railway switches, crossings and curved tracks depend on the microstructure of the applied steels. Various microstructural features such as phases, grain/phase boundaries, crystallographic grain orientations, precipitates and intermetallic inclusions affect the crack initiation and propagation in different materials [4–7]. Additionally, the studies show that the damage mechanisms in materials with different microstructures also depend on the operating deformation mechanisms [8–12]. Different steels such as pearlitic steels, cast austenitic Hadfield steels, and bainitic steels respond differently during the wheel-rail interaction in the abovementioned rail components [1]. The current understanding of the damage and deformation mechanisms in steels (*i.e.* pearlitic, austenitic and carbide free bainitic steels) that are used in railway switches/crossings and curved tracks, are discussed in this chapter.

## 2.2 Fine pearlitic steels

Pearlitic steels (R350HT) with eutectoid composition (the carbon concentration $x_C$ = 0.72 wt.%) and fully pearlitic microstructure are generally used both in switches and crossings and in curved tracks. Pearlite is a mixture of two phases: soft ferrite and hard cementite. In pearlite, the lamellar structures of ferrite (α) and cementite (θ) phase interpenetrate in three dimensions (Fig. 2.2(a,b)). R350HT steels offer high strength combined with acceptable ductility, toughness and wear resistance [13]. These steels contain around 0.8-1.7 wt.% Mn, which provides good corrosion resistance and reduces the α and θ lamellae thickness, providing high yield strength [14]. Even with a similar level of strength, fine pearlitic steels offer greater wear resistance than bainitic steels [15,16].

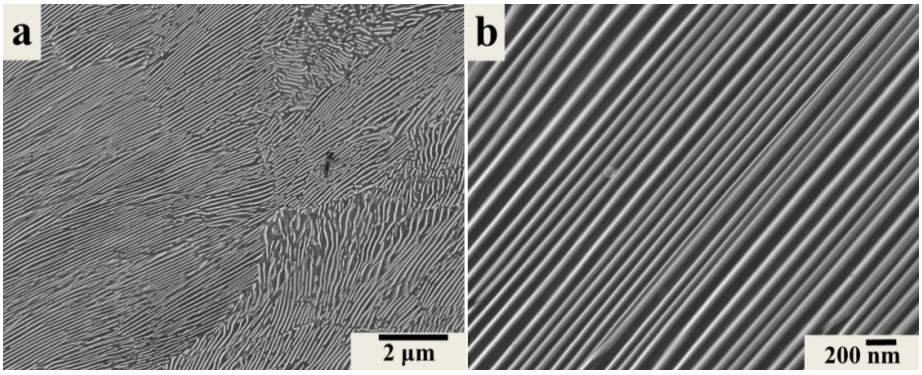


Fig. 2.2 (a) Secondary electron (SE) image of pearlitic microstructure of R350HT; (b) Magnified SE image of R350HT showing ferrite (α) (in dark grey) and cementite (θ) lamellae (in light grey).

Damage in the pearlitic steels strongly depends on their microstructure and microstructural evolution under wheel-rail contacts over time. It should be noted that the microstructure in the applied material often contains additional microstructural components, like MnS, $Al_2O_3$ inclusions or proeutectoid ferrite. In addition, mechanical loading and temperature increase during wheel-rail contact can lead to the formation of White and Brown Etching Layers [2,3,17–23]. Literature shows the following metallurgical features being responsible for damage initiation and propagation in pearlitic steels.

(i) Crack initiation and propagation from the strain flattened MnS inclusions at the rail subsurface [24].

(ii) Crack initiation and propagation from the interfaces between proeutectoid ferrite and pearlite [24].

(iii) Delamination and transverse fracture of White Etching Layers (WELs) formed on rail raceway during wheel-rail interaction [2,3,17–23].

(iv) Delamination and fracture of Brown Etching layers (BELs) formed on the rail surface or at the subsurface just below the WELs [25].

The WELs have been investigated by many researchers for a number of years [2,3,17–23]. However, there is still an ongoing debate on the formation mechanism of the WELs and the formation of BELs has not been investigated in detail. Therefore, the formation mechanisms of the WELs and BELs and the damage in rails associated with these layers is further studied in chapters 3 and 4 of this thesis.

## 2.3 Cast Hadfield steels/Mn13

Cast Hadfield steel/Mn13 with a chemical composition of Fe-1.1C-13Mn-0.4Si (in wt.%) is widely used in railway crossing applications due to its high toughness and high work hardening ability [26–30]. This steel is usually cast in the shape of railway crossings. The casting process leads to formation of the $(Fe,Mn)_3C$ carbides in the steel microstructure which may act as crack initiation sites [27]. Therefore, after casting, the Hadfield steel crossings are solution annealed at 1050 °C for 3 hours followed by quenching [27]. This gives a fully austenitic microstructure to the Hadfield steel [27,28]. The casting process and the high temperature in solution annealing also lead to large grain sizes (*i.e.* 230 ± 50 μm) in the Hadfield steels microstructure (Fig. 2.3(a)).

In the absence of a protective atmosphere during solution annealing, the high temperature produces considerable surface decarburization and loss of Mn in Hadfield steel. This causes formation of α'-martensite on the surface upon quenching, which is responsible for poor performance of cast Hadfield steel during initial loading cycles in rail crossings. The microcracks initiate due to the presence of this brittle α'-martensite on the crossing surface [27]. However, after some grinding cycles aimed to remove the α'-martensite surface layer, cast Hadfield steel offers good performance which is attributed to the high strain-hardening capability of its austenitic microstructure [28,30,31]. This strain hardening in cast Hadfield steels is due to their low Stacking Fault Energy (SFE) (*i.e.* 23 $mJ/m^2$) [32]. SFE refers to the energy per unit area required to produce a stacking fault and hence it determines the distance between the Shockley partial dislocations [33]. Metals with low SFE or wide stacking fault strain harden more rapidly because of the difficulty in dislocations cross-slip. Cast Hadfield steels in the initial deformation stage form stacking faults and a high dislocation density in their microstructure. Under a specific critical stress leading Shockley partials associated with a stacking fault separate from their trailing counterpart and a faulted region extends to form a deformation twin [34,35]. Fig. 2.3(b) shows such deformation twinning that formed under impact fatigue in a cast Hadfield steels crossing. These twinning features obstruct the motion of the dislocations in the Hadfield austenitic microstructure and thus provide good strain hardening response [36,37].

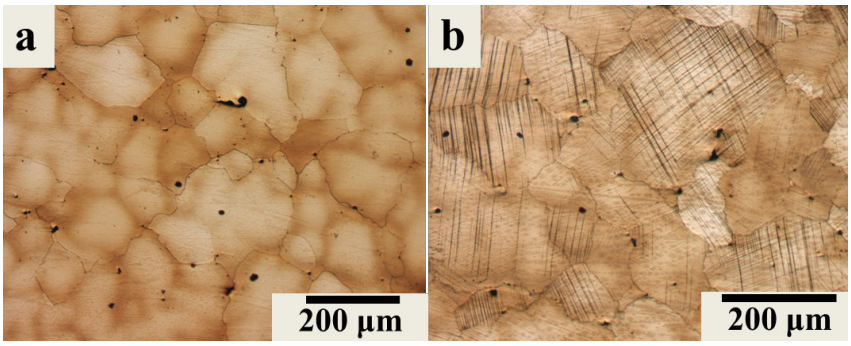


Fig. 2.3 (a) Optical micrograph showing the Hadfield steel microstructure, (b) Twin formation in the Hadfield steel microstructure under the impact fatigue loading in a rail crossing.

Various studies have been conducted to study the damage in cast Hadfield steel rail crossings [29,38,39]. Xiao *et al.* [38] showed that crack initiation and growth in cast Hadfield steel crossings generally occur at the crossing subsurface (0.8-1.0 mm below the surface), which is due to the combined effect of maximum contact stresses at the surface and the maximum residual stresses at 1.5-2.0 mm below the crossing surface. Lv *et al.* [29] claim that the grain boundaries, plastic deformation bands, twinning and the crystal orientation of austenitic grains in cast Hadfield steels have no correlation with the nucleation and growth of fatigue cracks in the crossing nose. They rather observed layers with a high concentration of vacancy clusters formed parallel to the working surface of the cast Hadfield steel crossing. These clusters are proposed to be responsible for the fatigue crack initiation at the crossing subsurface, where the density of the clusters was largest. These vacancy clusters coalesce to form micropores which further interconnect to form a fatigue crack under rolling contact/impact fatigue in cast Hadfield steel crossings. Yong *et al.* [40] also propose that the formation of microvoids and their coalescence in the region of high stresses in the crossings are responsible for damage in Hadfield steel and that the damage has no correlation with the crystal orientations. However, Harzallah *et al.* [26] showed that the crack initiation in a cast Hadfield steel crossing occurs at the surface rather than subsurface and further propagates into the material. They concluded that very fine twinning substructures are responsible for the crack initiation in the Hadfield steels.

Another possible damage mechanism in the Hadfield steel is strain-induced martensitic transformation from metastable austenite (ϒ) to ε-martensite or α' martensite. This transformation occurs due to motion of Shockley partial dislocations on an invariant set of planes [34,35,41–43]. This requires the displacement of $a/6\langle 11\bar{2}\rangle$ partials on every second {111} plane of the austenite [35]. Due to this, the crystal structure of the parent phase changes because of the change of stacking sequence of {111} atomic planes. Sato *et al.* [44] propose that an SFE smaller than 20 mJ/m$^2$ favors this transformation. In materials with an SFE above this value, it is rarely observed. However, Ronald *et al.* [45] showed this

ϒ to α'-martensite transformation in deep drawn high Mn austenitic steels with a SFE value in the range of 22-52 mJ/m$^2$. Hence, there is a considerable dispute in the scientific community for this transformation in low stacking fault alloys. Das *et al.* [46] showed that this transformation strongly depends upon the temperature, the magnitude of the stress/strain and the strain rate. They propose that this transformation is less likely to occur under the high strain rate loading condition. Studies show that the interfaces between α' martensite and ϒ can form potential damage initiation sites in low stacking fault alloys [44–46]. Microvoids are generally found to initiate at these interfaces and later combine to form a crack [46]. Additionally, a relative increase in volume due to martensite having a lower density than austenite will also affect the damage in the microstructure.

Based on the above described different damage mechanisms in cast Hadfield steels and the different opinions of different researchers, it is required to further explore the damage mechanisms in cast Hadfield steels under impact fatigue loading conditions in railway crossings. We investigate the detailed deformation and damage mechanisms in the cast Hadfield steel in chapter 5.

## 2.4 High strength carbide free bainitic steel

Carbide free bainitic steels have attracted much interest in recent years for the use in railways applications such as rail tracks, switches and crossings [15,16,47–52]. They offer excellent mechanical properties, such as high strength, high hardness and good toughness due to their fine complex microstructure [46–51]. The microstructure of bainitic steels primarily consists of fine bainitic laths, blocky retained austenite and thin film retained austenite [46–51]. The precipitation of interlath carbides in these steels is suppressed by their high Si content (1.5-2.0 wt.%) as these carbides are considered to be detrimental for the fatigue performance [51]. Silicon suppresses the precipitation of these carbides during the bainitic transformation due to its low solubility in cementite [47,50].

The damage in carbide free bainitic steels still lacks a thorough understanding due to their complex microstructure. Few studies have been reported in literature on the damage of carbide free bainitic steels in railway applications [47,53–55]. Leiro *et al.* [47] showed that the cracks in carbide free bainitic steels initiate and propagate due to deformation of bainitic ferrite laths in the sliding direction of rail wheel. The cracks were found to nucleate and grow along the bainitic ferrite lath interfaces which were oriented in the sliding direction. This indicates that the texture development or the change in the orientation of the grains during the sliding is an important factor for the damage study. Zhang *et al.* [54] studied the worn surfaces of a rail crossing made from the carbide free bainitic steel. They found the formation of a nanocrystalline layer on the crossing surface due to severe plastic deformation (SPD). The formation mechanism of this layer was strain induced dynamic recrystallization in the bainitic microstructure under the combined effect of temperature

rise and SPD. This hard nanocrystalline layer is considered to be detrimental under RCF and impact fatigue and leads to cracking at the surface of crossings. Yang *et al.* [53] observed the formation of similar nanocrystalline layers on the surface of a carbide free bainitic steel crossing. They showed crack initiation and propagation taking place by the delamination of these layers on the crossing surface. Bakshi *et al.* [55] propose that metastable austenite at the rail surface undergoes strain induced transformation into brittle martensite, which can also affect the damage in carbide free bainitic steels.

With respect to the complex microstructure of the carbide free bainitic steels, there exists a lack of understanding of damage in these steels in relation with their microstructural features. Therefore, a detailed study on the damage mechanism in carbide free bainitic steels is presented in chapter 6 of this thesis. Additionally, based on our understanding of the damage in relation with the carbide free bainitic microstructure, a high-strength and damage-resistant steel design is proposed in chapter 7 of this thesis.

## References


[1] M. Pletz, W. Daves, H. Ossberger, A wheel set/crossing model regarding impact, sliding and deformation—Explicit finite element approach, Wear. 294–295 (2012) 446–456. doi:10.1016/J.WEAR.2012.07.033.

[2] M. Steenbergen, R. Dollevoet, On the mechanism of squat formation on train rails – Part I: Origination, Int. J. Fatigue. 47 (2013) 361–372. doi:10.1016/J.IJFATIGUE.2012.04.023.

[3] M. Steenbergen, R. Dollevoet, On the mechanism of squat formation on train rails – Part II: Growth, Int. J. Fatigue. 47 (2013) 373–381. doi:10.1016/J.IJFATIGUE.2012.04.019.

[4] M. Herbig, A. King, P. Reischig, H. Proudhon, E.M. Lauridsen, J. Marrow, J.-Y. Buffière, W. Ludwig, 3-D growth of a short fatigue crack within a polycrystalline microstructure studied using combined diffraction and phase-contrast X-ray tomography, Acta Mater. 59 (2011) 590–601. doi:10.1016/J.ACTAMAT.2010.09.063.

[5] A. King, W. Ludwig, M. Herbig, J.-Y. Buffière, A.A. Khan, N. Stevens, T.J. Marrow, Three-dimensional in situ observations of short fatigue crack growth in magnesium, Acta Mater. 59 (2011) 6761–6771. doi:10.1016/J.ACTAMAT.2011.07.034.

[6] F. Ram, Z. Li, S. Zaefferer, S.M. Hafez Haghighat, Z. Zhu, D. Raabe, R.C. Reed, On the origin of creep dislocations in a Ni-base, single-crystal superalloy: an ECCI, EBSD, and dislocation dynamics-based study, Acta Mater. 109 (2016) 151–161. doi:10.1016/J.ACTAMAT.2016.02.038.

[7] T. Zhai, A.J. Wilkinson, J.W. Martin, A crystallographic mechanism for fatigue crack propagation through grain boundaries, Acta Mater. 48 (2000) 4917–4927. doi:10.1016/S1359-6454(00)00214-7.

[8] D. Taylor, J.F. Knott, Fatigue crack propagation behaviour of short cracks; the effect of microstructure, Fatigue Fract. Eng. Mater. Struct. 4 (1981) 147–155.

[9] L. Liu, J. Wang, S.K. Gong, S.X. Mao, Atomistic observation of a crack tip approaching coherent twin boundaries, Sci. Rep. 4 (2014) 4397.

[10] T. Sinha, Y. Kulkarni, Alternating brittle and ductile response of coherent twin boundaries in nanotwinned metals, J. Appl. Phys. 116 (2014) 183505.

[11] A. Grabulov, R. Petrov, H.W. Zandbergen, EBSD investigation of the crack initiation and TEM/FIB analyses of the microstructural changes around the cracks formed under Rolling Contact Fatigue (RCF), Int. J. Fatigue. 32 (2010) 576–583. doi:10.1016/J.IJFATIGUE.2009.07.002.

[12] A. Grabulov, U. Ziese, H.W. Zandbergen, TEM/SEM investigation of microstructural changes within the white etching area under rolling contact fatigue and 3-D crack reconstruction by focused ion beam, Scr. Mater. 57 (2007) 635–638. doi:10.1016/J.SCRIPTAMAT.2007.06.024.

[13] B. Panda, R. Balasubramaniam, A. Moon, Microstructure and mechanical properties of novel rail steels, Mater. Sci. Technol. 25 (2009) 1375–1382.

[14] W. Fu, T. Furuhara, T. Maki, Effect of Mn and Si addition on microstructure and tensile properties of cold-rolled and annealed pearlite in eutectoid Fe-C alloys, ISIJ Int. 44 (2004) 171–178.

[15] P. Clayton, X. Su, Surface initiated fatigue of pearlitic and bainitic steels under water lubricated rolling/sliding contact, Wear. 200 (1996) 63–73.

[16] N. Jin, P. Clayton, Effect of microstructure on rolling/sliding wear of low carbon bainitic steels, Wear. 202 (1997) 202–207. doi:10.1016/S0043-1648(96)07271-7.

[17] S.B. Newcomb, W.M. Stobbs, A transmission electron microscopy study of the white-etching layer on a rail head, Mater. Sci. Eng. 66 (1984) 195–204. doi:10.1016/0025-5416(84)90180-0.

[18] G. Baumann, H.J. Fecht, S. Liebelt, Formation of white-etching layers on rail treads, Wear. 191 (1996) 133–140. doi:10.1016/0043-1648(95)06733-7.

[19] J. Wu, R.H. Petrov, S. Kölling, P. Koenraad, L. Malet, S. Godet, J. Sietsma, Micro and Nanoscale Characterization of Complex Multilayer-Structured White Etching Layer in Rails, Met. . 8 (2018). doi:10.3390/met8100749.

[20] J. Wu, R.H. Petrov, M. Naeimi, Z. Li, R. Dollevoet, J. Sietsma, Laboratory simulation of martensite formation of white etching layer in rail steel, Int. J. Fatigue. 91 (2016) 11–20. doi:10.1016/J.IJFATIGUE.2016.05.016.

[21] J. Takahashi, K. Kawakami, M. Ueda, Atom probe tomography analysis of the white etching layer in a rail track surface, Acta Mater. 58 (2010) 3602–3612. doi:10.1016/J.ACTAMAT.2010.02.030.

[22] H.W. Zhang, S. Ohsaki, S. Mitao, M. Ohnuma, K. Hono, Microstructural investigation of white etching layer on pearlite steel rail, Mater. Sci. Eng. A. 421 (2006) 191–199. doi:10.1016/J.MSEA.2006.01.033.

[23] W. Österle, H. Rooch, A. Pyzalla, L. Wang, Investigation of white etching layers on rails by optical microscopy, electron microscopy, X-ray and synchrotron X-ray diffraction, Mater. Sci. Eng. A. 303 (2001) 150–157. doi:10.1016/S0921-5093(00)01842-6.

[24] J.E. Garnham, C.L. Davis, The role of deformed rail microstructure on rolling contact fatigue initiation, Wear. 265 (2008) 1363–1372. doi:10.1016/J.WEAR.2008.02.042.

[25] S. Li, J. Wu, R.H. Petrov, Z. Li, R. Dollevoet, J. Sietsma, "Brown etching layer": A possible new insight into the crack initiation of rolling contact fatigue in rail steels?, Eng. Fail. Anal. 66 (2016) 8–18. doi:10.1016/J.ENGFAILANAL.2016.03.019.

[26] R. Harzallah, A. Mouftiez, E. Felder, S. Hariri, J.-P. Maujean, Rolling contact fatigue of Hadfield steel X120Mn12, Wear. 269 (2010) 647–654. doi:10.1016/J.WEAR.2010.07.001.

[27] A.K. Srivastava, K. Das, Microstructural characterization of Hadfield austenitic manganese steel, J. Mater. Sci. 43 (2008) 5654–5658.

[28] W. Yan, L. Fang, K. Sun, Y. Xu, Effect of surface work hardening on wear behavior of Hadfield steel, Mater. Sci. Eng. A. 460 (2007) 542–549.

[29] B. Lv, M. Zhang, F.C. Zhang, C.L. Zheng, X.Y. Feng, L.H. Qian, X.B. Qin, Micro-mechanism of rolling contact fatigue in Hadfield steel crossing, Int. J. Fatigue. 44 (2012) 273–278.

[30] P.H. Adler, G.B. Olson, W.S. Owen, Strain hardening of Hadfield manganese steel, Metall. Mater. Trans. A. 17 (1986) 1725–1737.

[31] W. Yan, L. Fang, Z. Zheng, K. Sun, Y. Xu, Effect of surface nanocrystallization on abrasive wear properties in Hadfield steel, Tribol. Int. 42 (2009) 634–641.

[32] E. Mazancová, K. Mazanec, Stacking fault energy in high manganese alloys, Mater. Eng. 16 (2009) 26–31.

[33] R.P. Reed, R.E. Schramm, Relationship between stacking-fault energy and x-ray measurements of stacking-fault probability and microstrain, J. Appl. Phys. 45 (1974) 4705–4711. doi:10.1063/1.1663122.

[34] M.A. Meyers, O. Vöhringer, V.A. Lubarda, The onset of twinning in metals: a constitutive description, Acta Mater. 49 (2001) 4025–4039.

[35] L. Bracke, L. Kestens, J. Penning, Transformation mechanism of α′-martensite in an austenitic Fe–Mn–C–N alloy, Scr. Mater. 57 (2007) 385–388. doi:10.1016/J.SCRIPTAMAT.2007.05.003.

[36] I. Gutierrez-Urrutia, D. Raabe, Grain size effect on strain hardening in twinning-induced plasticity steels, Scr. Mater. 66 (2012) 992–996. doi:10.1016/J.SCRIPTAMAT.2012.01.037.

[37] I. Gutierrez-Urrutia, S. Zaefferer, D. Raabe, The effect of grain size and grain orientation on deformation twinning in a Fe–22 wt.% Mn–0.6 wt.% C TWIP steel, Mater. Sci. Eng. A. 527 (2010) 3552–3560. doi:10.1016/J.MSEA.2010.02.041.

[38] J.H. Xiao, F.C. Zhang, L.H. Qian, Contact stress and residual stress in the nose rail of a high manganese steel crossing due to wheel contact loading, Fatigue Fract. Eng. Mater. Struct. 37 (2013) 219–226. doi:10.1111/ffe.12108.

[39] X. Feng, F. Zhang, C. Zheng, B. Lü, Micromechanics behavior of fatigue cracks in Hadfield steel railway crossing, Sci. China Technol. Sci. 56 (2013) 1151–1154. doi:10.1007/s11431-013-5181-x.

[40] W. Wei-yong, L. Bing, K. Venkatesh, Effect of Temperature on Strength and Elastic Modulus of High-Strength Steel, J. Mater. Civ. Eng. 25 (2013) 174–182. doi:10.1061/(ASCE)MT.1943-5533.0000600.

[41] H. Beladi, I.B. Timokhina, Y. Estrin, J. Kim, B.C. De Cooman, S.K. Kim, Orientation dependence of twinning and strain hardening behaviour of a high manganese twinning induced plasticity steel with polycrystalline structure, Acta Mater. 59 (2011) 7787–7799. doi:10.1016/J.ACTAMAT.2011.08.031.

[42] H. Idrissi, K. Renard, L. Ryelandt, D. Schryvers, P.J. Jacques, On the mechanism of twin formation in Fe–Mn–C TWIP steels, Acta Mater. 58 (2010) 2464–2476. doi:10.1016/J.ACTAMAT.2009.12.032.

[43] A.. Bogers, W.. Burgers, Partial dislocations on the {110} planes in the B.C.C. lattice and the transition of the F.C.C. into the B.C.C. lattice, Acta Metall. 12 (1964) 255–261. doi:10.1016/0001-6160(64)90194-4.

[44] K. Sato, M. Ichinose, Y. Hirotsu, Y. Inoue, Effects of deformation induced phase transformation and twinning on the mechanical properties of austenitic Fe–Mn–Al

alloys, ISIJ Int. 29 (1989) 868–877.

[45] R.T.van Tol, Microstructure evolution in deformed austenitic Twinning Induced Plasticity steels, Delft University of Technology, 2014. doi:doi:10.4233/uuid:b2a057e2-c545-4bcc-854c-fe4b9344e486.

[46] A. Das, S. Tarafder, Experimental investigation on martensitic transformation and fracture morphologies of austenitic stainless steel, Int. J. Plast. 25 (2009) 2222–2247. doi:10.1016/J.IJPLAS.2009.03.003.

[47] A. Leiro, E. Vuorinen, K.-G. Sundin, B. Prakash, T. Sourmail, V. Smanio, F.G. Caballero, C. Garcia-Mateo, R. Elvira, Wear of nano-structured carbide-free bainitic steels under dry rolling–sliding conditions, Wear. 298 (2013) 42–47.

[48] L.C. Chang, The rolling/sliding wear performance of high silicon carbide-free bainitic steels, Wear. 258 (2005) 730–743.

[49] H.K.D.H. Bhadeshia, High performance bainitic steels, in: Mater. Sci. Forum, Trans Tech Publ, 2005: pp. 63–74.

[50] H.K.D.H. Bhadeshia, V. Jerath, Relating to carbide-free bainitic steels and method of producing such steels, (1999).

[51] F.G. Caballero, H.K.D.H. Bhadeshia, Very strong bainite, Curr. Opin. Solid State Mater. Sci. 8 (2004) 251–257.

[52] S. Sharma, S. Sangal, K. Mondal, Wear behaviour of bainitic rail and wheel steels, Mater. Sci. Technol. 32 (2016) 266–274. doi:10.1080/02670836.2015.1112537.

[53] J. Yang, T.S. Wang, B. Zhang, F.C. Zhang, Sliding wear resistance and worn surface microstructure of nanostructured bainitic steel, Wear. 282–283 (2012) 81–84. doi:10.1016/J.WEAR.2012.02.008.

[54] F.C. Zhang, B. Lv, C.L. Zheng, Q. Zou, M. Zhang, M. Li, T.S. Wang, Microstructure of the worn surfaces of a bainitic steel railway crossing, Wear. 268 (2010) 1243–1249. doi:10.1016/J.WEAR.2010.01.016.

[55] S. Das Bakshi, A. Leiro, B. Prakash, H. Bhadeshia, Dry rolling/sliding wear of nanostructured bainite, Wear. 316 (2014) 70–78.

# 3

# Microstructural evolution of white and brown etching layers in pearlitic rail steels*


## Abstract

The formation of White (WEL) and Brown Etching Layers (BEL) on rail raceways during service causes the initiation of microcracks which finally leads to failure. Detailed characterization of the WEL and the BEL in a pearlitic rail steel is carried out from micrometer to atomic scale to understand their microstructural evolution. A microstructural gradient is observed along the rail depth including martensite, austenite and partially dissolved parent cementite in the WEL and tempered martensite, ultrafine/nanocrystalline martensite/austenite, carbon saturated ferrite and partially dissolved parent cementite in the BEL. Plastic deformation in combination with a temperature rise during wheel-rail contact was found to be responsible for the initial formation and further microstructural evolution of these layers. The presence of austenite in the WEL/BEL proves experimentally that temperatures rise into the austenite range during wheel-rail contact. Each wheel-rail contact must be considered as an individual short but intense deformation and heat treatment cycle that cumulatively forms the final microstructure, as shown by diffusion length calculations of C and Mn. The presence of secondary carbides in the BEL indicates that the temperature in the BEL during individual loading cycles reaches levels where martensite tempering occurs. Partially fragmented primary cementite laths, enriched in Mn, depleted in Si, and surrounded by a C-gradient and dislocations were found in the BEL. The initial step in the formation of BEL and WEL is the defect- and diffusion-assisted decomposition of the original microstructure.


* This chapter is based on the article: A. Kumar, G.Agarwal, R. Petrov, S. Goto, J. Sietsma and M. Herbig, Microstructural evolution of white and brown etching layer in pearlitic rail steels, Acta Mater. 171 (2019) 48-64. https://doi.org/10.1016/j.actamat.2019.04.012.

## 3.1 Introduction

The loading conditions in curved tracks and switches of rails are more severe than in straight tracks, causing more irregular wear, severe rail corrugation and accumulated plastic deformation, which lead to in-service defects of these highly loaded parts [1,2]. Therefore, for the curved tracks, pearlitic steels with fine cementite laths (20-40 nm) and small interlamellar spacing (150-200 nm), also known as "heat treated pearlitic steels" or R350HT, are used. These steels possess mechanical properties that are superior over the conventional pearlitic steels (R260), which are used in straight tracks [3]. One of the main causes of microcracking in the rails of pearlitic steel is the formation of White Etching Layers (WEL) at the rail raceways [4–7]. Research shows that the microcracks are generally initiated because of the brittle fracture or delamination of these layers [2,4–7]. The WELs in curved tracks are 3-4 times thicker (100-120 μm) than the ones in the straight tracks (25-40 μm) [8,9]. Consequently, cracks in the WEL of curved tracks are deeper with correspondingly higher local stress intensity factors and faster fatigue crack propagation, as compared to the case of straight tracks. Therefore, there is a higher safety concern due to the WEL formation in curved tracks.

In the past, studies have been carried out for understanding the formation mechanism of WEL in conventional pearlitic steels employed for straight tracks [8–17]. Some of these studies [8,9,12,16] concluded that WEL form due to the austenitization under rapid frictional heating and subsequent fast cooling, leading to martensite formation. In contradiction with the above mechanism, some studies [10,11,17] claim that heavy plastic deformation is responsible for the formation of the WEL. According to this proposed mechanism, the plastic deformation causes stress-assisted cementite dissolution leading to the formation of nanocrystalline ferrite in the WEL microstructure. Pyzalla *et al.* [13] and Wang *et al.* [14] found strong texture components in martensite and austenite in the WEL and proposed rapid heating with subsequent cooling in combination with heavy loading as the formation mechanism of the WEL. However, these studies focus mainly on the microstructural alteration and residual stress measurements at the rail surface and do not provide in depth microstructural analysis of the evolution of the WELs. Zhang *et al.* [15] showed the formation of nanocrystalline martensite, severely deformed pearlite lamellae, austenite and cementite in the WEL on the rail surface. Al-Juboori *et al.* [2] found two different WELs, one containing fine martensite and the other having austenite and martensite. The existence of the former WEL was explained due to severe plastic deformation while the presence of latter was attributed to either thermal or thermomechanical conditions. Ahlström *et al.* [18] argued that the cooling rates in the WEL can allow the formation of fresh pearlite from austenite and ferrite precipitation at the grain boundaries. Thus, the microstructural evolution and formation mechanism of WEL are still a matter of debate and hence the topic requires further investigation. Moreover, most of the aforementioned studies of WEL focus on the microstructural alterations at the rail surface

only. Additionally, the particularities of the formation of the WEL in R350HT steels have so far not been investigated.

Another microstructural alteration called the Brown Etching Layers (BEL) in the pearlitic steels was first reported by Li *et al.* [19] in corrugated rails of straight tracks close to the rail raceway. The BEL and the WEL show brown and white contrast, respectively, in optical microscopy after etching with 2-4 vol.% Nital. Li *et al.* [19] proposed that the BELs primarily consists of tempered martensite and form after the WELs formation. Contrary to this, Al-Juboori *et al.* [20] proposed that the BELs are the precursor stage of the WELs. Another study by Messaadi *et al.* [21] claimed the formation of globular bainite in the BEL microstructure. Thus, there exists a discrepancy in the understanding of the microstructural evolution of the BELs.

Studies have shown that the formation of microstructures identical to those observed in WEL can be simulated using laboratory experiments such as rapid heating and cooling, machining, dry sliding wear testing, cold rolling in combination with heating with laser pulses and hard tuning [12,22–24]. Carroll *et al.* [6] demonstrated the formation of the WEL using spot welding and twin disk testing. However, these simulated microstructures are significantly different from the WEL microstructure formed on rail raceways. Therefore, there is a need to study the formation mechanism of WEL directly from the in-field loaded rails.

The current work aims at contributing to a better understanding of the microstructural evolution and formation mechanisms of the WEL and the BEL in rails in general, with a focus on the particularities of the R350HT alloy employed in curved tracks. We use experimental techniques such as Electron Channelling Contrast Imaging (ECCI), Electron Back Scatter Diffraction (EBSD), Atom Probe Tomography (APT), Transmission Electron Microscopy (TEM) and Scanning Electron Microscopy (SEM) to investigate the microstructure of the WEL and the BEL in terms of crystallography and chemistry. The results are compared with the thermodynamic and Finite Element Method (FEM) simulations. Based on this, the formation steps of the WEL and the BEL are reconstructed, which is summarized in schematic drawings.

## 3.2 Material and Methods

### *3.2.1 Material*

R350HT pearlitic rail steels were produced by hot rolling the steel slabs at 1000 °C into the shape of a rail, followed by annealing at 900 °C for 3 hours and cooling in accelerated air flow which yields a fine pearlitic microstructure. A specimen of R350HT pearlitic steel containing the WEL patches was cut from a curved track with 400 m radius that was exposed to service conditions in the Netherlands. The approximate load passage was 200 Mt with an axial load ranging from 12 t to 18 t. The exact loading history is unknown because of a large number of undefined variables that can vary with each train or wagon such as speed, acceleration, sinusoidal motion of wheel, wheel profile, lubrication conditions, and axle loads, etc.[8]. The chemical composition of the R350HT steel studied here is Fe-0.72C-1.1Mn-0.56Si-0.11Cr (in wt.%), or Fe-3.23C-1.09Si-1.1Mn-0.11Cr (in at.%). Fig. 3.1(a) shows a photograph of the sample extracted from the curved track with WEL patches on the raceway after etching with 2 vol.% Nital. The specimen on which the characterization of the WEL and the BEL was performed was extracted at around 5 mm distance towards the gauge side from the center of the running band (Fig. 3.1(b)).

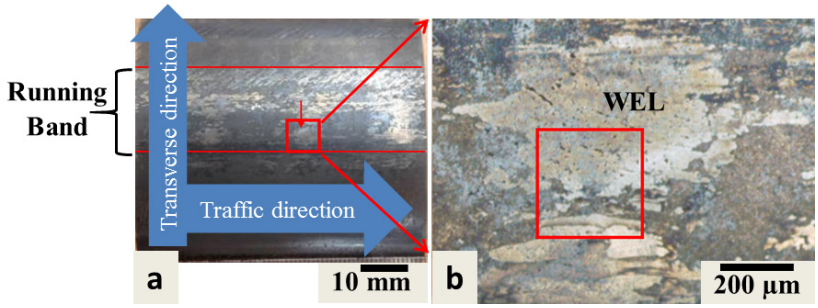


Fig. 3.1. (a) Rail specimen from a curved track with WEL patches along the running band, (b) Magnified view of the rail surface containing WEL patches. The region marked in red shows the location of the specimen selected for further cross-sectional characterization.

### *3.2.2 Simulations*

An analytical model suggested by Fischer *et al.* [25] is used for calculating the maximum temperature rise at the rail raceway. This model calculates the asperity flash temperature rise on the rail raceway by taking into account the frictional heating and heating due to plastic deformation [25]. The model also considers the surface roughness of the contact body together with pressure intensification by local surface asperities during wheel-rail contact and the relative slip in between wheel and rail. We assess the temperature changes over time for different depths below the rail raceway by coupling the analytical model with a 3-D transient heat transfer finite element simulation using COMSOL-Multiphysics [26]. The calculations were conducted assuming a friction coefficient of 0.5, 1500 MPa

maximum pressure, 30 m/s train speed and a slip of 10%. The physical material properties were taken from the pearlitic rail steel module in COMSOL-Multiphysics, *viz*. thermal diffusivity 1.317 x $10^{-5}$ $m^2/s$, thermal conductivity 50.2 W/mK, density 7850 $Kg/m^3$ and specific heat capacity 485.5 J/kgK. These properties were assumed to be constant over the entire temperature range. The friction coefficient, train speed and slip assumed in the simulation represent harsh wheel-rail contact conditions and relatively milder conditions may also exist. The effect of plastic deformation along the rail depth below the raceway was discussed using a mesoscale finite element simulation given in reference [1]. Thermodynamic calculations were performed using the Thermo-Calc software with the TCFE9 database.

### *3.2.3 Microstructure characterization*

The microstructure of the base material, the WEL and the BEL was characterized in the cross-sectional plane perpendicular to the traffic direction. After standard metallographic sample preparation, specimens were etched using 2 vol. % Nital solution to investigate them in the Keyence VHX 6000 light optical microscope. Vickers microhardness measurements were performed on a Dura scan 70 (Struers) hardness tester, using a load of 0.25 N for 10 s.

The ECCI measurements on the WEL, the BEL and the deformed pearlite region were performed on a Zeiss Merlin SEM equipped with a Gemini-type field emission gun using an accelerating voltage of 30 kV, a probe current of 3 nA and a working distance of 9.7 mm. The High Resolution EBSD (HR-EBSD) scans were conducted using a JEOL JSM 6500F SEM with a Schottky field emission gun SEM. The HR-EBSD scans were carried out at an accelerating voltage of 15 kV, a working distance of 18 mm and a step size of 40 nm using a hexagonal scan grid. The EBSD data was analyzed using TSL-OIM (Orientation Image Microscopy) software. The HR-EBSD data was used to quantify the phase fractions, grain size distributions, intra-grain crystallographic misorientations, orientation relationships and the distribution of high angle and low angle grain boundary (HAGB and LAGB) fractions along the depth of the WEL and the BEL. The Grains are defined containing a minimum number of two pixels and by the threshold misorientation of 5°.

The 3D distribution of alloying elements at the near-atomic scale, at different depths below the rail raceway, was quantified using APT. The specimens were prepared by Focused Ion Beam (FIB) milling in a FEI Helios Nanolab 600i dual beam FIB/SEM. The APT measurements were performed using a LEAP 3000X HR in voltage mode, using a set-point temperature of 65 K, a pulse fraction of 15% and a pulse frequency of 200 kHz. Data reconstruction following the procedure of Vurpillot *et al.* [27] and data analysis were done using the IVAS software. The alloy element partitioning was mainly investigated using proximity histograms (also called “Proxigrams”) [28]. TEM and APT were performed on

the same APT specimen with an experimental approach as described by Herbig *et al.* [29,30]. TEM analysis was carried out in a Jeol JEM-2200FS FEG-TEM operated at 200 kV.

The specimen was further imaged in Secondary Electron (SE) mode in a Zeiss Merlin SEM after etching with 2 vol. % Nital. An accelerating voltage of 30 kV, a probe current of 2.5 nA and a working distance of 9.8 mm was used for the SE imaging. The ECCI, EBSD, APT results in combination with SE imaging on the same location enabled classifying the etching behavior of the WEL and the BEL.

## 3.3 Results and discussion

### *3.3.1 Thermodynamic considerations*

Fig. 3.2 shows the dependence of the phase fraction of austenite, ferrite and cementite on temperature in the R350HT pearlitic steels in thermodynamic equilibrium. The plot was calculated for atmospheric pressure using the Thermo-Calc software. During heating the cementite starts to dissolve at 715 °C and the microstructure completely transforms into austenite at 730 °C. In the intermediate temperature range, cementite, ferrite and austenite coexist. According to these calculations, only if the temperature exceeds 715 °C austenite can form in this fully pearlitic steel. At an elevated pressure of 2 GPa, assumed to be representative for the moment of wheel-rail contact in curved tracks [31], the austenite start and finish temperatures are shifted slightly to 675 and 815 °C, respectively (see appendix).

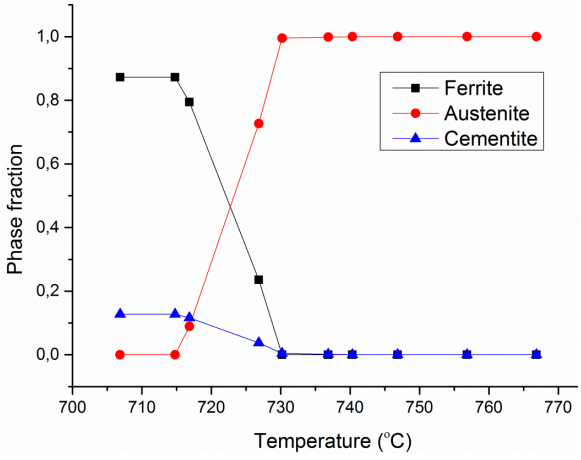


Fig. 3.2. Plot of phase fractions as a function of temperature at atmospheric pressure in R350HT generated using Thermo-Calc.

### *3.3.2 Temperature and contact stresses at the wheel-rail interface*

The interpretation of the WEL and the BEL microstructure requires an assessment of the temperature changes and stress distribution at the wheel-rail interfaces. According to finite element modelling by Vo *et al.* [32] the temperature at the rail raceway can reach 624 °C. Ertz *et al.* [33] also calculated a temperature rise of 630 °C at the rail surface in straight tracks. However, Takahashi *et al.* [8] estimated (using a FEM approach detailed in [34]) a temperature rise close to 1400 °C at the rail raceway. The peak temperature rise was also estimated by diffusion length calculations of Mn in the WEL and a rise of 1300-1400 °C was predicted at a depth of 2 μm below the rail raceway, which was calculated based on the assumption that all diffusion occurred during a single wheel-rail contact. There are thus pronounced variations in the estimations of the temperature rise at the wheel-rail interface in the literature. Such variations can be attributed to differences in the selected values of the parameters such as friction coefficient, train velocity, axle load, wheel/rail roughness, traction forces, slip rate and maximum shear stresses *etc*.

Our simulations allow an estimation of the temperature rise for the given case of the curved tracks (Fig. 3.3). Fig. 3.3 shows the finite element modelling estimations of the temperature changes at the rail raceway and at different depths (20, 40, 60 and 80 μm) over time. According to the simulation results, the temperature at the rail raceway reaches 1228 °C with a heating rate of 5 x $10^6$ °C/s. In 20 and 40 μm depth (the region where we observe the WEL (Fig. 3.4)), the temperature reaches 982 °C and 737 °C respectively, where austenite formation is possible (Fig. 3.2). In the BEL at 60 μm and 80 μm below the rail raceway (later shown in Fig. 3.4) the maximum temperature was estimated to be 491 °C and 246 °C respectively. The entire heating and cooling process in Fig. 3.3 takes place in less than 1 ms. The shortest possible time between two wheel-rail contacts at a rail speed of 30 m/s (108 km/h) and a wheel spacing of 2 meters (Dutch standard) is around 67 ms. This means that every wheel-rail contact must be considered as an individual heating and deformation cycle. The cooling rates range from 1.7 x $10^6$ to 2.5 x $10^5$ °C/s at the raceway and at 80 μm depth, respectively. At such high cooling rates any austenite that forms at elevated temperatures has no time to transform back into pearlite during cooling but will be either quenched-in as austenite or will transform into martensite [35].

Vo *et al.* [1] estimated the stress distribution in curved rails during the wheel-rail contact, which can be used to draw conclusions on the plastic deformation as a function of rail depth. They calculated the highest von-Mises stresses of about 750 MPa close to the rail raceway in the low curved rail (in worn wheel and worn rail conditions). These stresses are higher than the yield strength of undeformed R350HT pearlitic steel, which is 740 ± 10 MPa [36]. According to their simulations, the rail can deform plastically during the wheel-rail contact down to a depth of at least 200 μm [1]. However, yield stress is a macroscopic material property and the grains orientated in easy slip direction will also deform in deeper areas. Simultaneously, the yield point of the steels decreases with the increase in

temperature [37–39]. Chen *et al.* [38,39] showed that the yield point of the high strength steels decreases by a factor of 4 to 4.5 if the temperature increases from 22 °C to 720 °C. Hence, the calculated von-Mises stress levels in [1] represent a lower bound for the plastic deformation at high temperatures under wheel-rail contact. The rail surfaces are also subjected to dynamic wear which changes the wheel-rail contact area and thus the loading conditions are continuously altered during the service of the rails [18].

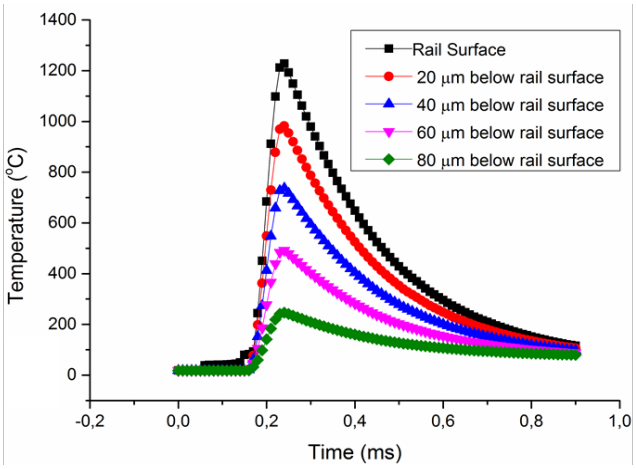


Fig. 3.3. Plot of temperature over time at rail raceway and at different rail depths during wheel- rail contact obtained by 3-D transient heat transfer finite element model.

### *3.3.3 Optical microscopy and micro-hardness testing*

Fig. 3.4(a,b) shows an optical micrograph of the WEL and the BEL. Cracks are found to initiate by the brittle fracture of the WEL (encircled in Fig. 3.4(a)) or delamination at the WEL/BEL interface (encircled in Fig. 3.4(b)). These cracks further propagate into the material below. The sample reference system is defined by three coordinate axes A1, A2, and A3 in Fig. 3.4. The results of Vickers micro-hardness testing are shown in Fig. 3.4(c). The highest hardness values between 900 and 1100 HV were measured in the WEL close to the raceway. The hardness was found to decrease gradually with depth, from 730-800 HV in the BEL to values around 400 HV in the base material. The hardness values in the deformed pearlite region vary in the range of 450-520 HV.

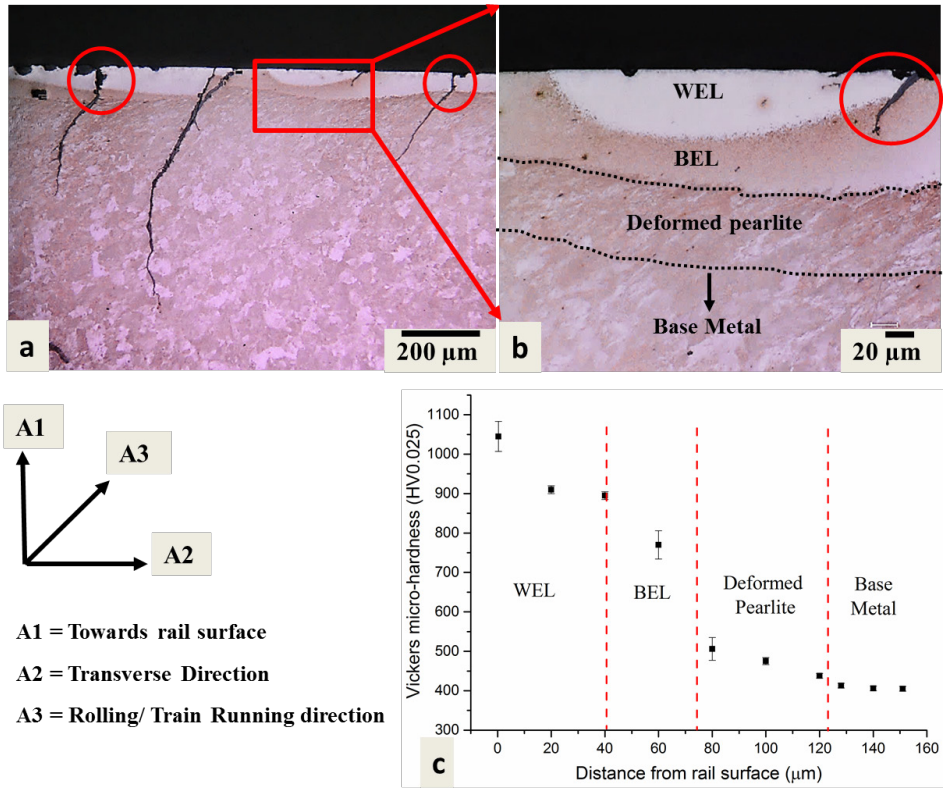


Fig. 3.4. (a,b) Optical micrograph of the rail cross-section showing crack initiation and propagation associated with the WEL and the BEL, (c) Microhardness along the rail depth. (The micro-hardness measurements at 0 µm position were performed on the rail surface whereas further measurements were done on the cross-section).

### *3.3.4 Study of microstructure evolution using ECCI*

ECCI is a powerful technique for observing crystal defects such as dislocations, stacking faults, twinning and grain boundaries in the SEM [40,41]. The ECCI micrograph shown in Fig. 3.5(a) is taken from the same area as that of the optical micrograph in Fig. 3.4(a). Fig. 3.5(b-e) show magnified subregions from Fig. 3.5(a). The WEL, the BEL and the deformed pearlite can be distinguished in ECCI according to their average backscattering intensities. A pronounced contrast difference between the WEL and the BEL is observed. The WEL appears brightest, the BEL darker and the deformed pearlite region the darkest (Fig. 3.5(a)). Additionally, the BEL also shows an intensity gradient along the depth (Fig. 3.5(a)).

The backscattering contrast, as a first order approximation, depends on the mass density, grain orientation and defect density [40]. The overall composition in the WEL and the BEL is equal; therefore there are no contrast changes related to mass density at the scale of Fig. 3.5. Also, there is no pronounced difference in the texture between the WEL, the BEL and

the deformed pearlite region (see appendix) that could give rise to a contrast change related to the average grain orientation. Thus, it can be concluded that the different average ECCI intensities mainly represent different densities of defects, *i.e.* dislocations and grain boundaries, being present in these regions. The WEL has the highest defect density giving rise to more backscattering and thus shows high brightness (Fig. 3.5(a)). The high defect densities present in the WEL are in good agreement with the high von-Mises stresses at the rail surface shown in reference [1]. The transition between the top and the bottom of the BEL shows an intensity gradient from dark to bright (Fig. 3.5(a)), which represents a gradient of increasing defect densities. At first view, this is in disagreement with the gradient of the von-Mises stresses in reference [1]. However, this point is experimentally confirmed by EBSD and will be discussed later.

The transition between the BEL and its adjacent regions is not sharp but appears like zones comprised of a mixture of patches belonging to each side (Fig. 3.5(b, e)). In the deformed pearlite region, ferrite (α) and cementite (θ) can be clearly distinguished (Fig. 3.5(e,f)). In these figures, shear bending and partial fragmentation of the cementite laths and an accumulation of dislocations within ferrite, especially at the ferrite/cementite interface, is observed. This indicates the onset of cementite decomposition under heat and plastic deformation, which is the first step that takes place in the formation process of WEL/BEL. The ferrite grains in this area are in the transition process to become part of the surrounding BEL. The ferrite/cementite islands that remain in the matrix of the BEL are mostly oriented parallel to the rail raceway (Fig. 3.5(e)), indicating the orientation-dependent microstructural decomposition of pearlite.

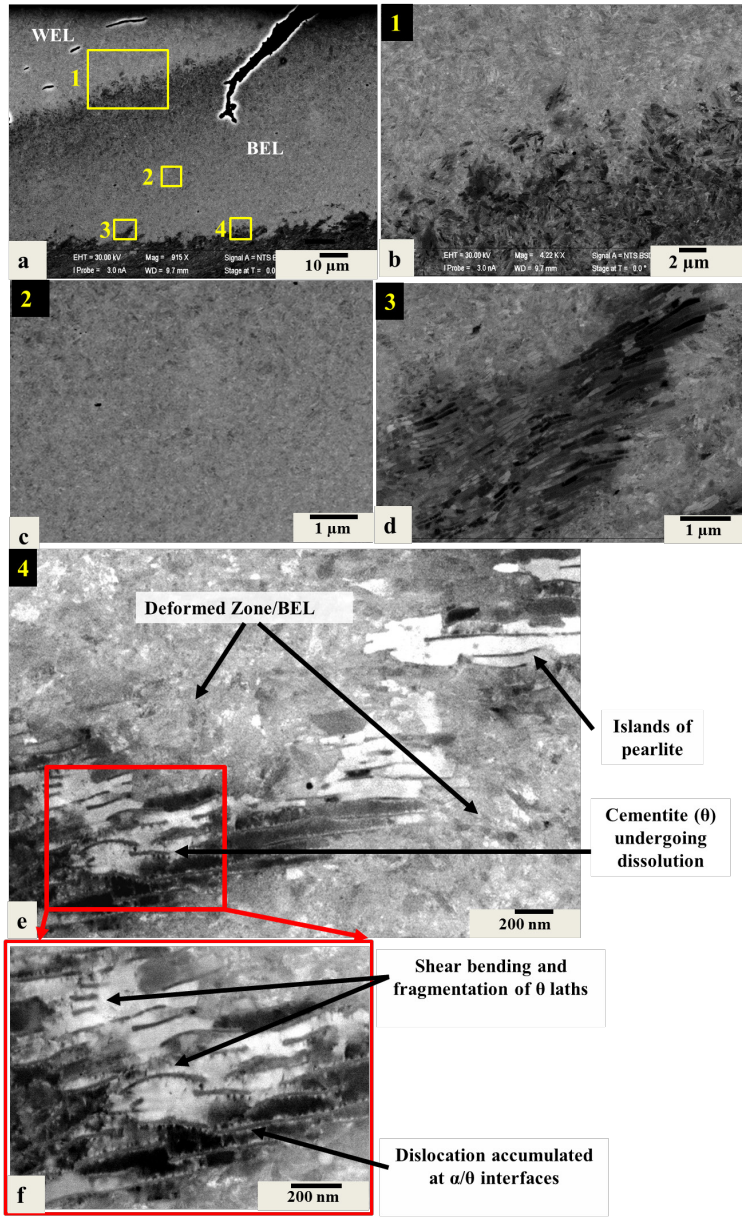


Fig. 3.5. ECCI micrographs of the region depicted in Fig 4(a). (a) Overview image showing the WEL, the BEL and the deformed pearlite region with different ECCI contrast, (b-d) Magnified subregions 1-3 from (a), (e,f) ECCI images at the interface of the BEL and the deformed pearlite region from subregion 4 in (a) showing breaking and shear bending of cementite (θ) laths.

### *3.3.5 Microstructural insight using electron backscatter diffraction*

EBSD scans were performed in an area marked in Fig. 3.6(a), covering the entire depth from the WEL over the BEL down to the deformed pearlite region (Fig. 3.6(b,c)). From the EBSD measurement, a phase map and a Kernel Average Misorientation (KAM) map were extracted (Fig. 3.6(b,c)). The black pixels in Fig. 3.6(b,c) represent measurement points with Confidence Index (CI) < 0.1 that were removed before the data analysis. The WEL, the BEL and the deformed pearlite region can be clearly distinguished in the EBSD maps (Fig. 3.6(b,c)). The EBSD phase map depicted in Fig. 3.6(b) shows the presence of austenite (in green) in the WEL and the BEL but not in the deformed pearlite region. The presence of austenite provides evidence that temperatures of about 700 °C (A1 temperature in Fig. 3.2) and above are reached in the WEL and the BEL, during the wheel-rail contact. The KAM map depicted in Fig. 3.6(c) plots the average misorientation to the second nearest neighboring pixels considering a maximum misorientation angle of 5 degrees. High KAM values represent high Geometrically Necessary Dislocation (GND) densities. The results show high, intermediate and low KAM values/GND densities in the WEL, the BEL and the deformed pearlite region, respectively, and thus confirm our interpretation of the ECCI micrograph in Fig. 3.5.

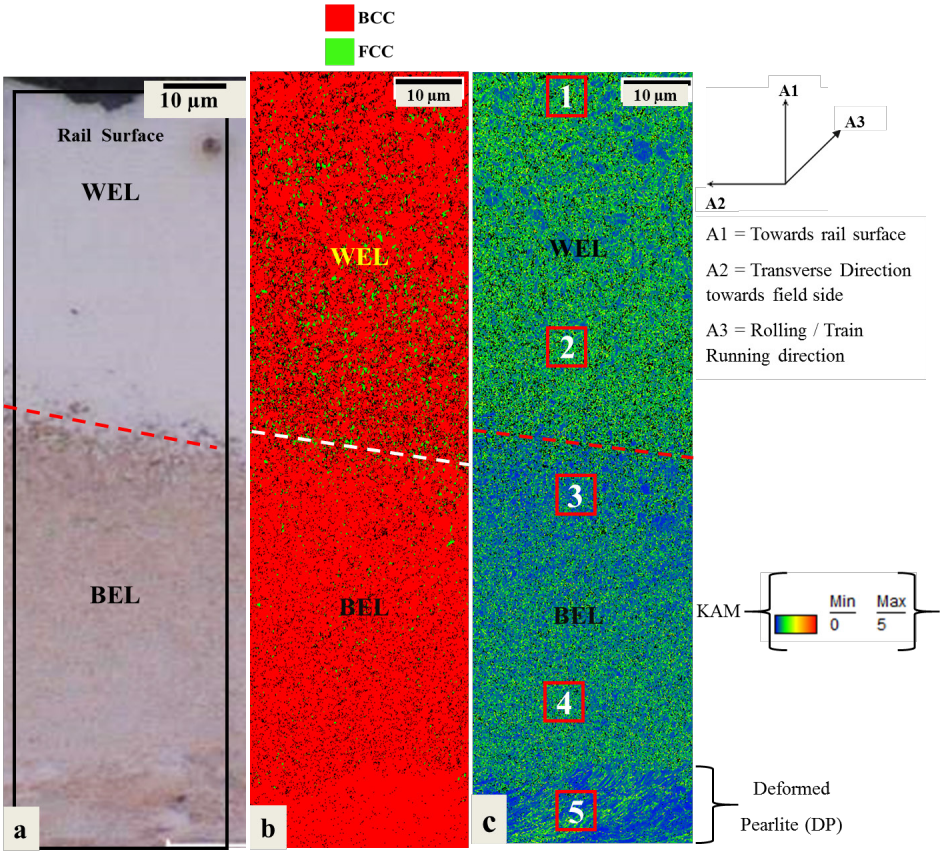


Fig. 3.6. (a) Optical micrograph showing the WEL, the BEL and the Deformed Pearlite (DP) region, (b) EBSD phase map and (c) EBSD-KAM map from the rectangular region marked in (a). The transition between the WEL and the BEL is marked with dashed lines.

In order to quantify and further discuss the microstructural alterations from the rail surface into the depth, the EBSD data depicted in Fig. 3.6 was segmented into 1 µm thick slices along the depth, which were statistically analyzed. The austenite fraction, the fraction of HAGBs and LAGBs, the KAM values and the average grain size are plotted from the rail surface into the depth and are depicted together with representative subregions of the EBSD map (Fig. 3.7(a,b)) and Fig. 3.8 (a-c). The origin of these subregions is marked by the rectangular boxes in Fig. 3.6(c). An additional subregion 6 containing undeformed pearlite/base material is also plotted in Fig. 3.7(a,b) and Fig. 3.8(a,c) for comparison with the WEL/BEL/deformed pearlite.

Fig. 3.7(a) shows the distribution of the austenite area fraction in the WEL, the BEL, the deformed pearlite and the base material. The fraction of the austenite phase in subregion 1 in the WEL is 0.25-2%, and increases towards the WEL/BEL interface (Fig. 3.7(a)). The

austenite fraction within the WEL reaches its maximum value of 9-11 % at a depth of 30-35 μm below the rail raceway. The austenite fraction in the BEL varies in the range of 0.5-2.5 % which is significantly lower than in the WEL. The higher austenite fraction in the WEL indicates that the WEL witnesses a higher temperature than the BEL, which is in agreement with the thermal simulations shown in Fig. 3.3. The austenite fraction decreases from 2.5 % at the WEL/BEL interface to approximately 0.5-0.7 % at the BEL/deformed pearlite interface (Fig. 3.7(a)). No austenite phase is detected in the deformed pearlite and undeformed pearlite region.

Fig. 3.7(b) shows the distribution of HAGB (15-65° misorientation) and LAGBs (5-15° misorientation) fractions from the rail raceway to the undeformed pearlite. The plot does not include boundaries with misorientations in the 0-5° range. The HAGBs and LAGBs are highlighted by blue and red lines, respectively, in the corresponding EBSD maps in Fig. 3.7(b). The WEL shows a low fraction of HAGBs (0.5-0.6) close to the rail raceway, which increases to a value of 0.82 at the WEL/BEL interface. The low HAGBs fraction close to the rail raceway is attributed to substantial grain growth of austenite in the WEL, which leads to an average martensite grain size of 0.7±0.4 μm, as shown in corresponding EBSD map in Fig. 3.7(b). The increase in the HAGBs fraction from the rail raceway to the WEL/BEL interface is due to the decrease in grain size in the WEL along the rail depth (Fig. 3.7(b)). The LAGBs fraction is found to be almost constant around 0.05 in the WEL. The fraction of HAGBs and LAGBs further increases in the BEL to a value of 0.8 and 0.1, respectively, indicating the presence of finer grains in the BEL (with an average grain size of 0.30 ± 0.15 μm) than in the WEL. An increase in the fraction of the LAGBs to 0.40 ± 0.02 is observed in the deformed pearlite region, which can be explained by the accumulation of dislocations in this region due to plastic deformation (also observed in Fig. 3.5(e,f)). The accumulation of dislocations will lead to the formation of LAGBs within the grains. However, the undeformed pearlite contains primarily HAGBs with a fraction of 0.82 (Fig. 3.7(b)).

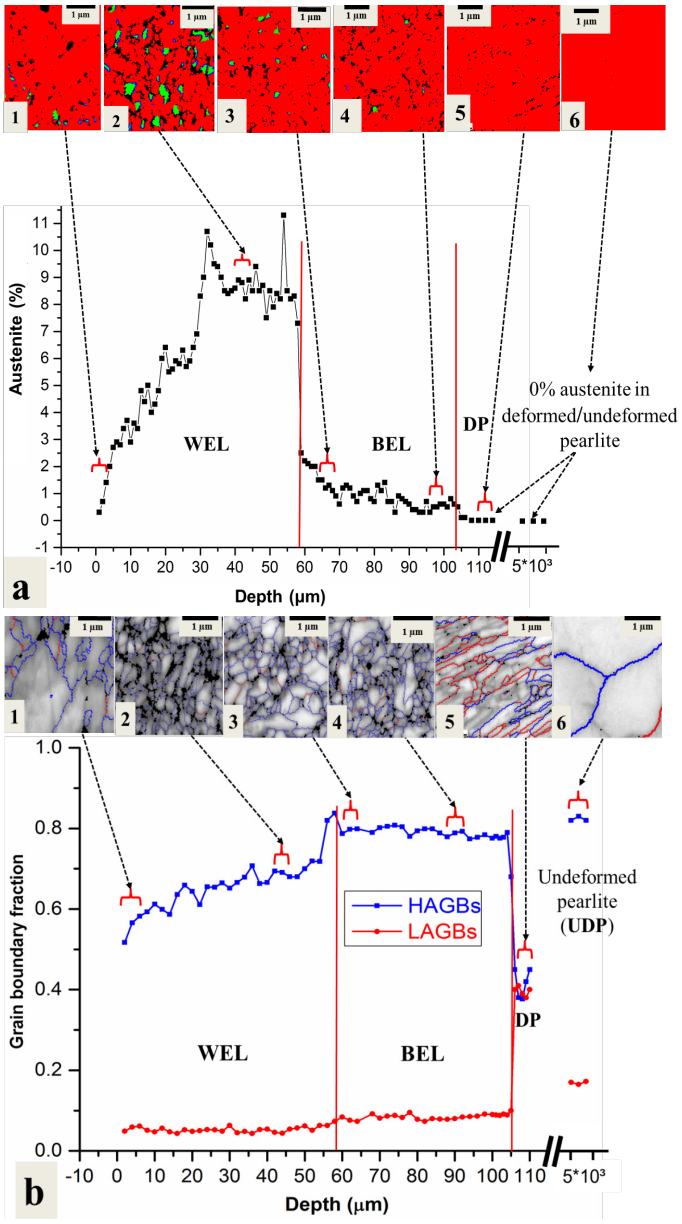


Fig. 3.7. Distribution of the microstructural features in WEL, BEL and deformed pearlite and a comparison with the undeformed pearlite. (a) Austenite distribution (in area %) shown with representative EBSD phase maps, (b) Distribution of HAGBs and LAGBs fractions shown with representative EBSD grain boundary maps.

Fig. 3.8(a) shows the distribution of the KAM in the WEL, the BEL, the deformed pearlite and the base material. The average KAM values in the WEL are higher (0.82-0.85°) than in the BEL (0.65-0.75°). GND densities ($\rho_{gnd}$) were calculated from the KAM values using equation,

$$\rho_{gnd} = \frac{\beta(KAM)}{ub} \tag{3.1}$$

Where $\beta$ is a constant ($\beta$ = 3 for mixed dislocations), $u$ is the distance between points/step size in the EBSD map (*i.e.* 4 x $10^{-8}$ m), $b$ is the magnitude of the Burgers vector (*i.e.* 2.47 x $10^{-10}$ m ) [42].

The KAM values mentioned above correspond to GND densities ($\rho_{gnd}$) of 4.3-4.5 x $10^{15}$ $m^{-2}$ and 3.4-3.9 x $10^{15}$ $m^{-2}$ in the WEL and the BEL, respectively. The high dislocation density in the WEL is due to high contact stresses, which lead to high amounts of plastic deformation in the grains close to the rail raceway. This is in agreement with the simulations in reference [1]. Additionally, the martensite formation will further increase the dislocation density due to the lattice strains associated with austenite to martensite transformation in the WELs. The GND values in the WEL/BEL are in agreement with the ECCI observations (Fig. 3.5). We observe low KAM values of 0.3-0.5° in some grains situated close to the rail raceway (encircled in the first KAM subfigure 1 in Fig. 3.8(a)). This is due to dynamic recovery in the WEL caused by the high temperatures close to the raceway which facilitate dislocation annihilation. The KAM increases within the WEL along the depth and reaches a maximum value of 0.85° in the WEL close to the WEL/BEL interface. The KAM decreases to 0.65° (*i.e.* equivalent to $\rho_{gnd}$ = 3.4 x $10^{15}$ $m^{-2}$) at the beginning of the BEL. The KAM is observed to increase further to 0.75° ($\rho_{gnd}$ = 3.9 x $10^{15}$ $m^{-2}$) in the BEL before it decreases again at the transition point of the deformed pearlite. The average KAM recorded in the deformed pearlite and the undeformed pearlite are 0.6° ($\rho_{gnd}$ = 3.1 x $10^{15}$ $m^{-2}$) and 0.25° ($\rho_{gnd}$ = 5 x $10^{14}$ $m^{-2}$), respectively. The overall variation in KAM is clearly visible in the corresponding EBSD KAM maps in Fig. 3.8(a).

Fig. 3.8(b) shows the KAM distribution in the austenite phase in the WEL and the BEL. The average KAM in the austenite phase is highest (1.1-1.3°) at a rail depth from 0 to 5 µm, indicating that the austenite phase close to the rail surface accommodates the highest plastic deformation. The lower austenite fraction close to the rail surface (Fig. 3.7(a)) is explained by the strain-induced transformation of austenite into martensite under plastic deformation. The KAM in austenite decreases along the depth in the WEL and reaches a minimum value of approximately 0.9° close to WEL/BEL interface (Fig. 3.8(b)).

Fig. 3.8(c) shows the average grain size distribution from the rail raceway into the depth. The average grain size in the WEL is 0.4-0.6 µm close to the rail surface (0-5 µm rail depth). The grain size decreases into the BEL and reaches a minimum value of 0.22 ± 0.13

μm towards BEL/deformed pearlite interface. The average grain size further increases in the deformed pearlite region to a value of 0.35 ± 0.3 μm and reaches a highest value of 4.7 ± 1.3 μm in the undeformed pearlite region (Fig. 3.8(c)).

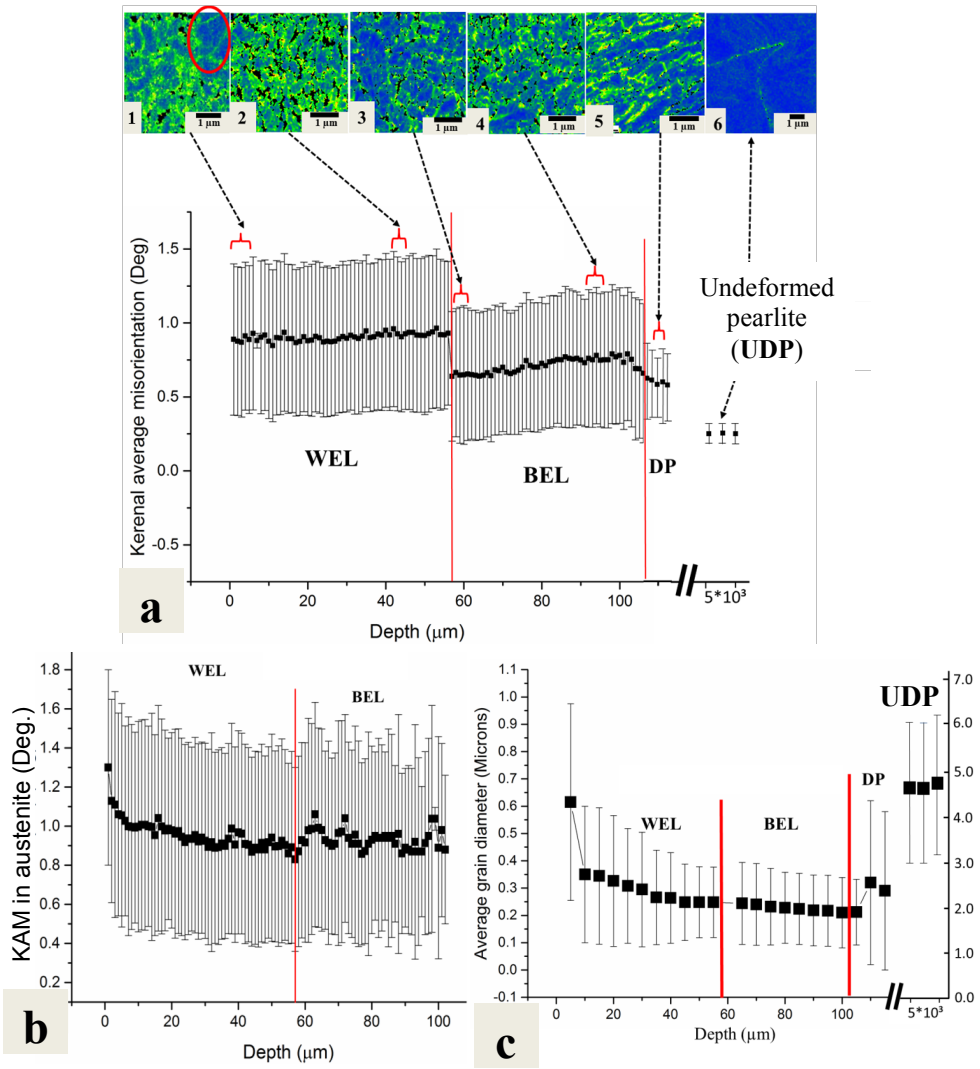


Fig. 3.8. (a) Distribution of the KAM in the WEL/BEL/Deformed Pearlite (DP) and Undeformed Pearlite (UDP) shown together with representative KAM maps, (b) KAM distribution in the austenite in the WEL and the BEL, (c) Grain size distribution. Vertical bars in the KAM charts indicate the width of distributions. Y axis on the right in (c) corresponds to grain size in UDP in microns.

### *3.3.6 Atomic scale characterization of the WEL, the BEL and the undeformed base material*

In order to further understand the formation mechanism of the WELs and the BELs, APT measurements were performed at various depths in the WEL and the BEL and compared with the undeformed pearlite as depicted in Fig. 3.9. Fig. 3.9(a) is a reference ECCI image showing four regions (in rectangles) where the APT measurements were performed. These regions are: the WEL at (1) 5 µm and (2) 30 µm below the rail raceway, (3) the BEL at 5 µm below the WEL/BEL interface and (4) the BEL at 10 µm above the BEL/deformed pearlite interface. Fig. 3.9(c-f) shows the APT results from the regions 1-4, respectively.

Fig. 3.9(b) depicts the C atom map from the undeformed pearlite that contains a cementite lath surrounded by ferrite. A proximity histogram ('proxigram') showing the compositional transition between ferrite and cementite is depicted below the C atom map. The proxigram was generated based on a 25 at.% C iso-concentration surface in the Region of Interest (ROI) marked with a rectangle. The size of the cementite lath in Fig. 3.9(b) is in the range of 25 to 40 nm. The proxigram in Fig. 3.9(b) shows the partitioning of C and Mn into the cementite and of Si out of the cementite. The cementite has a C content of up to 25 at.%, Mn of up to 4 at.% and Si of around 0.0012 at.%. The C in ferrite is found in the equilibrium concentration (at room temperature) *i.e.* 0.0046 at.% with a Si and Mn concentration of 1.29 at.% and 1.1 at.%, respectively.

In the WEL from region 1, grain boundary segregation of C is observed as shown in C atom map in Fig. 3.9(c). The C concentration at the grain boundary is 12-13 at.% as per proxigram analysis conducted with a 7 at.% C iso-concentration surfaces. The average C content in the matrix is found to be 3.25 ± 0.10 at.%. This indicates the presence of martensitic phase in the WEL in region 1. Additionally, many nanosized regions are observed within the martensitic matrix, with a high C concentration (> 7 at.%). These regions are shown by the arrows in the C atom map overlapped with 7 at.% C iso-concentration surfaces (in green) in Fig. 3.9(c). These regions can be attributed to C segregation at the dislocations in martensitic matrix. Mn and Si are found to be uniformly distributed in the WEL in region 1.

Fig. 3.9(d) shows a representative APT result from region 2. The result shows the segregation of C atoms at the grain boundary and the dislocations (shown by arrows) in the C atom map with 7 at.% C iso-concentration (in green). A cementite particle with a spherical morphology is observed in this region (in the rectangle in Fig. 3.9(d)). A proxigram analysis in Fig. 3.9(d) shows a C content of up to 25 at.%, an enrichment of Mn and the depletion of Si in this cementite particle. This indicates that the particle is the remainder of the parent cementite laths. The average C concentration in the cementite particle decreases from 25 at.% to 3.0 ± 0.2 at.% in the matrix. The high C concentration in the matrix indicates the presence of the martensitic phase. Additionally, the smaller size of

remnant cementite particles and C enrichment in the surrounding matrix indicate that the cementite is undergoing dissolution.

Fig. 3.9(e) shows the APT analysis of the BEL in region 3. Nanosized spherical carbide precipitates (indicated by arrows) are observed in the C atom map in Fig. 3.9(e). A proxigram analysis in the ROI (shown by a rectangle in Fig. 3.9(e)) shows that these carbides contain C up to 25 at.% but do not show partitioning of Mn and Si. Therefore, these carbides are cementite precipitates, which are not from the parent pearlitic microstructure but rather form due to the tempering of the martensitic matrix. The matrix in the vicinity of these carbides shows a C concentration of up to 1 at.%, which is lower than the C concentration in the WEL (regions 1 and 2). The temperature simulations in Fig. 3.3 indicate that the peak temperature in this region (can) reach around 500 °C, which can explain the tempering of the martensitic matrix. However, the temperature calculations in the BEL do not explain the martensitic transformation and the presence of austenite in the BEL (Fig. 3.7(a)). We conclude that the current simulations underestimate the peak temperature in this zone. It should be noted that that the temperature profiles in Fig. 3.3 strongly depend on the selected wheel-rail contact conditions. A higher- slip rate, friction coefficient, axle load, train speed, and smaller contact patch will result in an increase in the peak temperatures at the rail surface/subsurface, which can explain the microstructural observations in the BEL. Some wheel-rail contacts in this depth can lead to temperatures above A1 followed by the ones where only tempering occurs.

Fig. 3.9(f) shows the APT result from region 4. The APT tip was first imaged using BF-STEM and the same tip was then analyzed using APT by the correlative method discussed in sec. 3.2.3. The overlay of the C atom map and the TEM image (Fig. 3.9(f)) is in good agreement. A cementite particle with lath morphology similar to the base pearlite material is present (Fig. 3.9(b)). However, the size of this cementite is around 10 nm, which is less than the size of a cementite lath in the undeformed pearlite (25-40 nm) (Fig. 3.9(b)). A proxigram analysis with 25 at.% C iso-concentration surface in the ROI shows C enrichment of up to 25 at.% in cementite accompanied by Mn enrichment and Si depletion (Fig. 3.9(f)). The cementite lath is thus the remainder of the parent cementite from the original pearlite. The matrix in the vicinity of this cementite contains 1.6 ± 0.2 at.% C (Fig. 3.9(f)), which is far higher than the equilibrium concentration in ferrite (Fig. 3.9(b)) and lower than the C concentration in martensite in the WEL (Fig. 3.9(c,d)). The above observations of the cementite size and C enrichment in the ferrite matrix show evidence of parent cementite undergoing dissolution. This is in agreement with the ECCI results in Fig. 3.5(f) where the onset of cementite decomposition is captured.

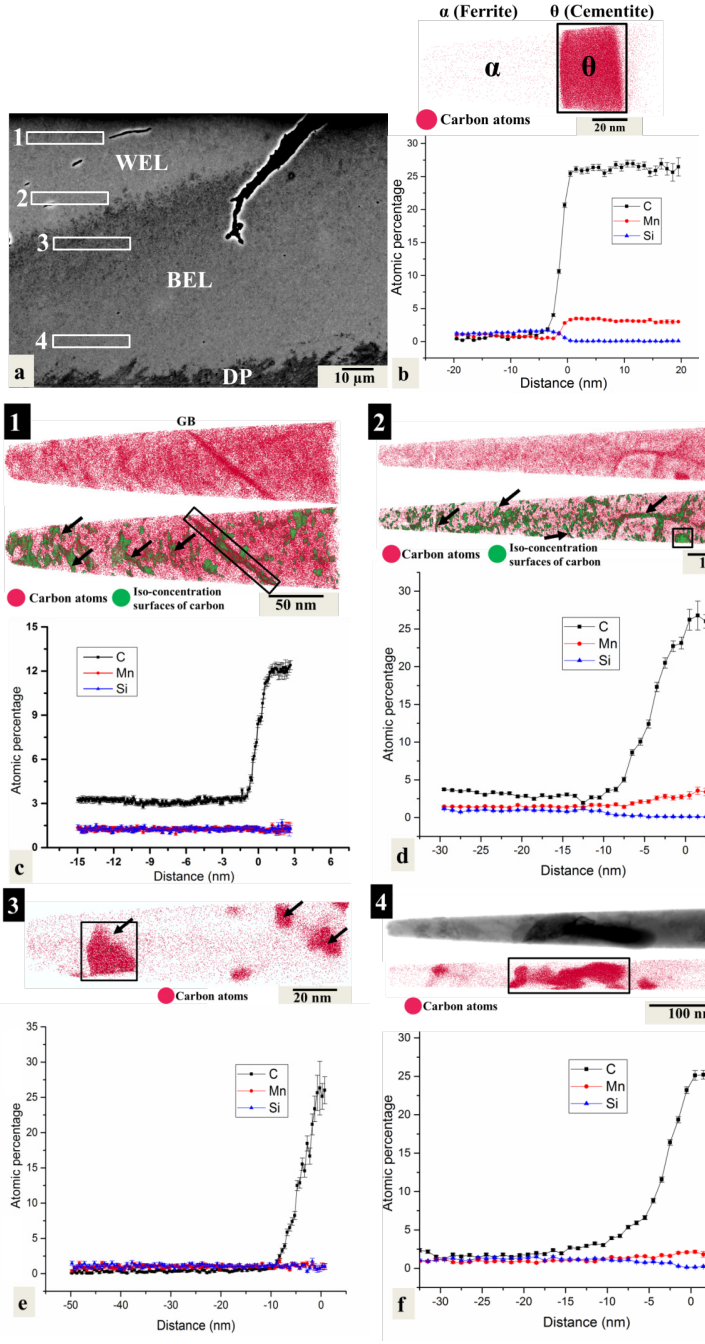
α (Ferrite)
θ (Cementite)
α
θ
Carbon atoms
20 nm
1
2
3
4
WEL
BEL
DP
10 μm
a
b
Atomic percentage
Distance (nm)
C
Mn
Si
GB
Carbon atoms
Iso-concentration surfaces of carbon
50 nm
100 nm
c
d
e
f

Fig. 3.9. (a) ECCI image showing regions 1-4 where APT specimens were prepared from, (b) C atom map from the base material showing a ferritic (α) grain and a part of a cementite (θ) lath with a proxigram based on a 25 at.% C iso-concentration surface in the ROI, (c) C atom map of the WEL (region 1), the same C atom map with 7 at.% C iso-concentration surfaces (in green) and a proxigram from the ROI, (d) C atom map (region 2) and the same map with 7 at.% C iso-concentration surfaces, (e) the C atom map (region 3) and a proxigram taken with 25 at.% C interface in the ROI, (f) Correlative BF-STEM image and C atom map (region 4) along with a proxigram based on a 25 at.% C interface in the ROI. All ROIs are marked by the rectangles.

### *3.3.7 Microstructural observations in the WEL and the BEL on etched samples using SE imaging*

To further investigate the role of C in the overall microstructural evolution in WEL/BEL, similar areas as depicted in Fig. 3.5 were etched and imaged in SE mode (Fig. 3.10(b-e)). The information gathered by light microscopy, EBSD and APT allows understanding the differences in the etching behavior of the WEL and the BEL. The etching behavior of polycrystalline alloys depends on various microstructural features such as crystal structure, crystallographic orientation, chemical composition, grain boundary energy, and grain boundary area *etc.* [43]. Nital attacks preferentially at the grain boundaries and primarily dissolves the ferrite phase in the pearlite, leaving the cementite phase intact [43,44]. This etching behavior is shown in the SE image of the undeformed pearlite in Fig. 3.10(f). Nital hardly attacks austenite and martensite phases in the steel microstructures [43].

The SE image in Fig. 3.10(b) from subregion 1 (rectangle within the ECCI image in Fig. 3.10(a)) shows weak SE contrast in the WEL due to the homogeneous and insufficient response to the etchant. This is due to the presence of martensite, austenite and nanosized cementite precipitates in the WEL and a homogenous distribution of C, Si and Mn in the martensitic matrix of the WEL (sec. 3.3.5 and 3.3.6). Additionally, the C segregation at the grain boundaries in the WEL (Fig. 3.9(c,d)) can also affect their etching behavior as C segregation reduces the free energy of the system and promotes grain boundary cohesion [45]. Thus the chemical reactivity of the grain boundaries in the martensitic matrix of the WEL is reduced [46]. Aforementioned arguments also explain the white contrast of the WEL under the light optical microscope (Fig. 3.4(a,b)).

A pronounced etching heterogeneity observed in the BEL in Fig. 3.10(b-e) results in more pronounced SE contrast. The magnified SE image in Fig. 3.10(c), shows the presence of a complex microstructure in the BEL. The microstructure consists of ferrite (α), Partially Dissolved parent Cementite (PDC), Tempered Martensite (TM) with Secondary Carbides (SCs) and freshly formed (not tempered) martensite/austenite (M/ϒ) islands. The presence of tempered martensite in this region is in agreement with our APT observations in Fig. 3.9(e). This also confirms our ECCI and EBSD KAM interpretation about the dislocation densities (sec. 3.3.4 and 3.3.5) as tempering leads to relaxation of lattice strains reducing

the dislocation density in martensite. The ferrite phase in Fig. 3.10(c) is etched deeply whereas partially dissolved parent cementite and martensite/austenite phases remain intact. The tempered martensite shows slightly lower etching resistance than the fresh martensite/austenite due to a lower C concentration, which results from the precipitation of secondary carbides in tempered martensite (Fig. 3.9(e) and Fig. 3.10(c)). Thus, the heterogeneous distribution of the C in the BEL results in etching heterogeneity which produces brown contrast under the light optical microscope (Fig. 3.4(a,b)).

The SE image of the BEL in Fig. 3.10(d) (taken from subregion 2 in Fig. 3.10(a)) shows the presence of deformed pearlite colonies with partially dissolved parent cementite, ferrite and ultrafine/nanocrystalline martensite/austenite islands. The average grain diameter of martensite/austenite islands is 210 ± 80 nm. The dissolution of cementite is clearly observed in this region as cementite laths are smaller and thinner than the cementite laths in the undeformed pearlite (Fig. 3.10(f)). A similar microstructure with partially dissolved parent cementite in deformed pearlite colonies and ultrafine/nanocrystalline martensite/austenite islands is also observed in the subregion 3 of the BEL (Fig. 3.10(e)). The area fraction of the ultrafine/nanocrystalline martensite/austenite islands in subregion 2 and 3 varies in the range of 8-10%. This indicates that austenite forms partially in the BEL leading to a low martensite/austenite fraction on subsequent cooling (Fig. 3.10(d,e)). High dislocation density exists in martensite due to shear induced diffusionless transformation. Since, the WEL contains martensite as a primary phase, the dislocation density due to martensitic transformation will be higher in the WEL than in the BEL which contains only 8-10% martensite. Hence, high GND density in the WEL (sec. 3.3.5) is not only due to high contact stresses [1] but also due to high martensite fractions.

The ultrafine/nanocrystalline martensite/austenite islands and partially dissolved parent cementite in subregion 2 and 3 are hardly etched by Nital. Additionally, the ferrite phase present in these regions (Fig. 3.9(d,e)) is not as deeply etched as in case of undeformed pearlite in Fig. 3.10(f)). The strong etching resistance of ferrite in the BEL is most likely due to its C enrichment by partial dissolution of cementite via defect assisted thermal diffusion (Fig. 3.9(f)).

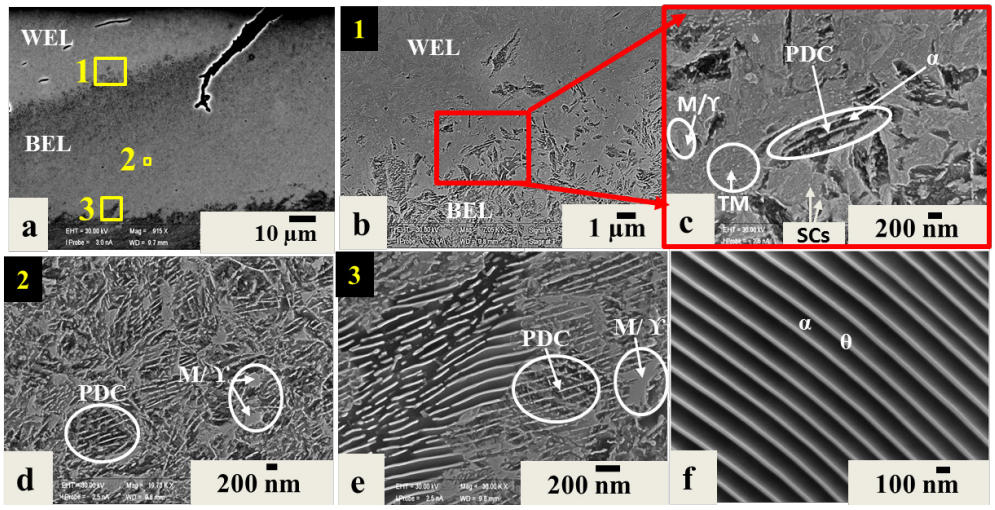


Fig. 3.10. (a) ECCI image repeated from Fig. 3.5(a) and Fig. 3.8(a) showing the positions (1-3) where SE images (b-e) were acquired after etching, (b-e) SE images of WEL, BEL and deformed pearlite, (f) SE image of original pearlite. Different phases such as ferrite (α), cementite (θ), Partially Dissolved parent Cementite (PDC), Martensite/Austenite (M/Υ), Tempered Martensite (TM) and Secondary Carbide (SCs) are marked in the figures.

### *3.3.8 Decomposition of cementite*

The cementite decomposition in pearlitic steels has been a point of debate in the steel research community and various mechanisms have been proposed to explain the decomposition as a consequence of plastic deformation, heating or both [47–54]. Takahashi *et al.* [47] have proposed a mechanism where temperature rise leads to the diffusion of C atoms from cementite to the excessive amounts of vacancies formed in ferrite during plastic deformation. This is because the vacancies in steels have a high interaction energy with the C atoms (*i.e.* 0.85 eV/atom) [54]. The second proposed mechanism is based on the strong interaction forces between C atoms and dislocations in the ferrite. The binding energy of C to the dislocations in ferrite (*i.e.* 0.8 eV/atom) is higher than the binding energy of C in cementite (*i.e.* 0.5 eV/atom) [47,55]. Hence, if dislocations are available in ferrite there is a thermodynamic driving force for C to leave cementite. Therefore, even temperatures below A1 can lead to the decomposition of cementite if the microstructure is plastically deformed.

The third mechanism is based on the Gibbs-Thomson effect in which the fragmentation of cementite (as shown in Fig. 3.5(e,f)) increases their free energy to an extent that the cementite becomes unstable and starts dissolving into ferrite [47–49]. The fragmentation of cementite in the BELs/deformed pearlite regions can further be explained by the large difference in the yield strength of ferrite and cementite, which generates strain incompatibility under severe plastic deformation. As a result, the dislocations nucleate from

the ferrite/cementite interfaces [50] (Fig. 3.5(f)) and their density in ferrite phase increases with further deformation. The motion of these dislocations is blocked by neighboring cementite laths forming tangled and jogged dislocations at the ferrite/cementite interfaces, which leads to the fragmentation of the cementite. Umemoto *et al.* [51] observed similar fragmentation, bending, cleavage fracture and shear cracking of the cementite in pearlite under the plastic deformation.

The fourth mechanism reported to cause cementite dissolution in pearlitic steels is the "C drag effect" where moving dislocations under plastic deformation can carry the C atoms from cementite to the ferrite phase [52,53]. In this mechanism, C atoms are trapped inside dislocations due to strong interaction forces between C atoms and the dislocations. However, this mechanism is only valid when the "diffusional rate of C atoms in ferrite" ($d_\alpha'$) is of the same order of magnitude or faster than the "dislocation velocity" ($v$) under wheel-rail contact [53]. In order to check the applicability of this mechanism, the dislocation velocity ($v$) is calculated by the relation, $v = \dot{\varepsilon}/b\rho$ [56], where $\dot{\varepsilon}$ is the strain rate, $b$ is the magnitude of the Burgers vector and $\rho$ is the density of mobile dislocations in ferrite. The dislocation velocity varies from $1.4\text{x}10^{-5}$ - $8\text{x}10^{-5}$ m/s, if $\dot{\varepsilon}$ = 1.0-6.0 $s^{-1}$ during wheel-rail contact [57], $b = 2.47\text{x}10^{-10}$ m and $\rho = 3\text{x}10^{14}$ $m^{-2}$ are used.

The diffusion rate of C in ferrite ($d_\alpha'$) is calculated by $d_\alpha' = \sqrt{(D_\alpha / t)}$ where $D_\alpha$ is the diffusivity of C atom in ferrite and $t$ is the average time at the elevated temperature as per thermal cycle in Fig. 3.3 (*i.e.* $1.6\text{x}10^{-4}$ s). The diffusivity of C in ferrite ($D_\alpha$) is expressed as

$$D_\alpha = D_0^\alpha \exp\left(-\frac{Q^\alpha}{RT}\right) \tag{3.2}$$

where $D_0^\alpha = 1.67\text{x}10^{-7}$ $m^2/s$ is the diffusion pre-factor for ferrite, $Q^\alpha$ = 80 kJ/mol is the activation energy for C diffusion in ferrite [53,58]. The diffusion rate of C in ferrite ($d_\alpha'$) varies from $1.4\text{x}10^{-5}$-$8\text{x}10^{-5}$ m/s for the temperature range of 348-535°C, respectively. Thus, the temperatures necessary for C drag by dislocations are reached during wheel-rail contact and thus this mechanism is also expected to be active for the formation of WEL/BEL.

### *3.3.9 Formation mechanism of the WEL*

The EBSD investigation in sec. 3.3.5 shows the presence of austenite in the WEL (Fig. 3.6(c)), whereas the microstructure before any loading cycle was fully pearlitic. The formation of austenite requires a temperature rise above the austenitization temperature (A1) (*i.e.* 715 °C for the present composition (Fig. 3.2)) followed by rapid cooling that

prevents the transformation back into pearlite[†]. This implies that during the wheel-rail contact in curved tracks, the temperature in the WEL must have exceeded A1. However, for complete austenization, the temperature must rise above the A3 temperature (730 °C ). The simulations, depicted in Fig. 3.3 are in agreement with the observed microstrcutural features in the WEL.

The equilibrium C concentration in austenite formed just above 715 °C is about 0.7 wt.% (calculated via Thermo-Calc). Hence, C partitioning is required for austenite to form in the pearlitic microstructure via diffusional transformation[‡]. Austenite will nucleate at the cementite/ferrite interfaces, because the cementite provides the necessary C for austenite formation. After austenite nucleation occurs, futher austenite growth requires the diffusion of C from cementite through austenite to the austenite/ferrite phase boundary, which is much slower than the diffusion through ferrite. As a result, the diffusion of C in the austenite phase is a limiting factor, controlling the austenite growth kinetics in the parent pearlite. In general, the austenite/ferrite interface mobility needs to be considered for transformation simulations. However, the lack of mobility data limits the calculation capability. Therefore, we neglect interface mobility and assume that the growth rate of austenite only depends on the average diffusion length of C in austenite. Estimation of average diffusion length of C in austenite is carried out based on the temperature simulations. The diffusivity of C in austenite ($D_\gamma$) is expressed as,

$$D_\gamma = D_0^\gamma \exp\left(-\frac{Q^\gamma}{RT}\right) \tag{3.3}$$

where $D_0^\gamma = 2.34 \times 10^{-5}$ m$^2$/s is the diffusion pre-factor for austenite, $Q^\gamma = 147.81$ kJ/mol [8] is the activation energy for C diffusion in austenite, $R = 8.31 \times 10^{-3}$ kJ mol$^{-1}$ K$^{-1}$ is the gas constant and $T$ is the temperature in Kelvin.

The average diffusion distance of C in austenite phase ($L_\gamma$) is calculated using

$$L_\gamma = \sqrt{D_\gamma t} \tag{3.4}$$

where $t$ is the diffusion time within the austenitic zone.

The diffusional calculations are performed for the thermal profiles (Fig. 3.3) at 0, 20 and 40 μm rail depth. Only temperatures above A1 (*i.e.* 715 °C) are taken into account for the calculations. In order to achieve reasonable accuracy, each thermal profile is subdivided

[†] High heating rates during wheel-rail contact (section 3.3.2) can lead to an increase in the austenitization temperatures (A1/A3), but this cannot be taken into account quantitatively. As a consequence, the effect of heating rates is not considered here.

[‡] The solute drag of C from cementite into the ferrite matrix would also affect the austenite formation, although this effect cannot be accurately quantified. The solute drag mechanism is discussed earlier in sec. 3.3.8.

into 18 equal intervals. The average diffusion distance for each individual interval is calculated and is integrated over the entire thermal profile. Following this procedure, the average diffusional length of C in austenite during a single loading cycle (*i.e.* one wheel contact) at 0, 20 and 40 μm rail depth is calculated to be about 85, 30 and 8 nm, respectively. The average interlamellar spacing of the undeformed pearlite is between 150-200 nm (Fig. 3.10(f)), which means that the C diffusion length required for complete austenite formation is between 75-100 nm (C diffuses through austenite from the two neighboring ferrite/cementite interfaces). Complete austenization is therefore only possible at 0 μm rail depth in a single wheel-rail contact. However, at rail depths of 20 and 40 μm, multiple wheel-rail contacts are required for complete austenitization. Therefore, considering the WEL as a single entity (rail depth up to 40 μm), multiple thermal cycles (Fig. 3.3) are needed for its formation.

Fig. 3.11 shows a schematic for the formation mechanism of the WEL where a progressive martensitic transformation is shown within multiple thermal cycles above A1/A3. During the initial heating cycles ($T$ > A1), austenite begins to form in the pearlitic microstructure. A fraction of the formed austenite transforms into martensite during cooling and the rest remains as austenite. Concurrently, cementite undergoes dissolution due to both, the plastic deformation and the temperature rise. Due to repeated heating cycles ($T$ > A1), the martensite and austenite areas grow progressively to form large austenitic areas. Simultaneously, during each cooling step (at the end of each wheel contact), part of the austenite transforms into martensite while another part remains as austenite. However, for the complete dissolution of cementite and the formation of martensite and austenite in the WEL microstructure, complete austenitization is needed which will require multiple thermal cycles of $T$ > A3[§].

APT investigations show that the Mn is uniformly distributed in the WEL close to the rail raceway (Fig. 3.9(c)), whereas Mn partitioning is observed in the undeformed pearlite (Fig. 3.9(b)). Thus, the Mn diffusion calculation also provides insight into the formation mechanism of the WELs. The Mn diffusional distance calculations were performed in the WEL using Eq. 3.2 and 3.3, where diffusion pre-factor and activation energy values (in Eq. 3.2) for Mn are taken from reference [8]. The diffusion length of Mn for the thermal cycle at 0 μm rail depth (Fig. 3.3) is 0.8 nm. This proves that multiple such thermal cycles (≈ 8789 cycles for 150 nm interlamellar spacing) are needed for homogenization of Mn in the WEL close to the rail raceway.

[§] Even after the final stage (shown in Fig. 3.11) is reached, the microstructure is repetitively changed. Thus, the final microstructure must be considered as being in dynamic equilibrium.

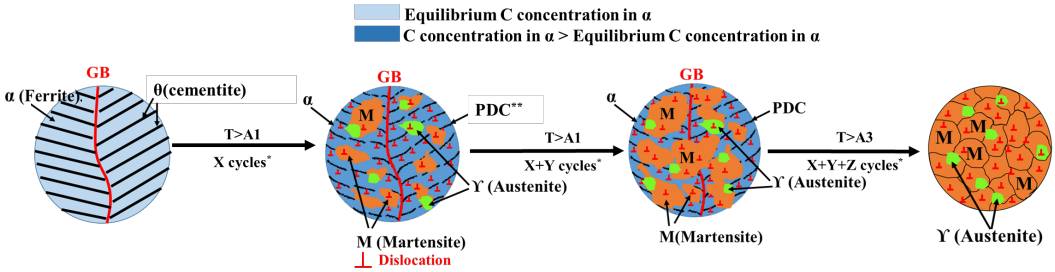


* One cycle refers to a single wheel-rail contact with plastic deformation and heating above A1 temperature.
** PDC refers to partially dissolved parent cementite.

Fig. 3.11. Schematic drawing showing the progressive transformation of the original pearlitic microstructure into the WEL during the wheel-rail contacts.

The WEL undergoes repetitive microstructural changes during their lifetime even after formation. For example, at the first full austenitization stage, the WEL consists of only fine austenite grains with different orientation due to the severe plastic deformation at the rail surface. However, over time, the repetitive rail contacts lead to accumulative effects close to the rail raceway caused by cyclic heat and deformation treatments. This leads to substantial grain growth of austenite grains during further austenitization, resulting in large martensitic grains upon cooling (especially close to the rail raceway) as shown in Fig. 3.8(c). Some martensitic grains close to the rail surface show significantly lower KAM (Fig. 3.8(a)), associated with the lattice strain relief caused by dislocation annihilation under high temperature and stress, referred to as dynamic recovery [24,59]. The lower fraction of austenite close to the rail surface (Fig. 3.7(a)) is explained by the high contact stresses, which can lead to strain-induced transformation of the austenite into martensite. The C segregation at the grain boundaries and dislocations close to the rail raceway in the WEL (Fig. 3.9(c,d)) is an indication of a temperature rise but not necessarily to an extent where austenitization occurs. This can be a consequence of the low temperatures at the rail surface depending on the wheel-rail contact conditions after the WEL formation. So, the overall microstructural evolution of the WELs close to the rail surface is governed by both the temperature rise (which can be above or below austenitization temperature) and the high contact stresses.

APT results at 40 μm below the rail raceway (Fig. 3.9(d)) show the presence of dissolving parent cementite, whereas no such cementite precipitates were found close to the rail raceway (Fig. 3.9(c)). The presence of such cementite precipitates can be explained by the lower temperature rise in the subsurface than the rail surface. It is concluded that the time

and temperature at the rail subsurface (*e.g.* region 2) in the WELs were not sufficient to dissolve all parent cementite particles into the martensitic matrix.

### *3.3.10 Formation mechanism of the BEL*

Fig. 3.12 illustrates the formation mechanism of the BEL in detail. The microstructure of the BEL can evolve in different ways. Two possible routes that can explain our experimental findings are marked by black (route 1) and green (route 2) arrows. In the first stage of route 1, the original pearlite microstructure can undergo multiple cycles of severe plastic deformation and temperature rise below the A1 temperature. The plastic deformation below the hard WEL causes the fragmentation of the parent cementite laths in the BEL. Concurrently, the plastic deformation and the moderate temperature rise that stays below A1 leads to the partial dissolution of the cementite laths, resulting in their refinement (Fig. 3.12). The partial dissolution of cementite laths also enriches the surrounding ferrite phase in C higher than the equilibrium C concentration in ferrite. The C concentration from these cementite laths towards the ferrite matrix varies gradually (Fig. 3.9(f)), confirming the partial dissolution of cementite laths.

The temperature in the BEL can also rise above the A1 temperature during individual wheel-rail contacts as shown in Fig. 3.12 (second stage of route 1 and first stage of route 2). Depending on the peak temperature above A1, the austenite fraction and size can vary in the BEL. The results in Fig. 3.10(c) indicate that the time and temperature in the BEL (just below the WEL/BEL interface) are sufficient for austenite growth. Therefore, on subsequent cooling, a high fraction of martensite is formed. This mechanism is shown in the first stage of route 2 (green arrow) in Fig. 3.12, where the microstructure of the BEL contains a large fraction of martensite phase, some austenite, some C enriched ferrite and partially dissolved parent cementite (PDC). Furthermore, depending on the wheel-rail contact conditions, the temperatures in the BEL can also go into the martensite tempering regime leading to secondary carbide precipitation, as shown by the second stage of route 2. Due to the tempering of martensite, BELs can also be considered as tempered WELs especially in the regions just below the WEL/BEL interface (Fig. 3.10(c)).

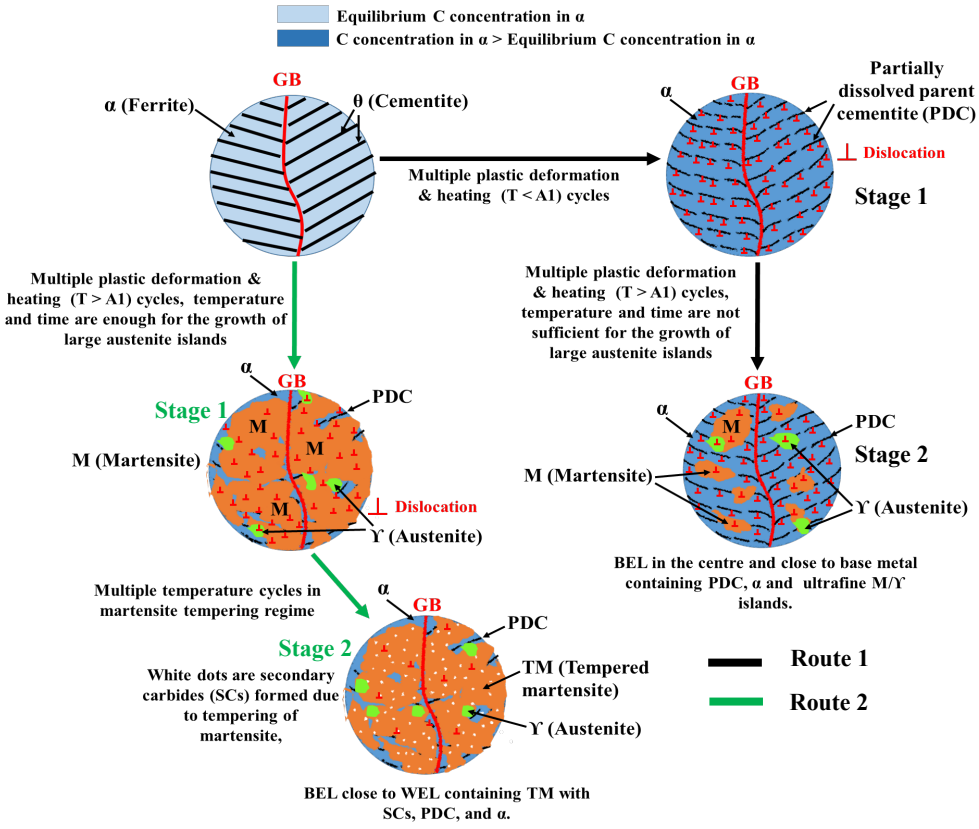


Fig. 3.12. Schematic showing the formation mechanism of the BEL. Each plastic deformation and heating cycle is an individual wheel-rail contact. Depending on the local amounts of deformation and heat different scenarios are possible.

Fig. 3.9(f) and Fig. 3.10(d-e) show the presence of C-enriched ferrite, partially dissolved parent cementite and ultrafine/nanocrystalline martensite/austenite islands in the mid-region of the BEL and the BEL-region just above the BEL/deformed pearlite interface. This indicates that the time and peak temperatures above A1 are not enough for the growth of austenite islands and the complete dissolution of cementite laths. The BEL in these regions may also be considered as a precursor of the WEL. As per the Thermo-Calc calculation in Fig. 3.2, the temperature must rise above 715 °C to form the austenite in the BEL. To understand the formation of martensite/austenite islands in the BEL, similar C diffusional length calculations as discussed in sec. 3.3.9 were performed. The average diffusional length of C in austenite in the BEL is 7 nm, if a temperature of 715 °C is assumed to be present for the duration of $1.6 \times 10^{-4}$ s (Fig. 3.3). Therefore, to achieve an average martensite/austenite island size of 210 ± 80 nm (sec. 3.3.7), multiple cycles of 715 °C peak

temperature are necessary. This mechanism is illustrated in the second stage of route 1 in Fig. 3.12.

## 3.4 Conclusions

According to our findings, the WEL and the BEL are formed by repetitive/multiple wheel-rail contacts, where each wheel represents an individual thermomechanical treatment. Following conclusions are drawn from this study:

1. The microstructure of the WELs at the surface consists of martensite and austenite. This proves that temperature must have risen above the A1 here. A lower austenite content at the surface than at the subsurface exists due to the strain-induced transformation of austenite into martensite.
2. Besides frictional heat, plastic deformation also plays a significant role in the microstructural evolution of the WEL. The WEL undergoes dynamic alteration with each wheel contact. Nonetheless, these continuous alterations cause a 'steady-state' microstructure with characteristic features such as a certain ratio between phases, dislocation densities, grain sizes, *etc.* that is representative for the temperature and deformation conditions.
3. The parent cementite is completely dissolved in the WEL at the rail surface whereas partially dissolved parent cementite particles are found at the subsurface. The presence of the parent cementite particles at the subsurface results in a lower C concentration in the martensitic matrix than at the rail surface.
4. Cyclic plastic deformation during wheel-rail contacts increases the defect density (dislocations and vacancies) in ferrite. High interaction energy between C and these defects facilitates cementite dissolution to form WELs/BELs. The temperature rise also promotes defect-assisted thermal diffusion of C from cementite to the dislocations in ferrite. Simultaneously, the "C drag effect" can also contribute to the cementite dissolution.
5. The temperature in the BEL is in general lower than in the WEL. The presence of austenite in the BEL shows that peak temperatures of 715 °C and above should be reached in some wheel-rail contacts. However, the cumulative heat and plastic deformation in the BEL is not sufficient for full austenitization and complete dissolution of parent cementite.

## References


[1] K.D. Vo, H.T. Zhu, A.K. Tieu, P.. Kosasih, FE method to predict damage formation on curved track for various worn status of wheel/rail profiles, Wear. 322–323 (2015) 61–75. doi:10.1016/J.WEAR.2014.10.015.

[2] A. Al-Juboori, D. Wexler, H. Li, H. Zhu, C. Lu, A. McCusker, J. McLeod, S. Pannil, Z. Wang, Squat formation and the occurrence of two distinct classes of white etching layer on the surface of rail steel, Int. J. Fatigue. 104 (2017) 52–60. doi:10.1016/J.IJFATIGUE.2017.07.005.

[3] H. Yahyaoui, H. Sidhom, C. Braham, A. Baczmanski, Effect of interlamellar spacing on the elastoplastic behavior of C70 pearlitic steel: Experimental results and self-consistent modeling, Mater. Des. 55 (2014) 888–897. doi:10.1016/J.MATDES.2013.10.062.

[4] M. Steenbergen, R. Dollevoet, On the mechanism of squat formation on train rails – Part I: Origination, Int. J. Fatigue. 47 (2013) 361–372. doi:10.1016/J.IJFATIGUE.2012.04.023.

[5] M. Steenbergen, R. Dollevoet, On the mechanism of squat formation on train rails – Part II: Growth, Int. J. Fatigue. 47 (2013) 373–381. doi:10.1016/J.IJFATIGUE.2012.04.019.

[6] R.I. Carroll, J.H. Beynon, Rolling contact fatigue of white etching layer: Part 1: Crack morphology, Wear. 262 (2007) 1253–1266. doi:10.1016/J.WEAR.2007.01.003.

[7] R.I. Carroll, J.H. Beynon, Rolling contact fatigue of white etching layer: Part 2. Numerical results, Wear. 262 (2007) 1267–1273. doi:10.1016/J.WEAR.2007.01.002.

[8] J. Takahashi, K. Kawakami, M. Ueda, Atom probe tomography analysis of the white etching layer in a rail track surface, Acta Mater. 58 (2010) 3602–3612. doi:10.1016/J.ACTAMAT.2010.02.030.

[9] J. Wu, R.H. Petrov, S. Kölling, P. Koenraad, L. Malet, S. Godet, J. Sietsma, Micro and Nanoscale Characterization of Complex Multilayer-Structured White Etching Layer in Rails, Met. . 8 (2018). doi:10.3390/met8100749.

[10] S.B. Newcomb, W.M. Stobbs, A transmission electron microscopy study of the white-etching layer on a rail head, Mater. Sci. Eng. 66 (1984) 195–204. doi:10.1016/0025-5416(84)90180-0.

[11] G. Baumann, H.J. Fecht, S. Liebelt, Formation of white-etching layers on rail treads, Wear. 191 (1996) 133–140. doi:10.1016/0043-1648(95)06733-7.

[12] J. Wu, R.H. Petrov, M. Naeimi, Z. Li, R. Dollevoet, J. Sietsma, Laboratory simulation of martensite formation of white etching layer in rail steel, Int. J. Fatigue. 91 (2016) 11–20. doi:10.1016/J.IJFATIGUE.2016.05.016.

[13] A. Pyzalla, L. Wang, E. Wild, T. Wroblewski, Changes in microstructure, texture and residual stresses on the surface of a rail resulting from friction and wear, Wear. 251 (2001) 901–907. doi:10.1016/S0043-1648(01)00748-7.

[14] L. Wang, A. Pyzalla, W. Stadlbauer, E.. Werner, Microstructure features on rolling surfaces of railway rails subjected to heavy loading, Mater. Sci. Eng. A. 359 (2003) 31–43. doi:10.1016/S0921-5093(03)00327-7.

[15] H.W. Zhang, S. Ohsaki, S. Mitao, M. Ohnuma, K. Hono, Microstructural investigation of white etching layer on pearlite steel rail, Mater. Sci. Eng. A. 421 (2006) 191–199. doi:10.1016/J.MSEA.2006.01.033.

[16] W. Österle, H. Rooch, A. Pyzalla, L. Wang, Investigation of white etching layers on rails by optical microscopy, electron microscopy, X-ray and synchrotron X-ray diffraction, Mater. Sci. Eng. A. 303 (2001) 150–157. doi:10.1016/S0921-5093(00)01842-6.

[17] W. Lojkowski, M. Djahanbakhsh, G. Bürkle, S. Gierlotka, W. Zielinski, H.-J. Fecht, Nanostructure formation on the surface of railway tracks, Mater. Sci. Eng. A. 303 (2001) 197–208. doi:10.1016/S0921-5093(00)01947-X.

[18] J. Ahlström, B. Karlsson, Microstructural evaluation and interpretation of the mechanically and thermally affected zone under railway wheel flats, Wear. 232 (1999) 1–14. doi:10.1016/S0043-1648(99)00166-0.

[19] S. Li, J. Wu, R.H. Petrov, Z. Li, R. Dollevoet, J. Sietsma, “Brown etching layer”: A possible new insight into the crack initiation of rolling contact fatigue in rail steels?, Eng. Fail. Anal. 66 (2016) 8–18. doi:10.1016/J.ENGFAILANAL.2016.03.019.

[20] A. Al-Juboori, H. Zhu, D. Wexler, H. Li, C. Lu, A. McCusker, J. McLeod, S. Pannila, J. Barnes, Evolution of rail surface degradation in the tunnel: The role of water on squat growth under service conditions, Eng. Fract. Mech. 209 (2019) 32–47. doi:10.1016/J.ENGFRACMECH.2019.01.018.

[21] M. Messaadi, M. Steenbergen, Stratified surface layers on rails, Wear. 414–415 (2018) 151–162. doi:10.1016/J.WEAR.2018.07.019.

[22] R.S. Tahany Ibrahim El-Wardany, Sergei F. Burlatsky, Changsheng GuoWayde, Control of white-etched layer during machining, US7827661B2, 2008. https://patents.google.com/patent/US7827661.

[23] Y. V Ivanisenko, R.Z. Valiev, W. Lojkowski, A. Grob, H.-J. Fecht, Nanostructure Formation and Carbides Dissolution in Rail Steel Deformed by High Pressure Torsion, Ultrafine Grained Mater. II. (2013). doi:doi:10.1002/9781118804537.ch6.

[24] S.B. Hosseini, U. Klement, Y. Yao, K. Ryttberg, Formation mechanisms of white layers induced by hard turning of AISI 52100 steel, Acta Mater. 89 (2015) 258–267. doi:10.1016/J.ACTAMAT.2015.01.075.

[25] F.D. Fischer, W. Daves, E.A. Werner, On the temperature in the wheel–rail rolling

contact, Fatigue Fract. Eng. Mater. Struct. 26 (2003) 999–1006.

[26] J.-M. Bergheau, R. Fortunier, Finite element simulation of heat transfer, John Wiley & Sons, 2013.

[27] F. Vurpillot, B. Gault, B.P. Geiser, D.J. Larson, Reconstructing atom probe data: A review, Ultramicroscopy. 132 (2013) 19–30. doi:10.1016/j.ultramic.2013.03.010.

[28] B. Gault, M.P. Moody, J.M. Cairney, S.P. Ringer, Atom probe crystallography, Mater. Today. 15 (2012) 378–386.

[29] M. Herbig, P. Choi, D. Raabe, Combining structural and chemical information at the nanometer scale by correlative transmission electron microscopy and atom probe tomography, Ultramicroscopy. 153 (2015) 32–39. doi:10.1016/J.ULTRAMIC.2015.02.003.

[30] M. Herbig, Spatially correlated electron microscopy and atom probe tomography: Current possibilities and future perspectives, Scr. Mater. 148 (2018) 98–105. doi:10.1016/J.SCRIPTAMAT.2017.03.017.

[31] A. Rovira, A. Roda, M.B. Marshall, H. Brunskill, R. Lewis, Experimental and numerical modelling of wheel–rail contact and wear, Wear. 271 (2011) 911–924. doi:10.1016/J.WEAR.2011.03.024.

[32] K. D. Vo, A. K. Tieu, H. T. Zhu, A Tool To Estimate The Wheel/rail Contact And Temperature Rising Under Dry, Wet And Oily Conditions, WIT Press, 2014. doi:http://dx.doi.org/10.2495/CR140151.

[33] M. Ertz, K. Knothe, A comparison of analytical and numerical methods for the calculation of temperatures in wheel/rail contact, Wear. 253 (2002) 498–508. doi:10.1016/S0043-1648(02)00120-5.

[34] F.D. Fischer, E. Werner, K. Knothe, The Surface Temperature of a Halfplane Heated by Friction and Cooled by Convection, ZAMM - J. Appl. Math. Mech. / Zeitschrift Für Angew. Math. Und Mech. 81 (2001) 75–81. doi:10.1002/1521-4001(200102)81:2<75::AID-ZAMM75>3.0.CO;2-H.

[35] E.B. Hawbolt, B. Chau, J.K. Brimacombe, Kinetics of austenite-pearlite transformation in eutectoid carbon steel, Metall. Trans. A. 14 (1983) 1803–1815. doi:10.1007/BF02645550.

[36] J. Pacyna, The microstructure and properties of the new bainitic rail steels, J. Achiev. Mater. Manuf. Eng. 28 (2008) 19–22.

[37] W. Wei-yong, L. Bing, K. Venkatesh, Effect of Temperature on Strength and Elastic Modulus of High-Strength Steel, J. Mater. Civ. Eng. 25 (2013) 174–182. doi:10.1061/(ASCE)MT.1943-5533.0000600.

[38] C. Ju, Y. Ben, U. Brian, Behavior of High Strength Structural Steel at Elevated Temperatures, J. Struct. Eng. 132 (2006) 1948–1954. doi:10.1061/(ASCE)0733-

9445(2006)132:12(1948).

[39] J. Chen, B. Young, Design of high strength steel columns at elevated temperatures, J. Constr. Steel Res. 64 (2008) 689–703. doi:10.1016/J.JCSR.2007.09.004.

[40] S. Zaefferer, N.-N. Elhami, Theory and application of electron channelling contrast imaging under controlled diffraction conditions, Acta Mater. 75 (2014) 20–50. doi:10.1016/J.ACTAMAT.2014.04.018.

[41] S.K. Makineni, A. Kumar, M. Lenz, P. Kontis, T. Meiners, C. Zenk, S. Zaefferer, G. Eggeler, S. Neumeier, E. Spiecker, D. Raabe, B. Gault, On the diffusive phase transformation mechanism assisted by extended dislocations during creep of a single crystal CoNi-based superalloy, Acta Mater. 155 (2018) 362–371. doi:10.1016/J.ACTAMAT.2018.05.074.

[42] Q. Liu, D. Juul Jensen, N. Hansen, Effect of grain orientation on deformation structure in cold-rolled polycrystalline aluminium, Acta Mater. 46 (1998) 5819–5838. doi:10.1016/S1359-6454(98)00229-8.

[43] E. Girault, P. Jacques, P. Harlet, K. Mols, J. Van Humbeeck, E. Aernoudt, F. Delannay, Metallographic Methods for Revealing the Multiphase Microstructure of TRIP-Assisted Steels, Mater. Charact. 40 (1998) 111–118. doi:10.1016/S1044-5803(97)00154-X.

[44] G.F. Vander Voort, E.P. Manilova, Hints for Imaging Phases in Steels-How-to article covers ways to improve the visibility and identification of" white-etching phases"--Ferrite, delta ferrite, cementite, and retained austenite--, Adv. Mater. Process. 163 (2005) 32–38.

[45] R. Wu, A.J. Freeman, G.B. Olson, Effects of carbon on Fe-grain-boundary cohesion: First-principles determination, Phys. Rev. B. 53 (1996) 7504.

[46] P. Lejček, S. Hofmann, Thermodynamics and structural aspects of grain boundary segregation, Crit. Rev. Solid State Mater. Sci. 20 (1995) 1–85. doi:10.1080/10408439508243544.

[47] J. Takahashi, M. Kosaka, K. Kawakami, T. Tarui, Change in carbon state by low-temperature aging in heavily drawn pearlitic steel wires, Acta Mater. 60 (2012) 387–395. doi:10.1016/J.ACTAMAT.2011.09.014.

[48] J. Languillaume, G. Kapelski, B. Baudelet, Cementite dissolution in heavily cold drawn pearlitic steel wires, Acta Mater. 45 (1997) 1201–1212. doi:10.1016/S1359-6454(96)00216-9.

[49] X. Sauvage, J. Copreaux, F. Danoix, D. Blavette, Atomic-scale observation and modelling of cementite dissolution in heavily deformed pearlitic steels, Philos. Mag. A. 80 (2000) 781–796. doi:10.1080/01418610008212082.

[50] L. Zhou, G. Liu, X.L. Ma, K. Lu, Strain-induced refinement in a steel with spheroidal cementite subjected to surface mechanical attrition treatment, Acta Mater.

56 (2008) 78–87. doi:10.1016/J.ACTAMAT.2007.09.003.

[51] M. Umemoto, Y. Todaka, K. Tsuchiya, Mechanical Properties of Cementite and Fabrication of Artificial Pearlite, Mater. Sci. Forum. 426–432 (2003) 859–864. doi:10.4028/www.scientific.net/MSF.426-432.859.

[52] A.V. Korznikov, Y.V. Ivanisenko, D.V. Laptionok, I.M. Safarov, V.P. Pilyugin, R.Z. Valiev, Influence of severe plastic deformation on structure and phase composition of carbon steel, Nanostructured Mater. 4 (1994) 159–167. doi:10.1016/0965-9773(94)90075-2.

[53] G.A. Nematollahi, B. Grabowski, D. Raabe, J. Neugebauer, Multiscale description of carbon-supersaturated ferrite in severely drawn pearlitic wires, Acta Mater. 111 (2016) 321–334. doi:10.1016/J.ACTAMAT.2016.03.052.

[54] A. Vehanen, P. Hautojärvi, J. Johansson, J. Yli-Kauppila, P. Moser, Vacancies and carbon impurities in $\ensuremath{\alpha}$- iron: Electron irradiation, Phys. Rev. B. 25 (1982) 762–780. doi:10.1103/PhysRevB.25.762.

[55] A.H. Cottrell, B.A. Bilby, Dislocation theory of yielding and strain ageing of iron, Proc. Phys. Soc. Sect. A. 62 (1949) 49.

[56] W.G. Johnston, D.F. Stein, Stress dependence of dislocation velocity inferred from strain rate sensitivity, Acta Metall. 11 (1963) 317–318.

[57] X. Jiang, X. Li, X. Li, S. Cao, Rail fatigue crack propagation in high-speed wheel/rail rolling contact, J. Mod. Transp. 25 (2017) 178–184. doi:10.1007/s40534-017-0138-6.

[58] J.R.G. da Silva, R.B. McLellan, Diffusion of carbon and nitrogen in B.C.C. iron, Mater. Sci. Eng. 26 (1976) 83–87. doi:10.1016/0025-5416(76)90229-9.

[59] F.J. Humphreys, A unified theory of recovery, recrystallization and grain growth, based on the stability and growth of cellular microstructures—I. The basic model, Acta Mater. 45 (1997) 4231–4240. doi:10.1016/S1359-6454(97)00070-0.

## Appendix chapter 3

### *3.A.1 Thermodynamic consideration at high pressure under wheel-rail contact*

Fig. 3.A.1 shows the dependence of the phase fraction of austenite, ferrite and cementite on temperature in the R350HT pearlitic steels in thermodynamic equilibrium. The plot was calculated for 2 GPa pressure using the Thermo-Calc software.

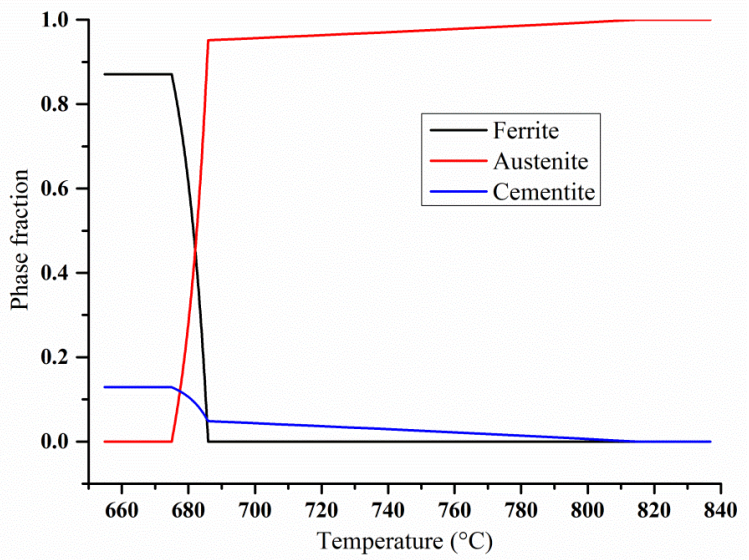


Fig. 3.A.1. Plot of phase fractions over temperatures at 2 GPa pressure in R350HT generated using Thermo-Calc.

### *3.A.2 Texture evolution in WEL and BEL*

The study of the texture evolution in the WELs and the BELs is conducted using the EBSD data shown in section 3.3.5 in this chapter.

#### *3.A.2.1 Region 1 (WEL close to the surface) (0-25 µm rail depth)*

Fig. 3.A.2 shows the texture analysis results from the WEL close to the rail surface (rail depth 0-25 µm). The texture intensity lies in the range between 1.4 and 2.4. Thus, no pronounced texture development is observed in this region.

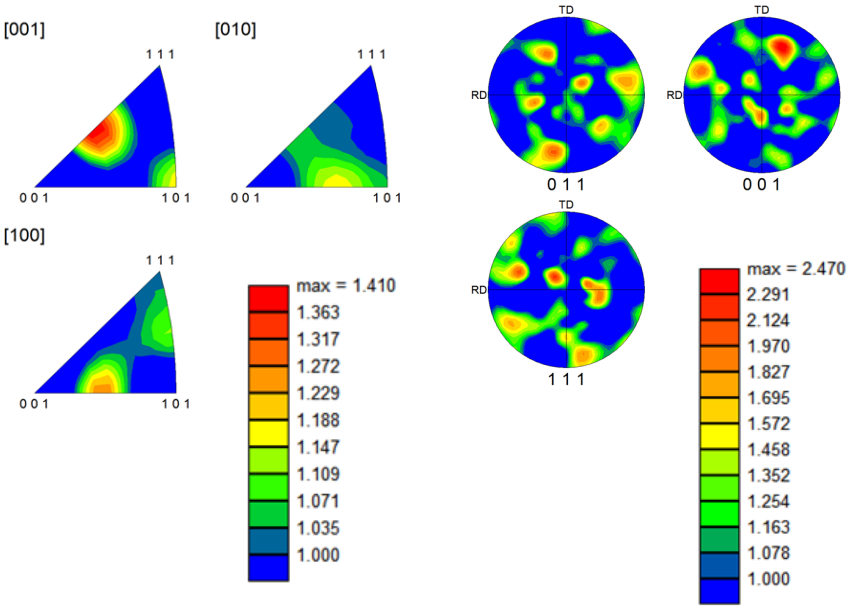


Fig. 3.A.2. Inverse pole figure and pole figures taken in the train running direction showing no pronounced texture development in the WEL close to the rail surface (0-25 µm rail depth).

### *3.A.2.2 Region 2 (WEL at the subsurface) (25-50 µm rail depth)*

Fig. 3.A.3 shows the texture results from the WEL at the subsurface (rail depth 25-50 µm). These results also show no pronounced texture development in this region as the texture intensity lies in a low range of 1.2 to 1.9.

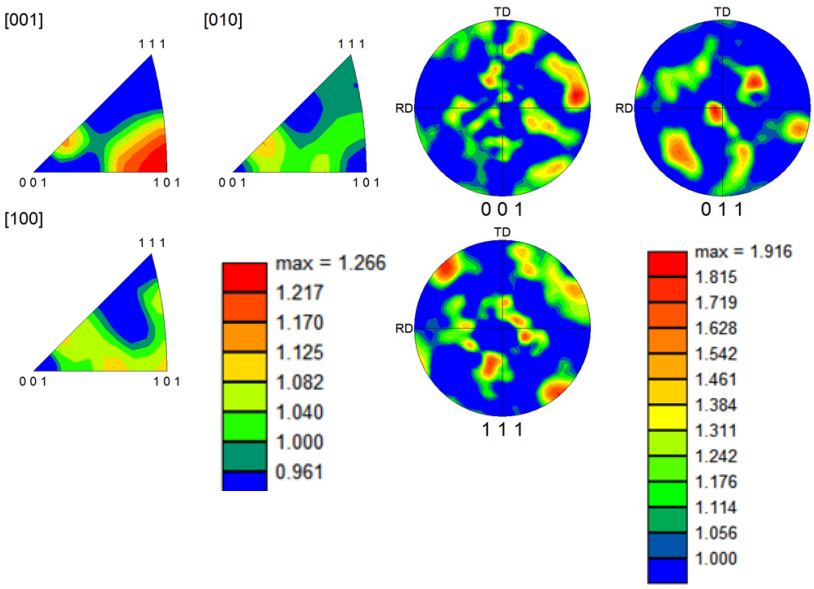


Fig. 3.A.3. Inverse pole figure and pole figures taken in the train running direction showing no obvious texture intensity in the WEL at the subsurface (25-50 µm rail depth).

### *3.A.2.3 Region 3 (BEL below the WEL) (60-80 µm rail depth)*

Fig. 3.A.4 shows the texture results from the BEL below the WEL (rail depth 60-80 µm). These results also show no pronounced texture in this region of the BELs as the texture intensity lies in the range from 1.2 to 2.1 which is low.

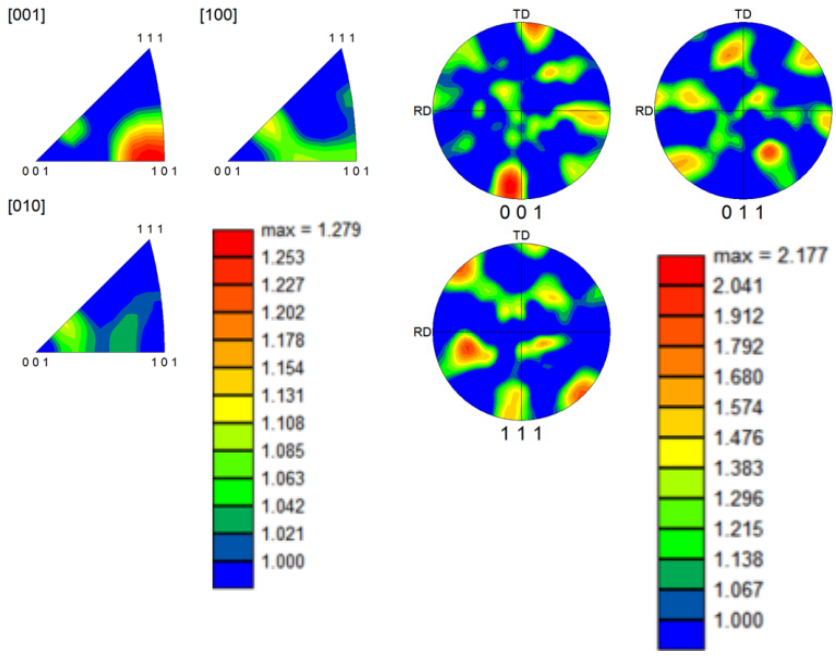


Fig. 3.A.4. Inverse pole figure and pole figures taken in the train running direction showing no obvious texture intensity in the BEL below the WEL (60-80 µm rail depth).

### *3.A.2.4 Region 4 (BEL above the deformed pearlitic matrix) (80-100 µm rail depth)*

Fig. 3.A.5 shows the texture results from the BEL above the deformed pearlitic matrix (rail depth = 80-100 µm). These results also show no pronounced texture in this region of the BELs as the texture intensity lies in the range from 1.2 to 2.4 which is low as well.

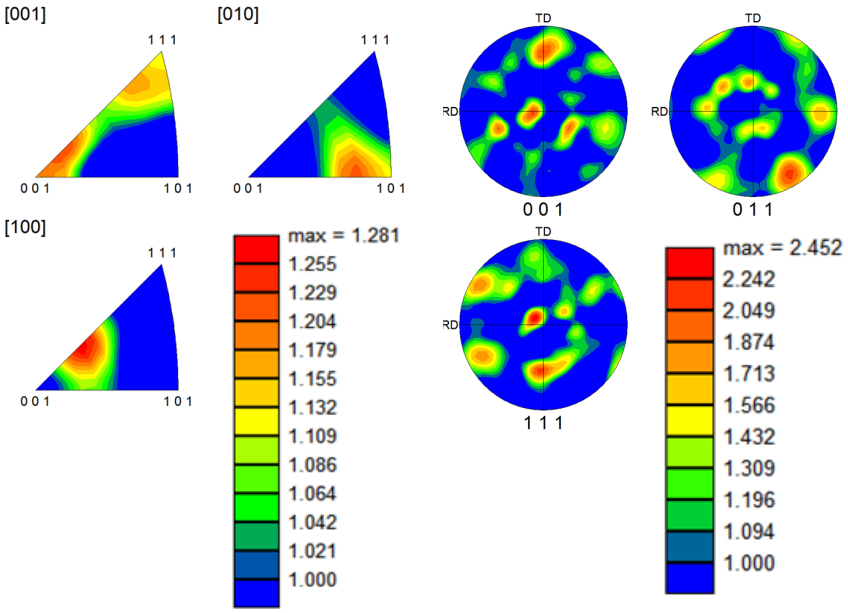


Fig. 3.A.5. Inverse pole figure and pole figures taken in the train running direction showing no obvious texture intensity in the BEL abobe the deformed pearlitic matrix (80-100 μm rail depth).

# 4

# *In-situ* study on fracture behaviour of white etching layers formed on rails**


## Abstract

Failure in engineering materials like steels is strongly affected by in-service deleterious alterations in their microstructure. White Etching Layers (WELs) are an example of such in-service alterations in the pearlitic microstructure at the rail surface. Cracks initiate in the rails due to delamination and fracture of these layers and propagate into the base material posing severe safety concerns. In this study, we investigate the microscale fracture behaviour of these WELs. We use *in-situ* elastic-plastic fracture mechanics using *J*-integral to quantify the fracture toughness. Although usually assumed brittle, the fracture toughness of 21 – 25 MPa√m reveals a semi-brittle nature of WELs. WELs show crack tip blunting, branching, and significant plasticity during crack growth due to their complex microstructure. The fracture behaviour of the WELs is governed by their microstructural constituents such as phases (martensite/austenite), grain size, dislocation density and carbon segregation to dislocations and grain boundaries. We observed dislocation annihilation in some martensitic grains in the WELs which also contributes to their fracture behaviour. Additionally, the strain-induced transformation from austenite to martensite affects the crack growth and fracture.


** This chapter is based on the article: A. Kumar, A. K. Saxena, C. Kirchlechner, M. Herbig, S. Brinkmann, R. Petrov, and J. Sietsma, *In-situ* study on fracture behaviour of white etching layers formed on rails, (Under review in Acta Materialia)

## 4.1 Introduction

The design of sustainable new materials with well-controlled structural integrity requires a macro- to microscale understanding of degradation and failure of the conventional materials. Steels are one of the most commonly used conventional materials around the world. The study of failure in steels is crucial to ensure the safety in engineering applications such as construction, transport, energy, *etc*. In the transport industry, railway consists of 1,370,782 km length of rail track worldwide [1] and this length is still growing. In this entire rail network, the pearlitic steels are the most commonly used steels [2]. Failure in pearlitic railway steels is strongly affected by the detrimental microstructural changes on the rail raceway due to the wheel-rail contact. Conventional pearlitic steels are prone to the formation of White Etching Layers (WELs) on the rail raceway during the wheel-rail interaction [3–11]. Delamination and partial brittle fracture of these WELs cause micro-crack initiation in the rails [4,5,9,10,12–14]. These micro-cracks grow into the base material and this propagation finally leads to rail track failure, posing a safety threat to the passengers. Worldwide, the rail industries invest tens of million dollars per year to grind various in-service surface defects and to remove the WELs before extended cracks form [15,16].

In the literature, two hypotheses are proposed for the formation mechanism of the WELs. The first hypothesis suggests that the WELs form only due to severe plastic deformation during wheel-rail contract and stress assisted cementite dissolution leads to the formation of nano-crystalline ferrite in the WEL microstructure [10,11,13]. The second hypothesis suggests that WELs form due to the temperature rise above austenite start temperature – followed by fast cooling [3,5,9]. This temperature variation leads to the formation of martensite and austenite. However, recent insights have shown that WELs form by the combination of the temperature rise above the austenite start temperature and the plastic deformation at the rail raceway [17–19]. Still, there is considerable debate among the research community concerning the WEL formation mechanism. Typically, the WELs consist of complex microstructural features such as martensite, retained austenite and partially dissolved parent cementite [7,17–19]. In addition, the overall microstructural evolution varies in different studies because of the variation in rail-wheel contact conditions such as wheel profile, axle load, train speed and slip rate. In spite of having a detailed understanding on formation mechanism and microstructural evolution of the WELs, there is no detailed study available in literature, which focuses on the fracture behaviour of the WEL on microstructural scale. Most of the available studies only focus on macro scale fracture due to the WELs in rails [4,20].

The WELs are considered to be among the metallurgical causes for crack initiation and propagation in rails because of their brittle nature [4,5,9,14,18,19]. However to date, there is no quantification of the fracture toughness of WELs and their fracture behaviour has not been studied in detail. This lack of fracture properties is primarily due to the small size of

in-service WELs. The fracture behaviour of such small features cannot be determined via conventional testing. Only small scale *in-situ* fracture mechanics allow studying the fracture behaviour of these microscale features. Micromechanics also allows analysing special microstructural features such as single crystals, grain boundaries, phase boundaries, coatings and multilayer microscale systems [21–28].

In the present study, we show *in-situ* microscale fracture experiments on the WELs. The fracture toughness values of the WELs can be of utmost importance for modelling the failure in rails due to the presence of WELs at the rail surface. They can also enable the estimation of quantities such as critical WEL thickness in rails and consequently the required grinding intervals in rails to avoid failure and also to minimize the grinding costs. For brittle materials, microscale fracture experiments use notched micro-cantilevers and apply Linear Elastic Fracture Mechanics (LEFM) [21–26,28–32] to quantify the fracture toughness. In these conditions, the size of the plastic zone at the crack tip should be significantly smaller than the specimen dimensions [33]. Thus, the LEFM approach is useful primarily for brittle materials, which fracture without any plastic deformation. Application of LEFM for ductile and semi-brittle materials will lead to the underestimation of the fracture toughness. We use both the LEFM and Elastic-Plastic Fracture Mechanics (EPFM) approach [33,34] to calculate the fracture toughness of the WELs.

In this study, the fracture toughness of the WELs is compared with those of undeformed pearlite, heavily drawn nanocrystalline pearlite, iron (Fe) and nanocrystalline Fe thin films in order to put the quantified fracture behaviour of the WELs into context. We discuss the effect of microstructural features such as the presence of austenite, grain size, dislocation density and carbon (C) segregation at the dislocations and the grain boundaries in the WELs on the fracture response. Additionally, we investigate the strain-induced transformation of austenite to martensite during crack growth in the WELs.

## 4.2 Materials and experimental methods

The specimens containing WEL were cut from an in-service curved rail track with 400 m radius. The approximate load passage was 200 Mt with an axial load ranging from 120 to 180 kN [19]. The chemical composition of the studied R350HT steel is Fe-0.72C-1.1Mn-0.56Si-0.11Cr (wt.%), or Fe-3.23C-1.09Si-1.1Mn-0.11Cr (at.%). These steels were produced by 6 pass hot rolling at 1000 °C into the form of a rail, followed by annealing at 900 °C for 3 hours and cooling the rail in the accelerated air flow which yields a fine fully pearlitic microstructure.

Specimens containing WELs were carefully ground after cutting with a low speed diamond saw in order to avoid microstructural alterations due to specimen preparation. Afterwards, the specimens were carefully polished with solutions containing 3 μm and 1 μm diamond

particles respectively, to remove the deformation layer from grinding. The specimens were then etched using 2% Nital solution to identify the WEL structure in the light optical microscope (Keyence VHX 6000). The WELs offer a higher resistance to chemical etching in comparison to the base pearlitic microstructure. Hence, chemical etching resulted in a better visibility of the WELs in the Scanning Electron Microscope (SEM) during the microcantilever preparation. The Vickers microhardness measurements were performed by a Dura-scan 70 (Struers) hardness tester using a load of 0.25 N for 10 s.

All microcantilevers in this study were prepared parallel to the rail surface and at a depth of approximately 10 µm from the rail surface within the WELs. The microcantilever are produced by mechanical polishing of the rail surface and followed by FIB milling. Micro-cantilevers of approximately 4 x 4 x 28 $\mu m^3$ were cut via FIB milling using a FEI Helios Dual Beam FIB microscope with an acceleration voltage of 30 kV. The 2.5 nA ion current was used for coarse milling, while intermediate milling was performed with an 86 pA ion current. Please note that higher currents cause severe re-deposition on the cantilever surface, which generates artefacts during mechanical testing. Thus, a final cleaning was performed with 40 pA ion current to remove the re-deposited layer. Afterwards, Electron Backscatter Diffraction (EBSD) analysis was performed on the cantilevers using a JEOL JSM 6500F SEM (SEM) to capture the WEL microstructure. All EBSD measurements were performed at an accelerating voltage of 15 kV, working distance of 18 mm, and a step size of 40 nm. The EBSD data was analysed using Orientation Image Microscopy (OIM) software (TSL-OIM). Bridge notches were cut in the Zeiss Auriga® dual beam microscope equipped with a Nano Patterning and Visualization Engine (NPVE). These notches were prepared with a 10 pA current and a 20 $nC/\mu m^2$ dose. The notch depth is in the range of 700 – 800 nm in different cantilevers.

The *in-situ* micromechanical tests were performed in a Zeiss Gemini 500 SEM microscope. The experiments were performed in a displacement controlled mode (0.02 µm/s) using a conductive diamond wedge indenter (ASMEC UNAT-II) with an opening angle of 60° and 10 µm wedge length. Videos of the crack propagation and cantilever deformation were also recorded.

The fracture toughness WELs was calculated by i) Matoy's *et. al.* LEFM approach [28] and ii) Wurster's *et.al.* EPFM approach [33].

LEFM was used to calculate the conditional stress intensity factor ($K_{IQ}$)

$$K_{IQ} = \frac{F_Q\, L}{B\, W^{3/2}}\, f(^{a}/_{W}) \tag{4.1}$$

$$f\left(\frac{a}{W}\right) = 1.46 + 24.36\left(\frac{a}{W}\right) - 47.21\left(\frac{a}{W}\right)^2 + 75.18\left(\frac{a}{W}\right)^3 \quad (4.2)$$

where $F_Q$ is the critical force, $L$ is the bending length, $a$ is the notch depth that is interpreted as the initial crack length, $B$ is the cantilever thickness, $W$ is the cantilever width and $f$ ($a/W$) is the shape factor for the specimen geometry [33].

The conditional linear elastic stress intensity factor $K_{IQ}$ is determined here (as opposed to the linear elastic fracture toughness $K_{IC}$) because the constraints on the sample geometry according to the ASTM Standards are not fulfilled in these experiments. In addition, the EPFM approach by Wurster *et al.* [33] was used to calculate the conditional fracture toughness ($K_{IQ,J}$) for WELs. This approach is detailed in Sec.4.3.2.

After *in-situ* micromechanical testing, cantilevers were polished using a 40 pA ion current and an approximate 1-2 µm layer was removed from the cantilever in a FEI Helios Dual Beam FIB. Afterwards, EBSD and SEM imaging of the fracture surface and crack morphology were carried out in a JEOL JSM 6500F SEM. The EBSD scans were used to characterize the microstructural changes in the WELs during crack growth.

Correlative Transmission Electron Microscopy (TEM) and Atom Probe Tomography (APT) measurements were conducted at a similar depth in the WEL (*i.e.* 10 µm below the rail surface) where micro fracture experiments were conducted. [35–40]. On the APT specimens, TEM analysis was carried out using a Philips CM-20 operated at 200 kV. After TEM inspection, the specimens were measured for near-atomic-scale compositional analysis in the APT. APT measurement were conducted using a LEAP 5000XS (CAMECA Instruments). The instrument was operated in laser pulsing mode at a rate of 200 kHz and with a pulse energy of 40 pJ. The specimen's base temperature was 50 K and the target detection rate was set to 5 ions per 1000 pulses. Data analysis was performed using the software package IVAS 3.6.12.

## 4.3 Results and discussion

### *4.3.1 Failure in rails due to the White Etching Layers (WELs)*

Fig. 4.1(a) is an optical micrograph showing the brittle failure of the WEL followed by fatigue crack propagation into the deformed and undeformed pearlitic matrix. The crack in the matrix grows at an angle of around 38° to the loading direction (opposite to the X direction in Fig. 4.1(a)), which is close to the direction of maximum resolved shear stresses (*i.e.* 45°). However, the crack in the WEL seems unaffected by the maximum resolved shear stresses and grows by brittle cleavage (Fig. 4.1(a)). The WELs are harder than the base pearlitic matrix: Fig. 4.1(b) shows the variation of micro hardness from the rail

raceway into the rail matrix material. The hardness in the WEL is maximum (1000 ± 25 HV) close to the rail raceway and decreases towards the base matrix (Fig. 4.1(b)). The hardness is 710 ± 20 HV close to WEL/deformed pearlite interface. The maximum thickness of the WEL in this case is around 80 µm.

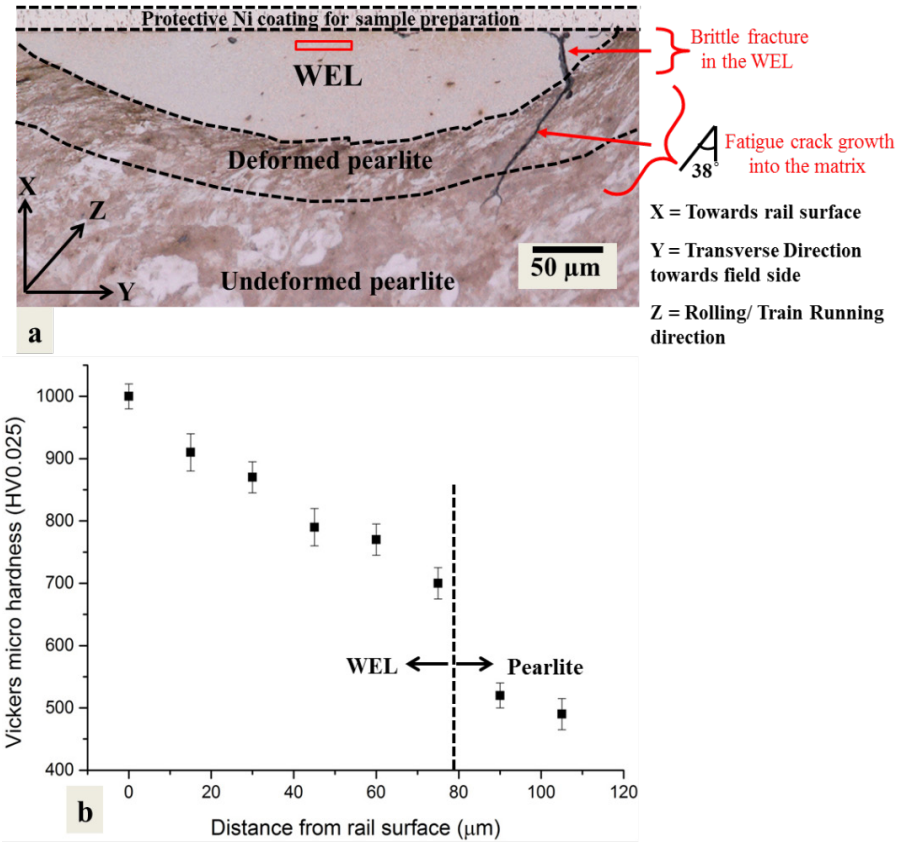


Fig. 4.1. Optical micrograph of brittle cleavage in the white etching layer that formed at the rail surface and crack propagation into the base pearlitic matrix. The red rectangle shows the position of the micro-cantilevers, (b) Micro hardness from the rail surface to the depth.

### *4.3.2 Calculation of fracture toughness of the WELs*

The schematic of the microcantilevers and the coordinate system of the cantilever with respect to the rail are shown in Fig. 4.2(a). A representative force ($F$) displacement ($d$) curve from the WEL microcantilever is shown in Fig. 4.2(b), in which the repeated loading/unloading sequences are used to measure the cantilever compliance and deduce the crack propagation evolution. The crack propagation at various steps (at 6 µm, 8 µm, 12 µm, and 15 µm) during the *in-situ* microcantilever deformation are shown in Fig. 4.2(c-h). The

force-displacement curve and crack tip behaviour highlight the elastic-plastic response of the WEL. The observed plasticity is attributed to the large plastic zone size and the complex microstructure of the WELs (discussed later in Sec. 4.3.5). The crack branching and micro-dimples are also observed (Fig. 4.2(h)), which reduce the effective crack intensity ahead of the primary crack tip and decrease the local driving force for crack propagation [41,42]. When applying LEFM (according to Eq. 4.1 and 4.2) to the force-displacement curve shown in Fig. 4.2(b), the linear elastic fracture toughness ($K_{IQ}$) of the WEL is determined as 4.2 ± 0.6 MPa√m (error margin is estimated from statistical error propagation).

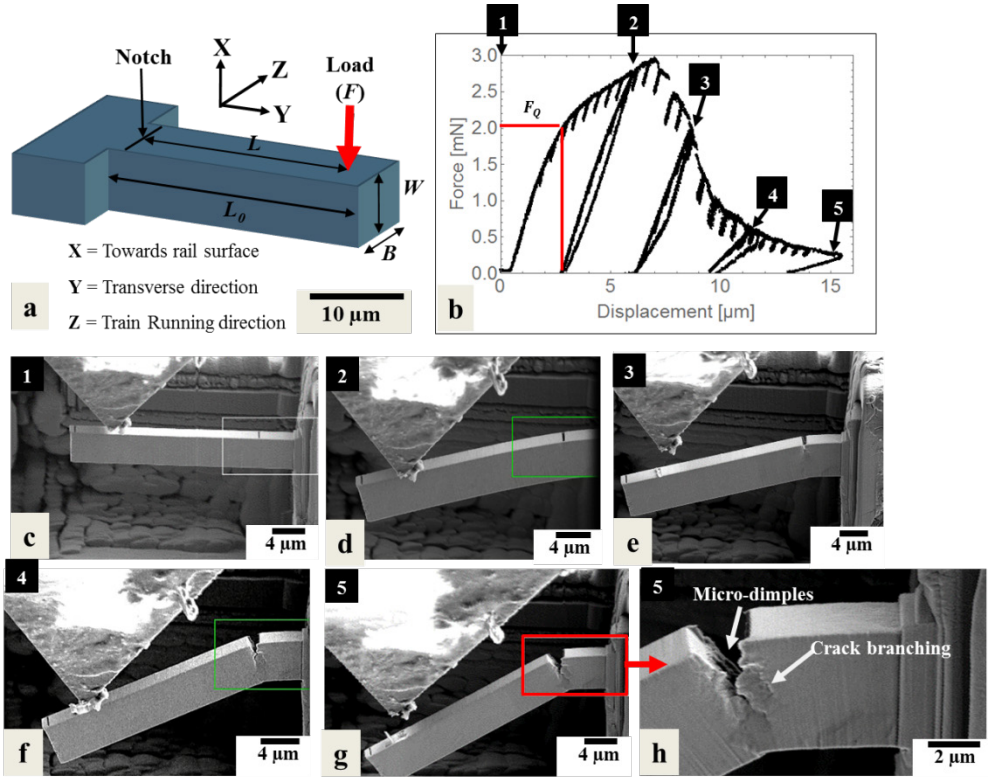


Fig. 4.2. *In-situ micro-cantilever deflection experiments:* (a) schematic of the microcantilever used for *in-situ* bending, (b) Load-displacement (*F-d*) curve of the WEL marked with four intermediate deformation steps (6 µm, 8 µm, 12 µm, and 15 µm), (c) WEL microcantilever before start of bending test, (d-g) SEM images of cantilever during four intermediate deformation steps *i.e.* (d) 6 µm, (e) 8 µm, (f) 12 µm and (g) 15 µm, (h) magnified SEM image of the WEL cantilever after 15 µm displacement, showing crack branching and micro-dimples on the fracture surface.

Significant plasticity is observed in the cantilever, as shown in Fig. 4.2(b). Thus, an elastic-plastic approach by Wurster *et al.* [33], is used to quantify the fracture toughness of the WEL. The unloading stiffness of cantilever is determined for each unloading segment and plotted against the displacement, as shown in Fig. 4.3(a). The cantilever stiffness continuously decreases with indenter displacement (Fig. 4.3(a)). The cantilever stiffness at each unloading step determines the instantaneous crack length ($a_i$), as evaluated by equation 4.3

$$a_i = W - \sqrt[3]{\frac{4\,k_i\,L^3}{B\,E}} \tag{4.3}$$

where $a_i$ is the crack length at the $i^{th}$ unloading step of unloading, $W$ is the cantilever width, $k_i$ is the cantilever stiffness at the $i^{th}$ unloading step, $B$ is the cantilever thickness, $E$ is the elastic modulus.

Fig. 4.3(b) shows the crack length plotted against the cantilever displacement (black symbols). This data shows that the crack length increases monotonically with the displacement. Afterwards, the $J$ integral is calculated as a sum of elastic and plastic components:

$$J_{(i)} = \frac{(K_{IQ(i)})^2(1-\nu^2)}{E} + \frac{\eta\,A_{Pl(i)}}{B\,(W-a_0)} \tag{4.4}$$

where $K_{IQ(i)}$ is the conditional stress intensity factor at the $i^{th}$ instant calculated from Eqs. (1) and (2), $\eta$ is a constant equal to 2, and $\nu$ is the Poisson ratio taken as 0.3. $A_{Pl(i)}$ denotes the area under the load-displacement curve Fig. 4.2(b).

The crack resistance curve is shown in Fig. 4.3(c), *i.e.* the crack extension against $J$ integral. The initial linear segment of crack resistance curve is known as blunting line and the later segment represents stable crack growth. The $J$ integral at intersection point of both lines is the critical $J$ integral ($J_c$) (Fig. 4.3(c)) according to Wurster *et al.* [33], which is used to calculate the fracture toughness ($K_{IQ,J}$):

$$K_{IQ,J} = \sqrt{\frac{J_c\,E}{1-\nu^2}} \tag{4.5}$$

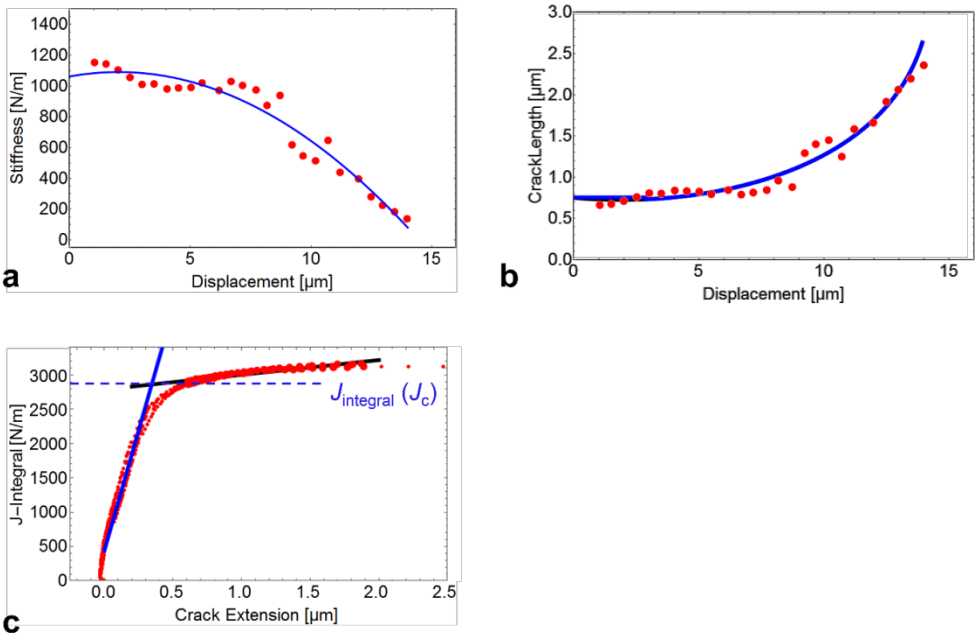


Fig. 4.3. ***Elastic-plastic fracture mechanics approach.*** (a) Stiffness variation of the micro-cantilever with respect to displacement, (b) Crack growth/extension with respect to cantilever displacement derived from unloading compliances of the micro-cantilever, (c) Variation of *J*-integral vs crack extension.

The critical J-integral is approximately 2900 N/m which corresponds to a conditional fracture toughness ($K_{IQ,J}$) of 25.4 ± 2.3 MPa√m for the WEL (error margin is estimated from statistical error propagation). It should be noted that the obtained conditional toughness depends on the geometry and definition of $J_c$. A thorough discussion about this can be found in [43].

The fracture toughness from four microcantilevers show significant plasticity, as shown in Table 4.1. It is observed that the linear elastic toughness $K_{IQ}$ for WELs is in the range of 4.2 – 7.6 MPa√m, whereas the $K_{IQ,J}$ vary from 21 – 25 MPa√m.

Table 4.1. Fracture toughness according to LEFM and EPFM ($K_{IQ}$ and $K_{IQ,J}$) of the WEL cantilevers, with corresponding dimensions, notch size, and calculated J integral values. Cantilever 4 is shown in Fig. 4.2. (Error margins are estimated from statistical error propagation).

| Sample Number | Dimensions ($B$ x $W$ x $L$) $\mu m^3$ | Notch size $a$ (µm) | Linear elastic fracture toughness $K_{IQ}$ (MPa√m) | J-integral (N/m) | Fracture toughness (EPFM) $K_{IQ,J}$ (MPa√m) |
|---|---|---|---|---|---|
| Cantilever 1 | 3.7x4.2x20 | 0.74 | 5.9 ± 0.9 | 2075 | 21.5 ± 3.5 |
| Cantilever 2 | 3.6x3.9x22 | 0.69 | 7.6 ± 1.1 | 2420 | 23.2 ± 3.3 |
| Cantilever 3 | 4.2x4.3x23 | 0.79 | 6.0 ± 0.9 | 2600 | 24.0 ± 3.4 |
| Cantilever 4 | 4.1x4.1x19 | 0.75 | 4.2 ± 0.6 | 2890 | 25.4 ± 2.3 |

Based on the fracture toughness values given in Table 4.1, the WELs show an average $K_{IQ}$ of 5.9 ± 0.6 MPa√m and an average $K_{IQ,J}$ of 23.5 ± 0.7 MPa√m. The error margins are expressed as standard error of the mean.

### *4.3.3 Fracture surface analysis and crack blunting in the WELs*

Fig. 4.4 shows the fracture surface images of the cracked cantilevers 1 and 2 from Table 4.1. Fig. 4.4(a) highlights crack blunting, which is an indication of plasticity induced crack arrest. Microdimples are also observed on the fracture surfaces of all cantilevers (Fig. 4.4(a,b)).

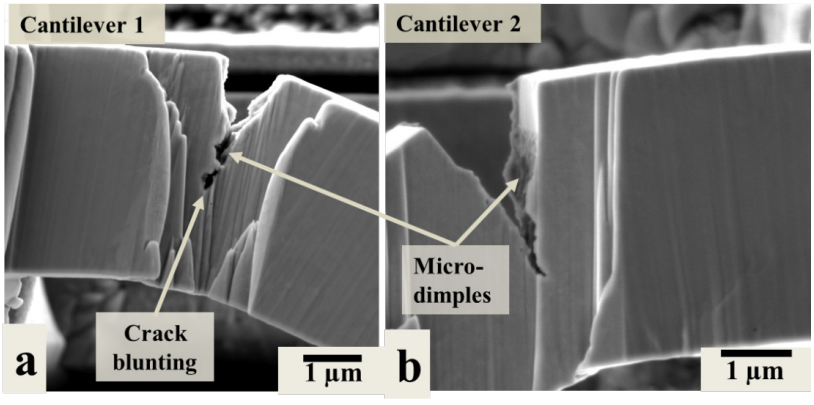


Fig. 4.4. (a-b) Fracture surface images of the cracked cantilevers 1 and 2 showing crack blunting and the presence of microdimples.

### *4.3.4 Comparison of fracture toughness of WELs with other Fe-based alloys*

Table 4.2 shows the comparison of fracture toughness of the present WEL specimens and of Fe-based alloys from literature [30,42,44,45]. It is worth to mention that the comparison is difficult due to the large differences in the chemical composition, processing routes and the microstructural features (*i.e.* grain sizes, phase constituents, *etc.*). Additionally, the limited data on the fracture toughness at the microscale, the lack of standardization at small dimensions dissatisfying ASTM standards and differences in the specimen sizes further complicates the precise comparison. However, the comparison shows the range of variation in Fe-based alloys.

The WELs formed from an initially fully pearlitic microstructure in the rails. We compare the reported fracture toughness of the WELs to that of undeformed pearlitic steels. Hohenwarter *et al.* [44] showed that fully pearlitic steels at the macroscale, with interlamellar spacing of around 200 nm, display ductile failure with a fracture toughness of $K_{IC}$ = 53 MPa√m (Table 4.2). This value is larger than the conditional fracture toughness ($K_{IQ,J}$) for WELs (21 – 25 MPa√m) reported in this study. This comparison indicates that the WELs are more brittle than undeformed pearlitic steels.

The fracture toughness of WELs is further compared to the toughness of nanocrystalline heavily drawn pearlitic steels wires (Table 4.2), due to some similarities between their microstructures. The WELs on the rail surface are formed due to the combined effect of temperature rise above the austenitization temperature followed by fast cooling, and heavy plastic deformation [17–19]. The microstructure of the WELs primarily consists of the martensite phase with some austenite and partially dissolved parent cementite. Therefore, the presence of martensite and plastic deformation under wheel-rail contact both contribute to a high dislocation density in the WEL microstructure [6,17–19]. Similarly, the heavily drawn pearlitic wires show a high dislocation density, the presence of partially dissolved cementite and deformation-induced martensite [46]. Due to these similarities, the heavily drawn pearlitic wires are a good system for comparison with the WELs. Jaya *et al.* [45] showed that heavily drawn pearlitic wires at $\varepsilon$ = 3.2 show elastic-plastic rupture with a conditional fracture toughness $K_{IQ,J}$ = 27 MPa√m (Table 4.2) in the wire drawing direction. That value is close to the fracture toughness of the WELs measured in the current study ($K_{IQ,J}$ = 21 – 25 MPa√m). The fracture toughness of the heavily drawn wires decreases with the increase in drawing strain. The wires show linear elastic fracture and brittle fracture surfaces for drawing strains of 4.2 ($K_{IQ}$ = 5.2 MPa√m) and 5.2 ($K_{IQ}$ = 4 MPa√m) (Table 4.2). Hohenwarter *et al.* [30] showed that fracture toughness of these wires depends strongly on the crack growth direction with respect to the wire axis. The fracture toughness ($K_{IQ,J}$) of these wires is around 40 MPa√m at $\varepsilon$ = 3.1 and 21 MPa√m at $\varepsilon$ = 6.5 in the direction perpendicular to the wire axis (Table 4.2). The WELs are not expected to show

similar anisotropy in the fracture toughness because of the absence of texture and the equiaxed grain shape [19].

We compare the WEL fracture toughness to that of ductile ferrite (BCC iron) and brittle nanocrystalline Fe thin films. Hohenwarter *et al.* [42] measured the fracture toughness ($K_{IC}$) of 202 MPa√m for Fe with an average grain size of 38 μm (Table 4.2). Nanocrystalline sputtered Fe thin films shows highly brittle rupture: $K_{IQ}$ = 2 MPa√m [45] (Table 4.2).

Based on those comparisons and based on the experimental evidence of plasticity in the microcantilever tests, it is concluded that the WELs are neither as ductile as Fe or pearlitic steels nor as brittle as nanocrystalline Fe thin films or heavily drawn pearlitic wires when tested in the drawing direction. The WELs rather show semi-brittle fracture response with intermediate fracture toughness values ($K_{IQ,J}$ = 21 – 25 MPa√m).

Table 4.2. Comparison of fracture toughness values of the WELs with other Fe based alloys [30,42,44,45]. The lower boundary of the fracture toughness ($K_{IQ}$) is calculated from linear elastic assumptions. The conditional fracture toughness ($K_{IQ,J}$) is the lower bound plus the correction according to the plastic hinge model of Wurster *et al.* [33]. The fracture toughness $K_{IC}$ fulfils all criteria of the ASTM standards.

| Materials | Linear elastic fracture toughness $K_{IQ}$ (MPa√m) | Fracture toughness $K_{IQ,J}$ (MPa√m) | Fracture toughness $K_{IC}$ (MPa√m) | Testing method |
|---|---|---|---|---|
| WELs (grain size $d$ = 350 ± 260 nm) | 4.2 – 7.6 | 21 – 25 | - | Micro cantilever tests |
| Pearlitic steels [44] (200 nm interlamellar spacing) | - | - | 53 | Macro scale tests |
| Nanocrystalline pearlitic steels at different true strain ($\varepsilon$) [45] (in the drawing direction) | 7.5 ($\varepsilon$ = 3.2, $d \approx$ 18 nm) | 27 ($\varepsilon$ = 3.2, $d \approx$ 18 nm) | - | Micro cantilever tests |

| | | | | |
|---|---|---|---|---|
| | 5.2 ($\varepsilon$ = 4.2, $d \approx$ 15 nm) | - | - | Micro cantilever tests |
| | 4 ($\varepsilon$ = 5.2, $d \approx$ 10 nm) | - | - | Micro cantilever tests |
| Nanocrystalline heavily drawn pearlitic steels at different true strain (ε) values (perpendicular to drawing direction) [30] | - | 40 ($\varepsilon$ = 3.1, $d \approx$ 20 nm) | - | Single edge notched tension tests, CTOD |
| | - | 21 ($\varepsilon$ = 6.5, $d \approx$ 10 nm) | - | Single edge notched tension tests, CTOD |
| Nanocrystalline heavily drawn pearlitic steels at different true strain (ε) values (in the drawing direction) [30] | 5.0 ($\varepsilon$ = 3.1, $d \approx$ 20 nm) | - | - | Micro cantilever tests |
| | 3.7 ($\varepsilon$ = 6.5, $d \approx$ 10 nm | - | - | Micro cantilever tests |
| Pure BCC Fe ($d$ = 38 μm) [42] | - | - | 202 | Macro scale tests |
| Nanocrystalline sputtered Fe thin films ($d \approx$ 200 nm) [45] | 2 | - | - | Micro cantilever tests |

### *4.3.5 Microstructural features affecting the fracture behaviour of the WELs*

Crack growth is a complex process in polycrystalline materials as it involves dislocation motion, dislocation pile ups at obstacles, crack tip blunting, work hardening, atomistic bond breaking *etc.* [47]. Various microstructural features such as grain size, grain orientations,

phase fractions, grain/phase boundaries, dislocation density *etc.* affect the crack initiation and growth. The WELs consist of an intricate microstructure due to complex rail-wheel contact [19]. Fig. 4.5 shows the EBSD Inverse Pole Figure (IPF), phase and Kernel Average Misorientation (KAM) maps of microcantilever 4 before (Fig. 4.5(a)) and after (Fig. 4.5(b)) the *in-situ* fracture tests. KAM maps were generated by taking the 2$^{nd}$ nearest neighbouring pixels with a maximum misorientation of 5°. It should be noted that the EBSD on the fractured cantilever is performed after removing a 1-2 µm thick slice from its surface as it is not possible to obtain the Kikuchi patterns directly on a deformed cantilever. Hence, the measured area after fracture is not the same as before fracture. We observe mixed intragranular and intergranular crack growth in the WEL in Fig. 4.5(b). The phase map in Fig. 4.5(a) shows the presence of austenite (in green) within the WEL cantilever. The austenite area fraction is initially approximately 3% before the *in-situ* experiments. The EBSD measurements did not show austenite in the vicinity of the crack after the *in-situ* test (phase map in Fig. 4.5(b)). This observation is evidence for strain-induced austenite to martensite transformation during the crack growth.

The KAM map of the WEL in Fig. 4.5(a) shows martensitic areas with low KAM (0.39-0.49°) (indicated by black arrows). These areas can be envisaged to have undergone dynamic recovery in martensitic microstructure of the WELs due to temperature rise under the wheel-rail contacts [19]. Such low KAM areas are not observed after the fracture experiments. The KAM map in Fig. 4.5(b) shows no sign of a distinguishable plastic zone in the vicinity of the crack after fracture in the WEL cantilever. The KAM maps in Fig. 4.5 show that the average KAM increases from 0.82 ± 0.54° to 0.85 ± 0.56° before and after fracture (0.54° and 0.56° are the standard deviation values of the KAM distribution). These KAM values are used to calculate the Geometrically Necessary Dislocation (GND) density using

$$\rho_{gnd} = \frac{\alpha\theta}{ub} \tag{4.6}$$

where $\alpha$ is a constant ($\alpha$ = 3 for mixed dislocations [48]), $\theta$ is the average KAM angle, $u$ is the distance between misoriented points, which is the step size in EBSD map (*i.e.* 4 x $10^{-8}$ m), $b$ is the magnitude of the Burgers vector (*i.e.* 2.47 x $10^{-10}$ m ).

The GND density in cantilever 4 changes from 4.3x$10^{15}$ to 4.5x$10^{15}$ m$^{-2}$ after the *in-situ* fracture test which is not a pronounced change.

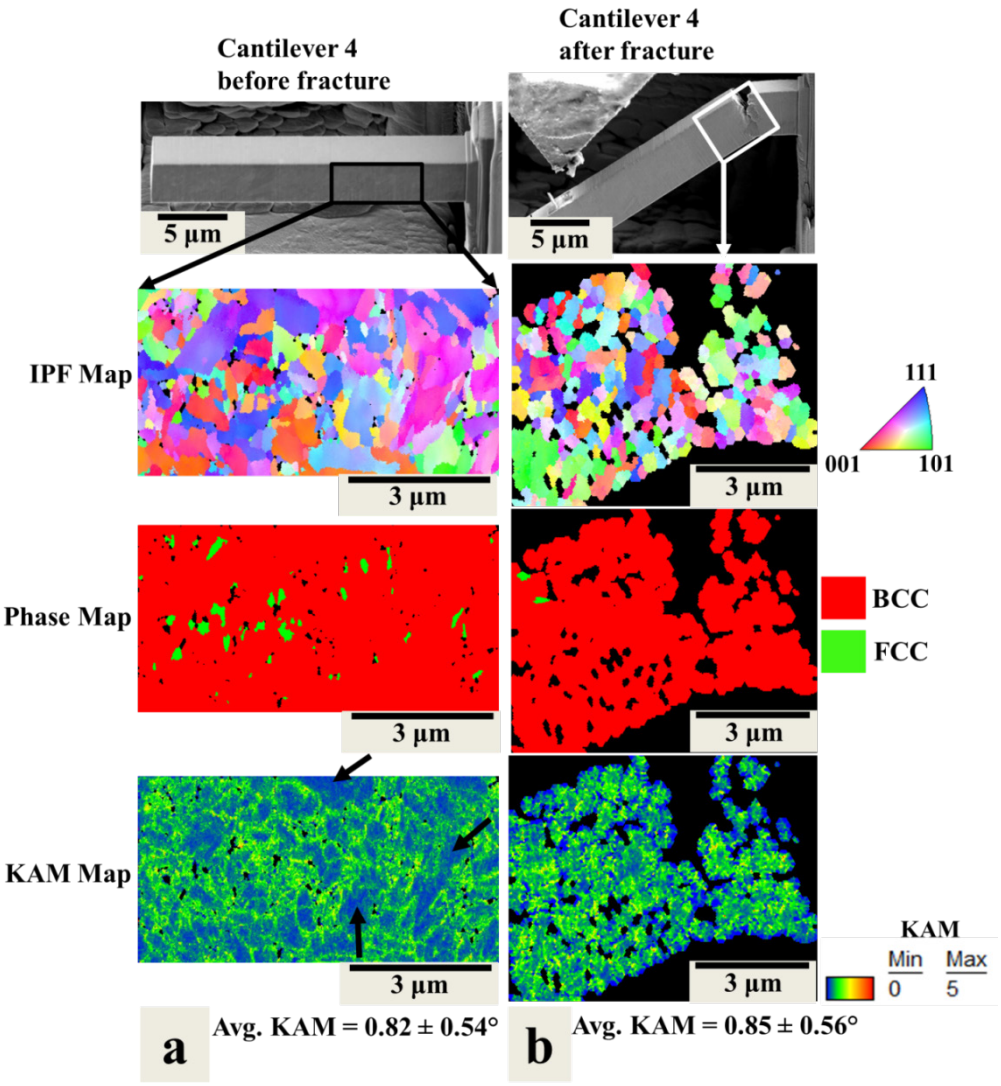


Fig. 4.5. EBSD results showing IPF, phase and KAM maps from the cantilever 4: (a) before (b) after the *in-situ* experiments. (Black colour arrows in the KAM map of WEL cantilever before fracture, show the martensitic grains with low KAM value (0.38-0.49°)).

Additional EBSD investigations were performed on cantilever 1 before and after fracture (Fig. 4.6). Alike cantilever 4, the observations show mixed intergranular and intra-granular fracture and strain-induced austenite to martensite transformation during the crack growth in cantilever 1 (as displayed in the IPF and phase map in Fig. 4.6(b)). We observe that the average KAM in cantilever 1 is 0.88°, with a standard deviation of ± 0.57°, before fracture (Fig. 4.6(a)), which corresponds to a GND density of 4.7 x $10^{15}$ $m^{-2}$. The KAM map in Fig.

4.6(a) displays low KAM areas (0.39-0.50°) (indicated by black arrows), which are not visible after the fracture experiments (Fig. 4.6(b)) as previously observed in cantilever 4 (Fig. 4.5).

Unlike cantilever 4, the KAM map from cantilever 1 (Fig. 4.6(b)) shows an area (enclosed in red lines) with a high average KAM of 0.96 ± 0.51° in the crack vicinity. This misorientation corresponds to an increased average GND density of 5.1 x $10^{15}$ $m^{-2}$ (Eq. 4.6). This high GND density area can be attributed to the plastic zone near the crack. The observed plastic zone shape is complex due to the complex WEL microstructure containing grains with different sizes and orientations. The average KAM outside the plastic zone is 0.91°, with a standard deviation of ± 0.52°, which corresponds to a GND density of 4.8 x $10^{15}$ $m^{-2}$.

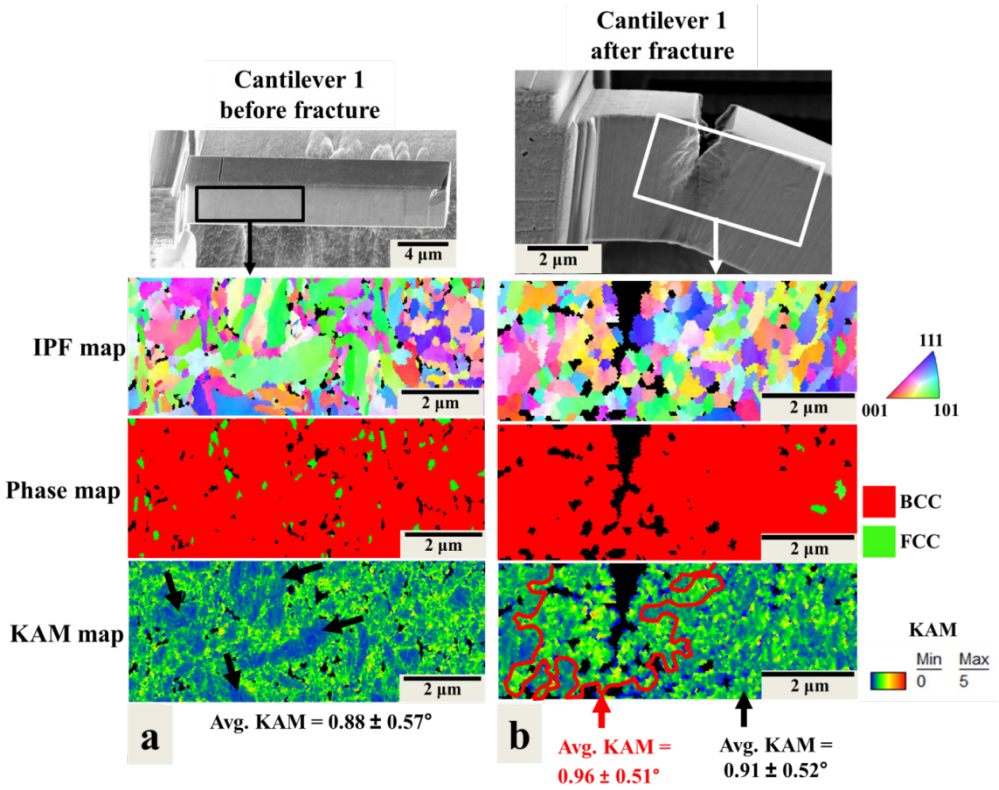


Fig. 4.6. EBSD results showing IPF, phase and KAM maps from the cantilever 1: (a) before and (b) after fracture. (Black colour arrows in the KAM map before the test show the martensitic grains with low KAM (0.39-0.50°)) (The high KAM area (enclosed in the red lines) on the KAM map in Fig. 4.6(b) represents the plastic zone associated with the crack).

The microstructural features, responsible for semi-brittle nature of the WELs and observed plastically in the WELs in *in-situ* tests, are further discussed below.

#### *4.3.5.1 Presence of austenite and its transformation into martensite during crack growth*

The presence of austenite phase in the microstructure of WELs (EBSD phase map in Fig. 4.5(a) and Fig. 4.6(a)) is one of the reasons for the observed plasticity in the *in-situ* fracture toughness experiments. This is because of the easy tendency of slip of the austenite phase due to its Face Centred Cubic (FCC) crystal structure in comparison with martensite with Body Centred Tetragonal (BCT) structure. We observe a reduction in austenite phase fraction after the *in-situ* fracture experiments (EBSD phase maps in Fig. 4.5 and Fig. 4.6). This reduction in austenite fraction is attributed to strain-induced transformation of austenite into martensite during the crack growth in the WELs. This transformation can result in crack closure during the crack growth in the WEL due to the crystal volume expansion concerning austenite (FCC) to martensite (BCC) transformation. In addition, this transformation relaxes the stress intensity ahead of the crack tip and causes the retardation in crack growth and hence contribute to increase the fracture toughness [49,50]. However, it is difficult to quantify the crack retardation due to this transformation.

#### *4.3.5.2 Grain size, dislocation density and dislocation annihilation in martensitic grains*

The fracture toughness is strongly affected by the grain size and the dislocation density [42,44,45,51]. Jaya *et al.* [45] showed the influence of the grain size and dislocation density on the fracture toughness for cold drawn pearlitic steels. They showed that the fracture toughness ($K_{IQ}$) decreases from 7.5 to 4 MPa$\sqrt{m}$ with the increase in drawing strain from 3.2 to 5.2. This is attributed to a decrease in average grain size from 18 to 10 nm, increase in dislocation density and increased carbon (C) supersaturation in the matrix (Table 4.2) [45]. Additionally, the fracture becomes more brittle with increase in drawing strain. It should be noted that it is difficult to delineate the effect of grain size, dislocation density and C supersaturation on the fracture response. We discuss the effect of grain size and dislocation density in this section whereas the C super saturation is discussed later in Sec. 4.3.5.3.

Zhang *et al.* [52] showed a dislocation density of around 1.4 x $10^{16}$ and 4.5 x $10^{16}$ $m^{-2}$ in cold drawn pearlitic wire at the drawing strain of 3.2 and 5.2, respectively. Similar order of dislocation density was quantified in the WEL using synchrotron X-ray diffraction in [9]. Thus, the contribution of dislocation density to fracture response of WELs and cold drawn pearlitic wire can be assumed to be similar and only grain size effects are discussed further.

In case of WELs, we observe a large variation in grain sizes (as shown in the IPF maps in Fig. 4.5 and Fig. 4.6). The average grain size in the WEL (350 nm, with a standard deviation of ± 260 nm) is higher than that for the drawn pearlitic wires (10-20 nm). The presence of larger grains in the WELs is one of the reasons for their elastic-plastic semi-brittle response, in comparison to the drawn wires (Table 4.2).

Li *et al.* [53] showed an increase in ductility for cold drawn pearlitic wires after low temperature tempering. They attributed this observation to the dislocation density reduction by dislocation annihilation and rearrangement. Similarly, the WELs also undergo dynamic recovery in the martensitic grains by dislocation annihilation due to temperature rises under wheel-rail contact [19]. Such martensitic grains with low KAM values (0.39-0.50°) are observed in the KAM maps in Fig. 4.5(a) and Fig. 4.6(a) (shown by arrows). The GND density in these low KAM areas ranges from 2.1 x $10^{15}$ $m^{-2}$ to 2.6 x $10^{15}$ $m^{-2}$ (Eq. 4.6). The dislocations in these areas will be more mobile during the crack growth due to the lower GND density than the high GND density areas in the WELs. Thus, these low KAM areas will contribute to the plasticity in the martensitic matrix of the WEL and are one of the reasons for elastic-plastic semi-brittle fracture response of the WELs.

#### *4.3.5.3 Segregation of carbon at grain boundaries and dislocations in the WELs*

Fig. 4.7 shows the correlative Transmission Electron Microscopy (TEM) and Atom Probe Tomography (APT) measurements on the WEL from a similar rail depth compared to the fracture experiments (10 μm below the rail surface). Another APT measurement from the similar depth is also presented in chapter 3 (Fig. 3.9(c)) which shows the similar observations like Fig. 4.7. Fig. 4.7(a) shows the bright field TEM image of an APT tip from the WEL with a selected area diffraction pattern from the encircled area. A grain boundary is observed in the TEM image. The selected area diffraction pattern in Fig. 4.7(a) shows the single phase present in the APT tip, which indicates that the cementite phase from initial pearlitic microstructure is completely dissolved in the martensitic matrix here. The APT measurement of this tip shows carbon (C) grain boundary segregation in Fig. 4.7(b). The C concentration at the grain boundary reaches around 13 ± 1 at.%, as shown by the proxigram analysis conducted with 7 at.% C iso-concentration surfaces around the grain boundary (Fig. 4.7(c)). However, the martensitic matrix shows a C concentration of around 3.2 at. %. A constant concentration of Mn (1.2 at.%) and Si (1.1 at.%) is found within the matrix and at the grain boundary (Fig. 4.7(c)).

The C concentration in the WEL matrix is compared with the APT measurements from heavily drawn pearlitic wires [53–55]. Li *et al.* [54] reported that the martensitic matrix in the drawn wires reach a C concentrations of 2 at.% at $\varepsilon = 5$ because of the presence of partially dissolved cementite. In the rails, the cementite from original pearlitic

microstructure is completely dissolved in the WELs at a depth of 10 μm (Fig. 4.7(a,c)). Thus, WELs contain around a 1.25 at.% higher C concentration in the martensitic matrix than the deformation-induced martensitic matrix in heavily cold drawn pearlitic wires. This is one of the reason that the maximum hardness in the WELs (910 ± 25 HV at 10 μm below rail surface in Fig. 4.1(b)) is higher than the hardness in the drawn wires (550 ± 20 HV at $\varepsilon$ = 5 [44]). It should be noted that the C atoms in the martensitic matrix of the WELs are not entirely in the interstitial sites but also segregate at vacancies and dislocations, which we discuss below.

The C segregation at grain boundaries (Fig. 4.7(b)) is attributed to the temperature rise during wheel-rail contact [19]. This C segregation increases the grain boundary cohesion [36,55–57] and affects the fracture of the Fe-based alloys [45]. Wu *et al.* [58] showed that the C segregation to the Fe grain boundaries reduces the free energy by 62 kJ/mol and thereby acts as strong cohesion enhancer. Hence, in the WELs, the observed grain boundary segregation of C strengthens the grain boundaries and minimizes the intergranular fracture. Consequently, due to redistribution of C to the grain boundaries, the C concentration will decrease in the martensitic matrix of the WELs. This C decrease in the matrix might increase the plasticity of the WELs with respect to supersaturated martensite.

The C atom probe map overlapped with the 7 at.% C iso-concentration surfaces (in green) in Fig. 4.7(c) shows the regions with high C concentrations (shown by arrows). These regions are attributed to C segregation at dislocations. Dislocations have a high interaction energy of around 0.8 eV/atom with the C atoms [59,60]. Hence, C atoms can redistribute to the dislocations in the martensitic matrix of the WELs due to temperature rise at the rail surface [19]. The crack growth in metals involves dislocation motion (*i.e.* slip) ahead of the crack tip. Thus, any obstacle in dislocation motion will affect the crack growth. The dislocations which are segregated with C require an extra force in order to be released for slip [60,61]. Hence, such dislocations can retard the crack growth when they are in the vicinity of the crack tip and increase the fracture toughness of the WELs.

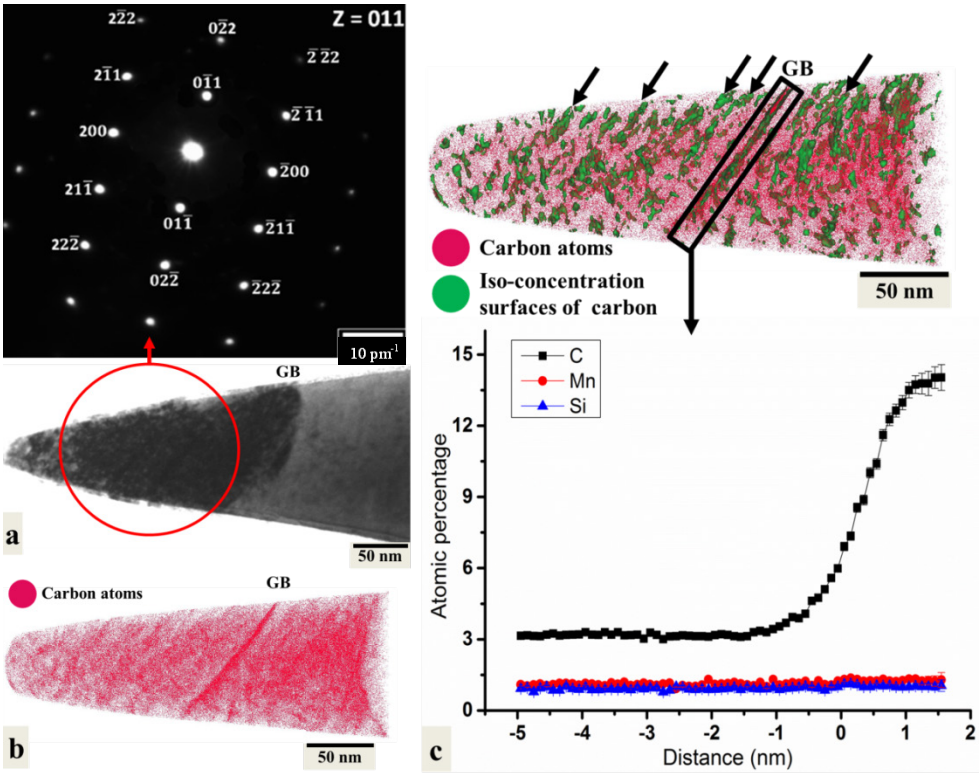


Fig. 4.7. Correlative TEM and APT measurements from the WEL at 10 µm below rail surface: (a) Bright field TEM image of APT tip showing a grain boundary and a selected area diffraction pattern from the encircled region, (b) APT measurement of the same tip showing C segregation at the Grain Boundary (GB), (c) C atom map overlapped with 7 at.% C iso-concentration surfaces (in green) showing regions of high C concentrations at dislocations. A proxigram analysis around the GB shows GB segregation.

## 4.4 Conclusions

The current study shows the first quantification of WEL fracture toughness and its correlation to the WEL microstructure. Results from the current study are of importance for the understanding of wheel-rail contact in the presence of the WELs. The results from WEL models can be used to estimate the critical WEL thickness for preventive maintenance to ensure safety and help minimizing grinding costs. Following conclusions are drawn based on the current investigation:

1. WELs show elastic-plastic and semi-brittle fracture during the micromechanical *in-situ* fracture experiments and the fracture toughness varies in the range of 21-25

MPa√m. WELs also show crack branching, crack blunting and micro-dimples at the fracture surface which validate the categorization as semi-brittle failure.

2. We observed a high GND density, ultrafine grain size and high C concentrations in the martensitic matrix of the WEL which leads to high hardness values in the WELs.
3. In contrast to the comparison with the cold drawn pearlitic wires, the plasticity and semi-brittle fracture in the WEL is attributed to its larger grain size, presence of retained austenite and strain-induced austenite to martensitic transformation during the crack growth.
4. Large martensite grains with low GND density are observed in the WEL which contribute to the increase in plasticity due to high dislocation mobility in these grains ahead the crack. This is also one of the reasons for the semi-brittle fracture of the WEL.
5. We observed the C segregation at the grain boundaries in the WELs which promotes the grain boundary cohension and softens the martensitic matrix by lowering the C concentration. Thus, this C redistribution is one of the reasons for semi-brittle fracture and high fracture toughness of the WELs.
6. The C segregation at the dislocations was observed in the WEL using APT which will affect the crack propagation and contribute to increase the fracture toughness as such dislocations in the vicinity of the crack require extra force to be released for slip.

## References


[1] Wikipedia contributors, List of countries by rail transport network size, (2017). https://en.wikipedia.org/wiki/List_of_countries_by_rail_transport_network_size.

[2] D. Nikas, K.A. Meyer, J. Ahlström, Characterization of deformed pearlitic rail steel, IOP Conf. Ser. Mater. Sci. Eng. 219 (2017) 12035. doi:10.1088/1757-899x/219/1/012035.

[3] J. Takahashi, K. Kawakami, M. Ueda, Atom probe tomography analysis of the white etching layer in a rail track surface, Acta Mater. 58 (2010) 3602–3612. doi:10.1016/J.ACTAMAT.2010.02.030.

[4] M. Steenbergen, R. Dollevoet, On the mechanism of squat formation on train rails – Part I: Origination, Int. J. Fatigue. 47 (2013) 361–372. doi:10.1016/J.IJFATIGUE.2012.04.023.

[5] J. Wu, R.H. Petrov, M. Naeimi, Z. Li, R. Dollevoet, J. Sietsma, Laboratory simulation of martensite formation of white etching layer in rail steel, Int. J. Fatigue.

91 (2016) 11–20. doi:10.1016/J.IJFATIGUE.2016.05.016.

[6] J. Wu, R.H. Petrov, S. Li, Z. Li, S. Godet, L. Malet, J. Sietsma, Characterization of structural change in rail surface using advanced automatic crystallographic orientation microscopy, in: COMPRAIL2016, WIT Press, 2016: pp. 367–376. doi:10.2495/CR160331.

[7] J. Wu, R.H. Petrov, S. Kölling, P. Koenraad, L. Malet, S. Godet, J. Sietsma, Micro and Nanoscale Characterization of Complex Multilayer-Structured White Etching Layer in Rails, Met. . 8 (2018). doi:10.3390/met8100749.

[8] F.C. Zhang, B. Lv, C.L. Zheng, Q. Zou, M. Zhang, M. Li, T.S. Wang, Microstructure of the worn surfaces of a bainitic steel railway crossing, Wear. 268 (2010) 1243–1249. doi:10.1016/J.WEAR.2010.01.016.

[9] W. Österle, H. Rooch, A. Pyzalla, L. Wang, Investigation of white etching layers on rails by optical microscopy, electron microscopy, X-ray and synchrotron X-ray diffraction, Mater. Sci. Eng. A. 303 (2001) 150–157. doi:10.1016/S0921-5093(00)01842-6.

[10] S.B. Newcomb, W.M. Stobbs, A transmission electron microscopy study of the white-etching layer on a rail head, Mater. Sci. Eng. 66 (1984) 195–204. doi:10.1016/0025-5416(84)90180-0.

[11] W. Lojkowski, M. Djahanbakhsh, G. Bürkle, S. Gierlotka, W. Zielinski, H.-J. Fecht, Nanostructure formation on the surface of railway tracks, Mater. Sci. Eng. A. 303 (2001) 197–208. doi:10.1016/S0921-5093(00)01947-X.

[12] M. Steenbergen, R. Dollevoet, On the mechanism of squat formation on train rails – Part II: Growth, Int. J. Fatigue. 47 (2013) 373–381. doi:10.1016/J.IJFATIGUE.2012.04.019.

[13] G. Baumann, H.J. Fecht, S. Liebelt, Formation of white-etching layers on rail treads, Wear. 191 (1996) 133–140. doi:10.1016/0043-1648(95)06733-7.

[14] A. Pyzalla, L. Wang, E. Wild, T. Wroblewski, Changes in microstructure, texture and residual stresses on the surface of a rail resulting from friction and wear, Wear. 251 (2001) 901–907. doi:10.1016/S0043-1648(01)00748-7.

[15] A.P. Patra, P. Söderholm, U. Kumar, Uncertainty estimation in railway track life-cycle cost: a case study from Swedish National Rail Administration, Proc. Inst. Mech. Eng. Part F J. Rail Rapid Transit. 223 (2008) 285–293. doi:10.1243/09544097JRRT235.

[16] P. Sroba, M. Roney, Rail grinding best practices, in: Proc. AREMA Annu. Conf.

Chicago, 2003.

[17] H.W. Zhang, S. Ohsaki, S. Mitao, M. Ohnuma, K. Hono, Microstructural investigation of white etching layer on pearlite steel rail, Mater. Sci. Eng. A. 421 (2006) 191–199. doi:10.1016/J.MSEA.2006.01.033.

[18] L. Wang, A. Pyzalla, W. Stadlbauer, E.. Werner, Microstructure features on rolling surfaces of railway rails subjected to heavy loading, Mater. Sci. Eng. A. 359 (2003) 31–43. doi:10.1016/S0921-5093(03)00327-7.

[19] A. Kumar, G. Agarwal, R. Petrov, S. Goto, J. Sietsma, M. Herbig, Microstructural evolution of white and brown etching layers in pearlitic rail steels, Acta Mater. (2019) Submitted for publication.

[20] A. Al-Juboori, H. Zhu, D. Wexler, H. Li, C. Lu, A. McCusker, J. McLeod, S. Pannila, J. Barnes, Evolution of rail surface degradation in the tunnel: The role of water on squat growth under service conditions, Eng. Fract. Mech. 209 (2019) 32–47. doi:10.1016/J.ENGFRACMECH.2019.01.018.

[21] B.N. Jaya, J.M. Wheeler, J. Wehrs, J.P. Best, R. Soler, J. Michler, C. Kirchlechner, G. Dehm, Microscale Fracture Behavior of Single Crystal Silicon Beams at Elevated Temperatures, Nano Lett. 16 (2016) 7597–7603. doi:10.1021/acs.nanolett.6b03461.

[22] D.E.J. Armstrong, M.E. Rogers, S.G. Roberts, Micromechanical testing of stress corrosion cracking of individual grain boundaries, Scr. Mater. 61 (2009) 741–743. doi:10.1016/J.SCRIPTAMAT.2009.06.017.

[23] D.E.J. Armstrong, A.J. Wilkinson, S.G. Roberts, Micro-mechanical measurements of fracture toughness of bismuth embrittled copper grain boundaries, Philos. Mag. Lett. 91 (2011) 394–400. doi:10.1080/09500839.2011.573813.

[24] H. Chan, S.G. Roberts, J. Gong, Micro-scale fracture experiments on zirconium hydrides and phase boundaries, J. Nucl. Mater. 475 (2016) 105–112. doi:10.1016/J.JNUCMAT.2016.03.026.

[25] A. Stratulat, D.E.J. Armstrong, S.G. Roberts, Micro-mechanical measurement of fracture behaviour of individual grain boundaries in Ni alloy 600 exposed to a pressurized water reactor environment, Corros. Sci. 104 (2016) 9–16. doi:10.1016/J.CORSCI.2015.10.019.

[26] Y. Zou, P. Okle, H. Yu, T. Sumigawa, T. Kitamura, S. Maiti, W. Steurer, R. Spolenak, Fracture properties of a refractory high-entropy alloy: In situ micro-cantilever and atom probe tomography studies, Scr. Mater. 128 (2017) 95–99. doi:10.1016/J.SCRIPTAMAT.2016.09.036.

[27] D. Di Maio, S.G. Roberts, Measuring fracture toughness of coatings using focused-ion-beam-machined microbeams, J. Mater. Res. 20 (2005) 299–302.

[28] K. Matoy, H. Schönherr, T. Detzel, T. Schöberl, R. Pippan, C. Motz, G. Dehm, A comparative micro-cantilever study of the mechanical behavior of silicon based passivation films, Thin Solid Films. 518 (2009) 247–256. doi:10.1016/J.TSF.2009.07.143.

[29] S. Massl, W. Thomma, J. Keckes, R. Pippan, Investigation of fracture properties of magnetron-sputtered TiN films by means of a FIB-based cantilever bending technique, Acta Mater. 57 (2009) 1768–1776. doi:10.1016/J.ACTAMAT.2008.12.018.

[30] A. Hohenwarter, B. Völker, M.W. Kapp, Y. Li, S. Goto, D. Raabe, R. Pippan, Ultra-strong and damage tolerant metallic bulk materials: A lesson from nanostructured pearlitic steel wires, Sci. Rep. 6 (2016) 33228. https://doi.org/10.1038/srep33228.

[31] V. Schnabel, B.N. Jaya, M. Köhler, D. Music, C. Kirchlechner, G. Dehm, D. Raabe, J.M. Schneider, Electronic hybridisation implications for the damage-tolerance of thin film metallic glasses, Sci. Rep. 6 (2016) 36556. https://doi.org/10.1038/srep36556.

[32] T.P. HALFORD, K. TAKASHIMA, Y. HIGO, P. BOWEN, Fracture tests of microsized TiAl specimens, Fatigue Fract. Eng. Mater. Struct. 28 (2005) 695–701. doi:10.1111/j.1460-2695.2005.00893.x.

[33] S. Wurster, C. Motz, R. Pippan, Characterization of the fracture toughness of micro-sized tungsten single crystal notched specimens, Philos. Mag. 92 (2012) 1803–1825. doi:10.1080/14786435.2012.658449.

[34] J. Ast, B. Merle, K. Durst, M. Göken, Fracture toughness evaluation of NiAl single crystals by microcantilevers—a new continuous J-integral method, J. Mater. Res. 31 (2016) 3786–3794.

[35] M. Herbig, P. Choi, D. Raabe, Combining structural and chemical information at the nanometer scale by correlative transmission electron microscopy and atom probe tomography, Ultramicroscopy. 153 (2015) 32–39. doi:10.1016/J.ULTRAMIC.2015.02.003.

[36] M. Herbig, D. Raabe, Y.J. Li, P. Choi, S. Zaefferer, S. Goto, Atomic-Scale Quantification of Grain Boundary Segregation in Nanocrystalline Material, Phys. Rev. Lett. 112 (2014) 126103. doi:10.1103/PhysRevLett.112.126103.

[37] M. Herbig, Spatially correlated electron microscopy and atom probe tomography:

Current possibilities and future perspectives, Scr. Mater. 148 (2018) 98–105. doi:10.1016/J.SCRIPTAMAT.2017.03.017.

[38] S.K. Makineni, M. Lenz, P. Kontis, Z. Li, A. Kumar, P.J. Felfer, S. Neumeier, M. Herbig, E. Spiecker, D. Raabe, B. Gault, Correlative Microscopy—Novel Methods and Their Applications to Explore 3D Chemistry and Structure of Nanoscale Lattice Defects: A Case Study in Superalloys, JOM. 70 (2018). doi:10.1007/s11837-018-2802-7.

[39] S.K. Makineni, A. Kumar, M. Lenz, P. Kontis, T. Meiners, C. Zenk, S. Zaefferer, G. Eggeler, S. Neumeier, E. Spiecker, D. Raabe, B. Gault, On the diffusive phase transformation mechanism assisted by extended dislocations during creep of a single crystal CoNi-based superalloy, Acta Mater. 155 (2018). doi:10.1016/j.actamat.2018.05.074.

[40] W. Lu, M. Herbig, C.H. Liebscher, L. Morsdorf, R.K.W. Marceau, G. Dehm, D. Raabe, Formation of eta carbide in ferrous martensite by room temperature aging, Acta Mater. 158 (2018) 297–312. doi:10.1016/J.ACTAMAT.2018.07.071.

[41] S. Suresh, Micromechanisms of fatigue crack growth retardation following overloads, Eng. Fract. Mech. 18 (1983) 577–593. doi:10.1016/0013-7944(83)90051-6.

[42] A. Hohenwarter, R. Pippan, Fracture and fracture toughness of nanopolycrystalline metals produced by severe plastic deformation, Philos. Trans. R. Soc. A Math. Phys. Eng. Sci. 373 (2015) 20140366. doi:10.1098/rsta.2014.0366.

[43] A. K. Saxena, A. Kumar, S. Brinckmann, M. Herbig, G. Dehm, C. Kirchlechner, Micro fracture investigations of white etching layers, Mater. Des. (2019) Submitted for publication.

[44] A. Hohenwarter, A. Taylor, R. Stock, R. Pippan, Effect of Large Shear Deformations on the Fracture Behavior of a Fully Pearlitic Steel, Metall. Mater. Trans. A. 42 (2011) 1609–1618. doi:10.1007/s11661-010-0541-7.

[45] B.N. Jaya, S. Goto, G. Richter, C. Kirchlechner, G. Dehm, Fracture behavior of nanostructured heavily cold drawn pearlitic steel wires before and after annealing, Mater. Sci. Eng. A. 707 (2017) 164–171. doi:10.1016/J.MSEA.2017.09.010.

[46] S. Djaziri, Y. Li, G.A. Nematollahi, B. Grabowski, S. Goto, C. Kirchlechner, A. Kostka, S. Doyle, J. Neugebauer, D. Raabe, Deformation-Induced Martensite: A New Paradigm for Exceptional Steels, Adv. Mater. 28 (2016) 7753–7757.

[47] R. Pippan, A. Hohenwarter, The importance of fracture toughness in ultrafine and

nanocrystalline bulk materials, Mater. Res. Lett. 4 (2016) 127–136.

[48] Q. Liu, D. Juul Jensen, N. Hansen, Effect of grain orientation on deformation structure in cold-rolled polycrystalline aluminium, Acta Mater. 46 (1998) 5819–5838. doi:10.1016/S1359-6454(98)00229-8.

[49] H. Li, M. Koyama, T. Sawaguchi, K. Tsuzaki, H. Noguchi, Importance of crack-propagation-induced ε-martensite in strain-controlled low-cycle fatigue of high-Mn austenitic steel, Philos. Mag. Lett. 95 (2015) 303–311. doi:10.1080/09500839.2015.1052029.

[50] A.G. Pineau, R.M. Pelloux, Influence of strain-induced martensitic transformations on fatigue crack growth rates in stainless steels, Metall. Trans. 5 (1974) 1103–1112. doi:10.1007/BF02644322.

[51] W.-L. Li, J.C.M. Li, The effect of grain size on fracture toughness, Philos. Mag. A. 59 (1989) 1245–1261. doi:10.1080/01418618908221173.

[52] X. Zhang, N. Hansen, A. Godfrey, X. Huang, Dislocation-based plasticity and strengthening mechanisms in sub-20 nm lamellar structures in pearlitic steel wire, Acta Mater. 114 (2016) 176–183. doi:10.1016/J.ACTAMAT.2016.04.040.

[53] Y.J. Li, P. Choi, S. Goto, C. Borchers, D. Raabe, R. Kirchheim, Evolution of strength and microstructure during annealing of heavily cold-drawn 6.3 GPa hypereutectoid pearlitic steel wire, Acta Mater. 60 (2012) 4005–4016. doi:10.1016/J.ACTAMAT.2012.03.006.

[54] Y.J. Li, P. Choi, C. Borchers, S. Westerkamp, S. Goto, D. Raabe, R. Kirchheim, Atomic-scale mechanisms of deformation-induced cementite decomposition in pearlite, Acta Mater. 59 (2011) 3965–3977. doi:10.1016/J.ACTAMAT.2011.03.022.

[55] Y. Li, D. Raabe, M. Herbig, P.-P. Choi, S. Goto, A. Kostka, H. Yarita, C. Borchers, R. Kirchheim, Segregation Stabilizes Nanocrystalline Bulk Steel with Near Theoretical Strength, Phys. Rev. Lett. 113 (2014) 106104. doi:10.1103/PhysRevLett.113.106104.

[56] R.P. Messmer, C.L. Briant, The role of chemical bonding in grain boundary embrittlement, Acta Metall. 30 (1982) 457–467.

[57] D. Raabe, M. Herbig, S. Sandlöbes, Y. Li, D. Tytko, M. Kuzmina, D. Ponge, P.-P. Choi, Grain boundary segregation engineering in metallic alloys: A pathway to the design of interfaces, Curr. Opin. Solid State Mater. Sci. 18 (2014) 253–261. doi:10.1016/J.COSSMS.2014.06.002.

[58] R. Wu, A.J. Freeman, G.B. Olson, Effects of carbon on Fe-grain-boundary cohesion:

First-principles determination, Phys. Rev. B. 53 (1996) 7504.

[59] J. Takahashi, M. Kosaka, K. Kawakami, T. Tarui, Change in carbon state by low-temperature aging in heavily drawn pearlitic steel wires, Acta Mater. 60 (2012) 387–395. doi:10.1016/J.ACTAMAT.2011.09.014.

[60] A.H. Cottrell, B.A. Bilby, Dislocation theory of yielding and strain ageing of iron, Proc. Phys. Soc. Sect. A. 62 (1949) 49.

[61] M. Calcagnotto, Y. Adachi, D. Ponge, D. Raabe, Deformation and fracture mechanisms in fine- and ultrafine-grained ferrite/martensite dual-phase steels and the effect of aging, Acta Mater. 59 (2011) 658–670. doi:10.1016/J.ACTAMAT.2010.10.002.

# 5

# Microstructural evolution and damage in the cast austenitic Hadfield steel[††]


## Abstract

In this chapter, we discuss the microstructural evolution and damage in a field-loaded railway crossing made of cast austenitic Hadfield steel and subjected to impact fatigue. A nanoscale twinning substructure surrounded by dislocation cells and a high dislocation density are identified using Electron Channeling Contrast Imaging (ECCI) and Transmission Electron Microscopy (TEM) in the deformed microstructure of Hadfield steels. The effect of these substructures as well as of the non-metallic inclusions and other casting defects on the damage development in the austenitic Hadfield steels was also discussed. Additionally, the strain-induced transformation of the austenite into martensite in the deformed crossing surface is studied by X-ray diffraction and magnetometer measurements. The results do not show evidence of strain-induced austenite-to-martensite transformation under impact fatigue loading of the railway crossings. ECCI in controlled diffraction conditions was used to study the fatigue crack growth in undeformed cast Hadfield steel specimens when subjected to laboratory scale fatigue testing. Furthermore, the role of twins and grain boundaries on the fatigue crack growth is discussed.


## 5.1 Introduction

Cast Hadfield steels are widely used in railway crossings as they exhibit high toughness, high ductility, excellent wear resistance and high work hardening ability [1–5]. Typical for the Hadfield steels is that they demonstrate their exclusive wear resistance only if the wear is combined with compressive stresses. Such combination of properties makes them irreplaceable material for production of switches and crossings, rock crushers, crawler

[††] This chapter is based on a book chapter: A. Kumar, R. Petrov and J. Sietsma, Damage and microstructure evolution in cast Hadfield steels used in railway crossings, Springer book (Submitted for publication).

treads of tractors and balls for mills etc. These steels typically have high carbon content (above 1 wt.% C) and high Mn content of around 13-14 wt.%. After quenching they attain a fully austenitic microstructure (Face Centered Cubic crystal structure) and sometimes combined with undissolved carbides. Under external load, Hadfield steels show planar slip and Twinning Induced Plasticity (TWIP) as primary mechanisms of deformation. These mechanisms strongly depend on the Stacking Fault Energy (SFE) of the alloy. The cast Hadfield steels have a low SFE (*i.e.* 23 $mJ/m^2$) [1,4]. This is why the Hadfield steels strain harden rapidly due to the difficulty in cross slip and show high strain hardening capability.

Railway crossings are subjected to impact fatigue, wear and rolling contact fatigue (RCF) during service. This leads to the formation of various surface and subsurface defects such as spalling, flaking, squats and microcracks, especially in the crossing nose. These defects can lead to fracture of the entire crossing nose during further wheel-rail contacts, and hence may pose severe safety threats to the passengers if they were not detected and repaired. Therefore, it is important to study the microstructural evolution and damage in rail crossings which can provide strategies for the sustainable material design and/or suitable maintenance of the railway crossings.

The formation of damage in the polycrystalline alloys strongly depends on their microstructural features such as phases, phase and grain boundaries, twin boundaries, grain orientations and grain size *etc*. [6–15]. Various studies [2,4,5,16–20] have been conducted to study the damage in the Hadfield steel rail crossings. However, they show different opinions regarding the damage mechanism in relation with the microstructure of the Hadfield steels. Xiao *et al.* [16] claim that the damage in Hadfield steels in crossing applications has no correlation with their microstructure and the cracks initiate and propagate due to the combined effect of maximum contact stresses at the crossing surface and the maximum residual stresses below the surface. Similarly, Lv *et al.* [4] claim that the grain boundaries, plastic deformation bands, twinning and crystal orientation of austenitic grains in the cast Hadfield steels have no correlation with the nucleation and growth of fatigue cracks. They rather propose that the high concentration of vacancy clusters distributed as layers below the crossing surface is responsible for the damage. Yong *et al.* [19] also suggest that the formation of micro-voids and their coalescence in the region of high stresses in the crossings are responsible for damage in Hadfield steel and the damage has no correlation with the crystal orientations. However, Harzallah *et al.* [5] show that fine twinning substructures formed under impact fatigue loading in the Hadfield steel crossings are responsible for the crack initiation. Hence, there is no unambiguous understanding of damage in Hadfield steels in crossings applications, in relation with their microstructure.

In this study, the microstructural evolution and microstructural features (deformation twinning, casting defects, non-metallic inclusions and possible martensite phase formed from austenite upon loading) which can be responsible for damage in the Hadfield steel in

a field-loaded crossing are discussed. Additionally, the effect of the microstructural features on the damage in Hadfield steels is studied in laboratory scale fatigue testing.

## 5.2 Material and experimental methods

The cast Hadfield steel used in this study has a chemical composition of Fe-1.1C-13Mn-0.4Si (in wt.%). The steel was first cast in the shape of a rail crossing. Afterwards, the crossing was solution annealed at 1050 °C for 3 hours and subsequently quenched to form a fully austenitic microstructure. The crossing was installed in the Dutch rail network and removed after an approximate load passage of 400 Mt in service. The region of the impact fatigue loading from this rail crossing was cut using a diamond saw (Fig. 5.1). A specimen was subsequently extracted from this region using wire cutting (shown by black arrow in Fig. 5.1(b)) and the microstructure was investigated on the XY plane (shown in blue in Fig. 5.1(b)), which is perpendicular to the train running direction. Furthermore, the features such as casting defects and non-metallic inclusions are also investigated which can affect the damage in a cast Hadfield steel crossings.

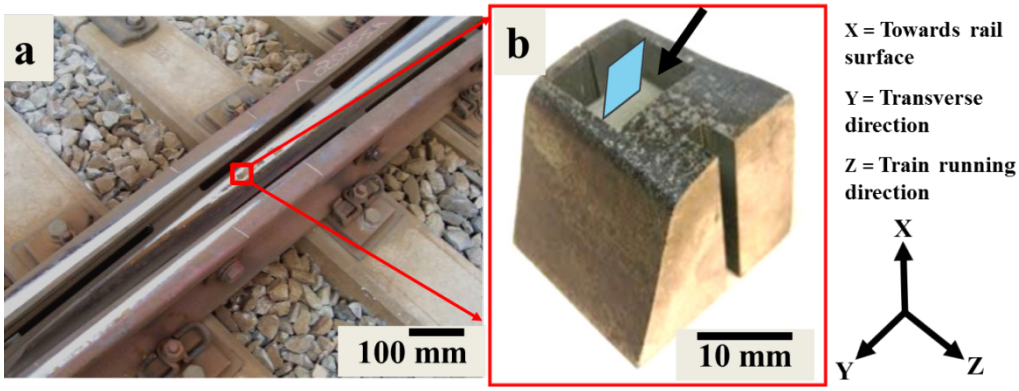


Fig. 5.1. (a) Photograph of a field loaded railway crossing, (b) Region of the crossing nose after cutting from the impact fatigue loading zone (black arrow shows the specimen cut from this region and rectangle shows the cross-sectional/XY plane where microstructural observations were carried out).

Various characterization methods such as Optical Microscopy (OM), Scanning Electron Microscopy (SEM), and Electron Channeling Contrast Imaging (ECCI) were used to study the microstructural evolution of Hadfield steel after the impact fatigue. The specimens for OM and SEM were prepared by a routine metallographic preparation sequence with final polishing using 1 µm diamond paste and etching with 2 vol.% Nital solution. An Olympus BX60M$^{TM}$ light optical microscope was used for the OM. The Vickers microhardness measurements were performed on a Dura-scan 70 (Struers) hardness tester, using a load of

1 N for 10 s. A JEOL JSM 6500F SEM with a field emission gun was used for Secondary Electron (SE) imaging and Energy Dispersive X-ray Spectroscopy (EDS) analysis. For ECCI investigation, the specimen was polished using an OPS colloidal silica solution containing 40 nm size particles after polishing with 1 μm diamond paste. A Zeiss Cross-beam SEM with a Gemini-type field emission gun was used for ECCI investigations, using an accelerating voltage of 30 kV, a probe current of 2 nA and a working distance of 7 mm. The specimens for Transmission Electron Microscopy (TEM) were prepared using a Focused Ion Beam (FIB) milling in a FEI Helios Nanolab 600i dual beam FIB/SEM. The TEM analysis was performed in a Jeol JEM-2200FS FEG-TEM microscope operated at 200 kV.

Specimens with a dimension of 10x10x1 $mm^3$ were taken from the crossing surface and measured for the phase analysis using X-Ray Diffraction (XRD) in a Bruker D8-advance diffractometer operating at 45 kV and 40 mA, using Cu Kα radiation ($\lambda$ = 0.15406 nm) and a scan rate of $0.002^{\circ}$ 2θ $s^{-1}$. Cubic specimens with 2x2x2 $mm^3$ dimensions were also cut from region shown by black arrow in Fig. 5.1(b) and measured in a Lake Shore 7307 Vibrating Sample Magnetometer (VSM) at room temperature for determination of the martensite fraction. Before the magnetic measurements, the magnetometer was calibrated using a standard nickel specimen (NIST). The martensite fraction ($f(\alpha')$) in the specimen is calculated as proposed in [21] using

$$f(\alpha') = \frac{M_S}{x_{Fe}\, M_{S,Fe}} \tag{5.1}$$

where, $M_s$ is the specimen saturation magnetization which was calculated from the measured magnetization of the specimen minus the contribution from paramagnetic austenite. $M_{s,Fe}$ is the saturation magnetization of pure iron (*i.e.* 215 $Am^2/kg$ [22]) and $x_{Fe}$ represents the atomic fraction of iron in the material.

Furthermore, the fatigue crack growth experiments were performed on notched rectangular specimens (Fig. 5.2) from an undeformed cast Hadfield steel. The tests were performed on a fatigue testing machine (Instron 8800 Electro plus), having a 10 kN load cell. A stress ratio of 0.1 (maximum load of 1400 N and minimum of 140 N) was used in load controlled tensile-tensile fatigue testing. Afterwards, the cracked specimens were investigated to study the crack growth in relation with microstructural features such as the pre-existing grain boundaries and the twin boundaries (evolving during the crack growth due to plasticity ahead the crack). A controlled ECCI (c-ECCI) in combination with EBSD is used for this investigation [23–27]. The specimens were first mapped using EBSD in a Zeiss Cross-beam SEM. The orientation data from EBSD is used to simulate the Kikuchi diffraction pattern with respect to the electron beam direction using TOCA software [23]. The software enables the calculation of specimen tilt and rotation values, required to achieve a two-beam diffraction/electron channeling condition for a well-defined lattice plane. This allows the

imaging of crystal defects such as stacking faults, dislocations and twinning in the microstructure.

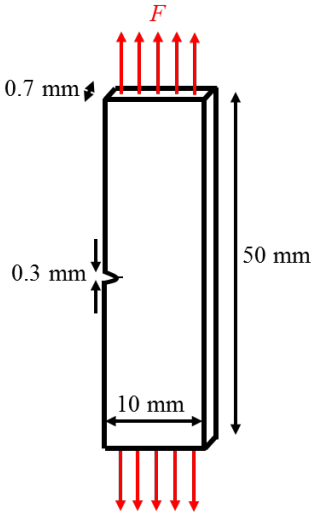


Fig. 5.2. Schematic drawing of a notched specimen for fatigue crack growth experiments (cut from an undeformed cast Hadfield steel)

## 5.3 Results and Discussion

### *5.3.1 Evolution of deformation twinning under impact fatigue*

Railway crossings are subjected to high impact fatigue, wear and RCF which leads to the changes in the steel microstructure used in them, due to the plastic deformation. Fig. 5.3 shows the microhardness distribution and microstructural evolution in a field-loaded cast Hadfield steel crossing. A maximum microhardness of 760±18 HV is reported close to the surface of this crossing and the hardness gradually decreases along the depth and reaches a minimum value of 330±5 HV. The high hardness close to the crossing surface is attributed to the high density of deformation twins evolved due to the plastic deformation during the wheel-crossing contacts (Fig. 5.3(b)). We observe that multiple twinning systems have been activated in the grains during the plastic deformation under wheel-crossing contact (Fig. 5.3(b-d)). The density of twins reduces along the depth of the crossing (Fig. 5.3(b-d)). Fig. 5.3(e) shows no indication of deformation twinning at the depth of 3.7 mm below the crossing surface. This indicates that the critical stress for deformation twinning is reached only up to a depth of approximately 3.7 mm in this crossing.

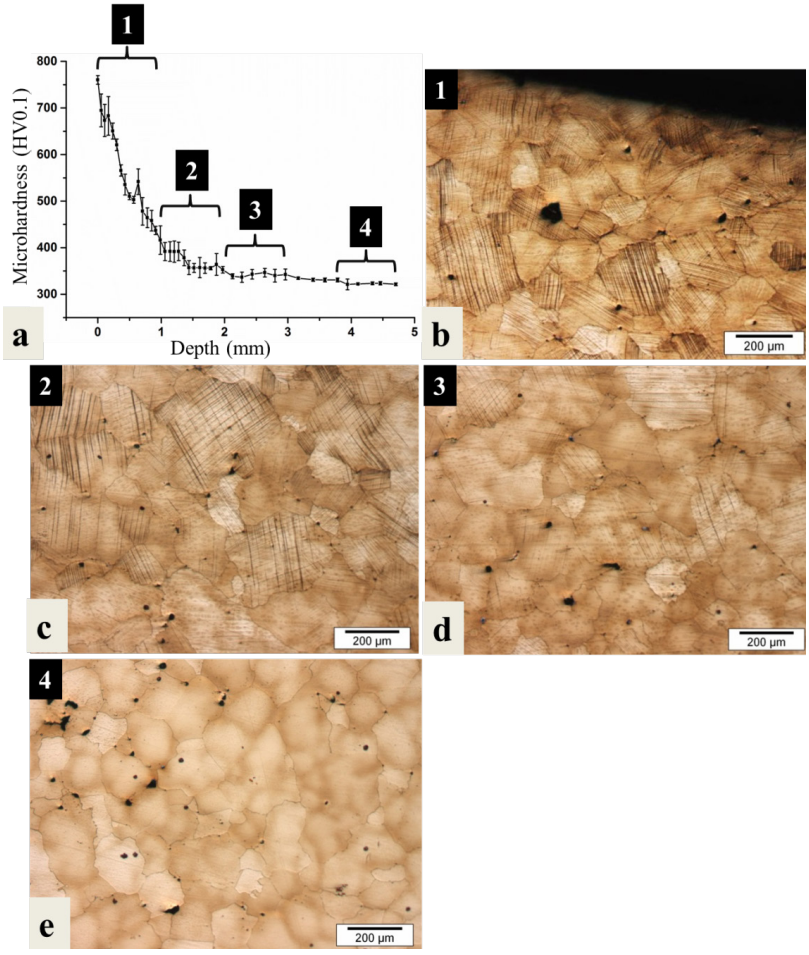


Fig. 5.3. Microhardness distribution from the surface of an infield loaded cast Hadfield steel crossing into the depth, (b-e) Optical micrographs showing the microstructural evolution in this crossing from the surface into the depth, (b) Region 1 close to the crossing surface showing high density of deformation twins, (c) Region 2 (≈ 1-2 mm below the crossing surface) showing lower density of deformation twinning than region 1, (d) Region 3 (≈ 2-3 mm below the crossing surface) showing lower density of deformation twinning than region 1 and 2, (e) Region 4 (≈ 3.7-4.7 mm below the crossing surface) showing no deformation twinning.

The deformation twinning is further characterized using ECCI and TEM on the surface of the field-loaded cast Hadfield steel crossing (Fig. 5.4). This enables to study the microstructural evolution and deformation mechanism of the cast Hadfield steel under the impact fatigue loading conditions. Fig. 5.4(a) depicts the ECCI micrograph showing the nano-sized twins and equiaxed dislocation cells (encircled) in the vicinity of these twins. The size of these dislocation cells varies from 100 to 200 nm (Fig. 5.4(a)). The formation of

these cells is commonly observed in low, medium and high stacking fault alloys [24,28,29]. It is also observed that multiple twin systems are present within a single grain (Fig. 5.4(a)). Fig. 5.4(b) is a magnified ECCI micrograph from Fig. 5.4(a) showing the twin size of the order of 10 nm. Fig. 5.4(c) shows the TEM image of the deformed microstructure of Hadfield steel under the impact fatigue loading with the corresponding Selected Area Electron Diffraction (SAED) Pattern. It is observed that five twinned zones are present within a width of 20 nm, which indicates a twin size of less than 5 nm in the deformed Hadfield steel microstructure (Fig. 5.4(c)). Such fine twins in the microstructure can lead to high strain hardening in the Hadfield steels [30,31]. Fig. 5.4(d) shows a TEM image of the deformed Hadfield steel indicating the accumulation of a high density of dislocations in the vicinity of the twins. Twin boundaries act as barriers to the dislocation motion, leading to high strength and strain hardening in Hadfield steels.

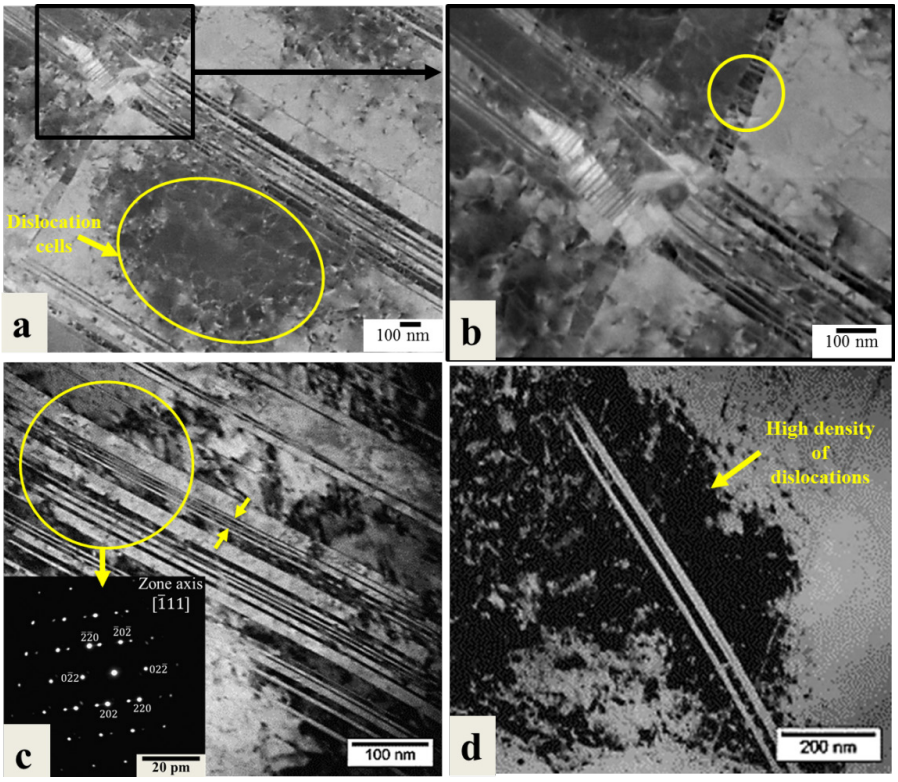


Fig. 5.4. (a) ECCI image showing the formation of dislocation cells (encircled) in the vicinity of twins, on the surface of an infield loaded Hadfield steel crossing, (b) Magnified ECCI micrograph from the region in (a), showing the twin size of the order of 10 nm, (c) TEM image with corresponding Selected Area Electron Diffraction (SAED) pattern, showing the nanosized deformation twinning (arrows show the presence of 5 twins in a width of approximately 20 nm), (d) TEM image showing the high density of dislocations (in black contrast) accumulated at the twin boundaries.

### *5.3.2 Solidification porosity and non-metallic inclusions and their role in damage*

The Hadfield steel used in railway crossing application is produced by conventional casting as explained in Sec. 5.2. The casting process leads to solidification defects such as gas porosity and solidification shrinkage porosities. The gas porosities generally form due to the entrapment of atmospheric gases such as oxygen and nitrogen in the casting mold and in the liquid metal especially due to turbulence in the liquid flow during casting. However, the solidification shrinkage porosities are formed due to volume changes caused by solidification and thermal contraction [32]. A poor riser design also can lead to formation of shrinkage porosities during casting when it provides insufficient liquid feeding (misrun). The casting defects in the cast Hadfield steel crossing can be in the range of few micrometers to few mm in size. These defects are considered to be detrimental for the fatigue life of the Hadfield steels depending on their size, shape, position, and stress concentration during loading and can be responsible for the crack initiation in crossings [33]. Fig. 5.5(a) shows a gas porosity size of around 220 μm and the solidification shrinkages at the grain boundaries. Fig. 5.5(b) depicts a magnified optical micrograph of cast Hadfield steel showing that the solidification shrinkages are mainly found at the grain boundaries. This can reduce the damage tolerance of the Hadfield steels due to intergranular crack propagation under the impact fatigue. Peter *et al.* [34] reported such intergranular cracking in the cast Hadfield steels crossings due to the presence of shrinkage porosities at the grain boundaries. Fig. 5.5(c) represents a SEM image showing intergranular microcracking from the solidification shrinkage porosity at 1 mm below the crossing surface**.** Fig. 5.5(d) shows a 3D optical micrograph from the cross-section of a failed Hadfield steel crossing (color coded scale shows the height distribution with respect to the deepest point). The crack is observed to follow the casting porosities which are represented by deeper areas in blue in Fig. 5.5(d). Crack branching is also observed at the casting porosities (Fig. 5.5(d)).

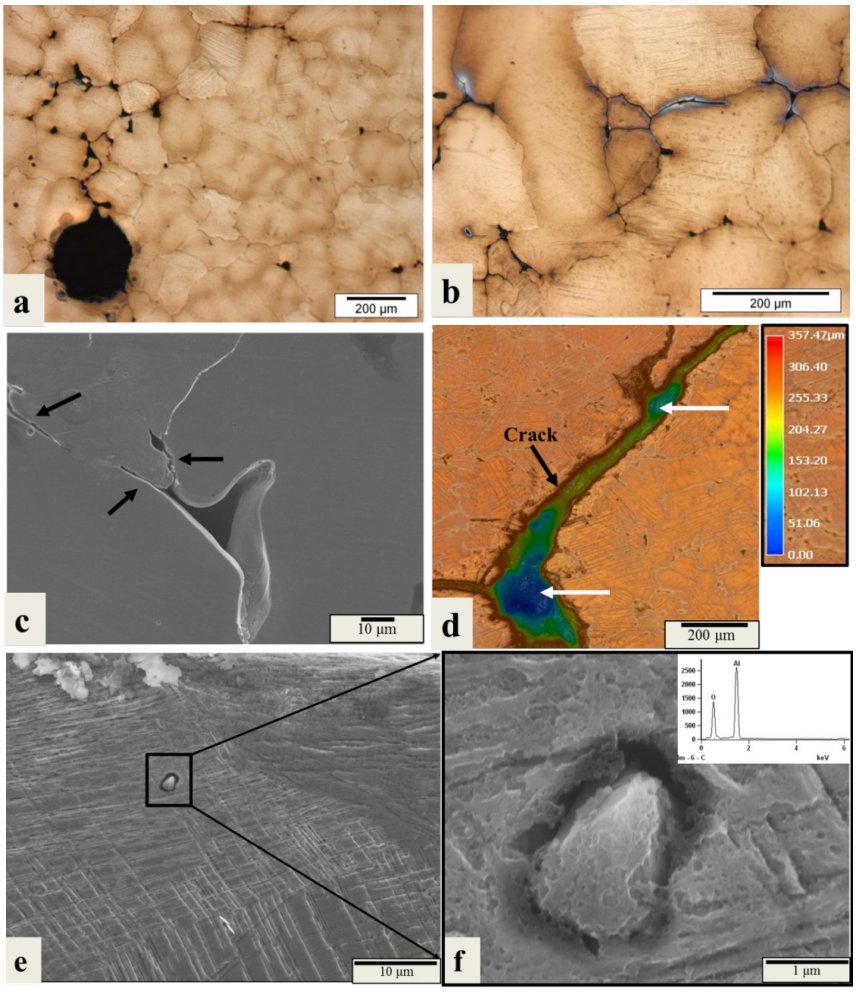


Fig. 5.5. (a) Optical micrograph showing gas porosities and solidification shrinkages in the cast Hadfield steel; (b) Magnified optical micrograph showing solidification shrinkages at the grain boundaries, (c) SEM image showing the intergranular microcracking from a solidification shrinkage at 1 mm below the crossing surface (black arrows show the microcracks), (d) 3D optical micrograph of a failed Hadfield steel crossings showing a crack following the casting porosities and the crack branching at the porosities (color coded scale shows the height distribution with respect to the deepest point), (e) SEM image showing the presence of aluminium oxide inclusion at 20 µm below crossing surface, (f) Magnified SEM image of the aluminium oxide inclusion (with EDS result) showing interface decohension.

Fig. 5.5(e) shows the presence of an aluminum oxide inclusion at 20 µm below the surface of the field- loaded Hadfield steel crossing. Such inclusions can affect the fatigue life of the crossings due to the fact that they can act as stress raisers in the steel microstructure during the wheel-rail contact. Studies show that the presence of such inclusions promotes

decohesion at the inclusion/matrix interface due high strain localization and can lead to void nucleation in the material [35]. Such interface decohesion between an aluminum oxide inclusion and the deformed Hadfield steel matrix is observed in the magnified SEM image in Fig. 5.5(f).

### *5.3.3 Strain-induced austenite to martensite transformation under the impact fatigue and its effect on the damage in Hadfield steel*

Some early studies show that one of the strain hardening mechanisms in the Hadfield steels is the strain-induced martensitic transformation from the metastable austenite [36,37]. This transformation occurs by a mechanism involving the dislocation motion on an invariant set of planes, which leads to the change in the crystal structure of parent austenite phase into ε or α' martensite due to the change in the stacking sequence of atomic planes [38]. However, Adler *et al.* [1] proposed that such transformation cannot occur in Hadfield steel (with a composition of 13 wt.% Mn and 1.1 wt.% C) due to its stacking fault energy being higher than 20 $mJ/m^2$. It is well known that during casting a heterogeneous distribution of some alloying elements (Mn, Cr, Mo, Ni *etc.*) is often observed in the as cast structure of steels [39]. The cast Hadfield steel studied in this work shows Mn segregation up to 18 wt.% in the vicinity of the grain boundary, whereas the Mn concentration varies in between 10 to 13 wt. % in the grain interiors (Fig. 5.6). This means that the time and temperature during the solutionizing (*i.e.* 3 hours at 1050 ˚C) of Hadfield steels after casting, are not sufficient for the homogenization of manganese. The Mn atoms can only diffuse up to a distance of approximately 3.5 μm during such solutionizing treatment. The Mn diffusion distance calculations were performed according to the procedure mentioned in [40]. Therefore, the variation in Mn content still exists in the studied cast Hadfield microstructure. This variation in the Mn content affects the stacking fault energy of the alloy locally. A locally high Mn content leads to a high stacking fault energy and minimizes the possibility of strain-induced martensite transformation [41,42]. However, regions with low Mn content (10-11 wt. %) can be potential sites for such transformations due to the low stacking fault energy in these regions [41].

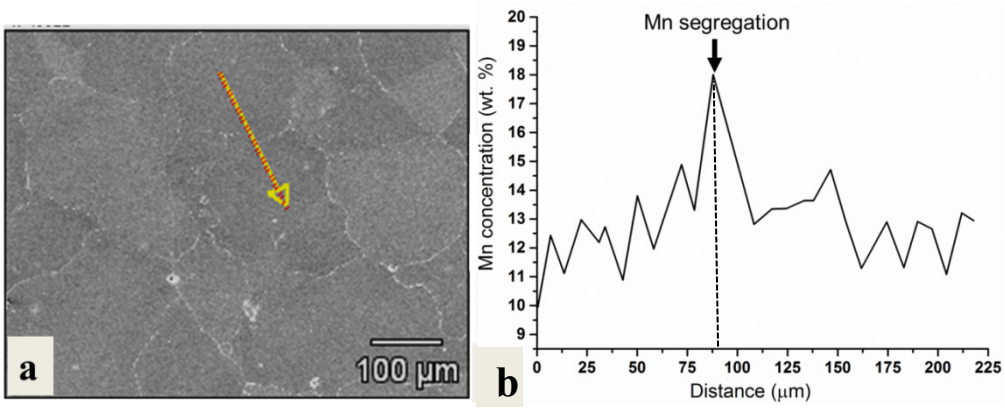


Fig. 5.6. SEM image of the cast Hadfield steel showing a line (in yellow) across a grain boundary (in white contrast) along which EDS analysis was performed; (b) EDS analysis showing the Mn segregation in the vicinity of the grain boundary (Dotted line show the position of the grain boundary).

Jost *et al.* [43] studied the strain-induced austenite to martensite transformation in Hadfield steels under dry sliding wear conditions. They showed that such transformation on the surface of the Hadfield steel can lead to crack initiation due to the brittle nature of the martensite. Adler *et al.* [1] later proposed that this transformation was primarily due to the decarburization at the Hadfield steel surface which leads to a decrease in the mechanical stability of austenite. Furthermore, some studies propose that such transformation in low stacking fault alloys leads to void nucleation at the interface of the martensite and austenite and negatively affects the fatigue life [22,44,45]. Therefore, it is important to study the strain-induced austenite to martensite transformation in the field-loaded cast Hadfield steel crossing in order to know if such critical regions containing martensite exist in the microstructure.

Fig. 5.7(a) shows the results of the XRD measurements from the surface of the field-loaded Hadfield steel crossing and 2 mm below the surface. Only the presence of austenite peaks is observed in these measurements, which indicates that no transformation to martensite has taken place under the impact fatigue loading in the Hadfield steels. Furthermore, this transformation is also investigated using magnetometer measurements at the crossing surface, a representative result of which is shown in Fig. 5.7(b). The result shows a specimen saturation magnetisation of 0.16 $Am^2/kg$, which is equivalent to a very low martensitic phase of around 0.09%. In addition to this, the martensitic phase is also not observed in the TEM analysis of multiple specimens taken from the crossing surface Fig. 5.4(c,d). Therefore, it can be concluded that no strain-induced austenite to martensite transformation took place in this Hadfield steel under the impact fatigue conditions. Das *et al.* [46] proposed that the probability of strain-induced martensite transformation decreases with an increase in strain rate in the low stacking fault alloys. Therefore, the high strain

rates in the case of railway crossings can be responsible for the absence of strain-induced martensite transformation in the Hadfield steels crossings.

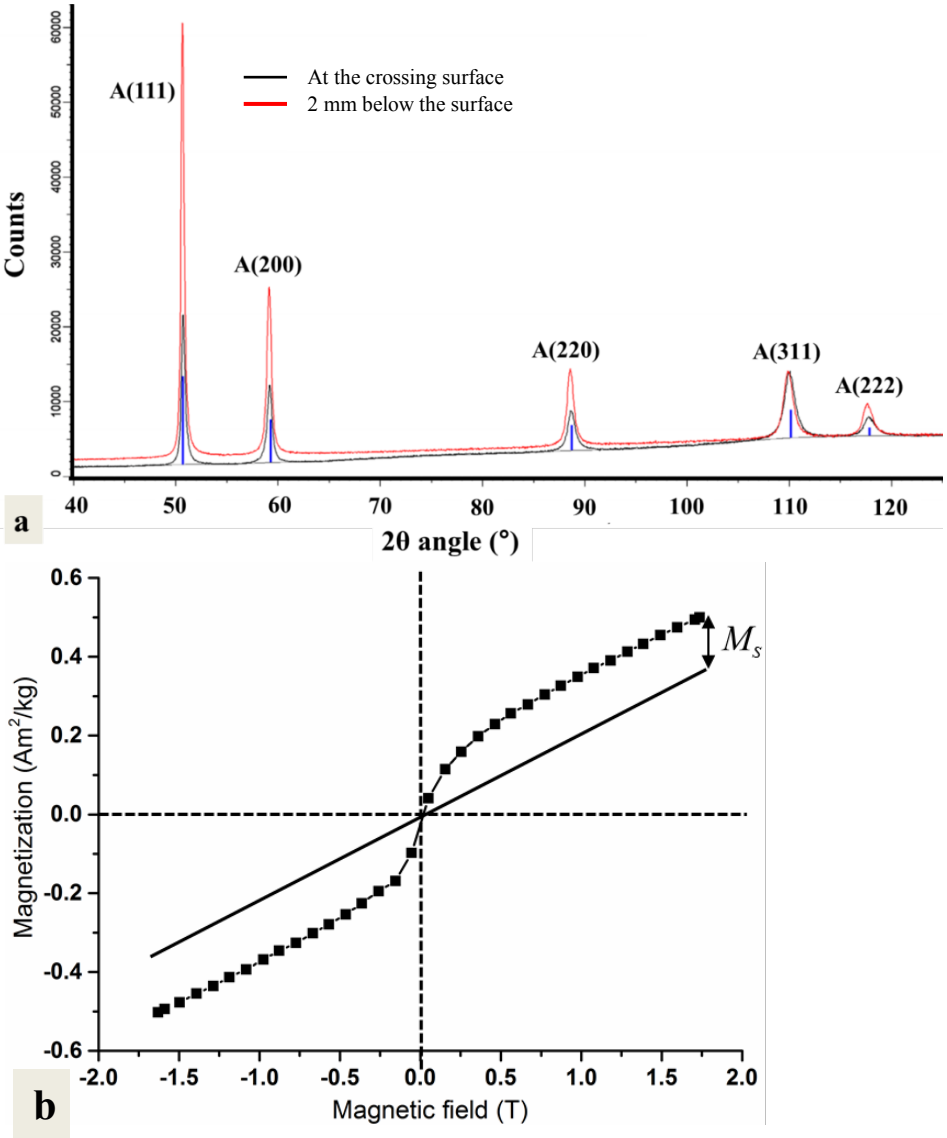


Fig. 5.7. X-Ray Diffraction (XRD) measurements from the surface (in black) and 2 mm below the surface (in red) of the infield loaded Hadfield steel crossing showing only the peaks of the austenite phase, (b) Results of magnetometer measurements from the surface of the infield loaded Hadfield steel crossing (Inclined solid straight line shows the contribution from the paramagnetic austenite (0.36 $Am^2/kg$ at 1.75 T)).

### *5.3.4 Effect of the grain and twin boundaries on fatigue crack growth in an undeformed cast Hadfield steel*

Crack growth in polycrystalline metals involves complex phenomena such as atomistic bond breaking, plastic deformation ahead of the crack tip, dislocation motion near the crack and dislocation pile ups at the microstructural obstacles *etc.* [7,12,47–50]. In metals, the microstructural features such as grain orientations, grain boundaries, twin boundaries, stacking faults and different phases in the microstructure are known to have a significant effect on their fatigue crack propagation characteristics [11,14,51–53]. Additionally, the microstructural evolution based on the stress intensity ahead of the crack tip also affects the fatigue crack growth behavior.

Fig. 5.8(a-f) show the microstructure of the undeformed cast Hadfield steel after the laboratory fatigue crack growth experiments. Fig. 5.8(a,b) show the EBSD Inverse Pole Figure (IPF) map and c-ECCI image of the undeformed cast Hadfield steel displaying the deflection of the fatigue crack at a grain boundary. Additionally, crack branching is observed near the grain boundary. This is in agreement with the observations of Chen *et al.* [51]. They showed that the grain boundaries resist the fatigue crack growth due to dislocation pile ups at the boundaries and cause large angle crack deflections at the boundaries. Zhai *et al.* [52] proposed a crystallographic model for the propagation of short fatigue cracks, which states that the crack plane twist and tilt angles are main factors responsible for crack retardation at the grain boundaries. These tilt and twist angles of the crack depend on the orientations of the grains.

The microstructural evolution in the vicinity of the crack tip is shown in Fig. 5.8(c-f). Fig. 5.8(c) shows the c-ECCI image displaying the formation of nano-sized deformation twins in the vicinity of the fatigue crack. Fatigue crack propagation is observed along these twins. Fig. 5.8(d) shows the formation of nano-sized deformation twins (shown by arrows) which are rather inclined to the fatigue crack growth direction. Repeated crack branching is observed in the primary fatigue crack in Fig. 5.8(d). The crack branching retards the fatigue crack growth by lowering the stress intensity ahead of the primary crack [50]. It is observed that the crack planes in the branched cracks are parallel to the deformation twins shown in Fig. 5.8(d). This indicates that the crack branching in cast Hadfield steels is associated with the deformation twins inclined to the fatigue crack growth direction. Fig. 5.8(e) shows the formation of deformation twins perpendicular to the direction of crack growth. Fig. 5.8(f) shows the magnified c-ECCI image from sub-region in Fig. 5.8(e) (shown by rectangle). We observe the formation of high density of dislocations (in white contrast) and dislocation cells in the vicinity of the deformation twins. The twin boundaries act as obstacles to the dislocation motion ahead of the crack tip and cause the retardation in the fatigue crack growth [14]. Based on the observations in Fig. 5.8(c-d), it can be concluded that the angle

between the crack growth direction and the deformation twins evolving ahead of the crack, is one of reasons affecting the fatigue crack growth behavior in cast Hadfield steels.

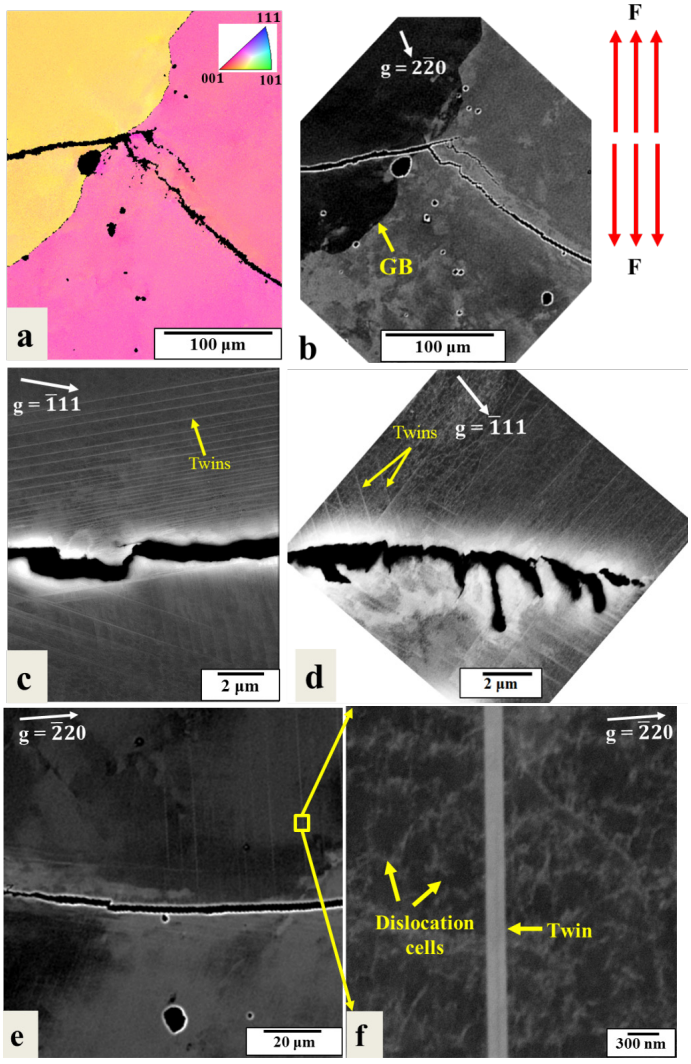


Fig. 5.8. *Microstructural observations after the fatigue crack growth experiments on undeformed cast Hadfield steel in laboratory settings,* (a,b) EBSD IPF map in normal direction and c-ECCI image showing the deflection of fatigue crack at the grain boundary, (c) c-ECCI image showing the formation of deformation twins ahead the crack and fatigue crack growing along the twins, (d) c-ECCI image showing the crack branching in the direction parallel to the deformation twins, (e) c-ECCI image showing the formation of deformation twins perpendicular to the fatigue crack growth direction, (f) Magnified c-ECCI image from the sub-region in (e) showing the formation of dislocation cells and high density of dislocations in the vicinity of deformation twins.

## 5.4 Conclusions

The understanding of the deformation and damage phenomena in cast Hadfield steels is important for sustainable design of steel microstructures for railway crossings application. Detailed study of the microstructure of in-field and laboratory loaded samples from a Hadfield steel allow drawing the following conclusions from the current study:

1. Deformation twinning is the main deformation mechanism in the cast Hadfield steels under impact fatigue due to their low stacking fault energy. Heavy plastic deformation is responsible for evolution of nano-sized deformation twins near the surface of the cast Hadfield steel rail crossing.
2. Formation of nano-sized deformation twinning at the crossing surface leads to accumulation of a high density of dislocations and formation of dislocation cells in the vicinity of twins. The nano-twins and the high density of dislocation structures are responsible for the strong strain hardening response of the cast Hadfield steels under studied conditions of impact fatigue.
3. Cast Hadfield steel contains casting defects like gas porosities/solidification shrinkages and non-metallic inclusions which can contribute to the crack initiation and propagation in crossings.
4. No evidence was found for strain-induced austenite-to-martensite transformation in the field-loaded cast Hadfield steels crossing. Therefore, the damage initiation cannot be correlated with such transformation in cast Hadfield steels in crossing application.
5. The grain boundaries can effectively deflect the growing fatigue crack in the cast Hadfield steel, which can result in crack retardation.
6. Fatigue crack growth in cast Hadfield is affected by the evolution of dislocations ahead the crack tip and the dislocation pile ups at the microstructural obstacles such as twin boundaries and grain boundaries. Furthermore, the angle between the fatigue crack growth direction and the deformation twins evolving ahead of the crack, affects the fatigue crack growth behavior.

## References


[1] P.H. Adler, G.B. Olson, W.S. Owen, Strain hardening of Hadfield manganese steel, Metall. Mater. Trans. A. 17 (1986) 1725–1737.

[2] W. Yan, L. Fang, K. Sun, Y. Xu, Effect of surface work hardening on wear behavior of Hadfield steel, Mater. Sci. Eng. A. 460 (2007) 542–549.

[3] A.K. Srivastava, K. Das, Microstructural characterization of Hadfield austenitic manganese steel, J. Mater. Sci. 43 (2008) 5654–5658.

[4] B. Lv, M. Zhang, F.C. Zhang, C.L. Zheng, X.Y. Feng, L.H. Qian, X.B. Qin, Micro-mechanism of rolling contact fatigue in Hadfield steel crossing, Int. J. Fatigue. 44 (2012) 273–278.

[5] R. Harzallah, A. Mouftiez, E. Felder, S. Hariri, J.-P. Maujean, Rolling contact fatigue of Hadfield steel X120Mn12, Wear. 269 (2010) 647–654. doi:10.1016/J.WEAR.2010.07.001.

[6] J.E. Garnham, C.L. Davis, The role of deformed rail microstructure on rolling contact fatigue initiation, Wear. 265 (2008) 1363–1372. doi:10.1016/J.WEAR.2008.02.042.

[7] A. Singh, M. Dao, L. Lu, S. Suresh, Deformation, structural changes and damage evolution in nanotwinned copper under repeated frictional contact sliding, Acta Mater. 59 (2011) 7311–7324. doi:10.1016/J.ACTAMAT.2011.08.014.

[8] W.L. Morris, The noncontinuum crack tip deformation behavior of surface microcracks, Metall. Trans. A. 11 (1980) 1117–1123. doi:10.1007/BF02668135.

[9] A. King, W. Ludwig, M. Herbig, J.-Y. Buffière, A.A. Khan, N. Stevens, T.J. Marrow, Three-dimensional in situ observations of short fatigue crack growth in magnesium, Acta Mater. 59 (2011) 6761–6771. doi:10.1016/J.ACTAMAT.2011.07.034.

[10] S. Güngör, L. Edwards, Effect of surface texture on the initiation and propagation of small fatigue cracks in a forged 6082 aluminium alloy, Mater. Sci. Eng. A. 160 (1993) 17–24. doi:10.1016/0921-5093(93)90493-X.

[11] M. Herbig, A. King, P. Reischig, H. Proudhon, E.M. Lauridsen, J. Marrow, J.-Y. Buffière, W. Ludwig, 3-D growth of a short fatigue crack within a polycrystalline microstructure studied using combined diffraction and phase-contrast X-ray tomography, Acta Mater. 59 (2011) 590–601. doi:10.1016/J.ACTAMAT.2010.09.063.

[12] S. Suresh, Crack deflection: Implications for the growth of long and short fatigue cracks, Metall. Trans. A. 14 (1983) 2375–2385. doi:10.1007/BF02663313.

[13] A. Navarro, E.R. De Los Rios, Fatigue crack growth modelling by successive blocking of dislocations, Proc. R. Soc. A Math. Phys. Eng. Sci. 437 (1992) 375–390. doi:10.1098/rspa.1992.0067.

[14] L. Liu, J. Wang, S.K. Gong, S.X. Mao, Atomistic observation of a crack tip approaching coherent twin boundaries, Sci. Rep. 4 (2014) 4397.

[15] T. Sinha, Y. Kulkarni, Alternating brittle and ductile response of coherent twin

boundaries in nanotwinned metals, J. Appl. Phys. 116 (2014) 183505.

[16] J.H. Xiao, F.C. Zhang, L.H. Qian, Contact stress and residual stress in the nose rail of a high manganese steel crossing due to wheel contact loading, Fatigue Fract. Eng. Mater. Struct. 37 (2013) 219–226. doi:10.1111/ffe.12108.

[17] W. Yan, L. Fang, Z. Zheng, K. Sun, Y. Xu, Effect of surface nanocrystallization on abrasive wear properties in Hadfield steel, Tribol. Int. 42 (2009) 634–641.

[18] J. Kang, F.C. Zhang, X.Y. Long, B. Lv, Cyclic deformation and fatigue behaviors of Hadfield manganese steel, Mater. Sci. Eng. A. 591 (2014) 59–68. doi:10.1016/J.MSEA.2013.10.072.

[19] W. Wei-yong, L. Bing, K. Venkatesh, Effect of Temperature on Strength and Elastic Modulus of High-Strength Steel, J. Mater. Civ. Eng. 25 (2013) 174–182. doi:10.1061/(ASCE)MT.1943-5533.0000600.

[20] L. Qian, X. Feng, F. Zhang, Deformed microstructure and hardness of Hadfield high manganese steel, Mater. Trans. 52 (2011) 1623–1628.

[21] L. Zhao, N.. van Dijk, E. Brück, J. Sietsma, S. van der Zwaag, Magnetic and X-ray diffraction measurements for the determination of retained austenite in TRIP steels, Mater. Sci. Eng. A. 313 (2001) 145–152. doi:10.1016/S0921-5093(01)00965-0.

[22] R.T.van Tol, Microstructure evolution in deformed austenitic Twinning Induced Plasticity steels, Delft University of Technology, 2014. doi:doi:10.4233/uuid:b2a057e2-c545-4bcc-854c-fe4b9344e486.

[23] S. Zaefferer, N.-N. Elhami, Theory and application of electron channelling contrast imaging under controlled diffraction conditions, Acta Mater. 75 (2014) 20–50. doi:10.1016/J.ACTAMAT.2014.04.018.

[24] I. Gutierrez-Urrutia, D. Raabe, Grain size effect on strain hardening in twinning-induced plasticity steels, Scr. Mater. 66 (2012) 992–996. doi:10.1016/J.SCRIPTAMAT.2012.01.037.

[25] I. Gutierrez-Urrutia, S. Zaefferer, D. Raabe, The effect of grain size and grain orientation on deformation twinning in a Fe–22 wt.% Mn–0.6 wt.% C TWIP steel, Mater. Sci. Eng. A. 527 (2010) 3552–3560. doi:10.1016/J.MSEA.2010.02.041.

[26] I. Gutierrez-Urrutia, S. Zaefferer, D. Raabe, Electron channeling contrast imaging of twins and dislocations in twinning-induced plasticity steels under controlled diffraction conditions in a scanning electron microscope, Scr. Mater. 61 (2009) 737–740. doi:10.1016/J.SCRIPTAMAT.2009.06.018.

[27] I. Gutierrez-Urrutia, S. Zaefferer, D. Raabe, Coupling of Electron Channeling with EBSD: Toward the Quantitative Characterization of Deformation Structures in the SEM, JOM. 65 (2013) 1229–1236. doi:10.1007/s11837-013-0678-0.

[28] B. Bay, N. Hansen, D.A. Hughes, D. Kuhlmann-Wilsdorf, Overview no. 96 evolution of f.c.c. deformation structures in polyslip, Acta Metall. Mater. 40 (1992) 205–219. doi:10.1016/0956-7151(92)90296-Q.

[29] N. Hansen, D.Juul Jensen, Development of microstructure in FCC metals during cold work, Philos. Trans. R. Soc. London A Math. Phys. Eng. Sci. 357 (1999) 1447–1469.

[30] H. Beladi, I.B. Timokhina, Y. Estrin, J. Kim, B.C. De Cooman, S.K. Kim, Orientation dependence of twinning and strain hardening behaviour of a high manganese twinning induced plasticity steel with polycrystalline structure, Acta Mater. 59 (2011) 7787–7799. doi:10.1016/J.ACTAMAT.2011.08.031.

[31] D.R. Steinmetz, T. Jäpel, B. Wietbrock, P. Eisenlohr, I. Gutierrez-Urrutia, A. Saeed–Akbari, T. Hickel, F. Roters, D. Raabe, Revealing the strain-hardening behavior of twinning-induced plasticity steels: Theory, simulations, experiments, Acta Mater. 61 (2013) 494–510. doi:10.1016/J.ACTAMAT.2012.09.064.

[32] D. Sun, S. V Garimella, Numerical and Experimental Investigation of Solidification Shrinkage, Numer. Heat Transf. Part A Appl. 52 (2007) 145–162. doi:10.1080/10407780601115079.

[33] R.A. Hardin, C. Beckermann, Effect of Porosity on Deformation, Damage, and Fracture of Cast Steel, Metall. Mater. Trans. A. 44 (2013) 5316–5332. doi:10.1007/s11661-013-1669-z.

[34] N.W. Peters, P. Eng, The performance of Hadfield's manganese steel as it relates to manufacture, Dostupné Na Internetu< Https//Www. Arema. Org/Files/Library/2005_Conference_Proceedings/00040. Pdf>.[Cit. 11. 5. 2015]. (2005).

[35] X.Xu and A. Needleman, Void nucleation by inclusion debonding in a crystal matrix, Model. Simul. Mater. Sci. Eng. 1 (1993) 111. http://stacks.iop.org/0965-0393/1/i=2/a=001.

[36] G. Collette, C. Crussard, A. Kohn, J. Plateau, G. Pomey, M. Weisz, Contribution à l'étude des transformations des austénites à 12 % Mn, Rev. Met. Paris. 54 (1957) 433–486. https://doi.org/10.1051/metal/195754060433.

[37] J. Spreadborough, Stacking faults in iron–manganese and cobalt–nickel, Acta

Crystallogr. 13 (2018) 603–605. doi:10.1107/S0365110X60001448.

[38] G.B. Olson, M. Cohen, A mechanism for the strain-induced nucleation of martensitic transformations, J. Less Common Met. 28 (1972) 107–118.

[39] E.J. Pickering, Macrosegregation in steel ingots: the applicability of modelling and characterisation techniques, ISIJ Int. 53 (2013) 935–949.

[40] J. Takahashi, K. Kawakami, M. Ueda, Atom probe tomography analysis of the white etching layer in a rail track surface, Acta Mater. 58 (2010) 3602–3612. doi:10.1016/J.ACTAMAT.2010.02.030.

[41] E. Mazancová, K. Mazanec, Stacking fault energy in high manganese alloys, Mater. Eng. 16 (2009) 26–31.

[42] D.T. Pierce, J.A. Jiménez, J. Bentley, D. Raabe, J.E. Wittig, The influence of stacking fault energy on the microstructural and strain-hardening evolution of Fe–Mn–Al–Si steels during tensile deformation, Acta Mater. 100 (2015) 178–190. doi:10.1016/J.ACTAMAT.2015.08.030.

[43] N. Jost, I. Schmidt, Friction-induced martensitic transformation in austenitic manganese steels, Wear. 111 (1986) 377–389. doi:10.1016/0043-1648(86)90134-1.

[44] A.G. Pineau, R.M. Pelloux, Influence of strain-induced martensitic transformations on fatigue crack growth rates in stainless steels, Metall. Trans. 5 (1974) 1103–1112. doi:10.1007/BF02644322.

[45] G. Baudry, A. Pineau, Influence of strain-induced martensitic transformation on the low-cycle fatigue behavior of a stainless steel, Mater. Sci. Eng. 28 (1977) 229–242. doi:10.1016/0025-5416(77)90176-8.

[46] A. Das, S. Tarafder, Experimental investigation on martensitic transformation and fracture morphologies of austenitic stainless steel, Int. J. Plast. 25 (2009) 2222–2247. doi:10.1016/J.IJPLAS.2009.03.003.

[47] R. Pippan, A. Hohenwarter, The importance of fracture toughness in ultrafine and nanocrystalline bulk materials, Mater. Res. Lett. 4 (2016) 127–136.

[48] J. LANKFORD, THE GROWTH OF SMALL FATIGUE CRACKS IN 7075–T6 ALUMINUM, Fatigue Fract. Eng. Mater. Struct. 5 (2018) 233–248. doi:10.1111/j.1460-2695.1982.tb01251.x.

[49] A. Singh, L. Tang, M. Dao, L. Lu, S. Suresh, Fracture toughness and fatigue crack growth characteristics of nanotwinned copper, Acta Mater. 59 (2011) 2437–2446. doi:10.1016/J.ACTAMAT.2010.12.043.

[50] S. Suresh, R.O. Ritchie, Propagation of short fatigue cracks, Int. Met. Rev. 29 (1984) 445–475. doi:10.1179/imtr.1984.29.1.445.

[51] Y.Q. Chen, S.P. Pan, M.Z. Zhou, D.Q. Yi, D.Z. Xu, Y.F. Xu, Effects of inclusions, grain boundaries and grain orientations on the fatigue crack initiation and propagation behavior of 2524-T3 Al alloy, Mater. Sci. Eng. A. 580 (2013) 150–158. doi:10.1016/J.MSEA.2013.05.053.

[52] T. Zhai, A.J. Wilkinson, J.W. Martin, A crystallographic mechanism for fatigue crack propagation through grain boundaries, Acta Mater. 48 (2000) 4917–4927. doi:10.1016/S1359-6454(00)00214-7.

[53] D. Taylor, J.F. Knott, Fatigue crack propagation behaviour of short cracks; the effect of microstructure, Fatigue Fract. Eng. Mater. Struct. 4 (1981) 147–155.

# 6

# *In-situ* observation of strain partitioning and damage development in continuously cooled carbide-free bainitic steels using micro digital image correlation‡‡


## Abstract

In this chapter, we probe the strain partitioning between the microstructural features present in a continuously cooled carbide-free bainitic steel together with damage nucleation and propagation. These features mainly comprise of phases (bainitic ferrite, martensite, and blocky/thin film austenite), interfaces between them, grain size and grain morphology. A micro Digital Image Correlation (μ-DIC) technique in scanning electron microscope is used to quantify the strain distribution between these microstructural features. The results show a strong strain partitioning between martensite, bainitic ferrite and retained austenite that provides weak links in the microstructure and creates conditions for the crack initiation and propagation during deformation. Blocky austenite islands accommodate maximum local strains in the global strain range of 0-2.3% and undergo strain-induced austenite to martensite transformation governing the local strain evolution in the microstructure. However, local strains are minimum in the martensite regions during entire *in-situ* deformation stage. Narrow bainitic ferrite channels in between martensitic islands and


‡‡ This chapter is based on the article: A. Kumar, A. Dutta, S. K. Makineni, M. Herbig, R. Petrov, and J. Sietsma, *In-situ* study of strain partitioning and damage development in a continuously cooled carbide-free bainitic steel using micro digital image correlation, Mat. Sci. & Eng. A, 757 (2019) 107–116, https://doi.org/10.1016/J.MSEA.2019.04.098

martensite-bainitic ferrite interfaces are recognised as primary damage sites with high strain accumulation of 30 ± 2% and 20 ± 3% respectively, at a global strain of 9%. The inclination of these interfaces with the tensile direction also affects the strain accumulation and damage.

## 6.1 Introduction

Conventional pearlitic steels are the most widely used steel grades in railway applications due to their good combination of mechanical properties such as strength, toughness and wear resistance. The reason for these good mechanical properties is the presence of a fine pearlitic microstructure (interlamellar spacing approximately 150-200 nm) where a single pearlitic colony comprises interpenetrating crystals of ferrite (α-Fe) and cementite (θ-$Fe_3C$). However, the fatigue life of the pearlitic rails is adversely affected by the presence of cementite in their microstructure [1,2]. Furthermore, the cementite dissolution caused by temperature rise and severe plastic deformation under wheel-rail contact leads to the formation of brittle microstructural features on the rail surface such as White Etching Layers (WELs) and Brown Etching Layers (BELs) [3–6]. Delamination and brittle fracture of these layers causes the initiation of micro-cracks in the rails [7–11]. Conventional pearlitic steels are also prone to formation of various in-service defects such as head checks and squats under rail-wheel contact [12–15]. These micro-cracks and defects may lead to failure of rails, posing safety threats and involving millions of euros of maintenance cost each year worldwide [16]. Hence, application of high strength, low carbon Continuously Cooled Carbide-Free Bainitic Steel (CC-CFBS) is thought to be an alternative to pearlitic steels for railway applications [12,15,17–19]. CC-CFBS offers better mechanical properties such as tensile strength (1150-1200 MPa), ductility (18-20%), and rolling contact fatigue strength compared to conventional pearlitic steels [19–24]. Moreover, the lower wear resistance of CC-CFBS (industrially termed as B360) in comparison with conventional pearlitic steels leads to in-service removal of head checks from the rail surface. That is why CC-CFBS steel is also called head check proof steel. Additionally, the absence of carbides in these steels avoids the formation of deleterious WELs on the rail surface during service [25,26]. The absence of carbides in CC-CFBS is attributed to the high Si content (1.3 wt.%) which supresses the precipitation of cementite in austenite during bainitic transformation [15,17,27,28]. This can be explained by extremely low solubility of Si in cementite, thereby increasing the cementite precipitation temperature in ferrite [8,9,11]. This cementite precipitation is also strongly retarded because of the negligible atomic mobility of Si at low bainitic transformation temperatures [29]. Large-scale production of the low carbon CC-CFBS in the industry has gained momentum recently for use in rails [25,28,30–32]. Implementing this steel in rails still requires rigorous understanding of local microstructural damage behaviour upon the application of stress.

During the rail-wheel contacts, the stresses generated in rails are of complex nature due to the complex loading conditions. It is difficult to produce such loading conditions in the laboratory environment. However, the uniaxial tensile testing in laboratory settings can itself help establish strong understanding of strain partitioning and damage in these steels. This understanding will provide new strategies for robust alloy design at microstructural scale with improved mechanical performance.

The damage behaviour in different steel grades used in any structural application is affected by the stress/strain partitioning in the microstructure. The damage phenomenon on microstructural scale has been widely investigated for Dual Phase (DP) and transformation-induced plasticity (TRIP) steels [33–39]. These steel types show a composite-like micromechanical response because of their complex microstructure containing ferrite, martensitic islands and martensite-ferrite interfaces [35,37–40]. Understanding of micromechanical damage in DP/TRIP steels helps achieving the optimum combinations of strength and ductility by altering the microstructure via the volume-fraction ratio between the soft ferrite and hard martensite, controlling the grain size and morphology. In Dual Phase steels, the most common damage sites are identified as martensite-ferrite interfaces (M/F) or martensite islands interiors, on the basis of strain partitioning analysis using high resolution Micro Digital Image Correlation (μ-DIC) [36]. However, there is no detailed study available in the literature till date concerning the damage evolution and strain partitioning in CC-CFBS. The reason behind this is the microstructural complexity of CC-CFBS, containing multiple phases with different volume fraction, different composition and crystallographic structure, different size and morphology, and differences in their mechanical stability. This complex heterogeneous microstructure can lead to strain partitioning among its constituents upon application of stresses. The understanding of the strain partitioning in CC-CFBS can provide the possibility of identifying the weak microstructural sites that can lead to initiation and propagation of cracks. This can also provide guidelines for designing a sustainable steel microstructure. Thus, in the present study, we aim to investigate the strain partitioning among the microstructural constituents of CC-CFBS, which is not well documented in the literature. Finally in this study, we will attempt to establish an understanding of microscale damage mechanisms in relation with the microstructure of CC-CFBS.

## 6.2 Experimental methods

### *6.2.1 Material and processing*

A low carbon Continuously Cooled Carbide-Free Bainitic Steel (CC-CFBS) with a nominal chemical composition of Fe-0.27C-1.55Mn-1.3Si-0.5Cr-0.03V-0.15Mo (in wt.%) was investigated in this work. The composition of this steel was confirmed by Optical Emission

Spectroscopy (OES) and X-Ray Florescence (XRF) measurements. The rails of this steel were produced at Corus, France by a six-pass hot rolling process in the temperature range 600-800 °C. Subsequently, the rolled rail sections were annealed in furnace at a temperature around 950 °C for 1 hour followed by air cooling to form a carbide-free bainitic microstructure.

### *6.2.2 Microstructural characterisation*

The microstructure of the as-received Continuously Cooled Carbide-Free bainitic steel (CC-CFBS) was characterised using Optical Microscopy (OM) in a Keyence VHX 6000 microscope. The microstructure was further characterised by combined/correlative utilisation of Electron BackScatter Diffraction (EBSD) and Secondary Electron (SE) imaging technique in a JEOL JSM 6500F scanning electron microscope. Orientation data were acquired at an acceleration voltage of 15 kV with a step size of 70 nm in a hexagonal scan grid. The Orientation Image Microscopy (OIM) software (TSL-OIM) was used to analyse the EBSD data. A quantitative Image Quality (IQ) criterion with a threshold absolute IQ value of 950 was used to quantify the fraction of martensite in the microstructure [41,42]. To apply this criterion, Face Centred Cubic (FCC) (*i.e.* austenite) data points were not taken into account; only the Body Centred Cubic (BCC) data points (*i.e.* martensite/bainitic ferrite) were used. The selection of the threshold value in absolute IQ criterion was done by comparing and fitting the results with the SEM image taken in the same area. The fraction of Retained Austenite (RA) phase was measured using both EBSD and X-Ray Diffraction (XRD). The XRD measurements were performed on a Bruker D8-advance diffractometer operating at 45 kV and 40 mA, using Cu Kα radiation ($\lambda$ = 0.15406 nm) and a scan rate of 0.002° 2θ $s^{-1}$. In order to minimize the texture effect, specimens were tilted and rotated during the measurement. The retained austenite fraction was calculated by comparing the intensities of the ferrite peaks {110}, {200}, {211} and {220} with the austenite peaks {111},{200}, {220} and {311} in the XRD measurements as depicted in references [43,44].

### *6.2.3 Interrupted tensile experiments*

Monotonic tensile experiments were conducted in displacement control mode at room temperature using an Instron 5500R electromechanical tester, equipped with a load cell of 10 kN capacity. Dog bone shaped rectangular tensile specimens with gauge dimensions of 25 mm × 4 mm × 0.8 mm were prepared from CC-CFBS steel for the interrupted tensile testing experiments. The axial direction of the samples was aligned along the rolling direction of the produced rail sections. A knife-edge type extensometer (Instron 2620-602, 12.5 mm gauge length, ±2.5 mm and an accuracy of ±0.5% of the read value) was used for average strain measurements. The crosshead speed was maintained constant at 1 mm/min during the tensile testing, implying an approximate initial strain rate of $7\times10^{-4}$ $s^{-1}$. Tensile

tests were interrupted at strain values of 0%, 3%, 9% and 14%. At each interruption step, the fraction of retained austenite in the specimens was measured using XRD.

### *6.2.4 In-situ Micro Digital Image Correlation (μ-DIC) experiments*

The μ-DIC experiments were performed by *in-situ* tensile tests of miniature specimens with gauge dimensions of 1 mm × 0.5 mm × 0.5 mm as shown in Fig. 6.1(a). The tensile test specimens were prepared by spark erosion/Electrical Discharge Machining (EDM). Prior to testing, the surfaces of the specimens were prepared by fine grinding and diamond polishing followed by metallographic preparation using colloidal silica (50-100 nm particle size). Subsequently, high resolution EBSD measurements were conducted to locate the specific regions of interest (ROI) on the specimen surfaces using a JEOL JSM 6500F scanning electron microscope with a Schottky field emission gun (FEG-SEM). An accelerating voltage of 15 kV, working distance of 18 mm and step size of 40 nm in a hexagonal scan grid were used for EBSD scanning. The ROI was then marked with Focused Ion Beam (FIB) milling in Helios NanoLab 600i microscope in order to locate it subsequently during the *in-situ* testing. The FIB markers were kept 50 μm from the each corner of the ROI to avoid ion beam damage in the ROI. After ROI selection and marking, a monolayer of $SiO_2$ particles (50-100 nm in size) was homogeneously dispersed on the sample surface (Fig. 6.1(b)) to perform local strain field measurements during deformation [36]. For *in-situ* deformation experiments, a KAMMRATH & WEISS stage was used inside the ZEISS Crossbeam XB 1540 microscope. Specimens were deformed at a cross head speed of 3 μm/sec, which corresponds to an initial strain rate of $6 \times 10^{-4}$ $s^{-1}$. In-lens SE detector was used at 1.5 kV acceleration voltage, to capture the high resolution images (2048 pixels × 1536 pixels) of the ROI with SiO2 particles on the specimen surface [36,37]. These images were taken after every 2% increase in strain. The recorded images were used for von Mises/equivalent micro-strain analysis using the ARAMIS software (V6.3.0, GOM GmbH). For this analysis, the facet size was set to 150 nm enabling to achieve a stochastic pattern structure within a facet, while the facet overlap was kept at a default of 20 ~ 25%. The global strain from each image was obtained from line strains across the measured area of the map. The von Mises strains in individual phases were obtained by taking multiple sections correlating the EBSD data. Additionally, the analysis (using EBSD and SE imaging) is performed after the fracture of the specimens in *in-situ* tests to investigate the detailed damage evolution in the microstructure.

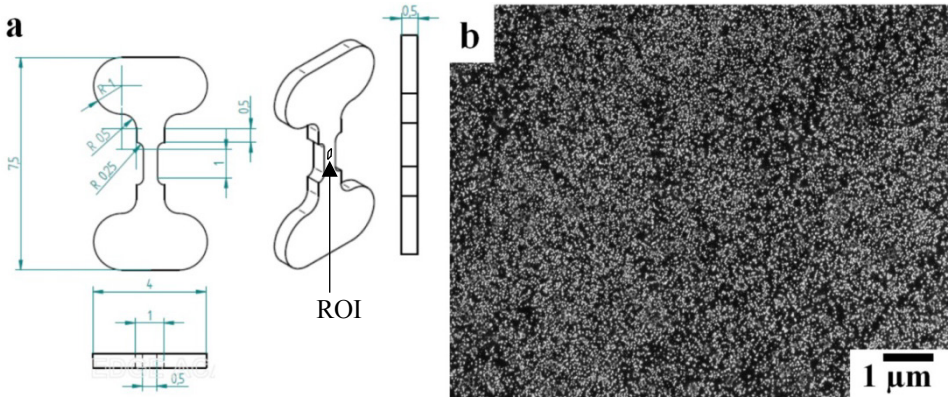


Fig. 6.1. Schematic representation of the geometry of the miniature tensile specimens with the location of a region of interest (ROI) (dimensions are given in mm), (b) Secondary Electron (SE) image showing dispersed monolayer of the $SiO_2$ particles in the ROI for µ-DIC strain measurements.

## 6.3 Results and Discussion

### *6.3.1 Microstructure characterisation and mechanical properties*

Fig. 6.2(a) shows an optical micrograph of the Continuously Cooled Carbide-Free Bainitic Steel (CC-CFBS) showing multiple phases present in the microstructure. Large white-contrast blocks/islands are identified as martensite (M) and/or Blocky Retained Austenite (BRA). Bainite is observed to have two typical microstructural morphologies: coarse bainite (also termed as upper bainite) (in brown contrast) and lower bainite with lath morphology, where Thin Film Retained Austenite (TFRA) (in white contrast) is sandwiched between Lath Bainitic Ferrite (LBF) (in brown contrast) (Fig. 6.2(a)). Martensite and blocky retained austenite have similar optical contrast after etching with 2% Nital. Hence, EBSD in combination with SE imaging was used to differentiate these two phases in further analysis. Fig. 6.2(b) shows the tensile stress-strain curve of the studied CC-CFBS showing yield strength $\sigma_y$ = 865 MPa and tensile strength $\sigma_{UTS}$ = 1175 MPa with a uniform elongation ($\varepsilon_{UTS}$) of 14.7 %. This combination of properties is better than of the conventional pearlitic steels having yield strength $\sigma_y$ = 650 MPa and tensile strength $\sigma_{UTS}$ = 893 MPa with an uniform elongation $\varepsilon_{UTS}$ = 8 % [45]. The martensite and bainitic ferrite were distinguished by micro-indentation hardness measurements as there is a significant difference in the hardness between martensite (534 HV0.01) and bainitic ferrite (344 HV0.01) (Fig. 6.2(c)).

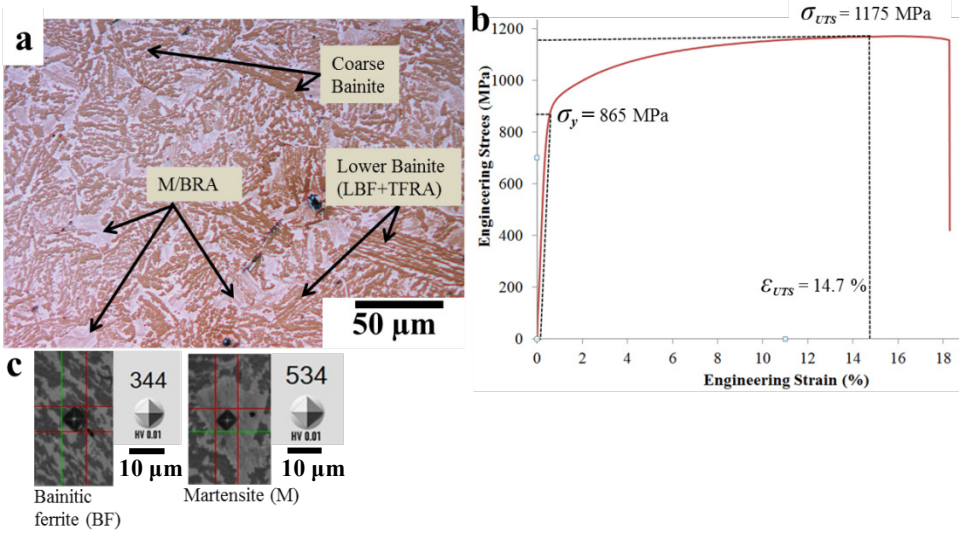


Fig. 6.2. (a) Optical micrograph of continuously cooled carbide-free bainitic steel (CC-CFBS) showing coarse bainite, Martensite (M), Blocky Retained Austenite (BRA), and lower bainite containing Lath Bainitic Ferrite (LBF) and Thin Film Retained Austenite (TFRA) in the microstructure, (b) tensile curve of CC-CFBS, (c) micro hardness indents showing significant difference in hardness between martensite (534 HV0.01) and bainitic ferrite (344 HV0.01).

Further detailed microstructural characterisation is performed by combined use of SE imaging and EBSD (Fig. 6.3)[§§]. SE imaging gives the topological contrast in the microstructure and EBSD enables the determination of various microstructural features by diffraction such as individual grain orientation, grain size, phase identification, grain/phase boundary misorientation, and internal grain misorientation [46]. Thus the use of both techniques helps to thoroughly understand the microstructure. Fig. 6.3(a) shows an SE image of the microstructure of CC-CFBS with respective phases marked, such as Martensite (M), Bainitic Ferrite (BF), Blocky Retained Austenite (BRA) and Lath Bainitic Ferrite (LBF). Phases in this image are recognised in correlation with the EBSD measurement performed in the same area prior to SE imaging. EBSD maps from the same region are shown in Fig. 6.3(b,d). Fig. 6.3(b) shows the EBSD Image Quality (IQ) map superimposed with the Retained Austenite (RA) phase map, shown by green islands. The measured RA fraction in EBSD is around 10.4 ± 1.2 % (Table 6.1). This fraction is also calculated using the X-Ray diffraction (later shown in this chapter in Fig. 6.4(a,f)) which shows slightly higher values, 12.5 ± 1.0 % (Table 6.1), due to the presence of some austenite grains finer than the spatial resolution limit of EBSD. The quantification of the martensite fraction in bainitic steels is difficult using only the EBSD technique due to the similarity in the crystal structure with bainitic ferrite [47]. Hence, correlative EBSD and SE

[§§] The detailed characterisation is essential to establish an understanding of the microstructural constituents in CC-CFBS for the in-situ strain partitioning and damage study.

imaging were carried out in the same region of microstructure of CC-CFBS to determine the martensite fraction.

Martensite phase contains large non uniform lattice strains and a high dislocation density which leads to diffuse Kikuchi bands in EBSD, deteriorating the quality of the diffraction pattern [48]. Hence, the absolute IQ values measured in the martensite will be lower than the one measured in bainitic ferrite where IQ represents the quality of the diffraction pattern. The absolute IQ values are determined by the average height of the Hough Transform peaks derived from a specific diffraction pattern in the EBSD [49]. The martensite regions which have a lower IQ are observed as dark contrast areas and bainitic ferrite phase appears bright on the grey scale EBSD IQ map in Fig. 6.3(b), having high IQ. After comparing the dark areas in Fig. 6.3(b) with the SE image in Fig. 6.3(a), it is clear that the martensite phase appears with white topological contrast in the SE image. Retained austenite shows a similar white topological contrast in SE mode (marked with BRA, *i.e.* Blocky Retained Austenite in Fig. 6.3(a)), but RA is distinguished from martensite by correlating the EBSD measurements (in Fig. 6.3(b)). Some regions with lath bainitic ferrite and martensite (low IQ) are also observed in the micrographs shown in Fig. 6.3(a,b) and labelled as LBF+M in Fig. 6.3(a). The appearance of microstructural constituents such as martensite (M), Bainitic Ferrite (BF), and Lath Bainitic Ferrite with martensite (LBF +M) marked in Fig. 6.3(a) are found to be consistent with the EBSD IQ + RA phase map in Fig. 6.3(b).

Fig. 6.3(c) shows the distribution of absolute IQ values of BCC in the microstructure shown in Fig. 6.3(b). A tendency for a bimodal distribution of IQ values is observed with a minimum at the IQ value of 950 (Fig. 6.3(c)). Thus, we used a threshold absolute IQ value of 950 in the BCC phase to estimate the fraction. The pixels below this threshold absolute IQ value are shown with blue regions in the EBSD map in Fig. 6.3(d). On comparing this map with the SE image in Fig. 6.3(a), blue regions fit very well with the white contrast martensitic islands in Fig. 6.3(a). Hence, these regions are the martensitic regions and used to calculate the area fraction of martensite. The total area fraction of martensite is estimated to be 20.0 ± 1.5 % in the microstructure of CC-CFBS (Fig. 6.3(d) and Table 6.1).

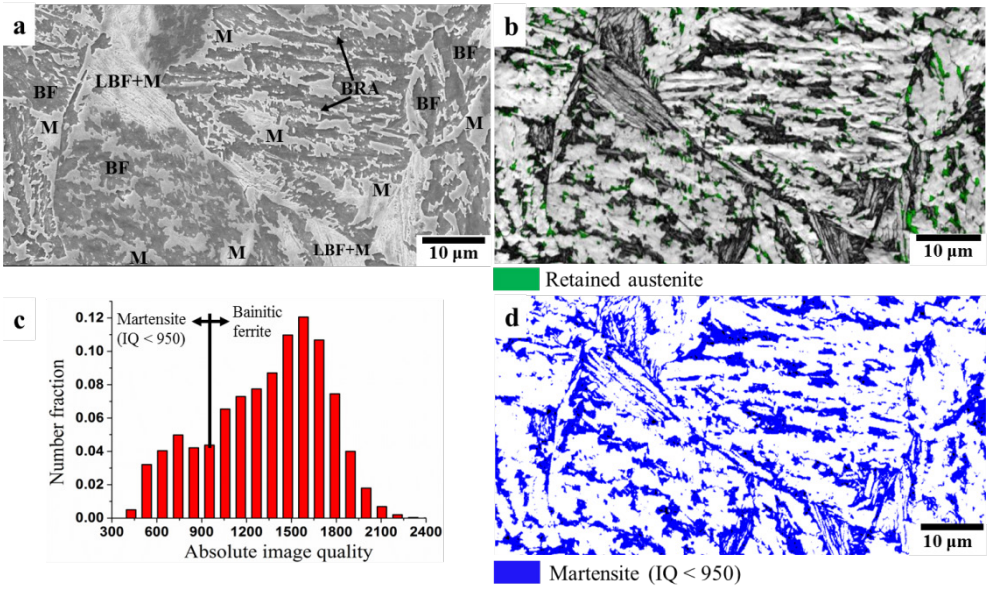


Fig. 6.3. (a) SEM micrograph of continuously cooled carbide-free bainitic steel showing different phases marked as martensite (M), Bainitic ferrite (BF), Lath Bainitic Ferrite (LBF), and Blocky Retained Austenite (BRA), (b) EBSD IQ map of the same area superimposed with retained austenite phase map (austenite in green) showing martensite phase with low IQ (dark areas) and bainitic ferrite islands with high IQ (bright areas), (c) plot showing the distribution of absolute IQ values in the microstructure, (d) IQ map showing low IQ areas below absolute IQ value of 950 (in blue) for quantitative estimation of martensite in the microstructure (Retained austenite pixels were excluded in the measurement).

Table 6.1. Fractions of different phases present in the microstructure of Continuously Cooled Carbide-Free Bainitic Steel (CC-CFBS).

| Phase | Fraction (%) |
|---|---|
| Retained austenite (EBSD) | 10.4 ± 1.2 |
| Retained austenite (XRD) | 12.5 ± 1.0 |
| Martensite (IQ criteria) | 20.0 ± 1.5 |
| Bainite | Rest |

### *6.3.2 Interrupted tensile testing: strain-induced transformation of retained austenite into martensite in CC-CFBS*

Fig. 6.4 shows the results of the interrupted tensile testing in combination with X-ray diffraction (XRD) measurements that were used to study the strain-induced transformation of retained austenite into martensite in CC-CFBS. Fig. 6.4(a-d) shows the X-ray diffraction patterns taken after global strain values of 0, 3, 9 and 14% respectively in an interrupted tensile test. The intensities of the austenite diffraction peaks ($A_{\{111\}}$, $A_{\{200\}}$, $A_{\{220\}}$ and $A_{\{311\}}$) decrease with increasing the global engineering strain (Fig. 6.4(a-d)). Fig. 6.4(e) shows a magnified view of the austenite $A_{\{111\}}$ peaks showing the decrease in the intensity with increase in strain. The austenite fraction is calculated from these XRD measurements (Fig. 6.4(a-d)) and plotted against the global engineering strain in Fig. 6.4(f). The austenite fraction decreases rapidly from 12.5 ± 1.0 % to 8.4 ± 1.0 % during initial stage of loading from 0 to 3% global engineering strain (Fig. 6.4(f)). Afterwards, the retained austenite fraction gradually decreases and reaches 5.1 ± 0.6 % at 14% global strain. This remaining austenite after 14% global engineering strain is either due to the presence of small austenitic regions (smaller than 250 nm) with high carbon concentration or due to the presence of thin film retained austenite which is considered to be chemically and mechanically more stable than large blocky retained austenite [50,51].

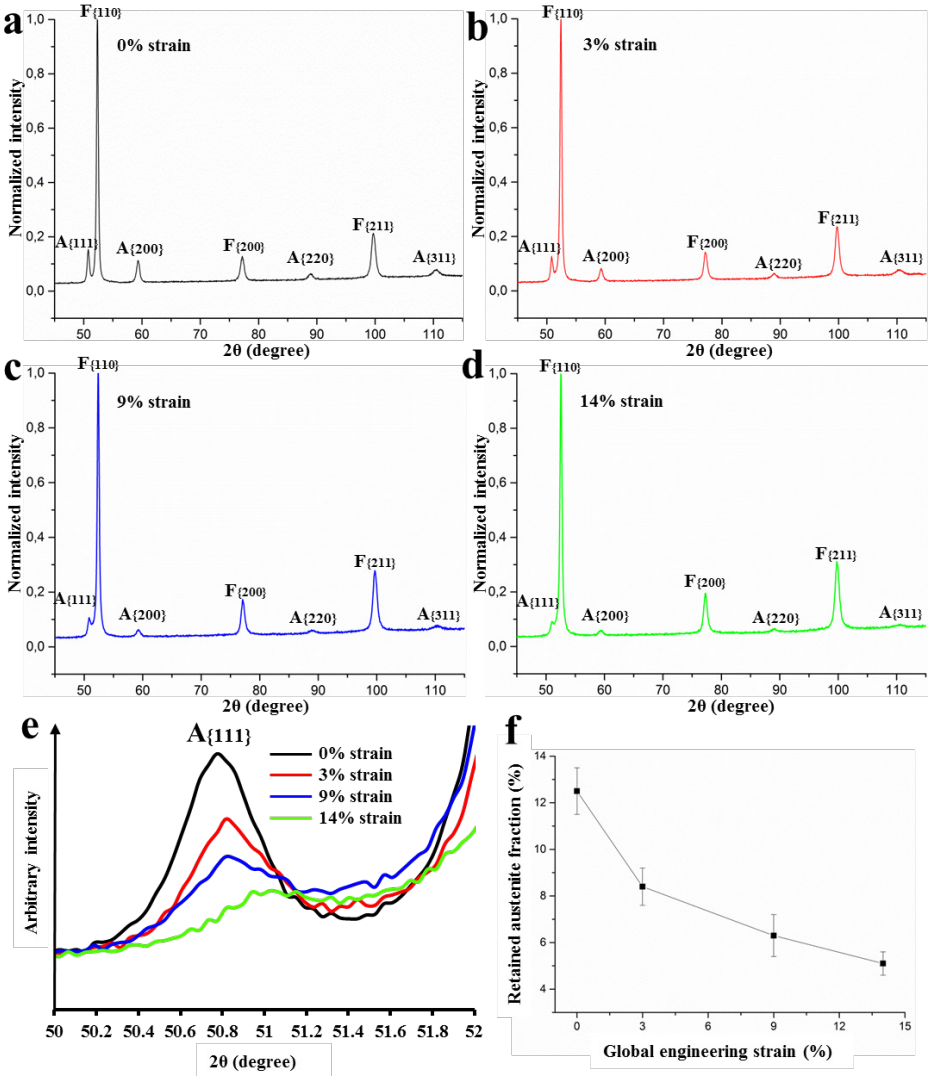


Fig. 6.4. (a-d) X-ray diffraction patterns showing continuous decrease in the intensity of austenitic peaks representing reduction in retained austenite fraction with increasing global strain (a) 0%, (b) 3%, (c) 9% and (d) 14% respectively during the interrupted tensile testing, (e) magnified view of austenite $A_{\{111\}}$ peaks showing reduction in their intensity with increase in the strain value, (f) graph showing retained austenite fraction vs global engineering strain calculated by comparing the intensities of the ferrite and austenite peaks.

### *6.3.3 In-situ microstructural strain mapping and damage*

Fig. 6.5 shows the results pertaining to *in-situ* μ-DIC experiments at different global engineering strain values from 0 to 9%. The obtained data show strong strain partitioning among the microstructural constituents in the presently investigated bainitic steel. Fig. 6.5(a) depicts overlapped EBSD phase map and IQ map of CC-CFBS with constituent phases marked. The green and red regions belong to retained austenite and bainitic ferrite respectively, whereas dark low-IQ regions correspond to martensite. Most of the Thin Film Retained Austenite (TFRA) is difficult to detect in the EBSD as its size is smaller than the EBSD resolution limit. Hence, the retained austenite islands shown in Fig. 6.5(a) are primarily the Blocky Retained Austenite (BRA). The map in Fig. 6.5(a) is a reference image of the undeformed microstructure, *i.e.* at 0% global strain, and it helps establishing the relationship between microstructure and μ-DIC results at higher strain values. Fig. 6.5(b-d) shows the local von Mises strain maps with increasing global strains of 2.7%, 4.7% and 9% respectively, where different colour represents different values of local strain as per the coloured local strain scale from 0 to 35 % shown with these maps. The local strain during *in-situ* testing is observed to be concentrating along a 45° to 50° angle with respect to the loading direction shown in μ-DIC maps in Fig. 6.5(b-d). This is due to the maximum resolved shear stress along 45° to the tensile direction, facilitating easy slip. It was found that the martensitic regions in the microstructure accommodate minimum local strain up to only ~ 2.1% at 9% global strain (as shown by the black arrows in Fig. 6.5(d)), whereas the largest strain accumulation is located in bainitic ferrite islands (Fig. 6.5(d)). The bainitic ferrite islands, especially in the form of thin channels between martensite islands, accumulate local strain, even up to 35% at 9% global strain. These channel-like areas are marked with red arrows in Fig. 6.5(d). The observed large difference in the local strain between martensite and bainitic ferrite mean that there is a strong strain incompatibility within the microstructure. Simultaneously, a clear damage event is observed at 9% global strain in Fig. 6.5(d), where the crack path is shown with the orange arrows. Due to such damage and cracking incidents, the displacement field correlation between the Si nano-particles for μ-DIC is lost at these damage locations and the crack path can be identified by white zones as shown in Fig. 6.5(d). In this figure, it is observed that the crack initially follows the interface between martensite and bainitic ferrite islands and then propagates through fracture in martensite regions (encircled at later stage of crack growth in Fig. 6.5(d)).

Fig. 6.5(e) shows the variation of the calculated average local von Mises strain ($\varepsilon_{vM}$) vs global engineering strain ($\varepsilon$) for individual microstructural constituents such as bainitic ferrite (in red), retained austenite (in green), lath bainitic ferrite + martensite (in blue), and martensite (in black). Martensite shows minimum average $\varepsilon_{vM}$ during the straining from 0 to 9% global strain, while LBF+M islands always show higher average $\varepsilon_{vM}$ than martensite but lower than retained austenite and bainitic ferrite. The lower strain accumulation in LBF+M

than in the coarse bainitic ferrite (BF) can be explained by the formation of fine lath morphology at low transformation temperatures during continuous cooling transformation [1]. This transformation introduces a higher dislocation density and carbon concentration in the lath bainitic ferrite than in the coarse bainitic ferrite. Subsequently, the lath bainitic ferrite is accompanied by martensitic laths (as shown by low IQ in Fig. 6.5(a)), which imparts more strength and less ductility to these islands.

In the initial straining stage up to 2.3 % global strain, retained austenite is found to be taking the highest local strain of all the other microstructural constituents (Fig. 6.5(e)). The strain localization in retained austenite can be attributed to easy slip tendency in its face centred cubic crystal structure at the initial loading stage, thereby facilitating the strain-induced transformation of austenite into martensite. This argument is well supported by the observation in Fig. 6.4(f) where the austenite fraction suddenly decreases in the global strain range from 0 to 3% in interrupted tensile testing. After 2.3% global strain, bainitic ferrite shows much higher average $\varepsilon_{vM}$ as compared to all other phases. The maximum average $\varepsilon_{vM}$ in bainitic ferrite reaches around 29% at 9% global strain (Fig. 6.5(e)). The average $\varepsilon_{vM}$ in retained austenite increases gradually after 2.3% global strain and reaches a maximum value of approximately 11% at 9% global strain. The lower average $\varepsilon_{vM}$ values in austenite in comparison to bainitic ferrite can be explained by the strain-induced phase transformation of austenite into martensite at global strain values above 2.3%. The locations where this transformation has already occurred, experience lower local strain accumulation than the untransformed regions. Hence, the average $\varepsilon_{vM}$ decreases with increasing global strain.

In Fig. 6.5(f), the local von Mises strain data from Fig. 6.5(d) is plotted for quantitative estimation of strain partitioning in the microstructure at 9% global strain. The local strain is observed to be distributed with a mean value of 9.2% and a standard deviation value of 6.8 % at 9% global strain. This high standard deviation value (*i.e.* 6.8%) in the local strain distribution quantitatively represents the strong strain partitioning in the CC-CFBS microstructure.

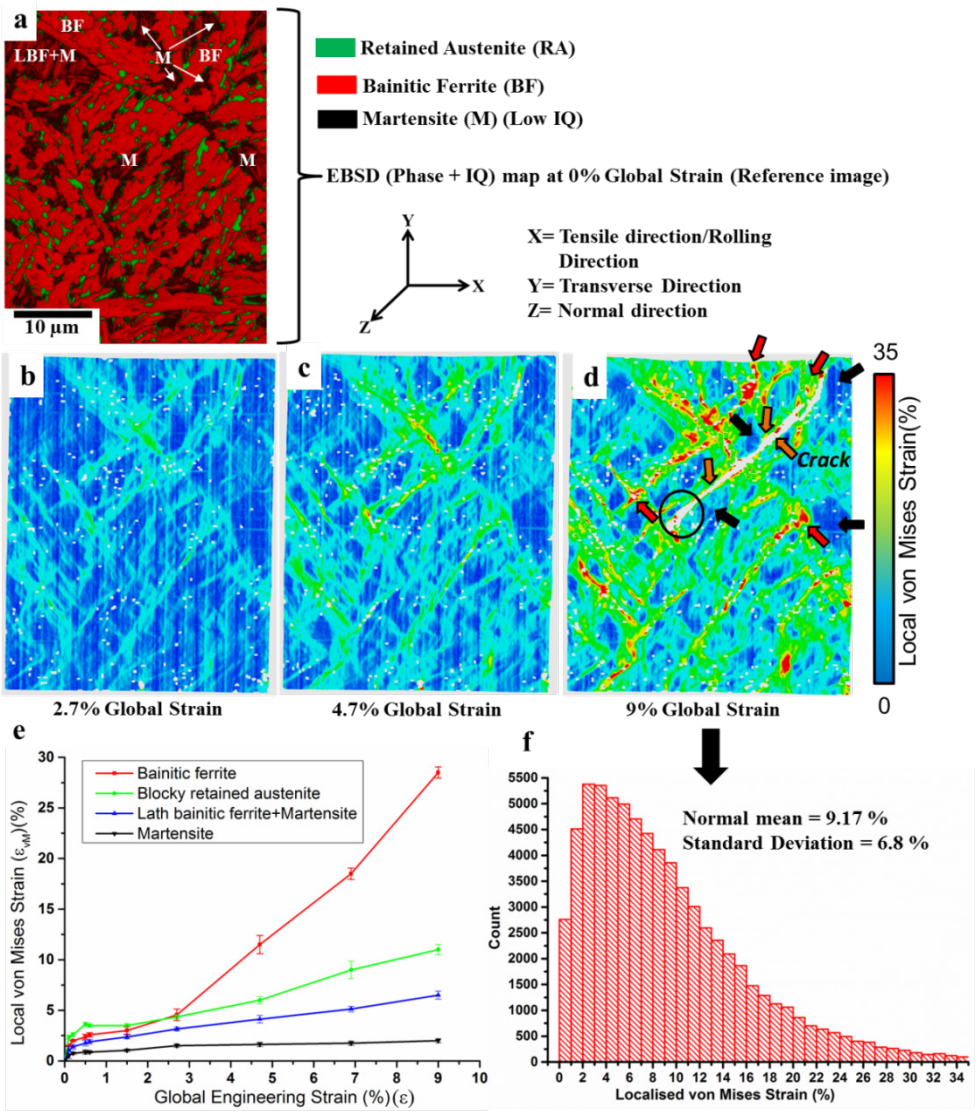


Fig. 6.5. (a) Overlapped EBSD phase and IQ map of reference microstructure of Continuously Cooled Carbide-Free Bainitic Steel at 0% global strain where Bainitic Ferrite (BF), martensite (M) and Lath Bainitic Ferrite with martensite (LBF+M) are marked, (BF shown in red, retained austenite shown in green), (b-d) µ-DIC results showing the local von Mises strain maps at global strain of (b) 2.7%, (c) 4.7%, (d) 9%, (e) average von Mises/equivalent local strain evolution in individual microstructural constituents such as, BF, retained austenite, LBF+M and M, (f) distribution of the local von Mises strain at 9% global strain corresponding to Fig.5(d), showing standard deviation value ≈ 6.8%, which gives a quantitative representation of strong strain partitioning in the CC-CFBS microstructure. (Red arrows show the strain localisation in thin bainitic ferrite channels between the martensitic islands, black arrows show the martensitic islands with minimum local strain and the orange arrows show the damage initiation and crack path evolution in the microstructure).

### *6.3.4 Post damage analysis*

For further understanding of the damage mechanism in CC-CFBS, an additional post damage analysis is performed by SE imaging and EBSD mapping after the fracture of the specimens in μ-DIC testing (Fig. 6.6). The most common damage initiation/void nucleation events are recorded at the narrow bainitic ferrite channels in between martensitic islands (Fig. 6.6(a,b)) and the Bainitic ferrite-Martensite (B/M) interfaces (marked by arrows in Fig. 6.6(b)). Fig. 6.6(c) shows the cleavage fracture of a martensitic island oriented at 45° to the tensile direction because of the high resolved shear stresses. Another kind of damage initiation incident can also be triggered by interface decohesion of the brittle inclusions such as $Al_2O_3$, followed by their fracture, as shown in Fig. 6.6(d). Furthermore, the EBSD analysis in Fig. 6.6(e) detects a void nucleation event at the B/M interface. Fig. 6.6(f) shows the presence of fine austenitic islands (in green) (grain size smaller than 0.25 μm) with blocky and thin film morphology in the EBSD phase map. These islands did not transform into martensite even after specimen fracture. This indicates the higher stability of these ultrafine/nanocrystalline retained austenite islands towards mechanical deformation than of the large blocky retained austenite islands (grain size larger than 0.25 μm).

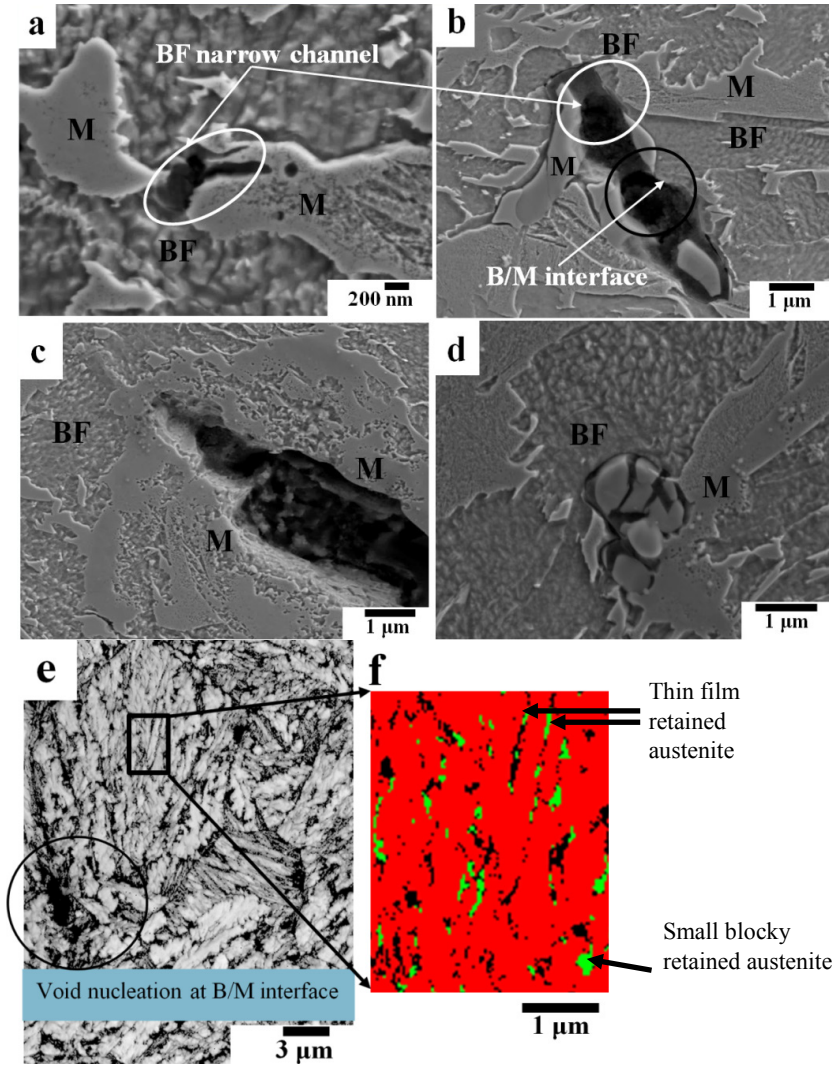


Fig. 6.6. Post mortem investigation to record damage incidents after fracture of specimens in µ-DIC tests: (a,b) damage nucleation in a narrow bainitic ferrite channel in between martensitic islands (shown in white circles), void nucleation at a Bainitic ferrite/Martensite (B/M) interface encircled in black, (c) cleavage fracturing of martensitic islands along 45° to the tensile direction, (d) interface decohesion and breaking of $Al_2O_3$ inclusion, (e) EBSD IQ map taken after specimen fracture showing void nucleation at a B/M interface; (f) magnified EBSD phase map showing the presence of untransformed thin film austenite and small austenitic islands (grain size larger than 0.25 µm) even after specimen fracture.

### *6.3.5 Active damage nucleation and growth mechanisms*

Nucleation and growth of damage in the CC-CFBS microstructure is affected by many factors such as crystallographic orientation, spatial distribution of phases, phase fraction, phase morphology and presence of brittle inclusions etc. (Fig. 6.5 and Fig. 6.6). The strains are predominantly concentrated inside the narrow/thin channels of bainitic ferrite in between large martensitic islands (shown by red arrows in Fig. 6.5(d)), whereas surrounding martensite islands take almost negligible strain at similar global strain values (shown by black arrows in Fig. 6.5(d)). This phenomenon is separately shown in Fig. 6.7(b) where the smaller bainitic ferrite channels (width smaller than 5 μm) can have average local strain concentration of 30.4 ± 1.6 % at 9% global strain. However, these strain values decrease to 20.5 ± 1.0% for BF channel above 5 μm width. Thus, the high strain incompatibility between martensite and thin BF islands, due to a large difference in their mechanical properties, forces the bainitic channels to accommodate large strain and thus provides potential sites for damage nucleation. These damage sites can grow to form a crack at large global strain values and the crack may follow the other damage sites in the vicinity. Hence, the spatial distribution of the bainitic ferrite and martensite islands is one of the important factors influencing the damage nucleation in CC-CFBS.

Another parameter which is investigated and discussed here is the inclination of bainitic ferrite/bainitic ferrite (BF/BF) boundaries to the tensile direction, which can play an important role for the mechanical response and the corresponding damage phenomenon [52,53]. The average von Mises local strain at the BF/BF phase boundaries is plotted with respect to their inclination angle (0°, 45°, and 90°) to the tensile direction in Fig. 6.7 (a). The boundaries of bainitic ferrite which are inclined at an angle of 45° to the tensile loading direction show large strain concentration (28 ± 4% at 9% global strain) because of the highest critical resolved shear stress. However, the localised strain values are minimum at the BF/BF boundaries with 0° angle to the tensile direction. A magnified region (EBSD map + local strain map) of almost 45° inclined BF/BF boundary is also shown with high local strain concentration (25-35%) at 9% global strain in Fig. 6.7(a). Yan *et al.* [36] showed a similar response of the ferrite/ferrite boundaries in DP steels and explained it as a ductility enhancing phenomenon in DP steels. Fig. 6.7(c) shows high concentration of average local strains (≈ 21 ± 3%) at the M/BF interfaces, which are also the potential sites for damage nucleation. A magnified region (EBSD map + local strain map) of M/BF interface is also shown with high local strain concentration (20-25%) at 9% global strain in Fig. 6.7(c). These interfaces can provide an easier path for crack growth because of high strain concentration and strain incompatibility between bainitic ferrite and martensite. Furthermore, M/BF interfaces when inclined close to 45° to the loading direction will increase both strain incompatibility and strain concentration due to high shear stresses along them.

The abovementioned mechanism of crack growth along M/BF interfaces is observed in the present study in Fig. 6.5(d). The crack originated during the *in-situ* experiments is observed to follow the phase boundaries of the martensite islands (shown by top three black arrows in Fig. 6.5(d)), which are inclined close to 45° to the tensile direction. So, there are two main factors playing a role in this crack growth phenomenon:

1. Strain incompatibility and strain accumulation at the bainitic ferrite and martensite interfaces because of large difference in their mechanical response.
2. Inclination of the martensite and bainitic ferrite interfaces to the tensile direction.

Sometimes cracks can also be seen to grow by cleavage fracturing of the martensitic islands because of their brittle nature and high stress concentration ahead of the crack tip, as shown in Fig. 6.5(d) (encircled) and Fig. 6.6(c).

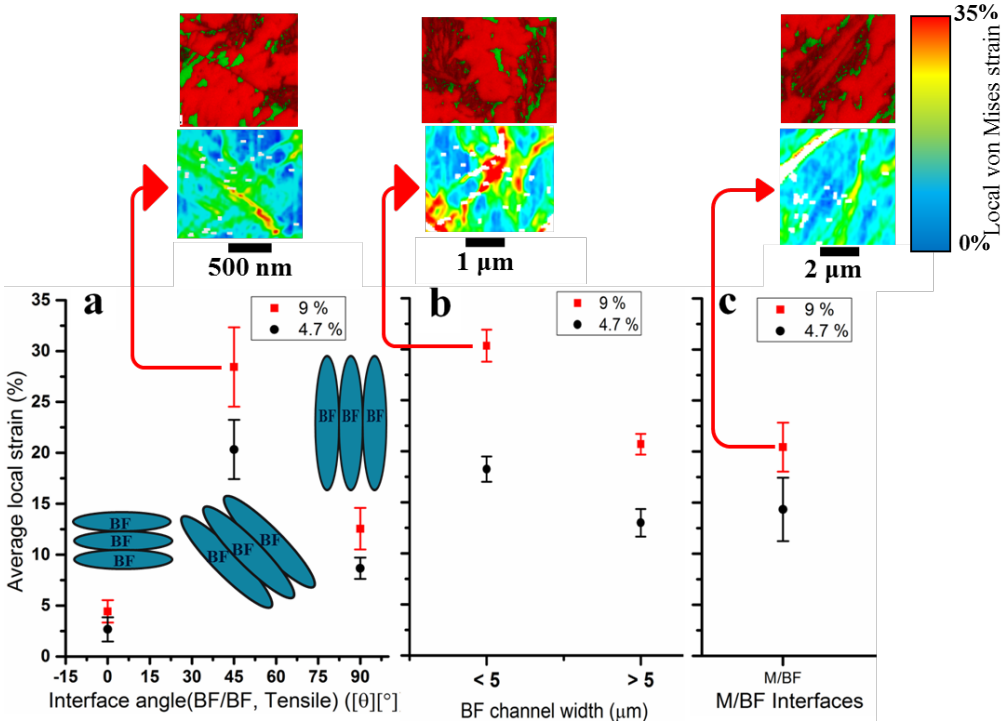


Fig. 6.7. Plot of average local strain with, (a) angle of BF/BF interface with tensile direction (0°, 45°, and 90°); (b) Bainitic Ferrite (BF) channel width below and above 5 µm; (c) Martensite/Bainitic Ferrite (M/BF) interfaces, at the fixed global strain of 4.7% and 9%. (Features with high local strain accumulation such as BF/BF interface at an angle of ≈ 45° to the tensile direction, BF islands below 5 µm width and M/BF interface are also shown with magnified EBSD (phase + IQ ) map and corresponding local strain maps at 9% global strain)

### *6.3.6 Mechanical stability of retained austenite and effect on damage*

Mechanical stability of the retained austenite in bainitic steels has been a long-standing point of debate. The stability of the retained austenite is governed by many parameters such as its morphology, size, composition and local variation in carbon composition [42,47,54–57]. The stability of blocky retained austenite also depends strongly on its crystallographic orientation [42,54–56]. De Knijf *et al.* [55] showed that the austenite grains with different crystallographic orientation with respect to tensile loading direction in quenching and partitioning steels have different martensite transformation potential. Blondé *et al.* [58] showed that the retained austenite grains oriented with the {200} plane along the tensile direction transform most easily into martensite as these are exposed to the highest resolved shear stress. Thus, all abovementioned parameters need to be taken into account when discussing the stability of retained austenite. There are two typical morphologies of retained austenite in bainite termed as blocky retained austenite and thin film retained austenite. Thin film retained austenite is considered mechanically more stable against transformation than the blocky retained austenite [59–61]. The better mechanical stability of thin film retained austenite in comparison to the blocky one in the case of bainitic steel can be well explained by its higher carbon enrichment and uniformity of carbon distribution [51,62]. Furthermore, the growth of the surrounding bainitic islands during displacive transformation leads to formation of defects such as twins, stacking faults and dislocations in thin film retained austenite [61]. This makes thin film retained austenite mechanically more stable as the dislocation motion on application of external stress will be more difficult in the presence of such defects [15,50,51,63]. We observe that the stability of blocky retained austenite stability is also governed by its grain size. Results shown in Fig. 6.6(f) indicate that the ultrafine islands of blocky retained austenite (grain size smaller than 0.25 μm) are found to be stable even after specimen fracture. This can be attributed to high carbon enrichment due to their formation at the last stage of bainitic transformation and plastic accommodation due to bainitic growth during displacive bainitic transformation. Therefore, in order to design new damage tolerant bainitic steels, it is suggested to engineer a microstructure containing retained austenite with small size and thin film morphology. This will provide good damage resistance and strength without compromising the ductility.

The damage and strain partitioning in CC-CFBS is strongly affected by the size, nature, and morphological distribution of the retained austenite. The large blocky retained austenite undergoes strain-induced transformation into martensite even at lower strain values of approximately 2-3% strain. This is the reason of blocky retained austenite taking substantially more strain at the earlier part of straining during *in-situ* testing (Fig. 6.5(e)). Furthermore, as the blocky retained austenite gradually transforms into martensite, the overall effective martensite content in the microstructure increases. Thus, the large blocky retained austenite adds to the fraction of brittle martensite at high global strain values. This also changes the overall spatial distribution of martensite in the microstructure with increased fraction of martensite and M/BF interfaces. These newly formed martensitic

regions will also introduce large strain partitioning/strain incompatibility in the microstructure under mechanical deformation, together with former martensitic regions. This will provide a larger density of weak links for damage nucleation and growth in the microstructure of CC-CFBS.

## 6.4 Conclusions

Following conclusions can be made based on the current study:

1. *In-situ* μ-DIC experiments demonstrate that CC-CFBS shows strong strain partitioning among its microstructural constituents, where for instance local strains in the microstructure are distributed with a standard deviation around 6.8% at 9% global strain.
2. Strain partitioning, damage nucleation and growth in CC-CFBS is affected by various microstructural features such as martensite, bainitic ferrite and blocky/thin film austenite), their fractions, spatial distribution, morphology, grain size and inclination of the interfaces with respect to loading direction (M/BF interfaces and BF/BF interfaces).
3. Narrow bainitic ferrite channels in between martensitic islands dominantly accommodate large strain and act as primary damage nucleation sites in CC-CFBS.
4. Martensite islands accommodate negligible von Mises local strain even at high global stain values during *in-situ* tensile testing, causing strong strain partitioning among bainitic ferrite and martensite. This in turns leads to large strain incompatibility among bainitic ferrite and martensite, especially at the phase boundaries.
5. Martensite/Bainitic ferrite phase boundaries provide easy pathways for crack growth when oriented along the direction of maximum resolved shear stresses (*i.e.* 45° to the tensile deformation)
6. Local strain concentration along 45° to the tensile direction also confirms the role of critical resolved shear stresses on strain partitioning. The BF/BF interfaces inclined at 45° to the tensile direction accommodates large local strains verifying the role of phase boundary orientations on the strain partitioning.
7. Large blocky retained austenite undergoes strain-induced transformation into martensite upon loading, which increases the overall martensitic fraction and density of M/BF interfaces in the microstructure. This increases the strain partitioning and incompatibility in the microstructure providing additional weak links for damage nucleation/growth in the microstructure.

8. Thin film and ultrafine retained austenite (size < 250 nm) are mechanically more stable than large blocky retained austenite in CC-CFBS and found to be present in the microstructure even after fracture.

## References


[1] H.K.D.H. Bhadeshia, J.W. Christian, Bainite in steels, Metall. Trans. A. 21 (1990) 767–797.

[2] H.K.D.H. Bhadeshia, High performance bainitic steels, in: Mater. Sci. Forum, Trans Tech Publ, 2005: pp. 63–74.

[3] J. Wu, R.H. Petrov, M. Naeimi, Z. Li, R. Dollevoet, J. Sietsma, Laboratory simulation of martensite formation of white etching layer in rail steel, Int. J. Fatigue. 91 (2016) 11–20. doi:10.1016/J.IJFATIGUE.2016.05.016.

[4] J. Wu, R.H. Petrov, S. Kölling, P. Koenraad, L. Malet, S. Godet, J. Sietsma, Micro and Nanoscale Characterization of Complex Multilayer-Structured White Etching Layer in Rails, Met. . 8 (2018). doi:10.3390/met8100749.

[5] S. Li, J. Wu, R.H. Petrov, Z. Li, R. Dollevoet, J. Sietsma, "Brown etching layer": A possible new insight into the crack initiation of rolling contact fatigue in rail steels?, Eng. Fail. Anal. 66 (2016) 8–18. doi:10.1016/J.ENGFAILANAL.2016.03.019.

[6] A. Kumar, G. Agarwal, R. Petrov, S. Goto, J. Sietsma, M. Herbig, Microstructural evolution of white and brown etching layers in pearlitic rail steels, Acta Mater. (n.d.) Submitted for publication.

[7] H.W. Zhang, S. Ohsaki, S. Mitao, M. Ohnuma, K. Hono, Microstructural investigation of white etching layer on pearlite steel rail, Mater. Sci. Eng. A. 421 (2006) 191–199. doi:10.1016/J.MSEA.2006.01.033.

[8] A. Pyzalla, L. Wang, E. Wild, T. Wroblewski, Changes in microstructure, texture and residual stresses on the surface of a rail resulting from friction and wear, Wear. 251 (2001) 901–907. doi:10.1016/S0043-1648(01)00748-7.

[9] W. Österle, H. Rooch, A. Pyzalla, L. Wang, Investigation of white etching layers on rails by optical microscopy, electron microscopy, X-ray and synchrotron X-ray diffraction, Mater. Sci. Eng. A. 303 (2001) 150–157. doi:10.1016/S0921-5093(00)01842-6.

[10] G. Baumann, H.J. Fecht, S. Liebelt, Formation of white-etching layers on rail treads, Wear. 191 (1996) 133–140. doi:10.1016/0043-1648(95)06733-7.

[11] J. Takahashi, K. Kawakami, M. Ueda, Atom probe tomography analysis of the white etching layer in a rail track surface, Acta Mater. 58 (2010) 3602–3612. doi:10.1016/J.ACTAMAT.2010.02.030.

[12] N. Jin, P. Clayton, Effect of microstructure on rolling/sliding wear of low carbon bainitic steels, Wear. 202 (1997) 202–207. doi:10.1016/S0043-1648(96)07271-7.

[13] M. Steenbergen, R. Dollevoet, On the mechanism of squat formation on train rails – Part I: Origination, Int. J. Fatigue. 47 (2013) 361–372. doi:10.1016/J.IJFATIGUE.2012.04.023.

[14] M. Steenbergen, R. Dollevoet, On the mechanism of squat formation on train rails – Part II: Growth, Int. J. Fatigue. 47 (2013) 373–381. doi:10.1016/J.IJFATIGUE.2012.04.019.

[15] F.G. Caballero, H.K.D.H. Bhadeshia, Very strong bainite, Curr. Opin. Solid State Mater. Sci. 8 (2004) 251–257.

[16] A.P. Patra, P. Söderholm, U. Kumar, Uncertainty estimation in railway track life-cycle cost: a case study from Swedish National Rail Administration, Proc. Inst. Mech. Eng. Part F J. Rail Rapid Transit. 223 (2008) 285–293. doi:10.1243/09544097JRRT235.

[17] F.G. Caballero, S. Allain, J. Cornide, J.D. Puerta Velásquez, C. Garcia-Mateo, M.K. Miller, Design of cold rolled and continuous annealed carbide-free bainitic steels for automotive application, Mater. Des. 49 (2013) 667–680. doi:10.1016/J.MATDES.2013.02.046.

[18] H.K.D.H. Bhadeshia, D. V Edmonds, The bainite transformation in a silicon steel, Metall. Trans. A. 10 (1979) 895–907. doi:10.1007/BF02658309.

[19] L. Qian, Q. Zhou, F. Zhang, J. Meng, M. Zhang, Y. Tian, Microstructure and mechanical properties of a low carbon carbide-free bainitic steel co-alloyed with Al and Si, Mater. Des. 39 (2012) 264–268. doi:10.1016/j.matdes.2012.02.053.

[20] K.M. Lee, A.A. Polycarpou, Wear of conventional pearlitic and improved bainitic rail steels, Wear. 259 (2005) 391–399. doi:10.1016/J.WEAR.2005.02.058.

[21] S. Das Bakshi, A. Leiro, B. Prakash, H. Bhadeshia, Dry rolling/sliding wear of nanostructured bainite, Wear. 316 (2014) 70–78.

[22] H.A. Aglan, Z.Y. Liu, M.F. Hassan, M. Fateh, Mechanical and fracture behavior of bainitic rail steel, J. Mater. Process. Technol. 151 (2004) 268–274.

[23] Q. Zhou, L. Qian, J. Meng, L. Zhao, F. Zhang, Low-cycle fatigue behavior and

microstructural evolution in a low-carbon carbide-free bainitic steel, Mater. Des. 85 (2015) 487–496. doi:10.1016/j.matdes.2015.06.172.

[24] X.Y. Long, J. Kang, B. Lv, F.C. Zhang, Carbide-free bainite in medium carbon steel, Mater. Des. 64 (2014) 237–245. doi:10.1016/j.matdes.2014.07.055.

[25] A. Leiro, E. Vuorinen, K.-G. Sundin, B. Prakash, T. Sourmail, V. Smanio, F.G. Caballero, C. Garcia-Mateo, R. Elvira, Wear of nano-structured carbide-free bainitic steels under dry rolling–sliding conditions, Wear. 298 (2013) 42–47.

[26] L.C. Chang, The rolling/sliding wear performance of high silicon carbide-free bainitic steels, Wear. 258 (2005) 730–743.

[27] H.K.D.H. Bhadeshia, C. Garcia-Mateo, P. Brown, Bainite steel and methods of manufacture thereof, (2015).

[28] F.G. Caballero, M.J. Santofimia, C. Capdevila, C. García-Mateo, C.G. de Andrés, Design of advanced bainitic steels by optimisation of TTT diagrams and T0 curves, ISIJ Int. 46 (2006) 1479–1488.

[29] E. Kozeschnik, H. Bhadeshia, Influence of silicon on cementite precipitation in steels, Mater. Sci. Technol. 24 (2008) 343–347.

[30] T. Sourmail, F.G. Caballero, C. García-Mateo, V. Smanio, C. Ziegler, M. Kuntz, R. Elvira, A. Leiro, E. Vuorinen, T. Teeri, Evaluation of potential of high Si high C steel nanostructured bainite for wear and fatigue applications, Mater. Sci. Technol. 29 (2013) 1166–1173.

[31] F.G. Caballero, M.J. Santofimia, C. García-Mateo, J. Chao, C.G. de Andrés, Theoretical design and advanced microstructure in super high strength steels, Mater. Des. 30 (2009) 2077–2083.

[32] F.G. Caballero, H. Bhadeshia, K.J.A. Mawella, D.G. Jones, P. Brown, Design of novel high strength bainitic steels: Part 1, Mater. Sci. Technol. 17 (2001) 512–516.

[33] G. Avramovic-Cingara, Y. Ososkov, M.K. Jain, D.S. Wilkinson, Effect of martensite distribution on damage behaviour in DP600 dual phase steels, Mater. Sci. Eng. A. 516 (2009) 7–16.

[34] J. Kang, Y. Ososkov, J.D. Embury, D.S. Wilkinson, Digital image correlation studies for microscopic strain distribution and damage in dual phase steels, Scr. Mater. 56 (2007) 999–1002.

[35] C.C. Tasan, J.P.M. Hoefnagels, M. Diehl, D. Yan, F. Roters, D. Raabe, Strain localization and damage in dual phase steels investigated by coupled in-situ

deformation experiments and crystal plasticity simulations, Int. J. Plast. 63 (2014) 198–210.

[36] D. Yan, C.C. Tasan, D. Raabe, High resolution in situ mapping of microstrain and microstructure evolution reveals damage resistance criteria in dual phase steels, Acta Mater. 96 (2015) 399–409.

[37] C.C. Tasan, M. Diehl, D. Yan, C. Zambaldi, P. Shanthraj, F. Roters, D. Raabe, Integrated experimental–simulation analysis of stress and strain partitioning in multiphase alloys, Acta Mater. 81 (2014) 386–400.

[38] C.C. Tasan, J.P.M. Hoefnagels, M.G.D. Geers, Identification of the continuum damage parameter: An experimental challenge in modeling damage evolution, Acta Mater. 60 (2012) 3581–3589.

[39] J.P.M. Hoefnagels, C.C. Tasan, F. Maresca, F.J. Peters, V.G. Kouznetsova, Retardation of plastic instability via damage-enabled microstrain delocalization, J. Mater. Sci. 50 (2015) 6882–6897.

[40] C.C. Tasan, M. Diehl, D. Yan, M. Bechtold, F. Roters, L. Schemmann, C. Zheng, N. Peranio, D. Ponge, M. Koyama, An overview of dual-phase steels: advances in microstructure-oriented processing and micromechanically guided design, Annu. Rev. Mater. Res. 45 (2015) 391–431.

[41] J. Wu, P.J. Wray, C.I. Garcia, M. Hua, A.J. DeArdo, Image quality analysis: A new method of characterizing microstructures, ISIJ Int. 45 (2005) 254–262.

[42] R. Petrov, L. Kestens, A. Wasilkowska, Y. Houbaert, Microstructure and texture of a lightly deformed TRIP-assisted steel characterized by means of the EBSD technique, Mater. Sci. Eng. A. 447 (2007) 285–297.

[43] L. Zhao, N.. van Dijk, E. Brück, J. Sietsma, S. van der Zwaag, Magnetic and X-ray diffraction measurements for the determination of retained austenite in TRIP steels, Mater. Sci. Eng. A. 313 (2001) 145–152. doi:10.1016/S0921-5093(01)00965-0.

[44] C.F. Jatczak, Retained Austenite and its Measurement by X-ray Diffraction, SAE Trans. (1980) 1657–1676.

[45] J.M. Hyzak, I.M. Bernstein, The role of microstructure on the strength and toughness of fully pearlitic steels, Metall. Trans. A. 7 (1976) 1217–1224.

[46] A.J. Schwartz, M. Kumar, B.L. Adams, D.P. Field, Electron backscatter diffraction in materials science, Springer, 2000.

[47] D. De Knijf, R. Petrov, C. Föjer, L.A.I. Kestens, Effect of fresh martensite on the

stability of retained austenite in quenching and partitioning steel, Mater. Sci. Eng. A. 615 (2014) 107–115.

[48] F. Ram, S. Zaefferer, D. Raabe, Kikuchi bandlet method for the accurate deconvolution and localization of Kikuchi bands in Kikuchi diffraction patterns, J. Appl. Crystallogr. 47 (2014) 264–275. https://doi.org/10.1107/S1600576713030446.

[49] S.I. Wright, M.M. Nowell, EBSD Image Quality Mapping, Microsc. Microanal. 12 (2006) 72–84. doi:10.1017/S1431927606060090.

[50] Z.J. Xie, Y.Q. Ren, W.H. Zhou, J.R. Yang, C.J. Shang, R.D.K. Misra, Stability of retained austenite in multi-phase microstructure during austempering and its effect on the ductility of a low carbon steel, Mater. Sci. Eng. A. 603 (2014) 69–75.

[51] C. Garcia-Mateo, F.G. Caballero, J. Chao, C. Capdevila, C.G. De Andres, Mechanical stability of retained austenite during plastic deformation of super high strength carbide free bainitic steels, J. Mater. Sci. 44 (2009) 4617–4624.

[52] F. Roters, P. Eisenlohr, L. Hantcherli, D.D. Tjahjanto, T.R. Bieler, D. Raabe, Overview of constitutive laws, kinematics, homogenization and multiscale methods in crystal plasticity finite-element modeling: Theory, experiments, applications, Acta Mater. 58 (2010) 1152–1211.

[53] T.R. Bieler, P. Eisenlohr, F. Roters, D. Kumar, D.E. Mason, M.A. Crimp, D. Raabe, The role of heterogeneous deformation on damage nucleation at grain boundaries in single phase metals, Int. J. Plast. 25 (2009) 1655–1683.

[54] L. Kestens, R. Petrov, Y. Houbaert, Orientation selective martensite transformation in an Fe-28Ni alloy, ISIJ Int. 43 (2003) 1444–1452.

[55] D. De Knijf, T. Nguyen-Minh, R.H. Petrov, L.A.I. Kestens, J.J. Jonas, Orientation dependence of the martensite transformation in a quenched and partitioned steel subjected to uniaxial tension, J. Appl. Crystallogr. 47 (2014) 1261–1266.

[56] D. De Knijf, C. Föjer, L.A.I. Kestens, R. Petrov, Factors influencing the austenite stability during tensile testing of Quenching and Partitioning steel determined via in-situ Electron Backscatter Diffraction, Mater. Sci. Eng. A. 638 (2015) 219–227.

[57] K.S. Choi, Z. Zhu, X. Sun, E. De Moor, M.D. Taylor, J.G. Speer, D.K. Matlock, Determination of carbon distributions in quenched and partitioned microstructures using nanoscale secondary ion mass spectroscopy, Scr. Mater. 104 (2015) 79–82.

[58] R. Blondé, E. Jimenez-Melero, L. Zhao, J.P. Wright, E. Brück, S. Van der Zwaag, N.H. Van Dijk, High-energy X-ray diffraction study on the temperature-dependent mechanical stability of retained austenite in low-alloyed TRIP steels, Acta Mater. 60

(2012) 565–577.

[59] S. Chatterjee, H.-S. Wang, J.R. Yang, H. Bhadeshia, Mechanical stabilisation of austenite, Mater. Sci. Technol. 22 (2006) 641–644.

[60] H.K.D.H. Bhadeshia, D. V Edmonds, Bainite in silicon steels: new composition–property approach Part 1, Met. Sci. 17 (1983) 411–419. doi:10.1179/030634583790420600.

[61] F.G. Caballero, H.-W. Yen, M.K. Miller, J.-R. Yang, J. Cornide, C. Garcia-Mateo, Complementary use of transmission electron microscopy and atom probe tomography for the examination of plastic accommodation in nanocrystalline bainitic steels, Acta Mater. 59 (2011) 6117–6123. doi:10.1016/J.ACTAMAT.2011.06.024.

[62] F.G. Caballero, M.K. Miller, A.J. Clarke, C. Garcia-Mateo, Examination of carbon partitioning into austenite during tempering of bainite, Scr. Mater. 63 (2010) 442–445. doi:10.1016/J.SCRIPTAMAT.2010.04.049.

[63] X.C. Xiong, B. Chen, M.X. Huang, J.F. Wang, L. Wang, The effect of morphology on the stability of retained austenite in a quenched and partitioned steel, Scr. Mater. 68 (2013) 321–324. doi:10.1016/J.SCRIPTAMAT.2012.11.003.

# 7

# Design of high-strength and damage-resistant carbide-free fine bainitic steels for railway crossing applications***


## Abstract

High strength steels, with fine bainitic microstructure free from inter-lath carbides, are designed for railway crossings applications. The steel design is based on the phase transformation theory and avoids microstructural constituents like martensite, cementite and large blocky retained austenite islands in the microstructure which are considered to be responsible for strain partitioning and damage initiation. The designed steel consists of fine bainitic ferrite, thin film austenite and a minor fraction of blocky austenite which contribute to its high strength, appreciable toughness and damage resistance. Atom probe tomography and dilatometry results are used to study the deviation of carbon partitioning in retained austenite and bainitic ferrite fractions from the $T_0/T_0^{'}$ predictions. A high carbon concentration of 7.9 at.% (1.8 wt.%) was measured in thin film austenite, which governs its mechanical stability. Various strengthening mechanisms such as effect of grain size, nano-sized cementite precipitation and Cottrell atmosphere at dislocations within bainitic ferrite are discussed. Mechanical properties of the designed steel are found to be superior to those of conventional steels used in railway crossings. The designed steel also offers controlled crack growth under the impact fatigue, which is the main cause of failure in crossings. *In-situ* testing using micro digital image correlation is carried out to study the micromechanical response of the designed microstructure. The results show uniform strain


*** This chapter is based on the article: A. Kumar, S. K. Makineni, A. Dutta, C. Goulas, M. Steenbergen, R. Petrov, and J. Sietsma, Design of a high strength and damage resistant carbide-free fine bainitic steels for railway crossings applications, Mat. Sci. & Eng. A, (2019), 759, 210-223, https://doi.org/10.1016/j.msea.2019.05.043.

distribution with low standard deviation of 1.5% from the mean local strain value of 7.7% at 8% global strain.

## 7.1 Introduction

Railway crossings are subjected to severe impact fatigue and wear during service. This leads to formation of various surface and subsurface defects, which can lead to failure of the crossings. This poses safety concerns, disruption in the proper transport flow, and high maintenance cost for the rail industries. Conventional pearlitic steels, which are commonly used for railway crossings, contain cementite laths which are considered to be disadvantageous for their fatigue life [1]. Presence of cementite, despite offering good strength and wear resistance to the steel microstructure, imposes strain incompatibility between soft ferrite and hard cementite [2]. This often results in breaking and shear bending of cementite laths under mechanical deformation during severe wheel-rail contact conditions [3,4]. Furthermore, cracks typically initiate at the ferrite-cementite interfaces and propagate along them [5]. Due to mechanical deformation and temperature rise during wheel-rail contact, the cementite dissolves due to the C diffusion into the dislocations in ferrite. Additionally, the cementite dissolves into the forming austenite in the microstructure at temperatures in the austenite range. Austenite formation and the consequent cementite dissolution cause the formation of detrimental white and brown etching layers, which are known to facilitate crack initiation and propagation in rails [4,6–13].

As far as railway crossings are concerned, due to the drawbacks of the conventional pearlitic steels, their performance is far from optimal. The extreme loading conditions in service, leading to impact fatigue and wear, impose the necessity to develop and use stronger and tougher steels. This requirement seemed to be fulfilled in rail industries by the use of the continuously-cooled, carbide-free bainitic steels. In these grades, the high silicon content of 1.3 wt.% suppresses the formation of brittle cementite from austenite during bainitic transformation [14]. Silicon exhibits very low solubility in cementite and retards it's growth from austenite during bainite formation. But the presence of martensite and blocky retained austenite in these steels causes strong strain partitioning among the microstructural constituents, which leads to crack initiation and propagation [15]. Strain-induced phase transformation of large blocky retained austenite islands at low strain values (≈ 3%) increases the cumulative fraction of martensite, providing sites such as martensite-bainitic ferrite interfaces which are prone to crack initiation and propagation [15].

In order to overcome the above-mentioned issues, carbide-free fine bainitic steels with high strength, damage resistance and appreciable toughness are designed for railway crossings application. The design strategy involves phase transformation theory and considers the design requirements with respect to the extreme loading conditions in railway crossings.

The term carbide-free in this chapter refers to the absence of cementite in between bainitic ferrite laths (inter-lath cementite). Hard and brittle phases such as martensite and cementite, which lead to strain partitioning under loading, are excluded from the designed microstructure by using the present design strategy. Similarly, mechanically unstable large blocky retained austenite islands (equivalent grain size > 2 μm), which transforms into martensite at low strain values, are also excluded in the steel design [15]. The fraction of blocky austenite in the microstructure is largely suppressed by selecting specific chemical composition of the steel and low isothermal transformation temperature to maximize the bainite fraction. During isothermal transformation, the large blocks of austenite transform to bainitic ferrite and thin film austenite. Thus, we achieved a steel microstructure either with thin film morphology or small austenite blocks which are considered to be mechanically stable. Thin austenite films between bainitic laths are more stable than large blocky austenite because of higher C concentration and transformation constraints exerted by the surrounding ferrite [14,16]. However, this stability of austenite laths is also affected by their crystallographic orientation with respect to the loading direction and orientation of the constraining phases surrounding them [17–19]. The microstructure of the designed steel is characterised using optical microscopy, scanning electron microscopy, electron backscatter diffraction, transmission electron microscopy and atom probe tomography. Furthermore, the displacive bainitic transformation mechanism and the variation of $T_0/T_0'$ theory from experimental observations are discussed using dilatometry data and characterization methods such as TEM and APT. The designed steel is tested under the static and dynamic loading conditions and its performance is compared with the conventional rail steels. The mechanical performance of the designed steel is correlated with its microstructural constituents such as grain size, nano-sized cementite precipitation within bainitic ferrite and Cottrell atmosphere at dislocations in bainitic ferrite. Additionally, *In-situ* micro digital image correlation experiments are carried out to study the micromechanical and damage response of the designed microstructure.

## 7.2 Material design aspects for complex loading in rail crossings

Railway crossings are subjected to complex loading conditions because of repetitive high impact, rolling contact fatigue and wear caused by rail-wheel transition from wing rail to crossing nose (Fig. 7.1 (a)). This leads to various defects such as shelling, lipping, squats, spalling etc. on the crossing nose during service. Fig. 7.1(b-d) show such defects observed on a crossing nose. Shelling and lipping are most commonly associated with localized plastic deformation at the point of impact (Fig. 7.1(b,c)). This increases the intensity of the next impacts and eventually causes failure in the crossing nose. Spalling is due to subsurface crack initiation under rolling contact fatigue, which leads to material removal when the crack propagates towards the crossing surface (Fig. 7.1(d)). Localized plastic deformation on the crossing nose can be well prevented by designing steels with high

resistance to plastic deformation, determined by yield strength. In addition, the toughness is also an important property for sustainable material design.

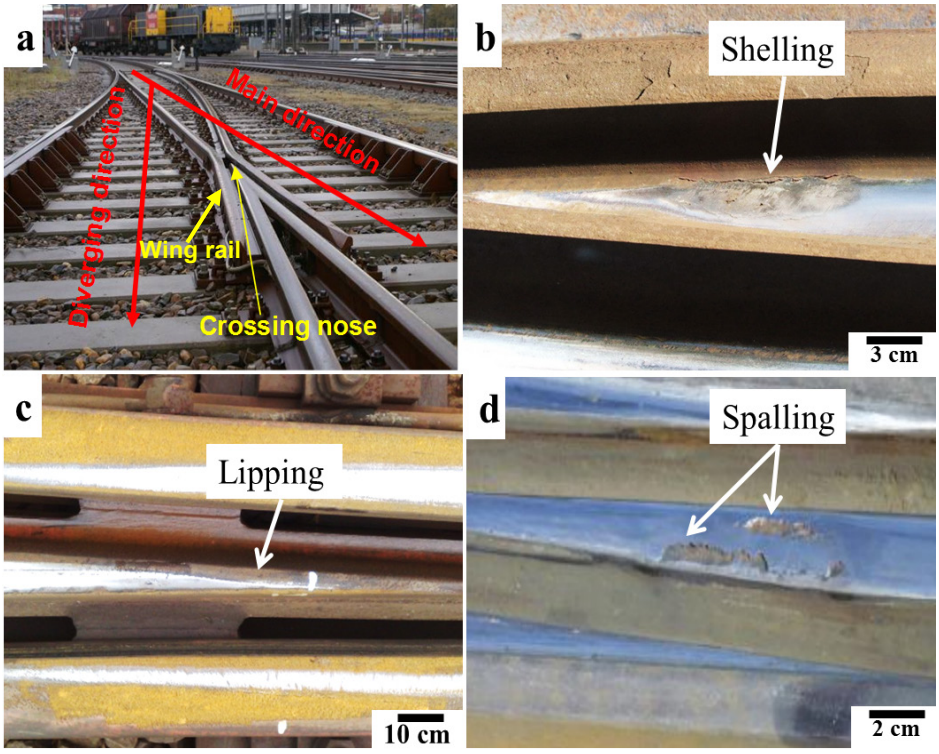


Fig. 7.1. (a) Image of railway crossing, (b-d) Common defects in railway crossing nose such as (b) shelling, (c) lipping and (d) spalling.

In order to explain the concept of material design for the crossing application, von Mises stress theory/distortion energy theory can be applied. The theory enables the simple uniaxial testing results to be transferred into complex loading conditions. For implementing this concept in crossings, the maximum distortion energy in the material system during loading in crossings ($U_d^c$) should not exceed the distortion energy stored by the material under uniaxial tension ($U_d^u$) in order to avoid failure. This can be expressed as:

$$U_d^c < U_d^u \tag{7.1}$$

where distortion energy ($U_d$) can be expressed as follows:

$$U_d = \frac{1+\nu}{3E}\left[\frac{(\sigma_1-\sigma_2)^2+(\sigma_2-\sigma_3)^2+(\sigma_3-\sigma_1)^2}{2}\right] \tag{7.2}$$

where $\sigma_1$, $\sigma_2$ and $\sigma_3$ are the principal stresses, $v$ is the Poisson's ratio and $E$ is the elastic modulus. During uniaxial tensile testing, the distortion energy at yielding will be

$$U_d^u = \frac{1+v}{3E}\left(\sigma_y\right)^2 \tag{7.3}$$

where $\sigma_y$ is the yield strength of the material during uniaxial tensile testing. Substituting Eq. 7.2 and Eq. 7.3 into Eq. 7.1 yields

$$\left[\frac{(\sigma_1-\sigma_2)^2+(\sigma_2-\sigma_3)^2+(\sigma_3-\sigma_1)^2}{2}\right]^{1/2} < \sigma_y \tag{7.4}$$

The left-hand expression in Eq. 7.4 represents the von Mises stresses (in which $\sigma_1, \sigma_2, \sigma_3$ concern the loading in crossing) which should be less than the yield strength of the material to avoid defects associated with localized plastic deformation.

Numerous studies have been conducted to understand the cyclic deformation of rail crossings using three-dimensional finite element simulations. However, the results differ significantly in terms of the maximum von Mises stresses in the crossing nose due to complex loading conditions. Xin *et al.* [20,21] in their three-dimensional finite element model using an elastic-plastic kinematic hardening approach show that the maximum von Mises stresses at the crossing nose can vary from 707 to 1085 MPa. These results are consistent with a similar study conducted by Xiao et al. in which the maximum von Mises stress at crossing nose is 936 MPa. However, these values of maximum von Mises stresses can further increase significantly with higher train velocity and axle load [22,23].

Conventional steels such as pearlitic steel and continuously cooled bainitic steels have lower yield strength than the equivalent von Mises stresses in the crossing nose. This is why it is required to design suitable bainitic steels with high yield strength, toughness and strain hardening capability.

## 7.3 Design strategy from thermodynamics and microstructural point of view

The alloy design strategy for carbide (inter-lath carbide) free bainitic steels here is primarily based on avoiding the incomplete formation of bainitic ferrite while also suppressing cementite precipitation. Additionally, from industrial point of view, it is needed to have fast bainitic transformation kinetics for rapidly achieving high fractions of bainite. Bainitic transformation is proposed to be governed by displacive and diffusionless growth of bainitic sub-units with nucleation via thermally-activated migration of pre-existing dislocations [24]. Then excess C partitions from bainitic ferrite to the residual austenite after the bainitic growth is complete. Bainitic transformation in steels can be explained by

the $T_0$ curve, which is defined by the temperature at which bainitic ferrite and austenite of the same chemical composition have the same free energy (Fig. 7.2(a)). Modifications in $T_0$ theory are done by introducing $T_0'$, where the stored energy in ferrite due to displacive transformation has been taken into account [16,25]. According to diffusionless transformation theory, bainitic transformation cannot proceed at a temperature below $T_0'$ curve because the C content in the retained austenite higher than the value given by $T_0'$ curve does not allow the growth of new bainitic ferrite laths [24,26,27]. This explains the incomplete bainite transformation in carbide-free bainitic steels and hence provides suitable guidelines for the alloy design. The maximum volume fraction of bainitic ferrite ($V_{\alpha b}$) can be calculated based on $T_0'$ by applying a simple lever rule equation (Fig. 7.2(b)), according to which

$$V_{\alpha b} = \frac{X_{T_0'} - X_{avg}}{X_{T_0'} - X_{\alpha}} \tag{7.5}$$

where $X_{T_0'}$ is the C concentration in retained austenite according to the $T_0'$ curve at the relevant temperature, $X_{avg}$ is the average C in the alloy system, and $X_{\alpha}$ is the C concentration in bainitic ferrite which is usually taken as a constant value. Caballero *et al.* [16] suggested that the C in bainitic ferrite ($X_{\alpha}$) is 0.03 wt.% in solid solution. According to Eq. 7.5, the volume fraction of bainitic ferrite can be increased in the following ways:

1. Shifting $T_0'/T_0$ in Fig. 7.2(b) to higher C concentrations in retained austenite ($X_{T_0'}$) by adjusting substitutional solid solution elements;
2. Adjusting $X_{avg}$ to the lower value in Fig. 7.2(b) (also good for weldability of steel);
3. Decreasing transformation temperature ($T$) to increase $X_{T_0'}$ (which also helps to achieve finer bainitic microstructure and hence increasing the strength).

Increasing the bainitic ferrite fraction leads to reduction of the fraction of blocky retained austenite, which causes strain partitioning in the microstructure and is mechanically unstable [15]. Together with the aforementioned guidelines, it is important to suppress the carbide precipitation in austenite by taking a high Si content. Additionally, kinetics of bainite formation is an important factor to be considered for industrial feasibility. Thus, the alloy composition selection should also be based on the criteria of maximizing bainite transformation kinetics.

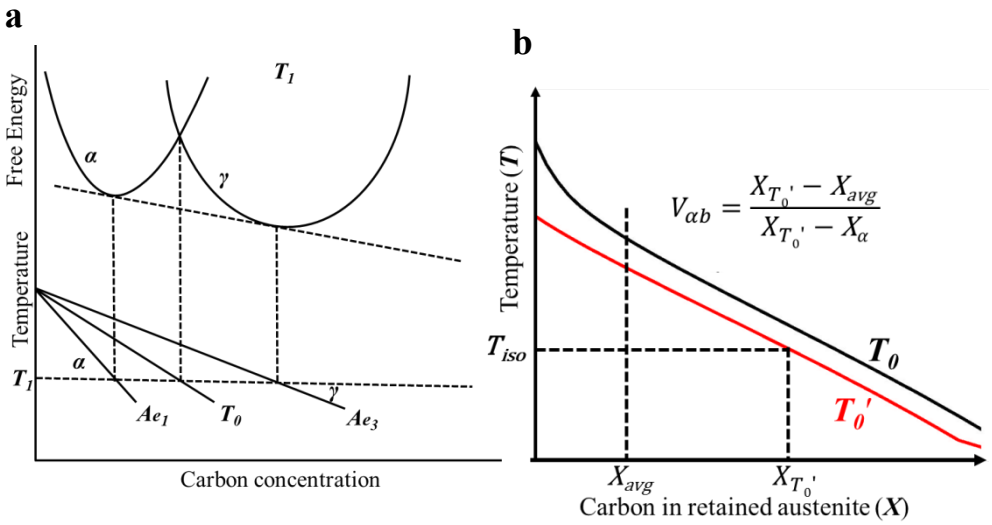


Fig. 7.2. (a) Schematic showing definition of $T_0$, (b) lever rule applied to $T_0$ and $T_0'$ curve for required bainitic ferrite fraction [1,16].

## 7.4 Materials, experimental methods and heat treatments

The chemical composition of the conventional pearlitic steel which is used to compare the mechanical response of the designed steel is Fe-0.72C-1.1 Mn-0.56 Si-0.11 Cr (wt.%). The composition of the steel designed for bainitic transformation is Fe-0.27C-1.55 Mn-1.30 Si-0.5 Cr-0.03 V- 0.15 Mo (wt.%), which is confirmed by Optical Emission Spectroscopy (OES) and X-Ray Florescence (XRF) measurements. Specimens were provided after casting and rolling by Corus, France. Cylindrical dilatometry samples were machined using Electro-Discharge Machining (EDM) with dimensions Ø4x10 $mm^2$ and homogenised at 1200 °C for 48 hrs in Ar atmosphere. The dilatometry tests were performed in a Bähr 805A quench dilatometer. The specimens were placed in the dilatometer with two thermocouples spot welded at the middle in order to control the temperature and at the edge to determine the temperature gradient during the treatment. Specimens were heated to the austenitization temperature (900 °C) with a heating rate of 10 °C/s and held for 120 seconds under vacuum. Afterwards specimens were cooled (cooling rate 50 °C/s) to 330 °C using Helium (He) and held for isothermal bainitic transformation for 2000 seconds. The cooling rate to the isothermal step was high enough to avoid austenite-to-ferrite transformation according to CCT diagrams for this specific chemical composition (Fig. 7.3(b)). After the isothermal holding, the samples were quenched to room temperature. Isothermal transformation temperature ($T_{iso}$) is selected just above the martensite start temperature (*Ms*) for the current composition in order to achieve fine bainitic microstructure. *Ms* was determined using

dilatometer experiments by similarly heating the samples up to austenitization temperature and directly quenching them to room temperature at a cooling rate of 300 °C/s.

The microstructure of the designed steel is characterized using light optical microscopy on Keyence VHX 6000 microscope and Secondary Electron (SE) imaging in a JEOL JSM 6500F Scanning Electron Microscope (SEM). Electron BackScatter Diffraction (EBSD) measurements were performed for microstructural characterization with an acceleration voltage of 15 kV and a step size of 40 nm using ZEISS crossbeam XB 1540 focused ion beam (FIB)-SEM instrument (Oberkochen, Germany). EBSD results were post-processed using TSL OIM$^{TM}$ analysis software. Due to limited spatial resolution of EBSD, the specimens were measured for the retained austenite fraction in Bruker D8-advance diffractometer operating at 45 kV and 40 mA, using Cu Kα radiation ($\lambda$ = 0.15406 nm). In order to minimize the effect of texture, specimens were tilted and rotated during measurement. Retained austenite fraction is calculated by comparing the total intensity of the ferrite peaks {110},{200}, {211} and {220} with the total intensity of the austenite peaks {111},{200}, {220} and {311} as proposed in [28,29].

Transmission Electron Microscopy (TEM) and Atom Probe Tomography (APT) specimens were prepared using Focused Ion Beam (FIB) milling in a Dual Beam FEI Helios 600i microscope. TEM investigation was carried out using a Phillips CM-20 instrument operated at 200 kV. APT is used for near atomic quantification of alloying elements partitioning in thin film retained austenite. The cementite precipitation in bainitic ferrite and C clustering at dislocations were also studied using APT. APT measurements were performed using local electrode LEAP 3000X HR in voltage mode. The temperature used for all APT measurements was 65 K with a pulse fraction of 15 % and a pulse frequency of 200 kHz. Reconstruction of the measured data was done on IVAS software according to the procedure proposed by Gault *et al.* [30].

Tensile testing for mechanical properties was performed on ASTM sub-sized cylindrical dog bone specimens (gauge length 25 mm and gauge diameter 8 mm) with a constant crosshead speed of 1 mm/min on an Instron 2200 machine. These specimens were treated for isothermal bainitic transformation at 330 °C for 1 hour in a salt bath. Hardness testing was performed on Vickers scale with a load of 10 gf (0.09 N). The specimens were also tested to study fracture behaviour under impact fatigue conditions using a special testing procedure developed for rail crossings (explained later in sec. 7.5.6).

For *in-situ* micro digital image correlation (μ-DIC) experiments, tensile samples with gauge dimensions of 1 mm x 1 mm x 0.5 mm were produced by spark erosion. Specimen surfaces were polished with colloidal $SiO_2$ particles ranging from 0.01 to 0.05 μm in size, following a conventional metallographic grinding, diamond polishing and etching procedure. Preliminary EBSD measurements were conducted to identify Regions of Interest (ROI). After the EBSD, ROI were marked using focused ion beam (FIB) milling for recognition

during *in-situ* tests. FIB markers were kept sufficiently apart from ROI to avoid beam damage. After the marking, a single monolayer of silica particles was uniformly dispersed on the specimen surface using drop casting methodology [31,32]. For *in-situ* deformation experiments, a KAMMRATH & WEISS stage was used inside the ZEISS Crossbeam XB 1540 microscope. Specimens were deformed at a cross head speed of 3 μm/sec, which corresponds to an initial strain rate of $6 \times 10^{-4}$ $s^{-1}$. In-lens SE detector was used at 1.5 kV acceleration voltage, to capture the high resolution images (2048 pixels × 1536 pixels) of the ROI with SiO2 particles on the specimen surface. These images were taken after every 2% increase in strain. The recorded images were used for von Mises/equivalent micro-strain analysis using the ARAMIS software (V6.3.0, GOM GmbH). For this analysis, the facet size was set to 150 nm enabling to achieve a stochastic pattern structure within a facet, while the facet overlap was kept at a default of 20 ~ 25%. The global strain from each image was obtained from line strains across the measured area of the map.

## 7.5 Results and discussion

### 7.5.1 *Alloy composition and isothermal bainitic transformation*

The composition of the studied alloy, following the design strategy described in sec. 7.3, is Fe-0.27 C-1.55 Mn-1.30 Si-0.5 Cr-0.03 V-0.15 Mo (wt.%). The C content is deliberately chosen low to achieve high bainitic fraction and good weldability during maintenance (sec. 7.3, guideline 2). The Si concentration is 1.3 wt.% to avoid carbide precipitation in retained austenite during bainitic transformation. Additionally, a low concentration of Mo (0.15 wt%) and V (0.03 wt%) is taken to avoid the temper embrittlement problem caused by phosphorous impurity [33,34] and to enhance the solid solution strengthening.

After the alloy selection, an adequate heat treatment has to be defined. Preliminary dilatometry experiments are conducted to determine the martensite start temperature (*Ms*) of the present alloy, as shown in Fig. 7.3(a). Repeated experimental trials show that the *Ms* for the selected alloy system varies from 310 to 318 °C. The quenching part of the dilatometer quenching experiments is fitted with a straight line represented in red (Fig. 7.3(a)). This shows the change in the slope of quenching part at 318 °C with respect to the slope of the fitted line. This point is defined as the *Ms* temperature where the onset of martensite formation is determined by the change in the slope of quenching part due to expansion of the crystal lattice by austenite to martensite transformation. The bainitic start temperature (*Bs*) and *Ms* are also determined by simulating the Time Temperature Transformation (TTT) and Continuous Cooling Transformation (CCT) diagrams using EWI software [35] (Fig. 7.3(b)). The values for *Ms* and *Bs* are 315 °C and 468 °C respectively.

In order to achieve a high fraction of bainitic ferrite, a low isothermal transformation temperature above *Ms* has to be selected as per $T_0/T_0'$ theory (sec. 7.3). However, slower

bainite formation kinetics at low isothermal temperatures should be avoided. So the temperature of 330 °C is selected for isothermal bainite formation. Fig. 7.3(c) shows the overall heat treatment scheme for isothermal bainite formation studied in this chapter. The dilatometer results in Fig. 7.3(d) show the isothermal line representing bainite formation by increase in specimen length. Furthermore, the final quenching part after the bainitic transformation does not show any change in the slope of the line (Fig. 7.3(d)). This is an indication that no martensite forms from the retained austenite during final quenching after the isothermal bainitic transformation step. This also ensures the high thermal stability of retained austenite in microstructure. Martensite formation has to be avoided because its presence in bainitic steels leads to damage initiation and propagation at the martensite-bainite interfaces and brittle fracturing of martensite [15]. Detailed microstructural characterization is carried out to ensure the absence of the martensitic phase in the designed microstructure.

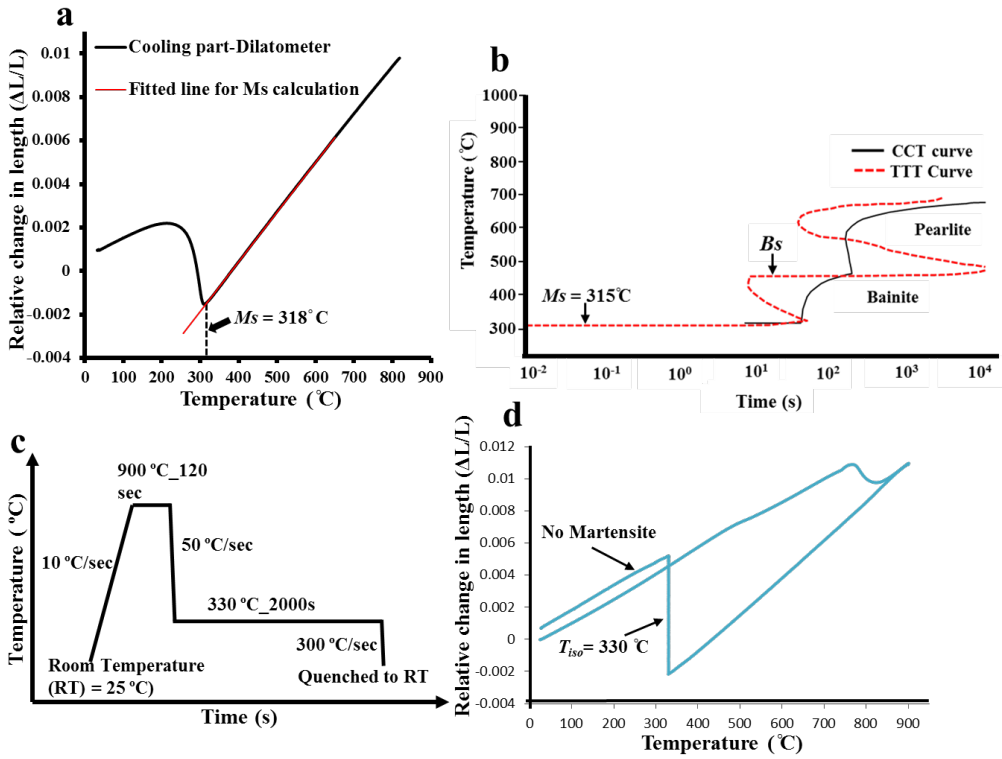


Fig. 7.3. (a) Determination of *Ms* temperature using dilatometry, (b) simulated TTT and CCT diagrams for selected alloy composition showing *Ms* and *Bs* temperatures (c) schematic showing the heat treatment used in the current study, (d) heating, cooling and isothermal step of the dilatometry test for bainitic transformation.

### 7.5.2 *Microstructural characterization*

Fig. 7.4(a-c) show the fine microstructure of the isothermally treated carbide-free bainitic steels using light optical microscopy, SEM and EBSD respectively. The microstructure shows the presence of fine laths of bainitic ferrite (in gray contrast) and thin film retained austenite between bainitic laths (in white contrast: shown by arrows) (Fig. 7.4(b)). Blocky retained austenite is also shown in the microstructure by arrows in Fig. 7.4(b). Further investigation using EBSD shows the presence of fine bainitic ferrite with lath morphology and blocky retained austenite (in green) (Fig. 7.4(c)). However, thin film retained austenite laths are not detected using EBSD because the size of these laths lies below the spatial resolution limit of EBSD. The area fraction of blocky retained austenite detected using EBSD is 2.6 %. Furthermore, the EBSD Image Quality (IQ) map in Fig. 7.4(c) does not show the areas of low IQ values (*i.e.* absolute IQ value < 950 [15]). This indicates the absence of the martensitic phase in the microstructure. The reason for martensite to show low IQ values is due to the presence of large non-uniform lattice strain and high dislocation density inside. The absence of martensite in the microstructure is also observed in dilatometry results in Fig. 7.3(d). The absence of martensite indicates that the blocky retained austenite formed during bainitic transformation is stable and does not transform into martensite during and after final quenching. Fig. 7.4(d) shows the grain size distribution of the blocky retained austenite in the microstructure with an average grain size 0.45 ± 0.27 μm. A low fraction and small size of these austenite grains lead to high and uniform C enrichment within these islands which makes them more thermally and mechanically stable.

Fig. 7.4(e) shows the X-Ray diffraction (XRD) measurements for determination of the austenite fraction in the microstructure. Measurements show that the total fraction of the retained austenite in the microstructure is 6.2 ± 1.0 %. The difference in the austenite fraction between EBSD (EBSD only detects blocky austenite) and XRD can be attributed to the thin film retained austenite. This shows that the designed microstructure consists of higher fraction of retained austenite in thin film morphology than in blocky morphology.

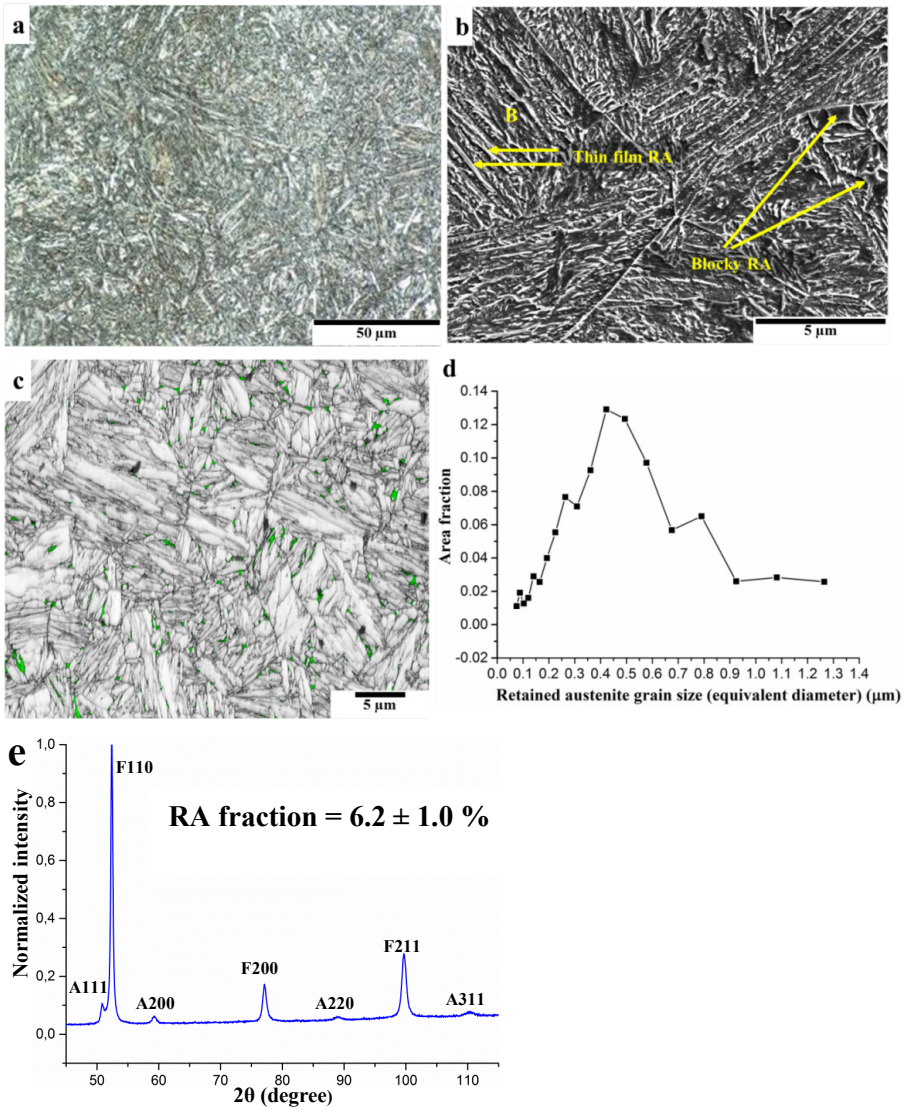


Fig. 7.4. (a) Microstructural characterization of the isothermally treated bainitic steel: (a) optical micrograph (b) SEM micrograph showing the presence of thin film retained austenite, blocky retained austenite and fine bainitic ferrite laths in the microstructure, (c) EBSD Image Quality (IQ) map overlapped with retained austenite (in green), (d) grain size distribution of blocky retained austenite, (e) X-Ray Diffraction measurements for calculation of retained austenite in the microstructure (A and F represent austenite and ferrite peaks respectively).

In summary, the microstructure of the designed steel contains 93.8 % bainitic ferrite and 6.2 % retained austenite with no signs of martensite and inter-lath carbides. Thus, the martensite-bainite and bainite-cementite interfaces are excluded from the designed microstructure. This leads to enhanced damage resistance in the designed steels [15].

### 7.5.3 *Characterization of thin film retained austenite and bainitic ferrite laths using TEM*

Fig. 7.5 shows the bright-field TEM images of the designed bainitic microstructure showing thin film retained austenite (thickness 30-40 nm) located between fine bainitic ferrite laths (thickness ≈ 150 nm). Corresponding micro-diffraction patterns from bainitic ferrite (zone axis [111]) and retained austenite (zone axis [011]) are also shown in Fig. 7.5. Such fine bainitic microstructure will lead to high yield strength and good toughness of the steel microstructure [36].

Another important observation in the TEM investigations is the presence of stacking faults in thin film austenite in Fig. 7.5(b). The similar phenomenon of formation of twinning and stacking faults has been shown by Caballero *et al.* [37] and Bhadeshia *et al.* [26], giving evidence of displacive/diffusionless nature of bainite formation. According to these studies, bainitic ferrite grows by a shear transformation mechanism. During transformation, substantial growth of the bainitic ferrite leads to plastic relaxation of retained austenite, generating defects such as stacking faults and twinning in austenite and high dislocation density in bainitic ferrite. This in turn controls the bainitic ferrite growth and determines the size of the bainitic laths by limiting bainite/austenite interface mobility [38]. High concentration of defects in the bainitic ferrite and retained austenite can affect the overall mechanical response of these steels.

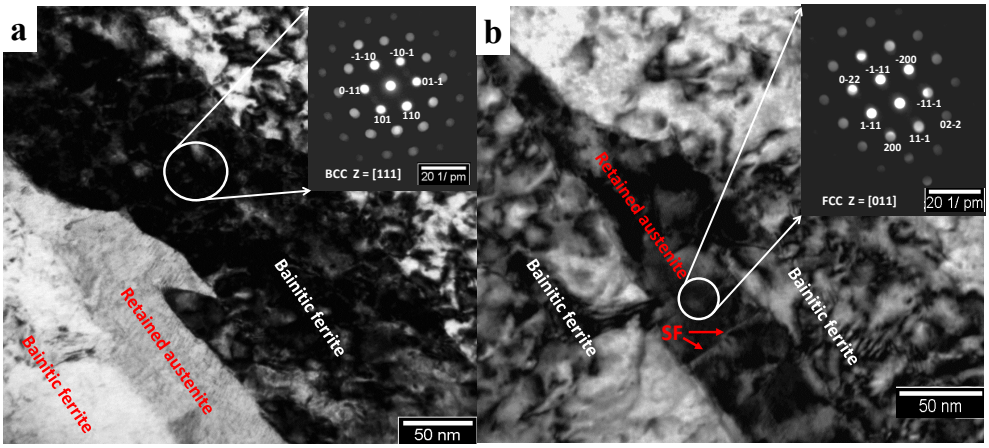


Fig. 7.5. Bright field TEM images showing alternative laths of bainitic ferrite and retained austenite and corresponding micro diffraction patterns: (a) bainitic ferrite in Bragg's condition with [111] zone axis, (b) thin film retained austenite in Braggs condition with [011] zone axis showing formation of stacking faults (SF) during bainitic growth (shown by red arrows).

### 7.5.4 *C enrichment in thin film retained austenite during bainitic transformation and comparison with $T_0$/$T_0$' theory*

Three dimensional atom probe tomography (3DAPT) provides precise knowledge of C partitioning in retained austenite during bainite formation [37]. The C concentration in retained austenite also determines the stability of the austenite under mechanical strain. Fig. 7.6(a) shows the 3DAPT image showing C atom maps (overlapped with 7 at.% C iso-concentration surface) of thin film retained austenite located in between bainitic ferrite plates. The C partitioning from bainitic ferrite to thin film retained austenite is observed, where concentration of C atoms in thin film retained austenite is seen to be higher than in bainitic ferrite. Fig. 7.6(b) shows the 1D concentration profiles of C, Mn and Si along the cylindrical ROI shown in Fig. 7.6(a). The average C concentration in thin film retained austenite and bainitic ferrite is measured to be 7.9 ± 0.7 at% and 0.7 ± 0.4 at% respectively. Such high C concentrations in thin film retained austenite govern its mechanical stability and introduce strength without compromising ductility. Additionally, no partitioning of Mn and Si is observed between bainitic ferrite and thin film retained austenite (Fig. 7.6(b)).

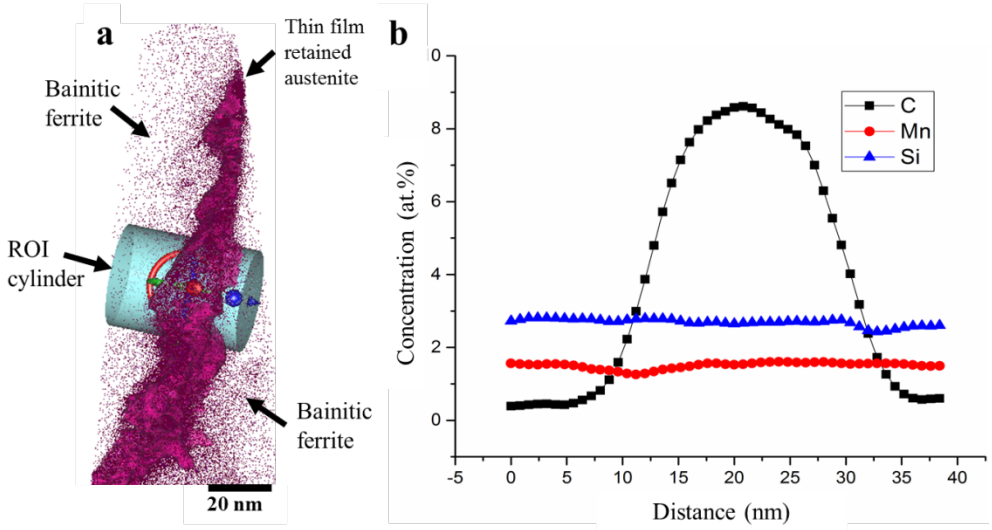


Fig. 7.6. (a) APT C map with 7 at% C iso-concentration surface showing the C partitioning between thin film retained austenite and bainitic ferrite, (b) 1D concentration profile showing variation of C, Mn and Si along cylindrical region of interest.

According to $T_0/T_0'$ theory, bainitic formation stops when the C concentration in retained austenite reaches the $T_0/T_0'$ curve. This explains the incomplete transformation phenomenon in bainite formation. Fig. 7.7(a) shows the $T_0$, $T_0'$ and para-equilibrium (PE) plot of the selected alloy composition in this work for the C in retained austenite. According to this plot, the maximum C concentration in retained austenite at 330 °C is 4.7 and 5.6 at.% as per $T_0'$ and $T_0$ theory, respectively (Fig. 7.7(a)). However, PE shows much higher C concentration (16.8 at.%) in the retained austenite for isothermal bainitic transformation at 330 °C. It is observed that the bainitic transformation proceeds exceeding the $T_0$ and $T_0'$ predictions. The average difference of C in retained austenite between experimental results (Fig. 7.6(b)) and $T_0$ /$T_0'$ calculations (Fig. 7.7(a)) is around 2.9 at.% and 3.2 at.% respectively. However, PE predicts more difference in the C concentration (*i.e.* 8.9 at.%) in the retained austenite than the experimental measurements. Thus, the APT results for C partitioning in thin film retained austenite cannot be precisely explained by $T_0/T_0'$/PE theory. In order to support $T_0/T_0'$ theory, Bhadeshia *et al.* [39] proposed that the austenite can still continue to absorb C atoms from C-saturated bainitic ferrite even after bainite growth stops and C content in austenite reaches $T_0'$. This statement is based on the fact that the C atom diffusion from bainitic ferrite is slow in comparison with formation kinetics of bainitic ferrite [40].

In sec. 7.5.2, the fraction of bainitic ferrite is calculated to be 93.8% with 6.2 ± 1.0 % untransformed islands of fine blocky austenite and thin film retained austenite in between bainitic ferrite laths (Fig. 7.4). Fig. 7.7(b) shows the dilatometry results of isothermal

bainitic transformation by plotting the graph of relative length changes of the specimen vs time. This graph is further normalized by experimentally measured bainitic ferrite fraction (*i.e.* 93.8%) to observe the incomplete bainitic transformation phenomenon by plotting bainitic fraction vs time (Fig. 7.7(c)). As discussed in sec. 7.3 (Eq. 7.5), it is possible to calculate the volume fraction of bainitic ferrite by applying the lever rule for $T_0$ and $T_0'$ curves, where the C concentration in bainitic ferrite is taken from the APT results shown in Fig. 7.6(b). The $T_0$ and $T_0'$ theory thus predicts a maximum bainitic ferrite fraction of 89.5 and 87.1 % in the current alloy (Fig. 7.7(c)). These values differ significantly from the experimentally measured bainitic ferrite phase fraction. This indicates that the bainite formation can proceed even after the $T_0$ and $T_0'$ limit is reached.

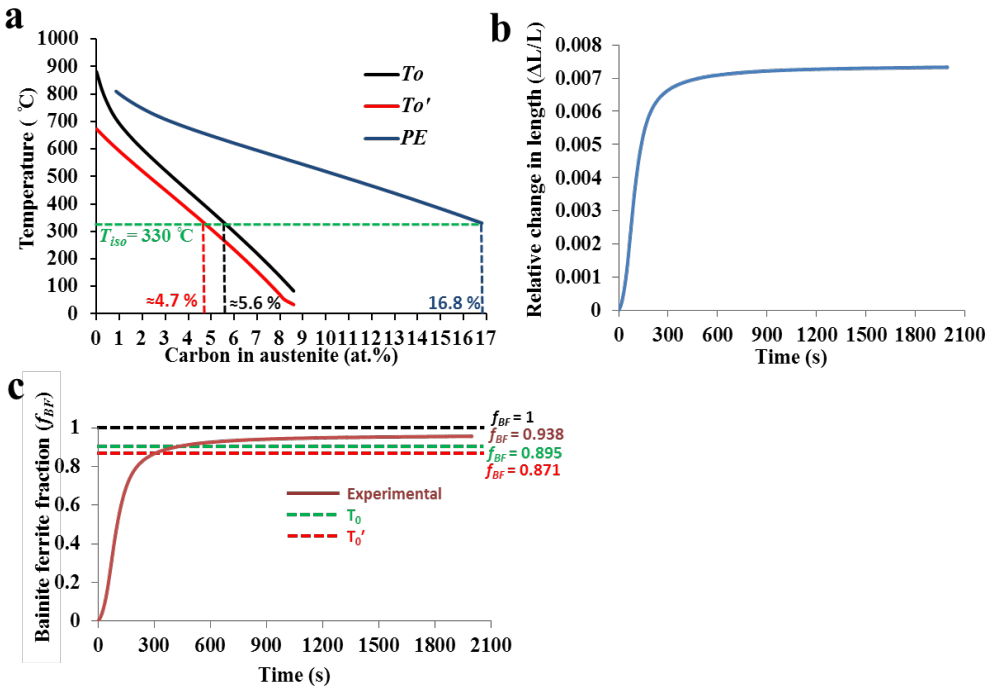


Fig. 7.7. (a) $T_0$, $T_0'$ and PE plots of studied alloy composition, (b) the relative change in length vs time during the isothermal bainitic transformation in dilatometry test, (c) bainitic ferrite fraction vs time in the dilatometry test during isothermal step and comparison of observed final bainitic ferrite fraction with bainitic ferrite fraction calculated using $T_0/T_0'$ theory.

### 7.5.5 *Nano-carbide precipitation and Cottrell atmosphere in bainitic ferrite and their contribution in strengthening mechanism*

Precipitation of two kinds of carbides has been reported in literature in C-saturated lower bainite: ε-carbide and cementite based on composition of alloy [24,26,41]. Matas *et al.* [42]

reported ε-carbide precipitation from lower bainite in hypo-eutectoid steels which later transforms into cementite. However, the precipitation of ε-carbide is more unlikely in low C bainitic steels [43]. Fig. 7.8 shows the APT results from lath bainitic ferrite in the designed microstructure. Fig. 7.8(a) represents the C atom map overlapped with 13 at.% C iso-concentration surface (in the rectangle). A proximity diagram (proxigram) is plotted about this iso-concentration surface to study the elemental variation of the carbon and other alloying elements (Mn, Si) (Fig. 7.8(b)). The proxigram analysis shows that the C concentration increases into the iso-concentration surface and reaches a maximum value of 23.9 ± 0.9 at.%. This indicates the precipitation of nano-sized cementite in lower bainite as the C concentration is close to the equilibrium C concentration in cementite (*i.e.* 25 at.%). Such slightly lower C concentrations in cementite are also reported by other researchers [44,45]. The difference with the theoretical value of 25 at.% can be attributed to APT artifact such as local magnification effect in measuring nano-sized precipitates [46]. Furthermore, the cementite precipitate does not show any partitioning of Si and Mn in Fig. 7.8(b), which indicates the para-equilibrium nature of the cementite precipitate. Additionally, the diffusion of substitutional atoms such as Mn and Si will be negligible at low isothermal temperature (*i.e.* 330 ℃). Bhadeshia *et al.* [26,43,47] showed a similar kind of cementite precipitation in lower bainite in high silicon steels. Thus, it is evident that the addition of high silicon suppresses the cementite precipitation from retained austenite but not from the lower bainite.

The APT result in Fig. 7.8(a) also shows clustering of C atoms within bainitic ferrite (shown by arrows). This C clustering is attributed to segregation of C atoms at the dislocations in bainitic ferrite termed as Cottrell atmospheres [48]. The APT result in Fig. 7.8(a) is further shown with 7 at.% C iso-concentration surfaces in Fig. 7.8(c). This shows the presence of a line-shaped 7 at.% C iso-concentration surface (in the rectangle) indicating clustering of C atoms at a dislocation. Fig. 7.8(c) also shows the plate-like morphology of cementite precipitate (indicated by an arrow) in bainitic ferrite which can lead to dislocation pinning during plastic deformation, improving the yield strength of the steel. A proxigram is further plotted in Fig. 7.8(d) around the dislocation with 7 at.% C interphase in Fig. 7.8(c). This shows a maximum C concentration of 10.8 ± 1.0 at.% at the dislocation. It should be noted that not only a dislocation with maximum C accumulation is present in the APT results in Fig. 7.8(c,d). Other C clustering regions/dislocations with relatively low C concentration are also present in bainitic ferrite as indicated by arrows in Fig. 7.8(a). Cottrell *et al.* [48] in their classical work have shown that dislocations with C segregation require an extra force to release them for slip. This in turn affects the strengthening of bainitic ferrite in the designed steel.

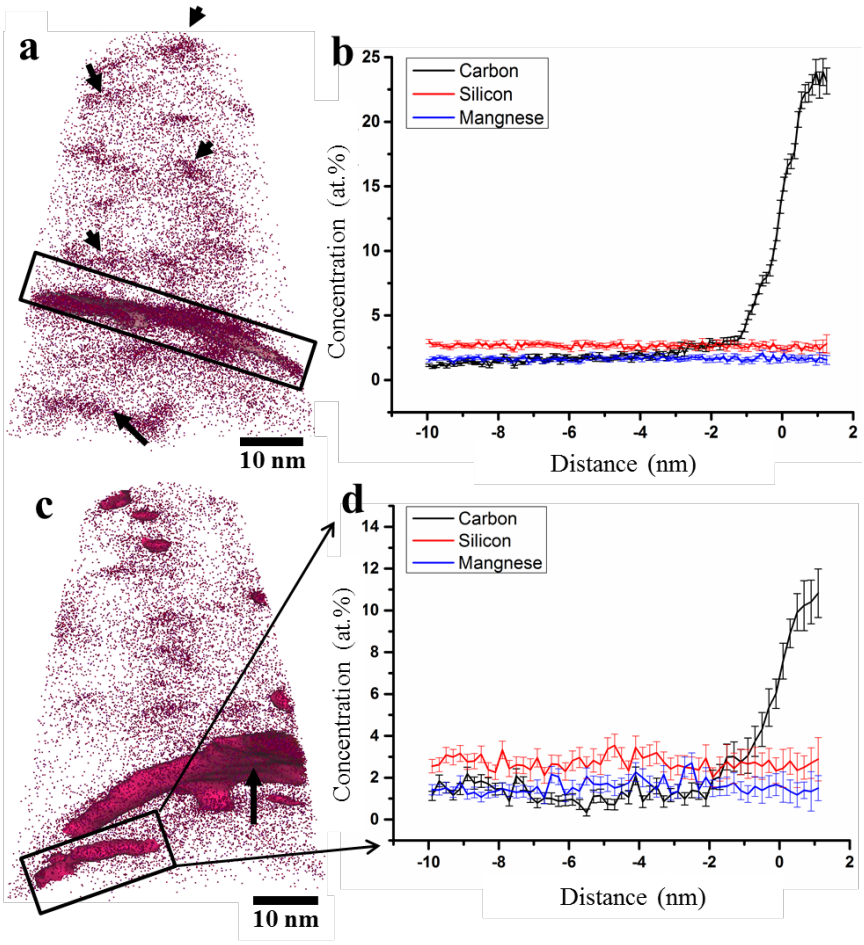


Fig. 7.8. 3DAPT measurements showing (a) nano-sized cementite precipitation within bainitic ferrite and C clustering at dislocation (shown by arrows), (b) proxigram plotted with 13 at% C iso-concentration surface showing the distribution of C, Mn and Si around the cementite precipitate, (c) C atom map with 7 at% C iso-concentration surface showing the plate morphology of cementite precipitate (shown by arrow) and a dislocation with C clustering (in rectangle) in its vicinity, (d) proxigram plotted with 7 at% C interface around the dislocation showing C segregation inside the dislocation core.

### 7.5.6 *Mechanical properties and fracture behaviour*

Fig. 7.9(a) and Table 7.1 show the comparison of the mechanical properties of designed isothermal fine bainitic steels with continuously cooled carbide-free bainitic steel (CC-CFBS/CC-CFB steels) and conventional pearlitic steel (industrially known as R350HT). Isothermally treated fine bainitic steel offers high yield strength, 1398 ± 13 MPa, which is above the maximum von Mises stresses in the crossings nose (707 to 1085 MPa) during train passage [20,21]. This satisfies the design criterion shown in Eq. 7.4. However, conventional steels such as continuously cooled CFB steels and pearlitic steels offer low yield strength (912 ± 11 and 811 ± 11 MPa respectively). The high yield strength of the designed isothermally treated steel is attributed to its fine bainitic microstructure (sec. 7.5.3), nano-cementite precipitation in bainitic ferrite and Cottrell atmospheres at the dislocations (sec. 7.5.5). Furthermore, isothermally treated fine bainitic steel shows high tensile strength (1834 ± 18 MPa) with good strain hardening response and appreciable ductility (12.7 ± 0.5 %) as shown in Fig. 7.9(a) and Table 7.1. They also show higher hardness values (533 ± 9 HV1) than conventional steels (Table 7.1), which is beneficial for high wear resistance for crossings applications.

In addition to the static mechanical behavior, it is also important to study the material response under impact fatigue loading in context of an application in crossings. Till date, there is no standard laboratory scale testing procedure available to study the impact fatigue response of materials. This becomes further complicated due to the fact that the high strain rates and complex loading conditions in crossing noses are difficult to simulate in laboratory environment. Efforts have been made to study the impact fatigue behavior of isothermally treated fine bainitic steels and conventional steels with an appropriate testing. The test comprises a double notched rectangular specimen with defined notch geometry (depth of 3 mm and notch radius of 0.15 mm) (Fig. 7.9(b)). The equipment for this testing is shown by a schematic drawing in Fig. 7.9(c). The specimen is fitted on an inclined platform/guide which allows the free movement of the specimen in axial direction. The specimen is loaded cyclically with an impact hammer having a defined mass and speed (and therefore momentum) at one of its free ends, until final fracture of the specimen. After each impact, the specimen moves upwards through the guide and comes back for the next impact after hitting the shock absorbing damper (Fig. 7.9(c)). Each individual impact leads to a longitudinal wave front (tension and compression) moving into the specimen and reflecting internally at the ends, the notches acting as a local stress amplitude raiser upon passage of the wave front. The propagation speed of a compression wave ($c$) depends only on the material properties and is given by the Newton-Laplace equation $c = \sqrt{(E/\rho)}$, where $E$ is the elastic bulk modulus (200 GPa) and $\rho$ is the density of the steel (8000 kg/m$^3$). For steel, $c$ is of the order of magnitude of 5000 m/s. This value is related to the local strain rate via the length of the compression wave, which depends on the hammer length. This length is chosen in such a way that the time from minimum to maximum stress in a cross-section

is an order of 0.015 ms, which is equivalent to a frequency of about 67 kHz. Frequency of such magnitude cannot be achieved in ordinary fatigue testing. The test leads to typical results in terms of fracture surfaces as shown in Fig. 7.9(d-f), with a clear partitioning between fatigue zones adjacent to the notch edges and a residual final fracture surface. The fracture surfaces of the different steel types are analyzed using 3D optical microscopy (Fig. 7.9(d-f)). The isothermally treated fine bainitic steel shows controlled crack growth under impact fatigue with striations observed on the fracture surface (Fig. 7.9(d)). Fatigued zone and residual fracture zone in the fracture surface of isothermally treated fine bainitic steels are marked in Fig. 7.9(d) by white and red curly brackets respectively. This controlled fatigue crack growth in the designed steels is due to the homogeneous microstructure with absence of detrimental phases like martensite and cementite. However, continuously cooled CFB steels and conventional pearlitic steels show uncontrolled crack growth phenomena under impact fatigue (Fig. 7.9(e,f)). The micro cracks in these steels can initiate at weak microstructural features such as martensite-bainitic ferrite and ferrite-cementite interphases, followed by martensitic and cementite brittle fracturing *etc*. [15]. This leads to nucleation and growth of micro-cracks at such weak microstructural features over the entire cross-section. These micro-cracks combine with the main crack from the specimen notch. Hence the conventional steels show uncontrolled crack growth/brittle crack propagation under impact fatigue (Fig. 7.9(e,f)) without clear distinction of fatigued and residual fracture zone. This also poses worst-case scenarios for preventive maintenance of crossings where it is very difficult to detect these micro-cracks and crossings can fail in an uncontrolled manner.

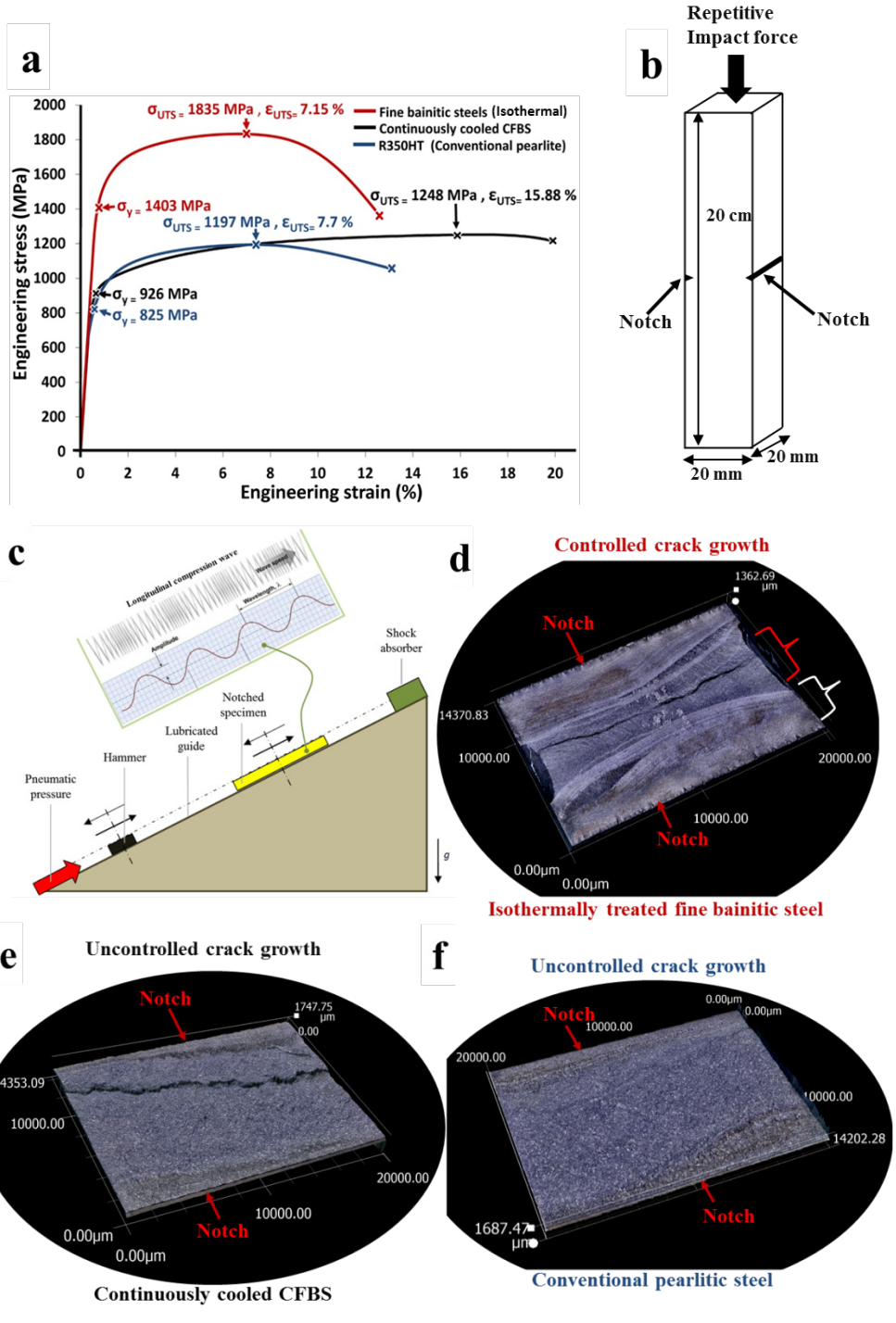
a
Engineering stress (MPa)
Engineering strain (%)
σUTS = 1835 MPa , εUTS= 7.15 %
Fine bainitic steels (Isothermal)
Continuously cooled CFBS
R350HT (Conventional pearlite)
σy = 1403 MPa
σUTS = 1197 MPa , εUTS= 7.7 %
σUTS = 1248 MPa , εUTS= 15.88 %
σy = 926 MPa
σy = 825 MPa
b
Repetitive
Impact force
20 cm
Notch
Notch
20 mm
20 mm
c
Longitudinal compression wave
Amplitude
Wavelength
Shock absorber
Notched specimen
Lubricated guide
Hammer
Pneumatic pressure
g
d
Controlled crack growth
Notch
1362.69 µm
14370.83
10000.00
20000.00
10000.00
Notch
0.00µm
0.00µm
Isothermally treated fine bainitic steel
e
Uncontrolled crack growth
Notch
1747.75 µm
0.00
14353.09
10000.00
20000.00
10000.00
Notch
0.00µm
0.00µm
Continuously cooled CFBS
f
Uncontrolled crack growth
Notch
0.00µm
0.00µm
10000.00
20000.00
10000.00
14202.28
Notch
1687.47 µm
Conventional pearlitic steel

Fig. 7.9. (a) Comparison of tensile properties of isothermally treated fine bainitic steels with continuously cooled CFBS and conventional pearlitic steel, (b) schematic showing the geometry of impact fatigue specimen, (c) schematic drawing of the impact fatigue testing equipment, (d-f) crack growth and fracture in isothermally treated fine bainitic steel, continuously cooled CFBS and conventional pearlitic steel under impact fatigue.

Table 7.1. Comparison of mechanical properties of designed isothermal bainitic steels with conventional steels.

| Steel | Yield Strength ($\sigma_y$) (MPa) | Tensile Strength ($\sigma_{UTS}$) (MPa) | Uniform strain ($\varepsilon_{UTS}$) (%) | Fracture strain ($\varepsilon_f$) (%) | Area reduction (%) | Hardness HV1 |
|---|---|---|---|---|---|---|
| R350HT | 811 ± 11 | 1181 ± 14 | 7.5 ± 0.4 | 14.5± 0.9 | 48 ± 3 | 365 ±10 |
| CC-CFBS | 912 ± 11 | 1232 ± 12 | 15.2 ± 0.5 | 20 ± 0.8 | 33 ± 3 | 360 ± 9 |
| Isothermally treated fine bainitic steels | 1398 ± 13 | 1834 ± 18 | 7.2 ± 0.3 | 12.7± 0.5 | 65 ± 2 | 533 ± 9 |

### 7.5.7 *In-situ strain partitioning in the designed bainitic microstructure using μ-DIC*

Overall mechanical and damage response of the materials is governed by the strain partitioning between the microstructural constituents. The micromechanical response of the material cannot be neglected when designing new materials. This material design strategy is usually termed as micromechanically-guided design [49]. Kumar *et al.* [15] showed the strong strain partitioning between the martensite, blocky retained austenite and bainitic ferrite in continuously cooled carbide-free bainitic steels. This leads to damage initiation and growth along the microstructural features such as martensite-bainitic ferrite interfaces and to brittle fracturing of the martensite. Various studies conducted on dual phase steels also show severe strain partitioning between martensite and ferrite islands [31,32,50]. The isothermally treated fine bainitic steel designed in the present work shows no trace of martensite in the microstructure (sec. 7.5.1, 7.5.2). Hence, the strain incompatibility due to presence of brittle martensite has been eliminated in the designed microstructure. Furthermore, elimination of the less stable large blocks of retained austenite also suppresses the strain partitioning effects. Fig. 7.10 shows a representative result of micromechanical response of the designed carbide-free bainitic steel. Fig. 7.10(a) shows IQ map overlapped

with retained austenite (in green) of the isothermally treated bainitic steel. This map is also a selected ROI for the *in-situ* tensile testing. Fig. 7.10(b) shows the normal direction Inverse Pole Figure (IPF) map with high angle grain boundaries (in black), showing different grain orientations in the ROI. Tensile direction, normal direction and transverse direction with respect to the ROI are labelled in Fig. 7.10. Fig. 7.10(c-e) show the strain partitioning results in the *in-situ* uniaxial tensile tests conducted inside the SEM using μ-DIC at 4% and 8% global strain respectively. The designed isothermally treated fine bainitic steel does not show strong strain partitioning in the microstructure (Fig. 7.10(c,d)) due to absence of phases like martensite and carbides (sec. 7.5.1, 7.5.2). In addition, the blocks of retained austenite do not show strain localization because of their high mechanical stability. This stability is governed by high C enrichment as a result of maximizing bainite fraction and the small size of austenite islands. Fig. 7.10(e) shows the distribution of local von Mises strains at 8% global strain. These local strains follow a log normal distribution with a mean strain value 7.7% with a Standard Deviation (SD) of 1.5%, at 8% global strain. Low SD value in the strain distribution (Fig. 7.10(e)) shows that the local strains are homogeneously distributed in the microstructure, which implies a limited degree of strain partitioning. If we compare these SD values with the case of continuously cooled carbide-free microstructures shown in a study conducted by Kumar *et al.* [15], continuously cooled CFB steels show that the local von Mises strains partition in the microstructure with high Standard Deviation (SD) values of 6.8% at 9% global strain. Such strong local strain partitioning occurs due to the presence of complex microstructure containing martensite, large blocky austenite, upper bainite and lower/lath bainite [15].

Thus, the micro-scale damage initiation in the steels can be suppressed by designing microstructures with minimum strain localization and hence more damage resistance is achieved.

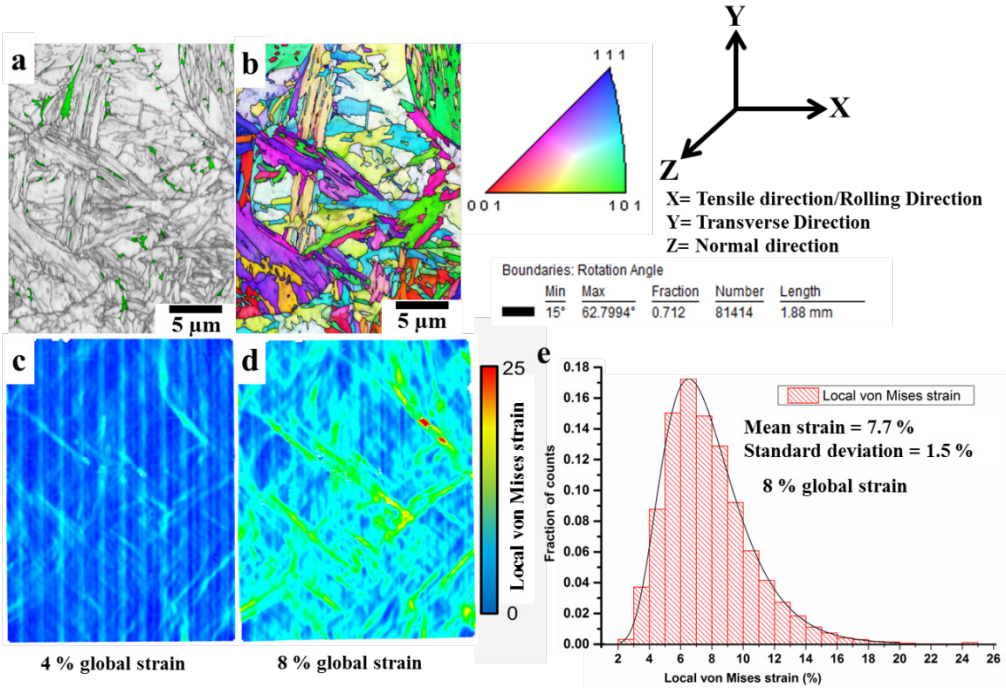


Fig. 7.10. *In-situ* strain partitioning in isothermal fine bainitic steels using micro digital image correlation (µ-DIC): (a) EBSD IQ map overlapped with retained austenite (in green) of the Region of Interest (ROI) for µ-DIC, (b) Inverse Pole Figure (IPF) map of the ROI, (c-d) local von Mises strain distribution in the ROI at 4% and 8% global strain, (e) distribution of the local von Mises strains at 8% global strain value.

## 7.6 Conclusions

Conclusions made based on the current study are:

1. Microstructure of the isothermally treated designed bainitic steel comprises fine bainitic ferrite, small blocky retained austenite and thin film retained austenite.
2. High C enrichment up to 7.9 at.% in thin film retained austenite and fine grain size (30-40 nm) govern its mechanical stability.
3. The designed steel offers exceptional mechanical properties such as yield strength, tensile strength, hardness, appreciable ductility, good strain hardening and controlled crack growth under impact fatigue. Hence, they can be used as potential candidate for use in railways crossings.

4. High yield strength of the designed bainitic microstructure stems from fine grain size in nanometer range, nano-sized cementite precipitation in bainitic ferrite with plate morphology, and C clustering at dislocations (Cottrell atmospheres).
5. The $T_0$ and $T_0'$ theory serves as a good basis for alloy design. However, appreciable variation in the predictions of $T_0/T_0'$ theory for isothermal bainitic transformation can be observed experimentally such as maximum achievable bainitic fraction and C concentration in retained austenite.
6. Absence of martensitic phase and large blocks of retained austenite in isothermally treated bainitic steel, unlike in continuously cooled carbide-free bainitic steel, decreases the strain localization in the microstructure during in-situ testing. This also improves the damage resistance due to elimination of martensite-bainitic ferrite interphases which are prone to damage nucleation and growth.
7. The Small size of blocky retained austenite islands present in the microstructure (grain size = 0.45 ± 0.27 μm) governs their high mechanical stability and does not contribute to strain partitioning/strain localization and hence improves the damage resistance.

## References


[1] H.K.D.H. Bhadeshia, High performance bainitic steels, in: Mater. Sci. Forum, Trans Tech Publ, 2005: pp. 63–74.

[2] L. Zhou, G. Liu, X.L. Ma, K. Lu, Strain-induced refinement in a steel with spheroidal cementite subjected to surface mechanical attrition treatment, Acta Mater. 56 (2008) 78–87. doi:10.1016/J.ACTAMAT.2007.09.003.

[3] M. Umemoto, Y. Todaka, K. Tsuchiya, Mechanical Properties of Cementite and Fabrication of Artificial Pearlite, Mater. Sci. Forum. 426–432 (2003) 859–864. doi:10.4028/www.scientific.net/MSF.426-432.859.

[4] A. Kumar, G. Agarwal, R. Petrov, S. Goto, J. Sietsma, M. Herbig, Microstructural evolution of white and brown etching layers in pearlitic rail steels, Acta Mater. (n.d.) Submitted for publication.

[5] T. Leitner, S. Sackl, B. Völker, H. Riedl, H. Clemens, R. Pippan, A. Hohenwarter, Crack path identification in a nanostructured pearlitic steel using atom probe tomography, Scr. Mater. 142 (2018) 66–69. doi:10.1016/J.SCRIPTAMAT.2017.08.025.

[6] H.W. Zhang, S. Ohsaki, S. Mitao, M. Ohnuma, K. Hono, Microstructural investigation of white etching layer on pearlite steel rail, Mater. Sci. Eng. A. 421 (2006) 191–199. doi:10.1016/J.MSEA.2006.01.033.

[7] J. Takahashi, K. Kawakami, M. Ueda, Atom probe tomography analysis of the white etching layer in a rail track surface, Acta Mater. 58 (2010) 3602–3612. doi:10.1016/J.ACTAMAT.2010.02.030.

[8] W. Österle, H. Rooch, A. Pyzalla, L. Wang, Investigation of white etching layers on rails by optical microscopy, electron microscopy, X-ray and synchrotron X-ray diffraction, Mater. Sci. Eng. A. 303 (2001) 150–157. doi:10.1016/S0921-5093(00)01842-6.

[9] S.B. Newcomb, W.M. Stobbs, A transmission electron microscopy study of the white-etching layer on a rail head, Mater. Sci. Eng. 66 (1984) 195–204. doi:10.1016/0025-5416(84)90180-0.

[10] J. Wu, R.H. Petrov, S. Kölling, P. Koenraad, L. Malet, S. Godet, J. Sietsma, Micro and Nanoscale Characterization of Complex Multilayer-Structured White Etching Layer in Rails, Met. . 8 (2018). doi:10.3390/met8100749.

[11] S. Li, J. Wu, R.H. Petrov, Z. Li, R. Dollevoet, J. Sietsma, "Brown etching layer": A possible new insight into the crack initiation of rolling contact fatigue in rail steels?, Eng. Fail. Anal. 66 (2016) 8–18. doi:10.1016/J.ENGFAILANAL.2016.03.019.

[12] A. Al-Juboori, H. Zhu, D. Wexler, H. Li, C. Lu, A. McCusker, J. McLeod, S. Pannila, J. Barnes, Evolution of rail surface degradation in the tunnel: The role of water on squat growth under service conditions, Eng. Fract. Mech. 209 (2019) 32–47. doi:10.1016/J.ENGFRACMECH.2019.01.018.

[13] A. Al-Juboori, D. Wexler, H. Li, H. Zhu, C. Lu, A. McCusker, J. McLeod, S. Pannil, Z. Wang, Squat formation and the occurrence of two distinct classes of white etching layer on the surface of rail steel, Int. J. Fatigue. 104 (2017) 52–60. doi:10.1016/J.IJFATIGUE.2017.07.005.

[14] F.G. Caballero, S. Allain, J. Cornide, J.D. Puerta Velásquez, C. Garcia-Mateo, M.K. Miller, Design of cold rolled and continuous annealed carbide-free bainitic steels for automotive application, Mater. Des. 49 (2013) 667–680. doi:10.1016/J.MATDES.2013.02.046.

[15] A. Kumar, A. Dutta, S.K. Makineni, M. Herbig, R.H. Petrov, J. Sietsma, In-situ observation of strain partitioning and damage development in continuously cooled carbide-free bainitic steels using micro digital image correlation, Mater. Sci. Eng. A. (n.d.) Submitted for publication.

[16] F.G. Caballero, H. Bhadeshia, K.J.A. Mawella, D.G. Jones, P. Brown, Design of novel high strength bainitic steels: Part 1, Mater. Sci. Technol. 17 (2001) 512–516.

[17] R. Blondé, E. Jimenez-Melero, L. Zhao, J.P. Wright, E. Brück, S. Van der Zwaag, N.H. Van Dijk, High-energy X-ray diffraction study on the temperature-dependent mechanical stability of retained austenite in low-alloyed TRIP steels, Acta Mater. 60 (2012) 565–577.

[18] D. De Knijf, C. Föjer, L.A.I. Kestens, R. Petrov, Factors influencing the austenite stability during tensile testing of Quenching and Partitioning steel determined via in-situ Electron Backscatter Diffraction, Mater. Sci. Eng. A. 638 (2015) 219–227.

[19] P. Hilkhuijsen, H.J.M. Geijselaers, T.C. Bor, E.S. Perdahcıoğlu, A.H. vd Boogaard, R. Akkerman, Strain direction dependency of martensitic transformation in austenitic stainless steels: The effect of γ-texture, Mater. Sci. Eng. A. 573 (2013) 100–105.

[20] L. Xin, V.L. Markine, I.Y. Shevtsov, Numerical analysis of the dynamic interaction between wheel set and turnout crossing using the explicit finite element method, Veh. Syst. Dyn. 54 (2016) 301–327.

[21] L. Xin, V.L. Markine, I.Y. Shevtsov, Numerical procedure for fatigue life prediction for railway turnout crossings using explicit finite element approach, Wear. 366 (2016) 167–179.

[22] J.H. Xiao, F.C. Zhang, L.H. Qian, Contact stress and residual stress in the nose rail of a high manganese steel crossing due to wheel contact loading, Fatigue Fract. Eng. Mater. Struct. 37 (2013) 219–226. doi:10.1111/ffe.12108.

[23] J. Xiao, F. Zhang, L. Qian, Numerical simulation of stress and deformation in a railway crossing, Eng. Fail. Anal. 18 (2011) 2296–2304.

[24] H. Bhadeshia, D. V Edmonds, The mechanism of bainite formation in steels, Acta Metall. 28 (1980) 1265–1273.

[25] F.G. Caballero, H.K.D.H. Bhadeshia, Very strong bainite, Curr. Opin. Solid State Mater. Sci. 8 (2004) 251–257.

[26] H.K.D.H. Bhadeshia, D. V Edmonds, The bainite transformation in a silicon steel, Metall. Trans. A. 10 (1979) 895–907. doi:10.1007/BF02658309.

[27] H.K.D.H. Bhadeshia, D. V Edmonds, Bainite in silicon steels: new composition–property approach Part 1, Met. Sci. 17 (1983) 411–419. doi:10.1179/030634583790420600.

[28] L. Zhao, N.. van Dijk, E. Brück, J. Sietsma, S. van der Zwaag, Magnetic and X-ray diffraction measurements for the determination of retained austenite in TRIP steels, Mater. Sci. Eng. A. 313 (2001) 145–152. doi:10.1016/S0921-5093(01)00965-0.

[29] C.F. Jatczak, Retained Austenite and its Measurement by X-ray Diffraction, SAE Trans. (1980) 1657–1676.

[30] B. Gault, M.P. Moody, F. de Geuser, G. Tsafnat, A. La Fontaine, L.T. Stephenson, D. Haley, S.P. Ringer, Advances in the calibration of atom probe tomographic reconstruction, J. Appl. Phys. 105 (2009) 34913. doi:10.1063/1.3068197.

[31] D. Yan, C.C. Tasan, D. Raabe, High resolution in situ mapping of microstrain and microstructure evolution reveals damage resistance criteria in dual phase steels, Acta Mater. 96 (2015) 399–409.

[32] C.C. Tasan, J.P.M. Hoefnagels, M. Diehl, D. Yan, F. Roters, D. Raabe, Strain localization and damage in dual phase steels investigated by coupled in-situ deformation experiments and crystal plasticity simulations, Int. J. Plast. 63 (2014) 198–210.

[33] Z. Qu, C.J. McMahon, The effects of tempering reactions on temper embrittlement of alloy steels, Metall. Trans. A. 14 (1983) 1101–1108.

[34] J. Yu, C.J. McMahon, The effects of composition and carbide precipitation on temper embrittlement of 2.25 Cr-1 Mo steel: Part I. Effects of P and Sn, Metall. Trans. A. 11 (1980) 277–289. doi:10.1007/BF02660632.

[35] http://calculations.ewi.org/vjp/secure/TTTCCTPlots.asp, EWI Virtual Joining Portal, TTT and CCT Diagram with Steel Composition, (2008).

[36] E.O. Hall, The deformation and ageing of mild steel: III discussion of results, Proc. Phys. Soc. Sect. B. 64 (1951) 747.

[37] F.G. Caballero, H.-W. Yen, M.K. Miller, J.-R. Yang, J. Cornide, C. Garcia-Mateo, Complementary use of transmission electron microscopy and atom probe tomography for the examination of plastic accommodation in nanocrystalline bainitic steels, Acta Mater. 59 (2011) 6117–6123. doi:10.1016/J.ACTAMAT.2011.06.024.

[38] L.C. Chang, H. Bhadeshia, Austenite films in bainitic microstructures, Mater. Sci. Technol. 11 (1995) 874–882.

[39] H. Bhadeshia, A rationalisation of shear transformations in steels, Acta Metall. 29 (1981) 1117–1130.

[40] H.-D. Wu, G. Miyamoto, Z.-G. Yang, C. Zhang, H. Chen, T. Furuhara, Incomplete bainite transformation in Fe-Si-C alloys, Acta Mater. 133 (2017) 1–9.

[41] H.K.D.H. Bhadeshia, J.W. Christian, Bainite in steels, Metall. Trans. A. 21 (1990)

767–797.

[42] S.J. Matas, R.F. Hehemann, The structure of bainite in hypoeutectoid steels, Trans. Metall. Soc. AIME. 221 (1961) 179–185.

[43] H.K.D.H. Bhadeshia, Bainite in steels: theory and practice, Maney Publishing, 2015.

[44] F.G. Caballero, M.K. Miller, S.S. Babu, C. Garcia-Mateo, Atomic scale observations of bainite transformation in a high carbon high silicon steel, Acta Mater. 55 (2007) 381–390.

[45] S.S. Babu, K. Hono, T. Sakurai, Atom probe field ion microscopy study of the partitioning of substitutional elements during tempering of a low-alloy steel martensite, Metall. Mater. Trans. A. 25 (1994) 499–508.

[46] T. Philippe, M. Gruber, F. Vurpillot, D. Blavette, Clustering and local magnification effects in atom probe tomography: a statistical approach, Microsc. Microanal. 16 (2010) 643–648.

[47] H. Bhadeshia, The lower bainite transformation and the significance of carbide precipitation, Acta Metall. 28 (1980) 1103–1114.

[48] A.H. Cottrell, B.A. Bilby, Dislocation theory of yielding and strain ageing of iron, Proc. Phys. Soc. Sect. A. 62 (1949) 49.

[49] C.C. Tasan, M. Diehl, D. Yan, M. Bechtold, F. Roters, L. Schemmann, C. Zheng, N. Peranio, D. Ponge, M. Koyama, An overview of dual-phase steels: advances in microstructure-oriented processing and micromechanically guided design, Annu. Rev. Mater. Res. 45 (2015) 391–431.

[50] C.C. Tasan, M. Diehl, D. Yan, C. Zambaldi, P. Shanthraj, F. Roters, D. Raabe, Integrated experimental–simulation analysis of stress and strain partitioning in multiphase alloys, Acta Mater. 81 (2014) 386–400.

# 8

# Recommendations for future work

Besides the understanding of microstructural evolution and damage in different rail steels established in this thesis, the following recommendations are given for future research:

1. In order to further understand the formation mechanism of WEL/BEL and the mechanism of austenite formation in pearlitic steels during the wheel-rail contacts, it is suggested to perform the laboratory scale ultrafast heating rate experiments (simulating the heating rates achieved in wheel-rail contacts). This can be achieved by the laser pulsing experiments or by the use of the recently developed railway test rig at the CiTG faculty in Delft University of Technology. This test rig can also be used to systematically study the effect of temperature and plastic deformation on the cementite dissolution in pearlitic steels and to study the damage in the presence of WELs on the rail surface. Furthermore, it is suggested to develop phase field models to understand the austenite formation in pearlitic steels at ultrafast heating occurring during the wheel-rail contacts.
2. It is suggested to utilize the fracture toughness values of the WELs for modelling the failure in rails due to the presence of WELs. These models can enable the estimation of quantities such as critical WEL thickness in rails and consequently the required grinding intervals in rails to avoid failure and also to minimize the grinding costs.
3. The BELs can be a cause of RCF damage in rails. Hence, study on the fracture behaviour of BELs requires further research. Hence, it is suggested to use similar *in-situ* fracture experiments (as shown in Chapter 4) on the BELs and compare their fracture response to the WELs and quenched martensite.
4. We discuss the microstructural evolution and damage in Cast austenitic Hadfield steels in Chapter 5 of this thesis. In order to achieve further understanding of crack growth under the impact fatigue with respect to the orientation of the deformation twins, it is suggested to develop a model using molecular dynamics for the crack growth in the presence of different twining orientations.
5. In this thesis, the damage and strain partitioning in carbide-free bainitic steels has been investigated *in-situ* under uniaxial loading conditions which undoubtedly provide a good scientific understanding. However, the damage can strongly be

affected by the complex loading conditions in switches, crossings and curved tracks. Thus, it is suggested to perform the damage and microstructural evolution study in these steels under real loading conditions via field testing. Furthermore, it is suggested to develop a micromechanical damage model for the carbide-free bainitic steels which can further expand our understanding of damage and microstructural evolution is these steels.

6. The design of carbide-free bainitic steels proposed in Chapter 7 of this thesis requires further research on the heat treatments of the real rail crossings. The crossings are dimensionally large rail components which might lead to heterogeneity in the bainitic formation characteristics from crossings surface to the depth. Hence, it is suggested to perform the isothermal bainitic heat treatment on the rail crossings and study the effect of microstructural variation in crossing depth on the damage. Additionally, it is required to study the weldability of the designed microstructure and develop a procedure for welding/repair welding.
7. Literature reports on some other bainitic steels variants such as B1400+ and Cr-B which are recently introduced for use in the railway crossings applications. It is suggested to study the damage initiation and propagation in relation with the microstructure of these steel grades.
8. The damage phenomenon in new and conventional rail steels can be affected by the use of friction modifiers. Effective application of fraction modifiers requires further research.

# Summary

In this PhD thesis, we investigate the microstructural evolution and damage in different steel grades used in railway applications such as switches, crossings and curved tracks, which are the key components in the rail transportation industries around the world. The damage in these components leads to a maintenance cost of billions of Euros per year worldwide and in the worst case scenario it can pose severe safety threats to the passengers. The damage mechanisms in these components depend on the microstructure of the steels used The increasing demand of high speed rail transportation and increasing traffic intensity require a thorough understanding of the damage mechanisms in the currently used steel grades in switches, crossings and curved tracks. This understanding can provide guidelines for the design of sustainable/damage resistant materials with an improved life time. Different rail steels such as fine pearlitic steels (R350HT), cast Hadfield steels and Continuously Cooled Carbide Free Bainitic Steels (CC-CFBS) have been investigated from the macro to the atomic scale to understand the physical mechanisms of the damage in relation with their particular microstructure.

One of the primary mechanisms of damage in fine pearlitic steels is the formation of White (WELs) and Brown Etching Layers (BELs) on rail raceways during service which cause the initiation of microcracks. These microcracks grow further into the material during the wheel-rail contacts and can finally lead to failure of the rail component. In chapter 3, we investigated the microstructural evolution of WEL and BEL from the micrometer to the atomic scale to understand their formation mechanism in pearlitic rail steels. We concluded that the plastic deformation in combination with a temperature rise during wheel-rail contact is responsible for the initial formation and further microstructural evolution of these layers. The presence of austenite in the WEL/BEL proves that the temperature rises above the austenitization temperature of pearlitic steels during the wheel-rail contact. Diffusional length calculations of C and Mn indicate that each wheel-rail contact must be considered as an individual short but intense deformation and heat treatment cycle that cumulatively determines the final microstructure of WELs/BELs. Partially fragmented primary cementite laths, enriched in Mn, depleted in Si, and surrounded by a C-gradient and dislocations were found in the BEL. We conclude that the initial step in the formation of BELs/WELs is the defect- and diffusion-assisted decomposition of the original microstructure.

In chapter 4, we investigate the microscale fracture behaviour of the WELs. We have used an *in-situ* elastic-plastic fracture mechanics approach using the J-integral to calculate the fracture toughness of the WELs. The WELs are usually considered as brittle. However, the measured fracture toughness values of 21.5 ± 3 MPa√m to 25.4 ± 2.3 MPa√m in this study reveal a semi-brittle nature of the WELs when compared with other steel microstructures.

WELs show crack branching, crack blunting and significant plasticity during crack growth due to their complex microstructure. It is found that the microstructural constituents in the WELs such as: phases (martensite/austenite), grain size, dislocation density and carbon segregation to dislocations/grain boundaries govern their fracture behaviour. The results indicate the annihilation of dislocations in some martensitic grains in the WELs. This also contributes to their semi-brittle fracture behaviour. In addition, the strain induced transformation from austenite to martensite affects the crack growth/fracture in the WELs.

In chapter 5, we discuss the microstructural evolution in the cast Hadfield steel deformed under impact fatigue loading conditions in a field-loaded railway crossing. A nanoscale twinning substructure surrounded by dislocation cells and a high density of dislocations is identified in the deformed microstructure using Electron Channelling Contrast Imaging (ECCI) and Transmission Electron Microscopy (TEM). Furthermore, the effect of intermetallic inclusions and casting defects on the damage in the Hadfield steels microstructure in rail crossings is discussed. Additionally, the strain-induced transformation of the austenite into martensite in the deformed crossing surface is studied by X-ray diffraction and magnetometer measurements. Results show no trace of this transformation under impact fatigue loading in railway crossings. ECCI in a controlled diffraction condition is used to study the fatigue crack growth behaviour in undeformed cast Hadfield steels using laboratory scale fatigue testing and the role of twin and grain boundaries on the fatigue crack growth is discussed.

In chapter 6, we probe the strain partitioning between the microstructural features present in a continuously cooled carbide-free bainitic steel together with damage nucleation and propagation. These features mainly comprise of: phases (bainitic ferrite, martensite, and blocky/thin film austenite), interfaces between them, grain size and grain morphology. An *in-situ* Micro Digital Image Correlation (μ-DIC) technique in the scanning electron microscope is used to quantify the strain distribution between the various microstructural features. The results show a strong strain partitioning between martensite, bainitic ferrite and retained austenite that provides weak links in the microstructure and creates conditions for crack initiation and propagation during deformation. Blocky austenite islands accommodate maximum local strains up to 2.3% global strain during the initial deformation and undergo a strain induced austenite to martensite phase transformation. However, the local strains are minimum in martensite regions during entire deformation stage. Narrow bainitic ferrite channels in between martensitic islands and martensite-bainitic ferrite interfaces are recognised as primary damage sites with a high strain accumulation of 30 ±1.5% and 20 ± 2.5% respectively, at a global strain of 9%. The inclination of these interfaces with the tensile direction also affects the strain accumulation and damage. Interrupted tensile testing in combination with X-Ray Diffraction (XRD) shows the strain induced transformation of large blocky retained austenite to martensite which strongly controls the local strain evolution in the microstructure.

In chapter 7, a design of high-strength steels, with fine bainitic microstructure free from inter-lath carbides, is proposed for railway crossings applications. The steel design is based on the phase transformation theory and excludes microstructural constituents like martensite, cementite and large blocky retained austenite islands from the steel's microstructure, because they are considered to be responsible for strain partitioning and damage initiation. The microstructure of the designed steels was studied using optical microscopy, scanning electron microscopy, electron backscatter diffraction, transmission electron microscopy and atom probe tomography. The microstructure consists of fine bainitic ferrite, thin film austenite and a minor fraction of blocky austenite which contribute to its high strength, appreciable toughness and damage resistance. Atom probe tomography and dilatometry results are used to assess the deviation of carbon partitioning in the retained austenite and bainitic ferrite fractions from $T_0/T_0'$ predictions. A carbon concentration of 7.9 at.% (1.8 wt.%) was measured in thin film austenite using atom probe tomography which governs its mechanical stability. Various strengthening mechanisms such as the effect of grain size, nano-sized cementite precipitation within bainitic ferrite and the Cottrell atmosphere at dislocations in bainitic ferrite are discussed. Mechanical properties of the designed microstructure are found to be superior to conventional steels used in railway crossings. The designed steel offers exceptional mechanical properties such as yield strength, tensile strength, ductility and microhardness. It also offers controlled crack growth under impact fatigue, which is the main cause of failure in crossings. *In-situ* testing using micro digital image correlation is carried out to study the micromechanical response of the designed microstructure. The results show a uniform strain distribution with low standard deviation of 1.5% from the mean local strain value of 7.7% at a global strain of 8%.

# Samenvatting

In dit proefschrift wordt de evolutie beschreven van de microstructuur en de schade in verschillende staalsoorten gebruikt in de spoorwegen zoals wissels, overgangen en in bochten in het spoor, Zij vormen de belangrijkste onderdelen in de spoorwegindustrieën over de hele wereld. De schade aan deze onderdelen leidt wereldwijd tot miljarden euro onderhoudskosten per jaar. In het ergste geval levert het ook ernstige veiligheidsrisico's op voor passagiers. De schade in genoemde componenten is afhankelijk van de microstructuur van de gekozen staalsoorten. De toenemende vraag naar hogesnelheidstreinen en de toenemende verkeersdruk vereist diepgaande kennis over de oorzaak van schade in de nu in gebruik zijnde staalsoorten in wissels, overgangen en bochten. Een beter begrip kan inzicht geven voor het ontwerp van duurzame/schadebestendige materialen met een langere levensduur. Verschillende spoorstaalsoorten zoals fijn perlitisch staal (R350HT), gegoten Hadfield-staal en "Continuously Cooled Carbide Free Bainitic Steels (CC-CFBS)" werden van macroscopische- tot atomaire schaal onderzocht om de fysische principes van schade in relatie met de microstructuur te begrijpen.

Een van de belangrijkste mechanismen van schade in fijn perlitische staalsoorten is de vorming van witte (WELs) en bruine etslagen (BELs) op railbanen Zij veroorzaken microscopische barsten. Deze microscopische scheuren groeien verder het materiaal in tijdens het wiel-railcontact en kunnen uiteindelijk leiden tot uitval van spooronderdelen. In hoofdstuk 3 bespreken we de microstructurele veranderingen van WEL en BEL van micrometer tot atomaire schaal om WELs and BELs formatiemechanisme in perlitisch railstaal te begrijpen. We concluderen dat de plastische vervorming in combinatie met een temperatuurstijging tijdens het wiel-rail contact verantwoordelijk is voor de initiële vorming en verdere microstructuurvorming van deze lagen. De aanwezigheid van austeniet in de WEL/BEL bewijst dat de temperatuur boven de austenitiseringstemperatuur van perlitisch staal stijgt tijdens het wiel-rail contact. Diffusielengte-berekeningen van C en Mn geven aan dat elk wiel-rail contact moet worden gezien als een afzonderlijke korte en intense vervorming en warmtebehandelingscyclus die tezamen de uiteindelijke microstructuur van WELs/BELs bepalen. Gedeeltelijk gefragmenteerde primaire cementiet-lamellen, verrijkt met Mn, verarmd in Si, en omgeven door een koolstof gradiënt en dislocaties zijn waargenomen in de BELs. We concluderen dat de eerste stap in de vorming van BELs/WELs is dat de oorspronkelijke microstructuur verloren gaat door defecten en diffusie.

In hoofdstuk 4 beschrijven we het breek- gedrag van de WELs op microscopische schaal. We gebruiken een in-situ benadering van elastisch-plastische breukmechanica met de J-integral om de taaiheid van de WELs te berekenen. De WELs worden gewoonlijk als broos

beschouwd, maar de gemeten taaiheid van 21.5 ± 3 MPa√m tot 25.4 ± 2.3 MPa√m in deze studie toont de semi-brosse aard van de WELs aan vergeleken met andere staalsoorten. WELs vertonen vertakking van de scheur, barstvorming en aanzienlijke plasticiteit tijdens scheurgroei, allemaal als gevolg van hun complexe microstructuur. Het blijkt dat de microstructurele bestanddelen in de WELs, zoals: fasen (martensiet/austeniet), korrelgrootte, dislocatiedichtheid en koolstofsegregatie naar dislocaties/korrelgrenzen hun breukgedrag bepalen. De resultaten wijzen op het verdwijnen van dislocaties in sommige martensitische korrels in de WELs met als gevolg de waargenomen semi-brosse breuk. Bovendien beïnvloedt de door rek tot stand gekomen transformatie van austeniet naar martensiet de scheurgroei/breuk in de WELs.

In hoofdstuk 5 bespreken we de verandering van de microstructuur in gegoten Hadfield-staal in spoorwegovergangen onderhevig aan impactvermoeiing. Een op nanoschaal gebaseerde twinning-substructuur omgeven door dislocatiecellen en dislocaties met hoge dichtheid is te zien in de vervormde microstructuur met behulp van “Electron Channelling Contrast Imaging (ECCI)” and “Transmission Electron Microscopy (TEM)”. Ook wordt het effect van intermetallische insluitingen en gietfouten op de schade in de microstructuur van Hadfield-staal in spoorwegovergangen besproken. Bovendien wordt de door rek tot stand gekomen transformatie van het austeniet naar martensiet in het vervormde materiaal bestudeerd met röntgendiffractie en magnetometermetingen. De resultaten tonen geen spoor van deze transformatie onder impact-vermoedheidsbelasting bij spoorwegovergangen. ECCI met gecontroleerde buigingstoestand wordt gebruikt om de groei van scheuren in de onvervormd gegoten Hadfield-staalsoorten te onderzoeken. Dit werd gedaan met vermoeiingstesten onder laboratiorum omstandigheden. De rol van twins en korrelgrenzen op de scheurgroei worden besproken.

In hoofdstuk 6 besteden we aandacht aan de rekverdeling tussen de onderdelen van de microstructuur van CC-CFBS, samen met het ontstaan en verspreiden van schade. Deze kenmerken bestaan voornamelijk uit fasen (bainitisch ferriet, martensiet en blokvormig / dun laags austeniet), oppervlaktes tussen fasen, korrelgrootte en korrelvorm. Een c in-situ “Micro Digital Image Correlation (μ-DIC)” optie in de elektronenmicroscoop wordt gebruikt om de rekverdeling tussen deze microstructurele kenmerken te kwantificeren. De resultaten tonen een sterke rekverdeling aan tussen martensiet, bainitisch ferriet en achtergebleven austeniet. Dit laatste vormt zwakke schakels in de microstructuur en biedt de mogelijkheid voor het ontstaan en verspreiden van scheuren tijdens vervorming. Blokvormige austeniet-eilanden ondervinden maximale lokale spanningen tot een globale spanning van 2.3% tijdens de eerste vervormingstap en ondergaan een door rek geïnitieerde transformatie van austeniet naar martensiet, terwijl anderzijds de lokale rek minimaal is in martensiet gedurende de gehele vervorming. Smalle bainitische ferrietkanalen tussen martensitische eilanden en martensiet-bainitische ferriet-grenzen worden aangemerkt als primaire locaties met hoge rekwaardes, met een additieve rek van 30 ± 1.5% en 20 ± 2.5%,

respectievelijk, voor een globaal gemeten rek van 9%. De hoeken tussen deze fasegrenzen en de trekrichting beïnvloeden eveneens de spanningsopbouw en schade door rek. Een onderbroken trekproef in combinatie met X-ray diffraction (XRD) toonde de transformatie door rek aan van groot “blocky retained” austeniet naar martensiet, welke dominant is voor de rekopbouw in de microstructuur.

In hoofdstuk 7 wordt een ontwerp voorgesteld voor zeer sterke staalsoorten, met een fijn bainitische microstructuur zonder tussenliggende carbiden, voor toepassing in spoorwegovergangen. Het staalontwerp is gebaseerd op de fasetransformatietheorie en voorkomt de vorming van microstructurele componenten zoals martensiet, cementiet en grote blokvormige austeniet-eilanden, welke naar verwachting verantwoordelijk zijn voor de rekverdeling en het ontstaan van schade. De microstructuur van de ontworpen staalsoorten werd onderzocht met behulp van optische microscopie, scanning elektronenmicroscopie, elektron backscatter diffraction, transmissie-elektronenmicroscopie en “atom probe tomography”. De microstructuur bestaat uit fijn bainitisch ferriet, dunlaags austeniet en een kleine fractie van blokachtig austeniet die bijdragen tot hun hoge sterkte, aanzienlijke taaiheid en schadebestendigheid. De resultaten van “atom probe tomography” en dilatometrie worden gebruikt om de koolstofverdeling in “retained” austeniet en bainitische ferrietfracties uit $T_0/T_0'$ voorspellingen te bestuderen. Een koolstofconcentratie van 7.9 at.% (1.8 wt.%) werd gemeten in dunne film austeniet met behulp van "atom probe tomography”, deze fractie beheerst de mechanische stabiliteit. Verschillende versterkingsmechanismen zoals het effect van korrelgrootte, “nano-sized” cementiet precipitaten in bainitisch ferriet en de Cottrell-atmosfeer bij dislocaties in bainitisch ferriet worden besproken. De mechanische eigenschappen van de ontworpen microstructuur blijken superieur te zijn aan die van conventionele staalsoorten gebruikt in spoorwegovergangen. Het ontworpen staal bezit uitzonderlijke mechanische eigenschappen zoals vloeigrens, treksterkte, ductiliteit en microhardheid. Het leidt ook tot gecontroleerde scheurgroei onder impactvermoeiing, waar scheurgroei de grootste veroorzaker is van het falen van spoorwegovergangen. In-situ testen op microschaal met behulp van μ-DIC werden uitgevoerd om het mechanische gedrag van de ontworpen microstructuur te bestuderen. De resultaten tonen een uniforme rekverdeling met een lage standaardafwijking van 1.5% ten opzichte van de gemiddelde lokale rek van 7.7% bij 8% globale rek.

# Acknowledgements

First of all, I would like to express my deepest gratitude to my promotors Prof. dr. ir. J. Sietsma and Prof. dr. ir. R. Petrov for giving me an opportunity to work on this project. This thesis would not have been possible without their continuous support and supervision. I always enjoyed the scientific discussion with both of them which led to the improvement in my knowledge and critical thinking. I spent significant amount of time at Ghent University during my research. I thank Prof. dr. R. Petrov to provide such an amazing platform for conducting this research.

I would like to thank NWO and ProRail for the funding this project. I would like to thank M2i and colleagues from M2i especially Dr. V. Savran for managing the project and helping me during my PhD in organising different collaborations. I express my gratitude to Dr. Ivan Shevstov from ProRail and Mr. Ruud van Bezooijen from ID2, for technical discussion in the project and arranging materials for this research. I thank to Dr. ir. M. Steenbergen for his ideas, discussions and help in this research.

During my exciting PhD journey, I had an opportunity to spend 1.5 years at MPIE, Dusseldorf. For this, I would like to thank Prof. Dr.-Ing. habil. Dierk Raabe and Dr. Dipl.-Ing. Michael Herbig from MPIE, Dusseldorf for providing very important platform to conduct the research in this project. Various characterisation methods such as TEM, APT, ECCI and EBSD used in the current research are performed at MPIE. I would like to thank Dr. Michael Herbig for his continuous supervision, support and scientific discussions during and even after my research stay at MPIE. Without his help and mentoring, it would not have been possible to generate high quality results in this work. I express my gratitude to him for correcting my manuscripts as well. I would also like to thank to my friends and colleagues at MPIE Dr. ir. S.K.Makeneni, Ir. A.Dutta, Ir. A. Hariharan, Ir. V. G. Arigela and Ir. A. Kini who always supported and helped me during my research stay at MPIE. I had a very pleasant time at MPIE in their company. I really appreciate their help, scientific suggestions, and moral support during my stay at MPIE. I would also like to thank Dr. C. Kirchlechner and Dr. A. K. Saxena for providing necessary facility to conduct micromechanical experiments in chapter 5 of this thesis. I express my gratitude for their help in performing these experiments, data analysis and discussions during this work. I really thank to Dr. B. Gault for discussions about the APT data reconstruction. Last but not least, I thank to my colleagues from MPIE lab: Mr. A. Strum, Mr. U. Tezins, Mr. V. Kree and Mrs. K. Angenendt for helping me during my training period at MPIE.

Working at MSE, TU Delft, I had the pleasure working with wonderful colleagues and friends: Dr. ir. C. Goulas, Mr. G. Agarwal, Dr. J. Wu, Dr. S. Karewar, Dr. Bij-Na Kim and Mr. A. M. Ravi. Thanks to you all! I always had good time in and out of the department and enjoyed your company.

I also express my deep gratitude to my colleagues from MSE Laboratories: Sander van Asperen for the support in metallography, Richard Huizenga for all the XRD measurements, Hans Homan for assistance in salt bath measurements, Dr. ir. Ton Riemslag for mechanical testing, Kees Kwakernaak for the support in SEM, and Nico Geerlofs for the help in dilatometer tests. I thank to Mrs. P. Koelman from our department for her continuous support regarding administrative processes.
I would like to thank Prof. dr. ir. J. van Turnhout and Mr. J. S. van Dokkum for translating the summary in Dutch.
After finishing my masters I left India and came to Netherlands in 2014 to purse my doctoral studies. I was new to this place and hardly knew people around me. I met Kavisha who always supported me during my stay in Netherlands. I thank her for her great company and for the time we spent together. Thank you so much for your moral and emotional support!!
Last but not least, I would like to thank my parents, Dr. Udai Raj Singh and Mrs. Vinod Bala and my elder sister Parul for the unconditional love and continuous support during my stay in the Netherlands. However, I was far away, you never let me feel the distance. I also thank my cousin brother and childhood friend Amit Sharma whom I lost recently. I thank him a lot for his continuous support and giving me the feeling that he was always there with me in tough times. I miss you a lot!!

# List of Publications

## A. International Peer-Reviewed Journals

1. A. Kumar, G. Agarwal, R. Petrov, S. Goto, J. Sietsma and M. Herbig, Microstructural evolution of white and brown etching layer in pearlitic rail steels, Acta Materialia. 171 (2019) 48-64. https://doi.org/10.1016/j.actamat.2019.04.012.
2. A. Kumar, A. Dutta, S. K. Makineni, M. Herbig, R. Petrov, and J. Sietsma, *In-situ* study of strain partitioning and damage development in a continuously cooled carbide-free bainitic steel using micro digital image correlation, Materials Science & Engineering A, 757 (2019) 107‑116, https://doi.org/10.1016/J.MSEA.2019.04.098.
3. A. Kumar, A. K. Saxena, C. Kirchlechner, M. Herbig, S. Brinkmann, R. Petrov, and J. Sietsma, *In-situ* study on fracture behaviour of white etching layers formed on rails, (Under review in Acta Materialia).
4. A. Kumar, S. K. Makineni, A. Dutta, C. Goulas, M. Steenbergen, R. Petrov, and J. Sietsma, Design of a high strength and damage resistant carbide-free fine bainitic steels for railway crossings applications, Materials Science & Engineering A, 759, 210-223, (2019) https://doi.org/10.1016/j.msea.2019.05.043.
5. A. Kumar, S. K. Makineni, R. Petrov, J. Sietsma and M. Herbig, A method to clean atom probe specimens after exposure to an electron beam, (To be submitted).
6. A.Kumar, R.Petrov, and J.Sietsma, Damage and microstructure evolution in cast Hadfield steels used in railway crossings, (Submitted as a chapter in Springer book).
7. S. K. Makineni, A. Kumar, M. Lenz, P. Kontis, T. Meiners, C. Zenk, S. Zaefferer, G. Eggeler, S. Neumeier, E. Spieker, D. Raabe, and B. Gault, On the diffusive phase transformation mechanism assisted by extended dislocations during creep of a single crystal CoNi-based superalloy, Acta Materialia. 155 (2018) 362–371. https://doi:10.1016/J.ACTAMAT.2018.05.074.
8. S. K. Makineni, M. Lenz, P. Kontis, Z.Li, A. Kumar, P.J. Felfer, S. Neumeier, M. Herbig, E. Spieker, D. Raabe, and B. Gault, Correlative microscopy - novel methods and their applications to explore 3D chemistry and structure of nanoscale lattice defects: A case study in super alloys, *JOM*, 2018, pp. 1-8. https://doi.org/10.1007/s11837-018-2802-7.
9. G. Agrawal, A. Kumar, M. Hermans, and I. Richardson, Study of solidification cracking in a transformation induced plasticity-aided steel, *Metallurgical and Materials Trans- actions*, 2018, https://doi.org/10.1007/s11661-018-4505-7.
10. A. Kwiatkowski da Silva, G. Inden, A. Kumar, D. Ponge, B. Gault, and D. Raabe, Competition between formation of carbides and reversed austenite during tempering of a medium-manganese steel studied by thermodynamic-kinetic simulations and atom

probe tomography, *Acta Materialia*, 2018, https://doi.org/10.1016/j.actamat.2018.01.022.

**11.** R. Kumar, R. Anant, P. K. Ghosh, A. Kumar, and B. P. Agrawal, Influence of PC-GTAW Parameters on the Microstructural and Mechanical Proper- ties of Thin AISI 1008 Steel Joints, *Journal of Materials Engineering and Performance*, 2016, pp. 3756-3765. https://doi.org/10.1007/s11665-016-2211-4.

**12.** C. Goulas, A. Kumar, M. G. Mecozzi, M. Herbig, D. Raabe, R. Petrov, and J. Siestma, Atomic-scale investigations of isothermally formed bainite microstructures in 51CrV4 spring steel, *Materials Characterization*, https://doi.org/10.1016/j.matchar.2019.03.038

**13.** A. K. Saxena, A. Kumar, S. Brinckmann, M. Herbig, G. Dehm, C. Kirchlechner, Micro fracture investigations of white etching layers, Materials & Design (2019), https://doi.org/10.1016/j.matdes.2019.107892.

**14.** G. Agarwal, A. Kumar, I.M. Richardson, and M.J.M. Hermans, Evaluation of solidification cracking susceptibility during laser welding in advanced high strength automotive steels, (Under review in Materials & Design).

**15.** A. M. Ravi, A. Kumar, M. Herbig, J. Sietsma, M. J. Santofimia, On the role of austenite grain boundaries during formation of bainite in steels, (To be submitted).

**16.** M. A. Valdes, C. A. Casero, A. Kumar, I. Sabirov and R. Petrov, Evolution of microstructure during conventional and ultrafast heating of a low carbon steel: the effect of soaking time, (Under review in Materials Characterization).

**17.** O. Hajizad, A. Kumar, Z. Li, R. Petrov, J. Sietsma and R. Dollevoet, Influence of microstructure on the mechanical properties of bainitic steels used in railway applications, (Submitted to Metals).

**18.** M. Messaadi, M. Oomen and A. Kumar, Friction modifiers effects on tribological behaviour of bainitic rail Steels, (Under review in Tribology International).

**19.** J. Wu, A. Kumar, A. Kini, R. Petrov and J. Sietsma, Advanced characterizations of white etching cracks in bearing steels using correlative transmission electron microscopy and atom probe tomography, (To be submitted).

**20.** J. Wu, A. Kumar, S. Makineni, B. Gault, J. Sietsma, D. Tran, B. Pennings, and R. Petrov, Characterization of complex precipitation in surface nitrided Fe-Ni-Mo-Co maraging steel using transmission electron microscopy and atom probe tomography, (To be submitted).

**21.** J. Wu, A. Kumar, S. Makineni, B. Gault, J. Sietsma, D. Tran, B. Pennings, and R. Petrov, Study of precipitations in maraging steel with multiple nitride-forming elements after surface nitriding, (To be submitted).

**22.** O. Hajizad, A. Kumar, Z. Li, R. Petrov, J. Sietsma and R. Dollevoet, Micromechanical modelling of strain partitioning and damage initiation in a continuously cooled carbide-free bainitic steels and validation using in-situ tensile experiments, (To be submitted).

## B. International conferences and symposiums

1. A. Kumar, M. Herbig, R. Petrov, and J. Sietsma, Microstructural evolution of white and brown etching layer in pearlitic rail steels, oral presentation in International Symposium on Nano & Micro Scale Damage in Metals, February 2018, Utrecht, the Netherlands.
2. A. Kumar, M. Herbig, R. Petrov, and J. Sietsma, In-situ study on strain partitioning and damage in a continuously cooled carbide-free bainitic steel using micro digital image correlation, Oral presentation in M2i Conference, December 2017, Utrecht, the Netherlands.
3. A. Kumar, M. Herbig, R. Petrov, and J. Sietsma, Study on strain partitioning and damage in a carbide-free bainitic steel, Oral presentation in the International Symposium on Metallurgical cause of Failure in Rail Steels, August 2017, Copenhagen, Denmark.
4. A. Kumar, M. Herbig, R. Petrov, and J. Sietsma, Metallurgical cause of rolling contact fatigue damage in rail steels, Oral presentation in International Conference on Fatigue and Failure Analysis in Materials, July 2017, Erlangen, Germany.
5. M. Herbig, Y. Li, A. Kumar, L. Morsdorf, Y. Qin, D. Mayweg, S. Goto, J. Sietsma, R. Petrov, D. Raabe, The role of carbon in the formation of white etching cracks, oral presentation at Thermes 2018 Annual Meeting & Exhibition, July 2018, Paris, France.

# About the Author

## Ankit Kumar

**Professional Experience and Education:**

| | |
|---|---|
| **07.2018-Present** | **PostDoc researcher, Delft University of Technology,**<br>**Project topic: UN**derstanding the microstructural essence of **D**amage **E**volution in **R**olling contact fatigue **(UNDER)**<br>**Supervisors:** Prof. J.Sietsma and Prof. R. H. Petrov |
| **05.2014-04.2018** | **Ph.D. candidate, Delft University of Technology,**<br>**Thesis title:** A multiscale study of microstructural evolution and damage in rail steels.<br>**Promoters:** Prof. J.Sietsma and Prof. R. H. Petrov |
| **01.2016-07.2017** | **Guest Researcher, Max Planck institute for Iron Research,**<br>**Supervisor:** Dr. M. Herbig |
| **07.2011-08.2013** | **Master of Technology in Metallurgy & Materials Engineering,**<br>**Indian Institute of Technology, Roorkee,**<br>Dissertation: Effect of pulse parameters and welding speed in PGTAW on the weld microstructure and the mechanical properties of high strength steels. |